

Dissertation zur Erlangung des Doktorgrades
der Fakultät für Chemie und Pharmazie
der Ludwig-Maximilians-Universität München

Electron energy loss spectroscopy of novel oxide-
and nitride-based nanostructured materials



LMU

LUDWIG-
MAXIMILIANS-
UNIVERSITÄT
MÜNCHEN

von
Teresa Katharina Dennenwaldt
aus Saarbrücken

2013

**Dissertation zur Erlangung des Doktorgrades
der Fakultät für Chemie und Pharmazie
der Ludwig-Maximilians-Universität München**

Electron energy loss spectroscopy of novel oxide- and
nitride-based nanostructured materials

Teresa Katharina Dennenwaldt

aus

Saarbrücken

2013

Erklärung

Diese Dissertation wurde in Sinne von § 7 der Promotionsordnung vom 28. November 2011 von Frau Professor Dr. Christina Scheu von der Fakultät für Chemie und Pharmazie betreut.

Eidesstattliche Versicherung

Diese Dissertation wurde selbständig und ohne unerlaubte Hilfe erarbeitet.

München, den 01.10.2013

.....

(Unterschrift des Autors)

Dissertation eingereicht am 01.10.2013

1. Gutachter: Prof. Dr. Christina Scheu

2. Gutachter: Prof. Dr. Wolfgang Schnick

Mündliche Prüfung am 04.11.2013

Meinen Eltern

Table of content

Table of content	I
List of abbreviations	V
List of symbols	IX
List of figures	XI
List of tables	XV
1 Introduction	1
1.1 Electron energy loss spectroscopy in the transmission electron microscope	1
1.2 Aim of the thesis	5
1.3 Chapter references	6
2 Materials	9
2.1 Nitride compounds.....	9
2.1.1 Silicon nitride.....	9
2.1.2 Phosphorus(V) nitride	11
2.1.3 Beryllium nitride	13
2.1.4 Beryllium phosphorus nitride.....	14
2.2 Silica and its chemical analogue phosphorus oxynitride.....	16
2.2.1 Silica.....	16
2.2.2 Phosphorus oxynitride	17
2.3 Iron oxides on alumina	19
2.3.1 Aluminium(III) oxide.....	19
2.3.2 Iron oxides and iron titanium oxide	20
2.4 Chapter references	21
3 Characterization methods	23
3.1 Powder X-ray diffraction	23
3.2 Electron microscopy and related techniques	24

3.2.1	Scanning electron microscopy	26
3.2.2	Focused ion beam microscopy	27
3.2.3	Transmission electron microscopy	28
3.2.4	Analytical techniques	35
3.2.5	Electron tomography.....	46
3.3	TEM sample preparation	48
3.3.1	Dropping method for TEM specimen preparation	48
3.3.2	FIB microscopy for TEM specimen preparation.....	48
3.4	Chapter references	49
4	Experimental details.....	51
4.1	Synthesis of silica-based nanotubes, hollow particles and flakes.....	51
4.1.1	Synthesis of the starting materials: phosphoryl triamide $OP(NH_2)_3$ and thiophosphoryl triamide $SP(NH_2)_3$	51
4.1.2	Silica-based nanotubes, hollow particles and flakes	51
4.2	Synthesis of BeP_2N_4	52
4.3	Synthesis of thin Fe-Ti-O films	52
4.4	Equipment.....	52
4.4.1	Powder X-ray diffraction	52
4.4.2	Electron and ion microscopes	53
4.5	Chapter references	55
5	Silica-based nanotubes	57
5.1	Template-free inorganic synthesis of silica-based nanotubes and their self-assembly to mesocrystals.....	57
5.1.1	Introduction	57
5.1.2	Experimental details.....	58
5.1.3	Results and discussion.....	59
5.1.4	Conclusion.....	64

5.1.5	Chapter references	65
5.2	Chemical stability and bonding behavior of silica-based nanotubes and their 3D assembly	67
5.2.1	Introduction	67
5.2.2	Experimental details.....	68
5.2.3	Results and discussion.....	69
5.2.4	Summary and conclusion	78
5.2.5	Chapter references	80
5.3	Further investigation of the silica-based nanotubes, their 3D assembly and flakes	82
5.3.1	Reaction products.....	82
5.3.2	Synthesis with an increased amount of O	83
5.3.3	Influence of the Si content on the SBNTs diameter.....	85
5.3.4	Focused ion beam lamella of a 3D assembly of SBNTs.....	87
5.3.5	Tomography of a SBNTs 3D assembly	89
5.3.6	Bonding behavior of the flakes.....	92
5.3.7	Chapter references	94
6	BeP ₂ N ₄ compound.....	95
6.1	High resolution spectroscopy of bonding in a BeP ₂ N ₄ compound	95
6.1.1	Introduction	95
6.1.2	Experimental details.....	97
6.1.3	Results and discussion.....	98
6.1.4	Conclusion.....	102
6.1.5	Chapter references	103
6.2	Band gap determination of BeP ₂ N ₄	105
6.2.1	Band gap determination in literature	105
6.2.2	Band gap determination of the phenakite-type BeP ₂ N ₄	109

6.2.3	Chapter references	111
7	$\text{Fe}_{2-x}\text{Ti}_x\text{O}_3/\text{Fe}_2\text{O}_3$ thin films grown on Al_2O_3	113
7.1	Insights into the structural, electronic and magnetic properties of $\text{Fe}_{2-x}\text{Ti}_x\text{O}_3/\text{Fe}_2\text{O}_3$ thin films with $x = 0.44$ grown on Al_2O_3 (0001).....	113
7.1.1	Introduction	113
7.1.2	Experimental details.....	115
7.1.3	Results and discussion.....	118
7.1.4	Summary and conclusion	134
7.1.5	Chapter references	135
7.2	Fe_2O_3 thin film grown on Al_2O_3 (0001) containing nominal one unit cell of $\text{Fe}_{2-x}\text{Ti}_x\text{O}_3$	138
7.2.1	EELS analysis	138
7.2.2	Chapter references	140
8	Summary and conclusion.....	141
8.1	Silica-based nanotubes	141
8.2	BeP_2N_4 compound	142
8.3	$\text{Fe}_{2-x}\text{Ti}_x\text{O}_3/\text{Fe}_2\text{O}_3$ thin films grown on Al_2O_3	143
9	Appendix.....	145
10	Curriculum vitae.....	147
11	List of publications and presentations.....	149
11.1	Scientific Publications	149
11.2	Conference contributions	150
12	Danksagung	151

List of abbreviations

2D	Two-dimensional
3D	Three-dimensional
ADF	Annular dark field
AE	Auger electrons
AFM	Atomic force microscopy
ALD	Atomic layer deposition
AO	Atomic orbital
BF	Bright field
BSE	Backscattered electrons
CCD	Charged-coupled device
CNT	Carbon NT
CTEM	Conventional TEM
CTF	Contrast transfer function
DART	Discrete algebraic reconstruction technique
DF	Dark field
DFT	Density functional theory
DOS	Density of states
EDX	Energy dispersive X-ray spectroscopy
EELS	Electron energy loss spectroscopy
E_F	Fermi energy
EFTEM	Energy-filtered TEM

ELNES	Electron energy loss near-edge fine structure
EM	Electron microscopy
ET	Electron tomography
EXELFS	Extended energy loss fine structure
FBP	Filtered back projection
FFT	Fast Fourier transform
FIB	Focused ion beam
FWHM	Full width at half maximum
HAADF	High angle annular dark field
HREELS	High-resolution EELS
HRTEM	High-resolution TEM
LDA	Local density approximation
LEED	Low energy electron diffraction
MBE	Molecular beam epitaxy
MO	Molecular orbital
NT	Nanotube
NW	Nanowire
OLCAO	Orthogonalized linear combination of atomic orbitals
PDA	Photodiode array
PDOS	Partial DOS
PEELS	Parallel EELS
PL	Plasmon

PXRD	Powder X-ray diffraction
SAD	Selected area diffraction
SBNTS	Silica-based NT
SE	Secondary electrons
SEM	Scanning electron microscopy
SIRT	Simultaneous iterative reconstruction technique
SNR	Signal-to-noise ratio
SNT	Silica NT
SQUID	Superconducting quantum interference device
STEM	Scanning TEM
TEM	Transmission electron microscopy
UHV	Ultra-high vacuum
VEELS	Valence EELS
XRD	X-ray diffraction
YAG	Yttrium aluminium garnet
ZLP	Zero loss peak

List of symbols

\AA	Ångström
a, b, c	Lattice parameters
c	Speed of light
C_A, C_B	Concentration of element A and B
C_c	Chromatic aberration
C_s	Spherical aberration
d	Distance of lattice plane
e	Elementary charge
E	Energy
E_g	Band gap energy
eV	Electron volt ($1,60 \cdot 10^{-19} \text{ kg} \cdot \text{m}^2 \cdot \text{s}^{-2}$)
h	Planck constant or hour
hkl	Miller indices
I_A, I_B	Intensity of element A and B
K	Kelvin
K_{AB}	Cliff-Lorimer factor
keV	Kilo electron volt
L	Litre
m_e	Effective electron mass
min	Minute
mm	Millimeter (10^{-3} m)

mrad	Milliradian
<i>n</i>	Order of diffraction
<i>N</i>	Number of particles
nm	Nanometer (10^{-9} m)
<i>p</i>	Pressure or momentum
R	Distance
s	Seconds
T	Temperature
U	Voltage or inner energy
V	Volume
<i>v</i>	Frequency or velocity
Δf	Defocus
ε	Extinction coefficient
θ	Bragg angle
λ	Wavelength
Λ	Mean free path
λL	Camera constant
μm	Micrometer (10^{-6} m)
ω	Angular frequency
\hbar	Reduced Planck constant

List of figures

Figure 2.1.1. The three polymorphs of Si_3N_4	10
Figure 2.1.2. The polymorphs of P_3N_5 and building units.....	12
Figure 2.1.3. Schematic drawing of the polymorphs of Be_3N_2	14
Figure 2.1.4. Schematic drawing of the two BeP_2N_4 polymorphs.....	15
Figure 2.2.1. Schematic drawing of crystalline and amorphous SiO_2	16
Figure 2.2.2. Schematic drawing of the polymorphs of PON.....	18
Figure 2.3.1. Schematic drawing of the two polymorphs of Al_2O_3	19
Figure 2.3.2. Schematic drawing of the crystal structures of different iron oxides.....	20
Figure 3.1.1. Description of the Bragg equation.....	24
Figure 3.2.1. Schematic drawing of the generated signals stemming from interaction of the electron beam with a thin sample.....	25
Figure 3.2.2. Schematic drawing of a SEM.	27
Figure 3.2.3. Schematic drawing of a FIB microscope.	28
Figure 3.2.4. Schematic drawing of the components of a TEM.....	29
Figure 3.2.5. Schematic drawing of the spherical aberration.....	30
Figure 3.2.6. Schematic drawing of the chromatic aberration effect.....	31
Figure 3.2.7. Schematic drawing of the ray path resulting in astigmatism.....	31
Figure 3.2.8. CTF for the Scherzer defocus.....	34
Figure 3.2.9. Schematic drawing of the different detectors used in STEM mode.....	35
Figure 3.2.10. Schematic drawing of a relaxation process of an inner shell electron and the corresponding standard spectroscopic notation.	38
Figure 3.2.11. Relationship between the DOS and the ELNES.....	40
Figure 3.2.12. Schematic drawing of the basic regions of an EEL spectrum.....	41
Figure 3.2.13. Schematic drawing of the five characteristic edge shapes showing.....	43
Figure 3.2.14. Schematic drawing of a Gatan PEELS system.	45
Figure 3.2.15. Schematic drawing of a single-axis tilt-series.....	47
Figure 3.3.1. Schematic drawing of the dropping method.....	48
Figure 3.3.2. Schematic drawing of a 3 mm TEM half-ring grid with a FIB lamella.....	49
Figure 5.1.1. SEM image of the as-synthesized sample showing nanotubes tending to form 3D networks, shapeless flakes and cluster of particles.....	60
Figure 5.1.2. TEM images of as-synthesized samples.....	62

Figure 5.1.3. SEM images of an as-synthesized sample.....	64
Figure 5.2.1. TEM image with the corresponding diffraction pattern of the SBNTs, EDX spectrum and EEL spectra of an individual SBNT	70
Figure 5.2.2. Comparison of the ELNES of the amorphous bulk compounds Si_3N_4 , SiO_2 and of an individual SBNT	72
Figure 5.2.3. SEM image of SBNTs assemblies synthesized at 700 °C.....	73
Figure 5.2.4. EDX mapping on a SBNT synthesized at 700 °C	73
Figure 5.2.5. STEM images of SBNTs and the corresponding EEL spectra	74
Figure 5.2.6. Low-loss region of the EELS spectrum of SBNTs	76
Figure 5.2.7. pH study of SBNTs synthesized at 400 °C.....	78
Figure 5.3.1. SEM image showing an overview of the specimen with the three reaction products.....	82
Figure 5.3.2. Sample synthesized with an increased O concentration at 500 °C.....	83
Figure 5.3.3. EDX measurements of SBNTs	84
Figure 5.3.4. Sample synthesized at 700 °C with a high Si content.....	85
Figure 5.3.5. Diagram and table showing the dependency of the SBNTs diameter depending on the synthesis temperature	86
Figure 5.3.6. Samples synthesized at 700 °C.....	87
Figure 5.3.7. TEM images of a lamella showing SBNTs synthesized with a low amount of Si.....	88
Figure 5.3.8. STEM image of a SBNT wall synthesized with a low amount of Si at 300 °C and the corresponding EELS measurements.....	89
Figure 5.3.9. STEM images of the SBNTs assembly for ET showing the network.....	90
Figure 5.3.10. ET of the SBNTs assembly	91
Figure 5.3.11. STEM images of SBNTs networks.....	91
Figure 5.3.12. TEM images of a flake, a P_3N_5 particle and a PON particle.....	92
Figure 5.3.13. EEL spectra of a flake, P_3N_5 and PON.....	93
Figure 6.1.1. Crystal structure of the phenakite-type phase.....	98
Figure 6.1.2. Calculated and experimental EEL spectra of the phenakite-type BeP_2N_4 .	100
Figure 6.2.1. ZLP acquired without and with a monochromator	105
Figure 6.2.2. Correlation between sample thickness and Cerenkov effects.....	107
Figure 6.2.3. VEEL spectra of diamond.....	108
Figure 6.2.4. Band gap determination of SiO_2	109

Figure 6.2.5. Band gap determination for the phenakite-type BeP_2N_4	110
Figure 7.1.1. L-scans of sample 3 along the hematite (01L) and (10L) rod.....	120
Figure 7.1.2. Interface between the substrate and the hematite thin film.....	121
Figure 7.1.3. Raman spectra of films grown by simultaneous deposition of Fe and Ti with different relations of Fe:Ti.....	122
Figure 7.1.4. TEM image of the thin film on Al_2O_3 with the diffraction patterns and the corresponding EDX spectra.....	124
Figure 7.1.5. HRTEM image of the interface between substrate and the hematite layer and HAADF-STEM image of the same interface with the resulting EDX spectrum.....	125
Figure 7.1.6. HRTEM image of the interface between the hematite and the $\text{Fe}_{2-x}\text{Ti}_x\text{O}_3$ layer and corresponding EEL spectra.....	127
Figure 7.1.7. Fe-L ₃ -edges of the hematite/ $\text{Fe}_{2-x}\text{Ti}_x\text{O}_3$ interface.....	129
Figure 7.1.8. 25 nm Fe_2O_3 annealed in O_2	131
Figure 7.1.9. 25 nm Fe_2O_3 + 0.4 nm $\text{Ti}_{1-x}\text{O}_2$ + 3 nm Fe_2O_3 annealed in O_2	132
Figure 7.1.10. 25 nm Fe_2O_3 + 25 nm $\text{Fe}_{2-x}\text{Ti}_x\text{O}_3$ + 3nm Fe_2O_3	133
Figure 7.2.1. Thin film of a Fe_2O_3 layer and nominal one unit cell of $\text{Fe}_{2-x}\text{Ti}_x\text{O}_3$	138
Figure 7.2.2. EEL spectra of the $\text{Fe}_{2-x}\text{Ti}_x\text{O}_3$ layer.....	139
Figure 9.3.1. EDX measurements of SBNTs and a flake.....	145
Figure 9.3.2. SEM image of a polymeric agglomeration indicating the starting point for NT growth.....	145

List of tables

Table 2.1.1. Crystallographic parameters of the three Si_3N_4 modifications.....	10
Table 2.1.2. Crystallographic parameters of the three P_3N_5 modifications.....	12
Table 2.1.3. Crystallographic parameters of the five Be_3N_2 modifications.....	13
Table 2.1.4. Crystallographic parameters of the BeP_2N_4 modifications.....	15
Table 2.2.1. Crystallographic parameters of the four PON modifications.....	17
Table 2.3.1. Crystallographic parameters of the three Al_2O_3 modifications.....	20
Table 2.3.2. Crystallographic parameters of the three iron oxides.....	21
Table 4.4.1. Used electron microscopes.....	54
Table 5.2.1. Position of the first maxima and their relative peak distances for the minor features of the Si-L-edge of the SBNTs and the two references SiO_2 and Si_3N_4	72
Table 5.3.1. Position of the first maxima and their relative peak distances for the minor features of the P-L-edge of the flakes and the two references P_3N_5 and PON.....	94
Table 6.1.1. Position of the first maxima of the experimental and calculated spectra for the Be-K-, P- $\text{L}_{2,3}$ -, and N-K-edges.....	100
Table 6.2.1. Band gap energies of <i>h</i> -GaN using different spectrum processing techniques of the ZLP.....	106
Table 7.1.1. Distances of the ELNES features A, B and C of the Ti- $\text{L}_{2,3}$ -, O-K- and Fe- $\text{L}_{2,3}$ -edges.....	128

1 Introduction

1.1 Electron energy loss spectroscopy in the transmission electron microscope

Nanotechnology is a current topic in science and engineering as nanomaterials exhibit many fascinating properties compared to their bulk counterpart. Nanoscience concerns with the design or synthesis of novel materials and their characterization for diverse applications, e.g. in semiconductor physics, electronics, medicine or molecular biology. Thereby, at least one dimension of the device is on the nanometer scale (10^{-9} m).¹ In these dimensions the interaction of individual molecules or even atoms becomes important and cannot be neglected as quantum mechanical effects arise. The investigation of nanomaterials is challenging due to their small sizes. A powerful technique for analyzing micro- and nanoobjects concerning their structural, chemical and electronic properties in depth is transmission electron microscopy (TEM).² Over the last decades, the development of spherical (C_s) and chromatic (C_c) aberration-correctors clearly improved the imaging in the TEM and lead to a spatial resolution less than 1 Ångström.³⁻⁶ Without these corrections images appear blurry and the information is limited or requires image simulation to get extracted.

The electron beam of a TEM interacts in many ways with the sample, such as elastic scattering which is used for imaging and diffraction experiments. Electron energy loss spectroscopy (EELS) studies the energy losses of electrons after they have been inelastically scattered by the sample. The achieved spectrum can be subdivided in three main regions, the zero loss peak (ZLP) region, the low loss region and the core loss region. EELS is widely used to analyze the chemical and electronic structure of nano- and micro-materials at the nanoscale with high spatial and energy resolution at the same time.⁷⁻⁹ This technique was developed in the 1940s by J. Hillier and R. F. Baker. EELS was not frequently applied until the 1990s where the instrumentation design has become much more advanced. The development of electron monochromators in the last decade even improved the energy resolution considerably. A monochromator reduces the energy spread of the electrons from the TEM source down to 0.1 eV.^{9,10} This achievement allows to study fine details of the electron energy loss near-edge fine structure (ELNES) in the core-loss region associated with each element specific

ionization edge and also the in depth analysis of the low loss region. With valence electron energy loss spectroscopy (VEELS) physical parameters like the dielectric function or the band gap of materials can be determined.⁷⁻⁹ A sub-Å spatial resolution for EELS can in principle be achieved by combining aberration-corrected TEMs with a monochromator.¹¹⁻¹⁴

The ELNES, arising within ~ 50 eV of the edge onset, carries information about the electronic structure and the bonding behavior of an element and acts as fingerprint for a material.⁷⁻⁹ In principle, the extended energy loss fine structure (EXELFS), occurring after 50 eV of the edge onset, can be used to study the bond lengths and the coordination number of an element but is not commonly investigated due to the low signal-to-noise ratio (SNR).^{7,8} As every element exhibits a characteristic energy loss, the chemical composition can be determined. In addition, the intensity of the ionization edge is proportional to the concentration of the element so that elements can be quantified and their distribution in the sample analyzed. A great advantage of EELS is the ability to investigate light elements ($Z > 2$) in solids, like e.g. B, Be, C, N or O.¹⁵ Most methods are not suitable for the quantification of light elements as they exhibit a very low fluorescence yield and their low energy X-rays cannot be recorded sufficiently due to the intrinsic characteristics of an energy dispersive X-ray spectroscopy (EDX) detector. The detection limit for EELS is in the range of 0.5 - 1 at.% and the error of the relative concentration ratios exhibits typically $\pm 10\%$.¹⁵ Brydson et al.¹⁵ showed nicely the potential of EELS for the characterization of carbon materials with incorporations of light elements at high spatial resolution concerning their composition and bonding.¹⁵ Idrobo et al.¹⁶ analyzed silicon nitride ceramics and could determine the atomic arrangement and electronic structure of light elements like N and O at their interfaces to amorphous SiO₂ with aberration-corrected TEM and EELS. Soto et al.¹⁷ investigated N containing thin films and compared their EEL spectra to the pure elements. A clear difference in the ELNES could be observed as the loss processes are strongly influenced by the incorporation of N atoms. This leads to a different electronic configuration and is visible in the change of the ELNES and in the chemical shift of the edge onset.¹⁷ The chemical shift in the edge onset carries information about the valence state or bonding behavior of a material. Cu alloys and oxides for example are widely studied and the Cu-L_{2,3}-edge exhibit a significant different chemical shift depending on the composition, i.e. CuO has a much lower edge onset than metallic Cu or CuO₂.^{9,18} Even more information

about the valence state and the coordination is given by the shape of the ELNES. For example, C exhibits diverse ELNES features depending on its hybridization state (sp^2 - or sp^3 -bonded).¹⁵ The same is true for the Cu- $L_{2,3}$ -ELNES features. Tan et al.¹⁹ investigated V/Mn/Fe oxides with high accuracy concerning their chemical shifts, white-line ratios and shape of the ELNES to correlate the oxidation state of the transition metals to their EELS data.²⁰ They found that the $L_{2,3}$ -edges of the transition metals exhibit a similar edge onset and ELNES when having the same oxidation state. Unknown compounds can therefore be compared to known materials and information about their electronic structure can be achieved. Another method to investigate new compounds concerning their local atomic environment and bonding behavior is the comparison of the experimental ELNES with theoretical calculations.^{7,21-23} The spectral details in the ELNES can be predicted and correlated to the electronic structure of the material.

High-energy resolution EELS (HREELS) with spatial resolution in the nanometer or sub-nanometer regime is a suitable method to analyze the electronic structure of materials. In combination with scanning TEM (STEM) imaging defect states, precipitates, grain boundaries or interfaces can directly be studied and correlated with the change in the local electronic structure.²⁴ This is for example of high interest for ceramic materials where their behavior is influenced by such point defects or amorphous interfacial films.²⁴ Furthermore, doped materials can be investigated on the atomic scale. Often, dopants are located at grain boundaries and with HREELS their atomic arrangement and their effect on the electronic structure of the material can be studied.^{24,25} Kimoto et al.¹², Muller²⁶ and Colliex et al.²⁷ performed atomic-column as well as single-atom and atom-by-atom EELS on heavy elements like lanthanides and on the light element C. They were able to show that two individual atoms, whose atomic number only differs by one can be distinguished. In addition, they were able to identify the valence state of a single atom with HREELS.

On the other hand, the investigation of heavy elements is not easy and EELS requires very thin samples to avoid multiple scattering. The interpretation of EEL data is not trivial as many factors can cause artifacts or influence the spectrum. Theoretical calculation and VEELS can also be combined for the investigation of the optical properties like the dielectric function and the band gap of specimen.^{23,28,29} The determination of the band gap in the TEM with VEELS offers the great advantage that it

can be studied at the nanometer scale due to the high spatial resolution but several effects, like Cerenkov losses³⁰ or the delocalization of low energy excitations³¹ can falsify the determined value or complicate the interpretation.³²⁻³⁴ Due to the delocalization a resolution in the Å regime (10^{-10} m) cannot be achieved in the low-loss region.^{12,26} To interpret the acquired data in the range of $\sim 0 - 10$ eV correctly, the ZLP has to be removed in the right way. This can be done by several methods such as the Fourier-log or ω -ratio deconvolution, the ZLP subtraction or the linear fit method and is strongly dependent on the material.^{32,35,36}

Overall, EELS is a powerful technique enabling the determination of electronic, physical, chemical and structural properties of materials with nanometer or sub-nanometer resolution. This method allows also the investigation of light elements in depth. The acquiring and interpretation of the data is not trivial and is strongly dependent on the material.

1.2 Aim of the thesis

The objective of this thesis is the synthesis and investigation of novel materials concerning their chemical, structural and physical behavior. For the characterization, TEM and its analytical techniques served as main analytical method. Especially EELS played a crucial role for the in depth analysis of the materials.

Three systems are selected and investigated covering the wide range of the analytical possibilities of EELS. The first system are silica-based nanotubes (SBNTs) and the two other reaction compounds, hollow particle and flakes. These materials are composed of Si, O, N and P. Synthesis parameters are varied to investigate the building behavior of the SBNTs. This system is ideal to study its structural and chemical properties with EELS as the light elements O and N cannot be analyzed quantitatively with other methods. The findings are described in Chapter 5.

The second system exhibiting another light element is the phenakite-type structure of BeP_2N_4 . This compound is investigated concerning the edge onsets, relative peak positions and shapes of the Be-K-, P-L_{2,3}- and N-K-ELNES. The results are correlated to density functional theory (DFT) calculations. The aim is the illumination of the coordination and bonding behavior of this material. Challenging is the structural investigation of the light element Be. The comparison of the experimentally data with theoretical calculations as well as the investigation of the low loss region are shown in Chapter 6.

Thin films of $\text{Fe}_{2-x}\text{Ti}_x\text{O}_3/\text{Fe}_2\text{O}_3$ with $x = 0.44$ grown on Al_2O_3 (0001) are analyzed concerning the growth conditions, magnetic properties, chemical composition and structural behavior. Therefore, the results obtained from Raman spectroscopy, X-ray diffraction (XRD) and superconducting quantum interference device (SQUID) experiments are combined and compared to TEM investigations. The crystallinity of the thin films is studied with high-resolution TEM (HRTEM) and electron diffraction. Their chemical composition and structural behavior are analyzed at the nanoscale with EDX and EELS experiments. Thereby, the interface area between Fe_2O_3 and $\text{Fe}_{2-x}\text{Ti}_x\text{O}_3$ is investigated in depth. The findings are discussed in Chapter 7.

1.3 Chapter references

- ¹ R. Saini, S. Saini, and S. Sharma, *Journal of Cutaneous and Aesthetic Surgery* **3**, 32 (2010).
- ² D.B. Williams and C.B. Carter, *Transmission Electron Microscopy*, 2 ed. (Springer Science+Business Media, New York, 2009), p. 760.
- ³ O.L. Krivanek, N. Dellby, and a. R. Lupini, *Ultramicroscopy* **78**, 1 (1999).
- ⁴ M. Haider, H. Müller, S. Uhlemann, J. Zach, U. Loebau, and R. Hoeschen, *Ultramicroscopy* **108**, 167 (2008).
- ⁵ P.C. Tiemeijer, M. Bischoff, B. Freitag, and C. Kisielowski, *Ultramicroscopy* **114**, 72 (2012).
- ⁶ P.C. Tiemeijer, M. Bischoff, B. Freitag, and C. Kisielowski, *Ultramicroscopy* **118**, 35 (2012).
- ⁷ R. Brydson, *Electron Energy Loss Spectroscopy*, 1 ed. (BIOS Scientific Publishers Limited, Oxford, 2001), p. 137.
- ⁸ R.F. Egerton, *Electron Energy-loss Spectroscopy in the Electron Microscope*, 3 ed. (Springer Science+Business Media, New York, 2011), p. 491.
- ⁹ V.J. Keast, *Materials Characterization* **73**, 1 (2012).
- ¹⁰ K. Kimoto, G. Kothleitner, W. Grogger, Y. Matsui, and F. Hofer, *Micron* **36**, 185 (2005).
- ¹¹ M. Bosman, V.J. Keast, J.L. García-Muñoz, A.J. D’Alfonso, S.D. Findlay, and L.J. Allen, *Physical Review Letters* **99**, 086102 (2007).
- ¹² K. Kimoto, T. Asaka, T. Nagai, M. Saito, Y. Matsui, and K. Ishizuka, *Nature* **450**, 702 (2007).
- ¹³ D.A. Muller, L. Fitting Kourkoutis, M. Murfitt, J.H. Song, H.Y. Hwang, J. Silcox, N. Dellby, and O.L. Krivanek, *Science* **319**, 1073 (2008).
- ¹⁴ K.W. Urban, *Science* **321**, 506 (2008).
- ¹⁵ R. Brydson, A.V.K. Westwood, X. Jiang, S.J. Rowen, S. Collins, S. Lu, B. Rand, K. Wades, and R. Coult, *Carbon* **36**, 1139 (1998).
- ¹⁶ J.C. Idrobo, W. Walkosz, R.F. Klie, and S. Oğüt, *Ultramicroscopy* **123**, 74 (2012).
- ¹⁷ G. Soto, W. de la Cruz, and M. Farías, *Journal of Electron Spectroscopy and Related Phenomena* **135**, 27 (2004).
- ¹⁸ C. Scheu, G. Dehm, M. Rühle, and R. Brydson, *Philosophical Magazine A* **78**, 439 (1998).
- ¹⁹ H. Tan, J. Verbeeck, A. Abakumov, and G. Van Tendeloo, *Ultramicroscopy* **116**, 24 (2012).
- ²⁰ R.D. Leapman and C.R. Swyt, *Ultramicroscopy* **26**, 393 (1988).
- ²¹ W.-Y. Ching, S. Aryal, P. Rulis, and W. Schnick, *Physical Review B* **83**, 155109 (2011).
- ²² P. Rez and D.A. Muller, *Annual Review of Materials Research* **38**, 535 (2008).
- ²³ C.B. Samantaray, H. Sim, and H. Hwang, *Applied Surface Science* **242**, 121 (2005).
- ²⁴ R.F. Klie, I. Arslan, and N.D. Browning, *Journal of Electron Spectroscopy and Related Phenomena* **143**, 105 (2005).

- ²⁵ N.D. Browning, J.P. Buban, H.O. Moltaji, S.J. Pennycook, G. Duscher, K.D. Johnson, R.P. Rodrigues, and V.P. Dravid, *Applied Physics Letters* **74**, 2638 (1999).
- ²⁶ D.A. Muller, *Nature Materials* **8**, 263 (2009).
- ²⁷ C. Colliex, a Gloter, K. March, C. Mory, O. Stéphan, K. Suenaga, and M. Tencé, *Ultramicroscopy* **123**, 80 (2012).
- ²⁸ T. Kiguchi, N. Wakiya, K. Shinozaki, and T.J. Konno, *Materials Science and Engineering: B* **161**, 160 (2009).
- ²⁹ K.S. Viridi, Y. Kauffmann, C. Ziegler, P. Ganter, B. V. Lotsch, W.D. Kaplan, P. Blaha, and C. Scheu, *Physical Review B* **87**, 115108 (2013).
- ³⁰ M. Stöger-Pollach, H. Franco, P. Schattschneider, S. Lazar, B. Schaffer, W. Grogger, and H.W. Zandbergen, *Micron* **37**, 396 (2006).
- ³¹ D.A. Muller and J. Silcox, *Ultramicroscopy* **59**, 195 (1995).
- ³² J.A. Aguiar, B.W. Reed, Q.M. Ramasse, R. Erni, and N.D. Browning, *Ultramicroscopy* **124**, 130 (2013).
- ³³ R. Erni, S. Lazar, and N.D. Browning, *Ultramicroscopy* **108**, 270 (2008).
- ³⁴ L. Laffont, a Lonjon, E. Dantras, P. Demont, and C. Lacabanne, *Materials Letters* **65**, 3411 (2011).
- ³⁵ L. Gu, V. Srot, W. Sigle, C.T. Koch, P.A. van Aken, F. Scholz, S.B. Thapa, C. Kirchner, M. Jetter, and M. Rühle, *Physical Review B* **75**, 195214 (2007).
- ³⁶ J. Park, S. Heo, J.-G. Chung, H. Kim, H. Lee, K. Kim, and G.-S. Park, *Ultramicroscopy* **109**, 1183 (2009).

2 Materials

2.1 Nitride compounds

Formally, nitrides are compounds consisting of N and a less electronegative element. There are ionic, metallic and covalent nitride compounds. Covalent nitrides in particular have promising properties due to the strength of the covalent bonds and their building units in the solid being highly cross-linked, leading to a high lattice energy. They are often used as refractory materials and as very hard alloys exhibiting outstanding thermal, mechanical and chemical stability. In these compounds the covalent cations typically are elements of the third to fifth main group of the periodic table. In the following the nitride compounds most relevant for this thesis are described.

2.1.1 Silicon nitride

Silicon nitride (Si_3N_4) exhibits chemical and physical properties which are of great interest for high-performance applications. Si_3N_4 possesses a high hardness, a high thermal and fracture toughness and high chemical stability. Therefore, Si_3N_4 is used for cutting tools, as insulator or as passivating material to name only a few of the technological applications.^{1,2} Thereby, $\alpha\text{-Si}_3\text{N}_4$ is the thermodynamical stable modification. Si_3N_4 can be synthesized via several routes. One is the direct nitridation where silicon powder is heated up between 1300 °C and 1400 °C in nitrogen atmosphere.³ Si_3N_4 can also be synthesized by using the carbothermal reduction of silicon dioxide under a nitrogen or ammonia atmosphere.³ For preparative applications the ammonolysis of silane (SiH_4) or silicon tetrachloride (SiCl_4) are commonly used.³

Three polymorphs of Si_3N_4 are known. $\alpha\text{-Si}_3\text{N}_4$ and $\beta\text{-Si}_3\text{N}_4$ crystallize in the trigonal ($P31c$) and hexagonal ($P6_3$) space group, respectively. Both modifications are built up of condensed corner-sharing SiN_4 tetrahedra building three-dimensional (3D) networks, whereby the structure of $\beta\text{-Si}_3\text{N}_4$ is analogous to the phenakite (Be_2SiO_4) structure. The N atoms form a hexagonal closed packed lattice and three eighth of the tetrahedral sites are occupied with Si atoms. In general, silicon nitrides possess a higher degree of condensation resulting in more covalent bonds per volume than silicon dioxide (Chapter 2.2.1) and exhibit therefore a higher hardness.⁴ $\gamma\text{-Si}_3\text{N}_4$ is a high-pressure/high-temperature phase and its synthesis requires pressures higher than 15 GPa and

temperatures above 2000 K. This polymorph crystallizes in the cubic structure ($Fd\bar{3}m$).^{2,5} It is built up of SiN_4 tetrahedra and SiN_6 octahedra resulting in a spinel-type structure. The N atoms build a cubic closed packed package where one third of all Si atoms occupy one eighth of the tetrahedral sites and the remaining two third occupy one half of the octahedral sites. The three modifications exhibit different band gaps. α - Si_3N_4 has a band gap of 4.4 eV⁶, β - Si_3N_4 of 4.6 and γ - Si_3N_4 of 3.4.⁷ The crystal structures of the three Si_3N_4 polymorphs are shown in Figure 2.1.1 and their crystallographic parameters are summarized in Table 2.1.1.

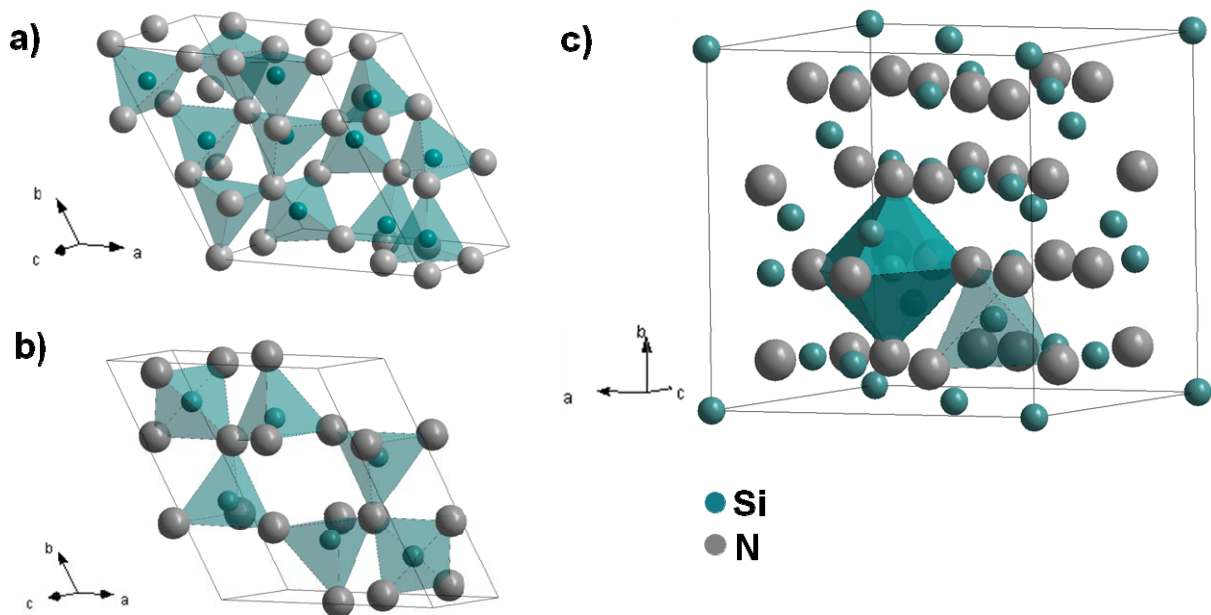


Figure 2.1.1. The three polymorphs of Si_3N_4 . Corner-sharing condensed SiN_4 tetrahedra illustrated in blue build up a) the trigonal α - Si_3N_4 and b) the hexagonal β - Si_3N_4 . c) The crystal structure of the cubic γ - Si_3N_4 is composed of SiN_4 tetrahedral units (light blue) and SiN_6 octahedral units (dark blue) of which one each were drawn exemplarily. Si atoms are drawn in blue and N atoms in gray.

Table 2.1.1. Crystallographic parameters of the three Si_3N_4 modifications.

	α - Si_3N_4	β - Si_3N_4	γ - Si_3N_4
crystal system	trigonal	hexagonal	cubic
lattice constants [\AA]	$a = 7.75193(3)$ $c = 5.61949(4)$	$a = 7.60440(10)$ $c = 2.90630(10)$	$a = 7.7729$
space group	$P31c$	$P6_3$	$Fd\bar{3}m$

2.1.2 Phosphorus(V) nitride

Since phosphorus(V) nitride (P_3N_5) is chemically and structurally related to Si_3N_4 it is predicted to exhibit similar properties. As for Si_3N_4 , solely PN_4 tetrahedral building blocks forming 3D networks are expected for this compound. Therefore, it has attracted much attention in the last decades although its structure has not been solved until 1997.⁸ P_3N_5 has potential applications as pigments or as a microporous material.^{9,10} The three modifications of P_3N_5 are α - P_3N_5 , β - P_3N_5 and γ - P_3N_5 . Monoclinic (Cc or $C2/c$) α - P_3N_5 is obtained via ammonolysis of hexachlorophosphazene $(PNCl_2)_3$ and ammonium chloride (NH_4Cl) at temperatures between 770 and 1050 K as colorless powder.⁹ However, small amounts of β - P_3N_5 cannot be excluded. The crystal structure of β - P_3N_5 is not known in detail so far but is based on the crystal structure of α - P_3N_5 .⁹ Another synthesis route to obtain pure, stoichiometric α - P_3N_5 is through the thermal condensation of tetraaminophosphonium iodide $[P(NH_2)_4]I$.^{8,10} α - P_3N_5 is built up of corner- and edge-sharing PN_4 tetrahedra forming zweier single chains leading to a covalent 3D network. In this network two fifth of the N atoms are coordinated planar with three P atoms and the other three fifth of the N atoms are coordinated angled with two P atoms.^{8,10,11} The threefold coordination of P enables not only corner-sharing but also edge-sharing tetrahedra being a unique building block for binary nitrides.¹² The high-pressure phase γ - P_3N_5 , which is synthesized at 11 GPa and 150 °C exhibits an orthorhombic ($Imm2$) crystal structure and is built up of one third corner-sharing PN_4 tetrahedra and two third transedge-sharing distorted PN_5 square pyramids.¹³ γ - P_3N_5 is expected to transform into the hypothetical triclinic ($P\bar{1}$) kyanite-type δ - P_3N_5 at pressures above 43 GPa. In this modification edge-sharing PN_6 octahedra build a 3D network with PN_4 tetrahedra which share corners with the octahedra. However during the quenching to lower pressures, δ - P_3N_5 may undergo a shear distortion resulting in the more symmetrical monoclinic δ' - P_3N_5 . This structure is built up of PN_6 octahedra, PN_5 bipyramids and PN_4 tetrahedra.¹¹ The modifications of P_3N_5 are pictured in Figure 2.1.2 and their crystallographic details are summarized in Table 2.1.2.

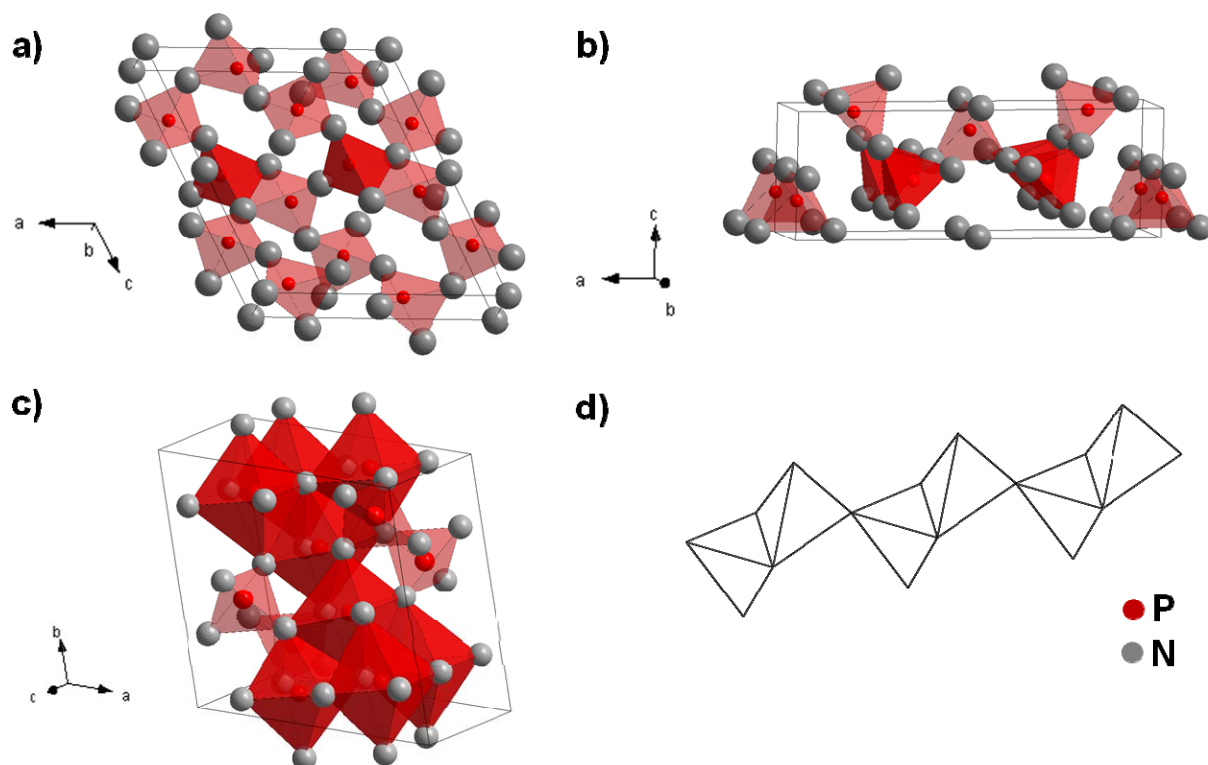


Figure 2.1.2. The polymorphs of P_3N_5 and building units. a) The monoclinic α - P_3N_5 with corner- (light red) and edge-sharing (dark red) condensed PN_4 tetrahedra and b) the high-pressure orthorhombic γ - P_3N_5 with corner-sharing PN_4 tetrahedra (light red) further exhibiting PN_5 square pyramids (dark red). c) The crystal structure of hypothetical δ - P_3N_5 is composed of PN_4 tetrahedral units (light red) and PN_6 octahedral units (dark red). d) Corner- and edge-sharing PN_4 tetrahedra forming a zweier single chain. P atoms are drawn in red and N atoms in gray.

Table 2.1.2. Crystallographic parameters of the three P_3N_5 modifications.

	α - P_3N_5	γ - P_3N_5	δ - P_3N_5
crystal system	monoclinic	orthorhombic	triclinic
lattice constants [\AA]	$a = 8.12077(4)$ $b = 5.83433(4)$ $c = 9.16005(5)$	$a = 12.8721(4)$ $b = 2.61312(6)$ $c = 4.4003(2)$	$a = 6.6026$ $b = 7.1731$ $c = 5.1076$
space group	Cc or $C2/c$	$Imm2$	$P\bar{1}$

2.1.3 Beryllium nitride

Beryllium nitride (Be_3N_2) is another promising nitride material considering its chemical stability and mechanical properties.¹⁴ It finds application as refractory ceramics or e.g. in the nuclear industry for reactors.^{15,16} The synthesis of Be_3N_2 is done via a high-temperature reaction (800 – 1000 °C) of the metal Be in a N_2 flow.¹⁷ There are two known polymorphs of Be_3N_2 , $\alpha\text{-Be}_3\text{N}_2$ and $\beta\text{-Be}_3\text{N}_2$. Both are colorless powders. The first crystallizes in a defect anti-fluorite type structure and exhibits a cubic ($Ia\bar{3}$) crystal structure. The N atoms are arranged in a distorted cubic closed packing and the Be atoms occupy three quarter of the tetrahedral sites.¹⁷ This modification exhibits a wide direct band gap of 4.43 eV and is interesting for optoelectronic devices.^{15,17,18} The second polymorph crystallizes in the hexagonal ($P6_3/mmc$) crystal structure and is obtained by heating $\alpha\text{-Be}_3\text{N}_2$ up to 1400 °C.¹⁹ This modification has an indirect band gap of 12.5 eV.¹⁹ A metastable cubic ($Pn\bar{3}m$) $\gamma\text{-Be}_3\text{N}_2$ is predicted and supposed to have a high hardness.^{15,20} Two superhard Be_3N_2 polymorphs with rhombohedral ($R3mH$, $s1\text{-Be}_3\text{N}_2$) and hexagonal ($P\bar{3}m1$, $s2\text{-Be}_3\text{N}_2$) symmetry are also predicted.¹⁵ In contrast to the other Be_3N_2 modifications, these two polymorphs are assumed to be stable against decomposition. In the rhombohedral crystal structure the N atom are either coordinated by five Be atoms or by six N atoms. In the hexagonal modification even a coordination with seven bonded N atoms is forecasted. These polymorphs should exhibit band gaps of around 3.6 – 5.6 eV and 5.6 – 8.6 eV, respectively.¹⁵ The modifications of Be_3N_2 are given in Figure 2.1.3 and their crystallographic details are listed in Table 2.1.3.

Table 2.1.3. Crystallographic parameters of the five Be_3N_2 modifications.

	$\alpha\text{-Be}_3\text{N}_2$	$\beta\text{-Be}_3\text{N}_2$	$\gamma\text{-Be}_3\text{N}_2$	$s1\text{-Be}_3\text{N}_2$	$s2\text{-Be}_3\text{N}_2$
crystal system	cubic	hexagonal	cubic	rhombohedral	hexagonal
lattice constants [\AA]	$a = 8.14518(6)$	$a = 2.8413$ $c = 9.693$	$a = 4.072$	$a = 2.850$ $c = 14.659$	$a = 2.820$ $c = 4.669$
space group	$Ia\bar{3}$	$P6_3/mmc$	$Pn\bar{3}m$	$R3mH$	$P\bar{3}m1$

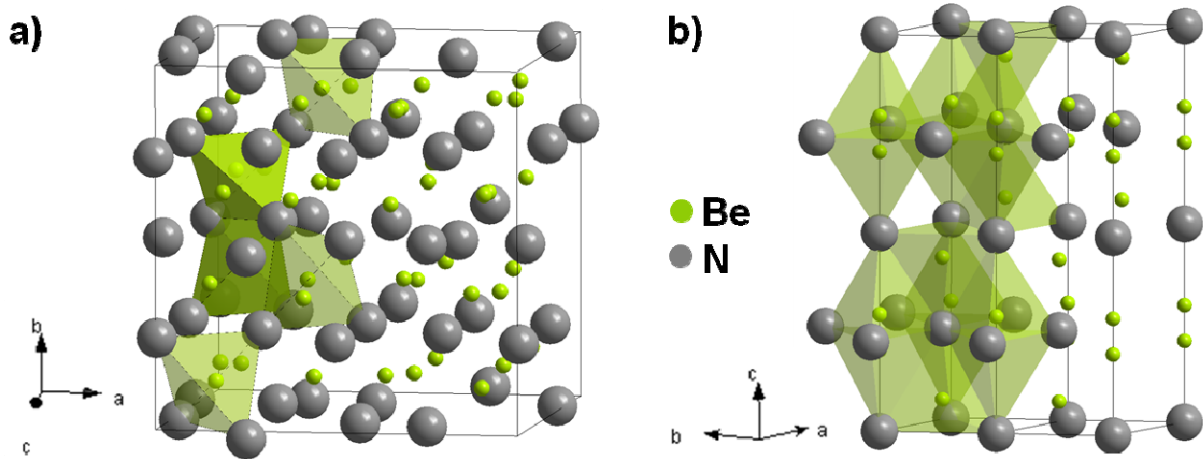


Figure 2.1.3. Schematic drawing of the polymorphs of Be_3N_2 . a) The cubic $\alpha\text{-Be}_3\text{N}_2$ with corner- (light green) and edge-sharing (dark green) condensed BeN_4 tetrahedra highlighted exemplarily and b) the hexagonal $\beta\text{-Be}_3\text{N}_2$ built up of corner- and edge-sharing condensed BeN_4 tetrahedra. Be atoms are drawn in green and N atoms in gray.

2.1.4 Beryllium phosphorus nitride

Beryllium phosphorus nitride BeP_2N_4 is isostructural and isoelectronic to Be_2SiO_4 and $\beta\text{-Si}_3\text{N}_4$. Therefore, it is expected to transform under high-pressure and -temperature into a possibly even harder material than spinel-type $\gamma\text{-Si}_3\text{N}_4$, which forms under these conditions from $\beta\text{-Si}_3\text{N}_4$.¹² BeP_2N_4 was synthesized by heating P_3N_5 and Be_3N_2 to 1500 °C at a pressure of 5 GPa. BeP_2N_4 (p- BeP_2N_4) crystallizes in the rhombohedral ($R\bar{3}h$) phenakite structure type. Here, corner-sharing BeN_4 and PN_4 tetrahedra build dreier, vierer and sechser rings.^{12,21} The N atoms are trigonal planar coordinated by one Be and two P atoms. Under high-pressure (24 GPa) a transformation to a super hard, cubic ($Fd\bar{3}m$) spinel-type structure (s- BeP_2N_4) is predicted.^{12,22} This would increase the coordination number of P from four to six leading to PN_6 octahedra, which so far have never been observed. Be atoms would occupy the tetrahedral and the P atoms the octahedral sites. A coordination number greater than six has so far only been predicted for hypothetical $\delta\text{-P}_3\text{N}_5$. Both BeP_2N_4 polymorphs have been calculated to be wide band gap semiconductors exhibiting a direct band gap of 3.97 eV (p- BeP_2N_4) and an indirect band gap of 3.6 eV (s- BeP_2N_4), respectively. Both crystal structures are schematically drawn in Figure 2.1.4 and their crystallographic parameters are summarized in Table 2.1.4. Furthermore, BeP_2N_4 is discussed in more detail in Chapter 6.

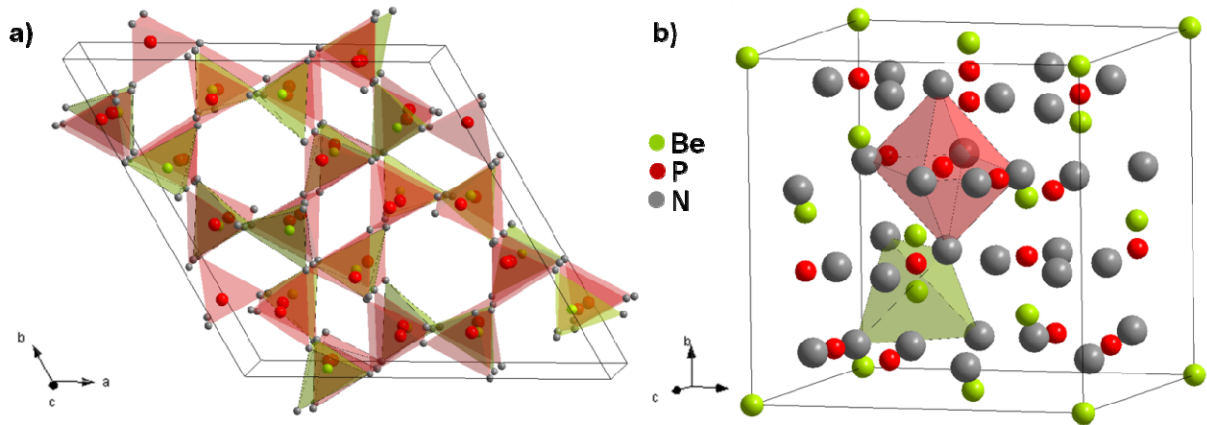


Figure 2.1.4. Schematic drawing of the two BeP₂N₄ polymorphs. a) Phenakite-type structure where the BeN₄ tetrahedra are drawn in green and the PN₄ tetrahedra in red, N atoms are drawn in gray and b) spinel-type structure with BeN₄ tetrahedra (green) and PN₆ octahedra (red) with gray N atoms.

Table 2.1.4. Crystallographic parameters of the BeP₂N₄ modifications.

	p-BeP₂N₄	s-BeP₂N₄
crystal system	rhombohedral	cubic
lattice constants [Å]	a = 12.69451 c = 8.34858(15)	a = 7.4654
space group	$R\bar{3}h$	$Fd\bar{3}m$

2.2 Silica and its chemical analogue phosphorus oxynitride

2.2.1 Silica

Silica (SiO_2) occurs in a variety of amorphous and crystalline modifications. In most SiO_2 compounds Si is tetrahedrally coordinated by four O atoms. The crystalline polymorphs of SiO_2 which are stable or metastable at room temperature are moganite, α - and β -quartz, α - and β -tridymite, α - and β -cristobalite, and the high-pressure modifications coesite, keatite and stishovite.²³ Besides, a fibrous SiO_2 is known where the SiO_4 tetrahedra are connected via their edges. In this thesis amorphous SiO_2 (a- SiO_2) is the most relevant modification, which is why the crystalline SiO_2 forms are mentioned but not further described. a- SiO_2 is built up of corner-sharing SiO_4 tetrahedra as well but in contrast to crystalline SiO_2 consists of a non-repeating random network of these building units. No long range periodicity can be found in a- SiO_2 .²⁴ In Figure 2.2.1 an exemplarily crystalline network of SiO_4 tetrahedra is shown (Figure 2.2.1a) as well as a cutout of an a- SiO_2 network (Figure 2.2.1b). a- SiO_2 exhibits a high dielectric strength and can easily be modified with silane chemistry and can therefore be made suitable for a broad range of applications. The band gap of a- SiO_2 is 8.9 eV.²⁵ Besides microelectrical applications like in semiconductor chips or optical fibers, a- SiO_2 is used for biological applications, e.g. as drug delivery system.²⁶

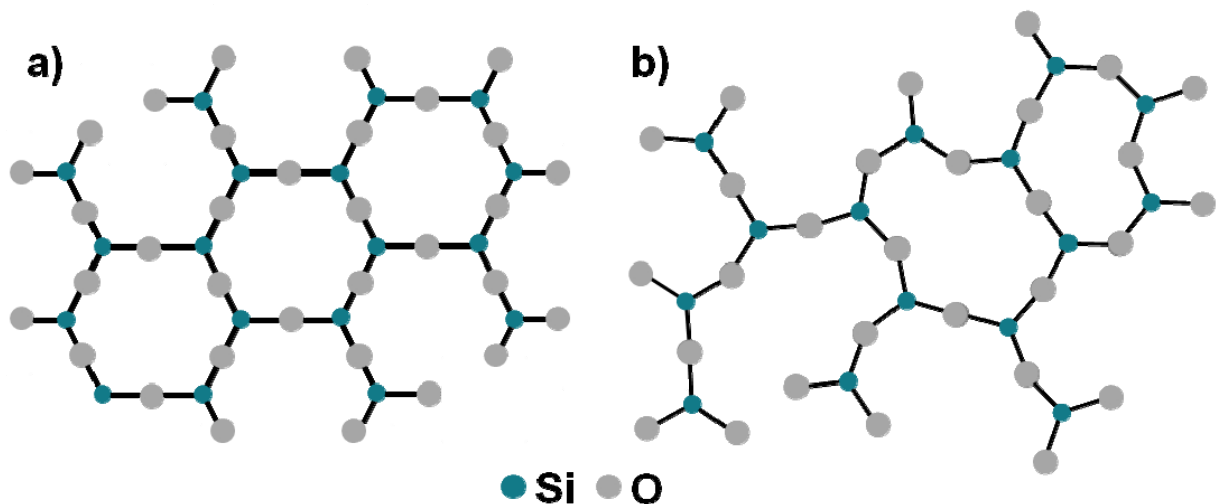


Figure 2.2.1. Schematic drawing of a) crystalline and b) a- SiO_2 . The Si atoms are drawn in blue and the O atoms in gray.

2.2.2 Phosphorus oxynitride

Phosphorus oxynitride (PON) is isoelectronic to SiO_2 and is therefore expected to exhibit similar structural properties.²⁷ Four polymorphs of this compound are known, the β -cristobalite type structure (c-PON), the α -quartz type structure (q-PON), the moganite type structure (m-PON) and the high-pressure phase δ -PON. All modifications have corner-sharing $\text{P}(\text{O},\text{N})_4$ tetrahedra in common. c-PON is obtained by keeping ammonium dihydrogen phosphate ($\text{NH}_4\text{H}_2\text{PO}_4$) and urea ($\text{CH}_4\text{N}_2\text{O}$) or melamine ($\text{C}_3\text{H}_6\text{N}_6$) at 700 - 800 °C for several days.²⁸ This PON modification exhibits a tetragonal ($I\bar{4}2d$) crystal structure. Under high-pressure (4.5 GPa) and -temperature (750 °C) c-PON transforms to the trigonal ($P3_221$) q-PON polymorph.²⁹ The m-PON modification exhibits a monoclinic ($I2/a$) crystal structure and is obtained by starting with c-PON and applying a pressure of 2.5 GPa and a temperature of 850 °C.^{30,31} Monoclinic ($P2_1/c$) δ -PON is obtained by heating amorphous phosphorus oxonitride imide up to 1350 °C and applying a pressure of 12 GPa.³² The $\text{P}(\text{O},\text{N})_4$ tetrahedra build a 3D network consisting of 4-, 6- and 8-rings.³² This structure type of δ -PON is the first polymorph so far which has no SiO_2 analogue. The four polymorphs of PON are illustrated in Figure 2.2.2 and their crystallographic details are summarized in Table 2.2.1.

Table 2.2.1. Crystallographic parameters of the four PON modifications.

	c-PON	q-PON	m-PON	δ-PON
crystal system	tetragonal	trigonal	monoclinic	monoclinic
lattice constants [\AA]	a = 4.61865(4) c = 6.97882(9)	a = 4.757(4) c = 5.246(2)	a = 8.5194(2) b = 4.7448(1) c = 10.3970(3)	a = 12.2472(2) b = 4.83618(6) c = 10.8604(2)
space group	$I\bar{4}2d$	$P3_221$	$(I2/a)$	$P2_1/c$

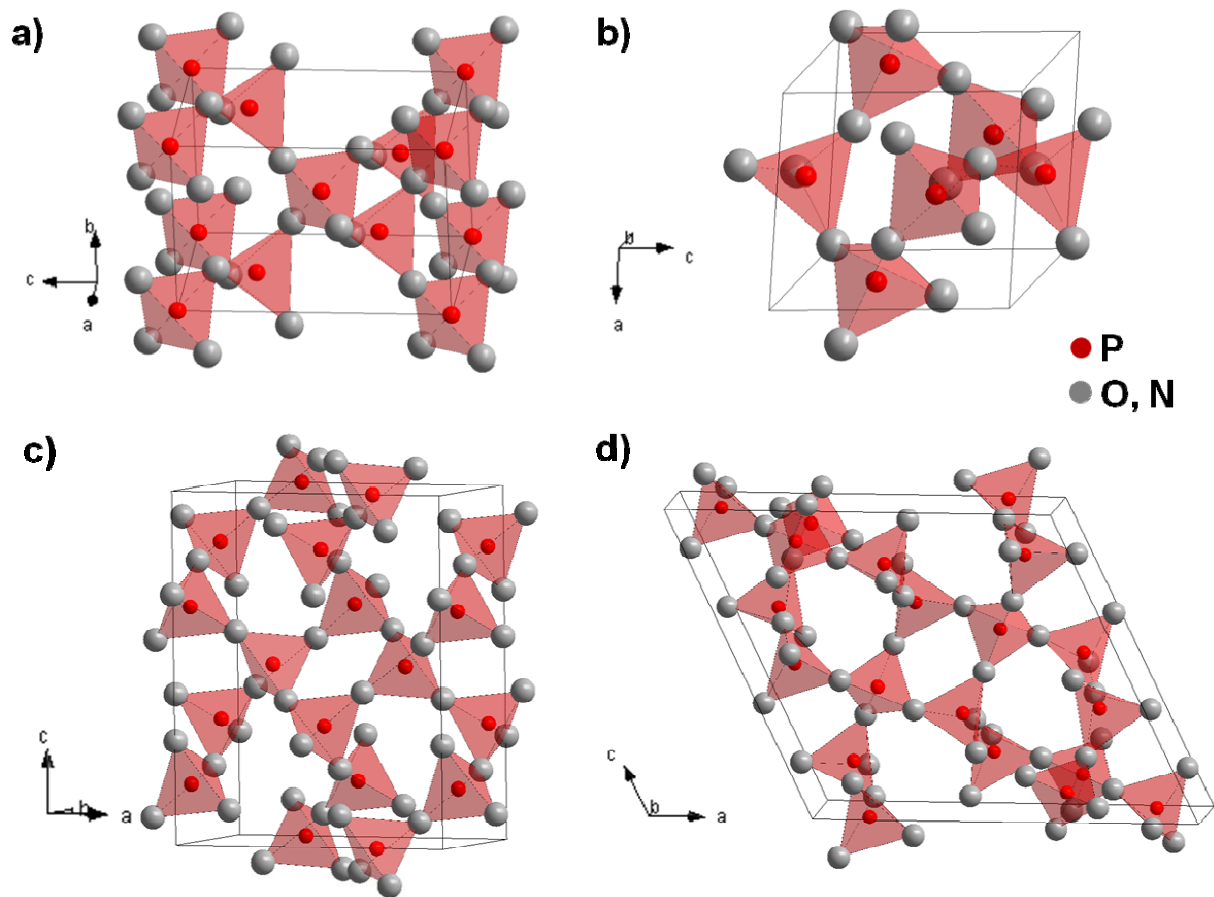


Figure 2.2.2. Schematic drawing of the polymorphs of PON. Corner-sharing condensed $P(O,N)_4$ tetrahedra illustrated in red built up a) the tetragonal c-PON, b) the trigonal q-PON, c) the monoclinic m-PON and d) the monoclinic δ -PON. P atoms are drawn in red and O and N atoms in gray.

2.3 Iron oxides on alumina

2.3.1 Aluminium(III) oxide

Aluminium(III) oxide (Al_2O_3), or alumina, exhibits a high melting point, a high hardness and is a good electrical insulator. Therefore, it is used, beside the production of Al metal, as a refractory ceramic material, as an abrasive or as catalytic support.^{23,33,34} Alumina occurs mostly in two modifications, $\alpha\text{-Al}_2\text{O}_3$ and $\gamma\text{-Al}_2\text{O}_3$, with the former being the thermodynamically stable phase. This polymorph crystallizing in the rhombohedral ($R\bar{3}c$) crystal structure is also called corundum or sapphire.³⁵ The O atoms are arranged in a hexagonal closed packed lattice. The Al atoms occupy two third of the octahedral sites leading to a slightly distorted hexagonal closed packed lattice. The second modification is obtained by heating gibbsite ($\gamma\text{-Al}(\text{OH})_3$) up to 400 °C. $\gamma\text{-Al}_2\text{O}_3$ crystallizes in a cubic ($Fd\bar{3}m$) crystal structure where the O atoms are arranged in a cubic closed package. The Al atoms occupy the tetrahedral and octahedral sites. There are cation vacancy sites so that not all tetrahedral and octahedral sites are occupied (defect spinel structure).³³ The Al_2O_3 modifications $\delta\text{-Al}_2\text{O}_3$ and $\vartheta\text{-Al}_2\text{O}_3$ are based on this structure. The most important polymorphs of Al_2O_3 are shown in Figure 2.3.1 and their structural details are given in Table 2.3.1.

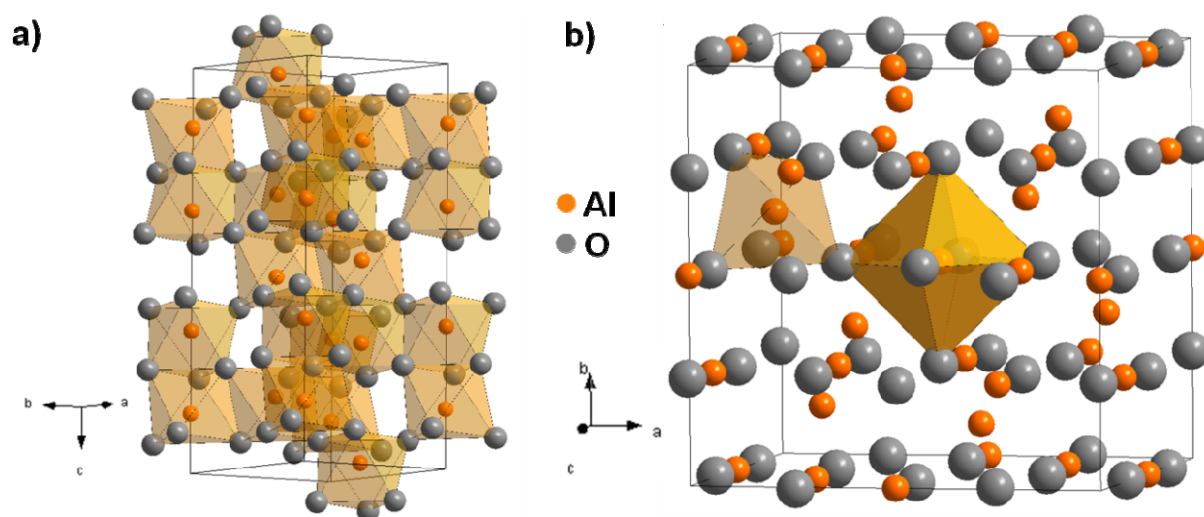


Figure 2.3.1. Schematic drawing of two polymorphs of Al_2O_3 . a) The hexagonal $\alpha\text{-Al}_2\text{O}_3$ is built up of AlO_6 octahedra and b) the cubic $\gamma\text{-Al}_2\text{O}_3$ exhibits AlO_4 tetrahedra (light orange) and AlO_6 octahedra (dark orange) of which one each were drawn exemplarily. The Al atoms are drawn in orange and the O atoms in gray.

Table 2.3.1. Crystallographic parameters of the two main Al_2O_3 modifications.

	$\alpha\text{-Al}_2\text{O}_3$	$\gamma\text{-Al}_2\text{O}_3$
crystal system	hexagonal	cubic
lattice constants [Å]	$a = 4.7607(7)$ $c = 12.997(2)$	$a = 7.887$
space group	$R\bar{3}c$	$Fd\bar{3}m$

2.3.2 Iron oxides and iron titanium oxide

Iron oxides exhibit a wide range of technological applications like in heterogeneous catalysis, redox reactions or as magnetic films.³⁶ Thin film systems of hematite (Fe_2O_3), magnetite (Fe_3O_4) and of the iron titanium oxide ilmenite (FeTiO_3) in particular are widely studied. Like $\alpha\text{-Al}_2\text{O}_3$, Fe_2O_3 possesses the corundum crystal structure (see Chapter 2.3.1).³⁵ Fe_3O_4 ($\text{Fe(III)}_2\text{Fe(II)}$) forms an inverse spinel structure ($Fd\bar{3}m$) where Fe(III) occupy one fourth of the octahedral sites and Fe(II) one fourth of the octahedral and one eighth of the tetrahedral sites of a cubic closed O package.³⁷ FeTiO_3 exhibits a corundum-derived crystal structure ($R\bar{3}$). Here, every second (0001) layer of Fe atoms is replaced by a layer of Ti atoms leading to the so called ilmenite structure.³⁸ The crystal structures are drawn in Figure 2.3.2 and their structural details are summarized in Table 2.3.2.

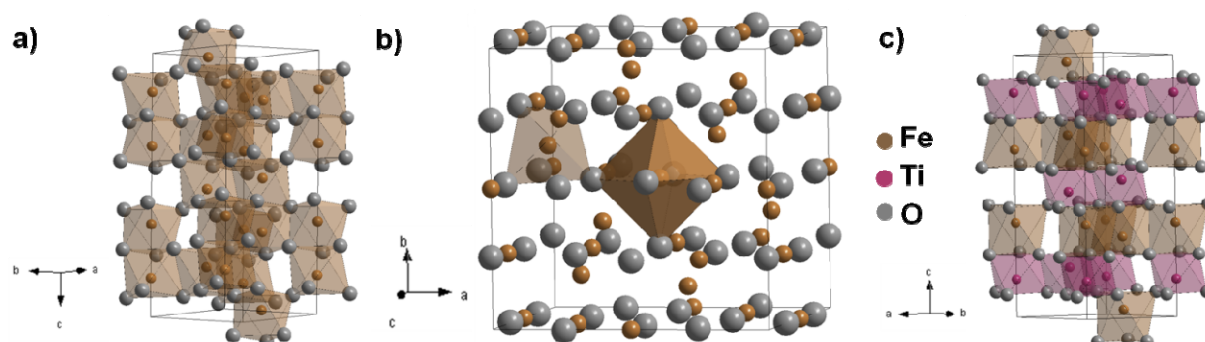


Figure 2.3.2. Schematic drawing of the crystal structures of a) the rhombohedral Fe_2O_3 , b) Fe_3O_4 crystallizing in the inverse spinel structure and c) the trigonal FeTiO_3 . Fe atoms are drawn in brown, Ti atoms in purple and O atoms in gray.

Table 2.3.2. Crystallographic parameters of the three iron oxides relevant for the present work.

	Fe₂O₃	Fe₃O₄	FeTiO₃
crystal system	hexagonal	inverse spinel	trigonal
lattice constants [Å]	a = 5.038(2) c = 13.772(12)	a = 8.34	a = 5.18 c = 14.27
space group	<i>R</i> $\bar{3}$ <i>c</i>	<i>Fd</i> $\bar{3}$ <i>m</i>	<i>R</i> $\bar{3}$

2.4 Chapter references

- ¹ W. Schnick, *Angewandte Chemie International Edition* **32**, 806 (1993).
- ² A. Zerr, G. Miehe, G. Serghiou, M. Schwarz, E. Kroke, R. Riedel, H. Fueß, P. Kroll, and R. Boehler, *Nature* **400**, 340 (1999).
- ³ B.H. Lange, G. Wotting, and G. Winter, *Angewandte Chemie International Edition* **30**, 1579 (1991).
- ⁴ M. Zeuner, S. Pagano, and W. Schnick, *Angewandte Chemie International Edition* **50**, 7754 (2011).
- ⁵ J.Z. Jiang, K. Stahl, R.W. Berg, D.J. Frost, T.J. Zhou, and P.X. Shi, *Europhysics Letters* **51**, 62 (2000).
- ⁶ C. S en emaud, M. Driss-Khodja, a. Gheorghiu, S. Harel, G. Dufour, and H. Roulet, *Journal of Applied Physics* **74**, 5042 (1993).
- ⁷ D. du Boulay, N. Ishizawa, T. Atake, V. Streltsov, K. Furuya, and F. Munakata, *Acta Crystallographica B* **60**, 388 (2004).
- ⁸ S. Horstmann, E. Irran, and W. Schnick, *Angewandte Chemie International Edition* **36**, 1873 (1997).
- ⁹ W. Schnick, J. L ucke, and F. Krumeich, *Chemistry of Materials* **8**, 281 (1996).
- ¹⁰ S. Horstmann, E. Irran, and W. Schnick, *Zeitschrift f ur anorganische und allgemeine Chemie* **624**, 620 (1998).
- ¹¹ P. Kroll and W. Schnick, *Chemistry - A European Journal* **8**, 3530 (2002).
- ¹² F.J. Pucher, S.R. R omer, F.W. Karau, and W. Schnick, *Chemistry - A European Journal* **16**, 7208 (2010).
- ¹³ K. Landskron, H. Huppertz, J. Senker, and W. Schnick, *Zeitschrift f ur anorganische und allgemeine Chemie* **628**, 1465 (2002).
- ¹⁴ W. de la Cruz, G. Soto, and F. Yubero, *Optical Materials* **25**, 39 (2004).
- ¹⁵ Y. Xia, Q. Li, and Y. Ma, *Computational Materials Science* **49**, S76 (2010).
- ¹⁶ R.C. Ropp, *Encyclopedia of the Alkaline Earth Compounds*, 1 ed. (Elsevier Ltd, Oxford, 2013), p. 1250.
- ¹⁷ O. Reckeweg, C. Lind, A. Simon, and F.J. DiSalvo, *Zeitschrift f ur Naturforschung* **58b**, 159 (2003).
- ¹⁸ M.G.M. Armenta and A. Reyes-Serrato, *Computational Materials Science* **21**, 95 (2001).

- ¹⁹ A. Reyes-Serrato, G. Soto, A. Gamietea, and M.H. Farias, *Journal of Physics and Chemistry of Solids* **59**, 743 (1998).
- ²⁰ H. Gou, L. Hou, J. Zhang, Z. Wang, L. Gao, and F. Gao, *Applied Physics Letters* **90**, 191905 (2007).
- ²¹ F. Liebau, *Structural Chemistry of Silicates* (Springer, Berlin, 1985), p. 347.
- ²² W.-Y. Ching, S. Aryal, P. Rulis, and W. Schnick, *Physical Review B* **83**, 155109 (2011).
- ²³ A.F. Hollemann and N. Wiberg, *Lehrbuch der anorganischen Chemie*, 102 ed. (Walter de Gruyter & Co., Berlin, 2007), p. 2149.
- ²⁴ W.H. Zachariasen, *Journal of the American Ceramic Society American* **54**, 3841 (1932).
- ²⁵ J. Park, S. Heo, J.-G. Chung, H. Kim, H. Lee, K. Kim, and G.-S. Park, *Ultramicroscopy* **109**, 1183 (2009).
- ²⁶ X. Yang, H. Tang, K. Cao, H. Song, W. Sheng, and Q. Wu, *Journal of Materials Chemistry* **21**, 6122 (2011).
- ²⁷ J.M. Léger, J. Haines, C. Chateau, G. Bocquillon, M.W. Schmidt, S. Hull, F. Gorelli, A. Le Sauze, and R. Marchand, *Physics and Chemistry of Minerals* **28**, 388 (2001).
- ²⁸ L. Boukir, R. Marchand, Y. Laurent, Z.J. Chao, C. Parent, and G. Le Flem, *Journal of Solid State Chemistry* **87**, 423 (1990).
- ²⁹ J.-M. Léger, J. Haines, L.S. de Oliveira, C. Chateau, A. Le Sauze, R. Marchand, and S. Hull, *Journal of Physics and Chemistry of Solids* **60**, 145 (1999).
- ³⁰ C. Chateau, J. Haines, J.-M. Leger, A. Le Sauze, and R. Marchand, *American Mineralogist*, **84**, 207 (1999).
- ³¹ J. Haines, C. Chateau, J.M. Léger, A. Le Sauze, N. Diot, R. Marchand, and S. Hull, *Acta Crystallographica B* **55**, 677 (1999).
- ³² D. Baumann, S.J. Sedlmaier, and W. Schnick, *Angewandte Chemie International Edition* **51**, 4707 (2012).
- ³³ G. Gutiérrez, A. Taga, and B. Johansson, *Physical Review B* **65**, 012101 (2001).
- ³⁴ G. Paglia, E.S. Bozin, and S.J.L. Billinge, *Chemistry of Materials* **18**, 3242 (2006).
- ³⁵ L. Pauling and S.B. Hendricks, *Journal of the American Chemical Society* **47**, 781 (1925).
- ³⁶ Y. Gao, Y.J. Kim, S.A. Chambers, and G. Bai, *Journal of Vacuum Science & Technology A* **15**, 332 (1997).
- ³⁷ W.H. Bragg, *Nature* **95**, 561 (1915).
- ³⁸ T.F.W. Barth and E. Posnjak, *Zeitschrift für Kristallographie* **88**, 265 (1934).

3 Characterization methods

3.1 Powder X-ray diffraction

The powder X-ray diffraction (PXRD) technique was developed by Peter Debye and Paul Scherrer in 1916 and is therefore named Debye-Scherrer method. For this technique Debye was awarded with the Nobel Prize in chemistry in 1936. Small amounts of material can be characterized quantitatively and qualitatively with X-rays concerning their phase composition and crystalline structure. X-rays possess wavelengths between 0.1 and 100 Å and exhibit a high energy. When X-rays hit the sample under specific Bragg angles (2θ) they are elastically scattered on the lattice planes of the crystal and constructive interference occurs. The relation of the distance of the lattice planes to the scattering angle (2θ) is given by the Bragg equation (Figure 3.1.1):

$$n\lambda = 2d_{hkl}\sin\theta \quad (3.1).$$

n is a positive integer corresponding to the order of diffraction, λ the wavelength of the X-rays, d_{hkl} the distance of the lattice planes with the Miller indices hkl and θ the Bragg angle or scattering angle, respectively. With the distance of the lattice planes d_{hkl} and the intensity distribution the crystal structure, lattice constants and even the phase composition of the sample can be analyzed and compared to data from literature.

For the Debye-Scherrer method monochromated X-rays are required. In general, by irradiating the sample, the incident electron beam excites inner shell electrons to unoccupied states. When they relax back to their ground state energy is released. This energy can be used to emit a X-ray photon which is characteristic for every material. In addition, so called *bremstrahlung* arises by slowing down the electrons in the Coulomb field of the atomic nucleus. Its contribution to the spectrum is much weaker than the characteristic X-rays but leads to a background in the data. This is a direct radiation loss process. Several secondary effects like absorption, scattering and reflection occur while irradiating the sample. To obtain a monochromated beam and to remove the *bremstrahlung*, the X-rays are focused through several metal filters, a collimator and a monochromator. The resulting radiation, mostly Cu K_α radiation, exhibits a well defined wavelength which can be used for the measurements. For the measurements, the

powder is filled in a glass capillary which is consequently rotating during the measurement to avoid preferred orientations or texturing effects of the crystallites.¹⁻³

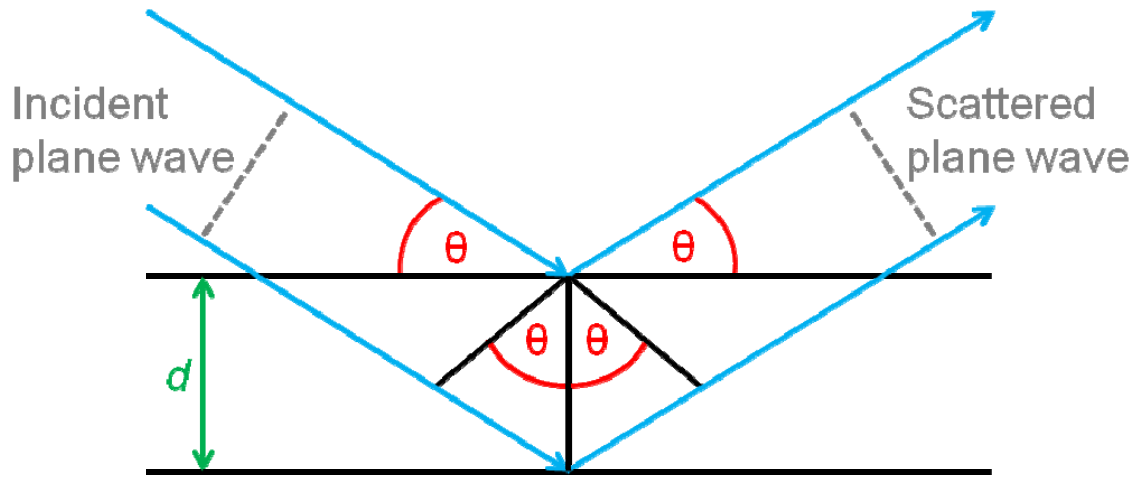


Figure 3.1.1. Description of the Bragg equation where θ is the Bragg angle and d the distance of the lattice planes. Modified from Williams and Carter.⁴

3.2 Electron microscopy and related techniques

In 1924 Louis de Broglie discovered the matter wave. He postulated that every matter exhibits an intrinsic wavelength and that every particle possesses both wave and particle properties. This wave-particle dualism assumption won him the Nobel Prize in 1929 in Physics and was the beginning of electron microscopy (EM). The resolution of light microscopes is limited by diffraction effects to approximately 200 nm. With decreasing the wavelength by using electrons, their wavelength is about 100,000 times shorter than that of light, the resolution increases drastically. Therefore, EM is ideal for analyzing materials with micro- or nanometer sizes. The principle behind an electron gun is that electrons are accelerated in an ultra-high vacuum through an electric field. The nonrelativistic approximation of the kinetic energy of an electron can be described as:

$$E_{kin} = \frac{1}{2} m_e v^2 = eU \quad (3.2)$$

$$v = \sqrt{\left(\frac{2eU}{m_e}\right)} \quad (3.3),$$

where e is the elementary charge, m_e the mass of the electron, v its velocity and U the acceleration voltage. Together with the wave-particle dualism the de Broglie equation (3.4) correlates the wavelength λ to the momentum p and the velocity v :

$$\lambda = \frac{h}{p} = \frac{h}{m_e v} = \frac{h}{\sqrt{2m_e e U}} \quad (3.4).$$

h is defined as the Planck constant.

Different radiation processes occurs when the electron beam hits the sample. The electrons can be elastically or inelastically scattered (Figure 3.2.1). The latter process can lead to backscattered (BSE), secondary (SE), or Auger electrons (AE) and the emission of X-rays and light. In the electron microscope these signals serve for imaging, diffraction or analytical methods and are elucidated in the next sections. In general, electron microscopes are run in ultra-high vacuum to avoid interactions of the electron beam with atoms or molecules from air.

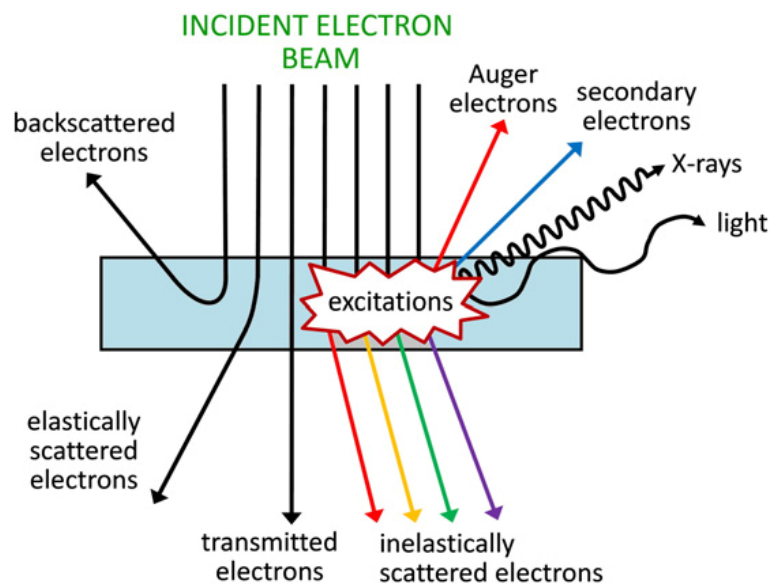


Figure 3.2.1. Schematic drawing of the generated signals stemming from interaction of the electron beam with a thin sample.⁵

3.2.1 Scanning electron microscopy

The scanning electron microscope (SEM) was invented by Manfred von Ardenne in 1937 and first introduced commercially in the late 1950's. An image in the SEM is achieved by scanning an electron beam over a specimen and collecting a signal like SE and BSE at each point. Through the interaction of the electron beam with the sample its surface structure is obtained. The resulting images provide a high depth of field which makes it a useful technique for analyzing micro- and nanostructures of materials. The electron beam is generated by heating up a tungsten (W) wire or a lanthanum hexaboride (LaB₆) crystal which serve as electron source (thermal emitter). In addition, there are thermally assisted field emitters (Schottky field emitter) or cold field emitters. To create electrons in a Schottky or cold field emitter, the work function of the tip is reduced by applying a high electrical field. The electrons can then leave the tip into the vacuum. In the case of thermally assisted field emitters the tunneling is supported by applying elevated temperatures. By applying an electric field between the cathode and the anode the electrons in a SEM are accelerated to energies between 1 and 30 keV. The electron beam is focused to a point with a diameter between 2 and 10 nm by a condenser lens system and is scanned across the sample with the help of scanning coils. The image is produced by detecting backscattered or low energy SE exiting the scanned surface. The latter have a relatively low energy of few eV and are collected by an Everhart-Thornley detector. They are the most commonly used signal for visualizing the topography or morphology of a specimen because the SE arise from the first ~50 nm of a sample's surface. In contrast, the backscattered electrons possess a much higher energy (around the initial beam energy) and their signal is strongly dependent of the atomic number which is why they serve for characterizing a sample's composition distribution. Their signal is collected by semiconductor devices. The main components of an SEM are pictured in Figure 3.2.2. If an isolating material shall be analyzed, charging effects of the sample occur. The electrons are trapped in the specimen and cannot leave the surface. One method to avoid this effect is to sputter the isolating material before investigation with thin conductive layers of e.g. graphite or gold.^{1,6}

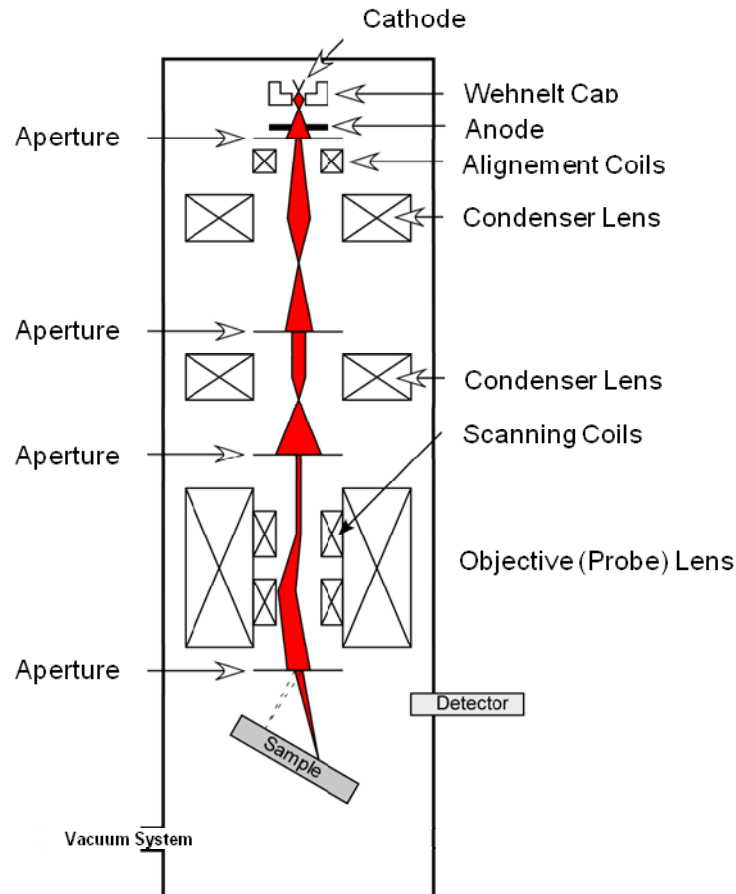


Figure 3.2.2. Schematic drawing of a SEM.⁷

3.2.2 Focused ion beam microscopy

The focused ion beam (FIB) microscope was developed in the 1970's and is not an electron microscope but has a lot in common with these instruments. It allows the preparation of thin specimen as materials can be deposited or ablated which is important for microstructural analysis. With a FIB, samples can be sputtered and milled precisely, which is of great interest for e.g. micromachining. One great advantage of this technique is that site-specific TEM samples can be prepared. This can be useful for looking at a particular specimen area.^{8,9} Instead of electrons, high energy ions are focused and scanned across the sample. In general, the FIB can be combined with an SEM so that materials can be analyzed and the specimen modified with one instrument. Ga⁺ ions produced in a liquid ion source are commonly used for investigating and treating the sample. The ions are accelerated usually to voltages of 0 - 30 kV. Subsequently, the ion beam is focused onto the specimen with asymmetric electrostatic lenses. Beam blanking plates scan the beam across the sample and SE or ions are detected with different detectors. A schematic drawing of a FIB is shown in Figure 3.2.3.

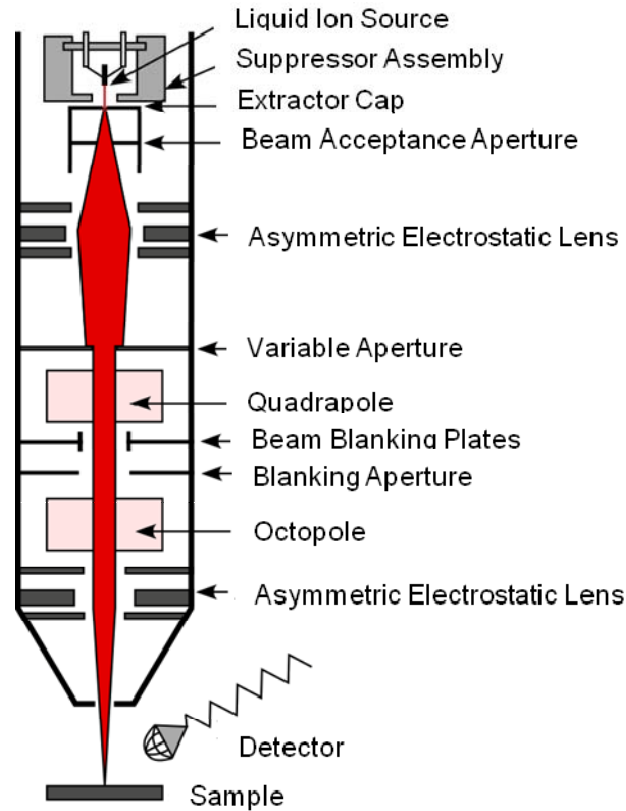


Figure 3.2.3. Schematic drawing of a FIB microscope.¹

FIB allows the cross section preparation of TEM specimen. The ion beam interacts with the surface of the sample and removes material in nanometer steps. Often, a protection layer of e.g. C or Pt is deposited prior cutting in order to avoid damage of the surface structure of the specimen. After cutting the specimen to the requested thickness the sample is polished and transferred to a Cu grid with a manipulator needle.^{1,10}

3.2.3 Transmission electron microscopy

The first TEM was invented by Ernst Ruska and Max Knoll in the beginning of the 1930's. The use of an electron beam highly improved the resolution and allows by the current state of scientific knowledge the analysis of specimen in the sub-nanometer regime.^{11,12} A TEM consists of several components. These are illustrated in Fig. 3.5. The electron beam is produced by an electron gun. Several electron sources exist as described in Chapter 3.2.1. The acceleration voltage, usually between 80 and 300 kV, determines the energy and thus the wavelength of the electrons. Several electromagnetic lenses are used to focus and deflect the electron beam. The condenser lens system bundles the electrons, a parallel illumination or a convergent beam can be

achieved. This system regulates the intensity and the convergence angle of the electron beam. The objective lens creates a first intermediate image of the specimen. Hence, the sample is inserted between the pole pieces of the objective lens system. The specimen has a diameter of 3 mm and a thickness of about 2 - 100 nm at its thinnest point. In the back focal plane of the objective lens the diffraction pattern is obtained. The contrast of the specimen can be enhanced by using an objective aperture which blocks specific electrons. With a selected area diffraction (SAD) aperture, inserted in the plane where the first intermediate image occurs, an area of the sample can be chosen and limited to a specific area. The objective lens system is followed by intermediate and projector lenses which enlarge the first intermediate image. The image of the specimen is projected on a fluorescent screen and recorded with a charge-coupled device (CCD) camera. A diffraction pattern is achieved by changing the strength of the intermediate lenses and projecting the back focal plane of the objective lens instead of the intermediate image on the screen (Figure 3.2.4).

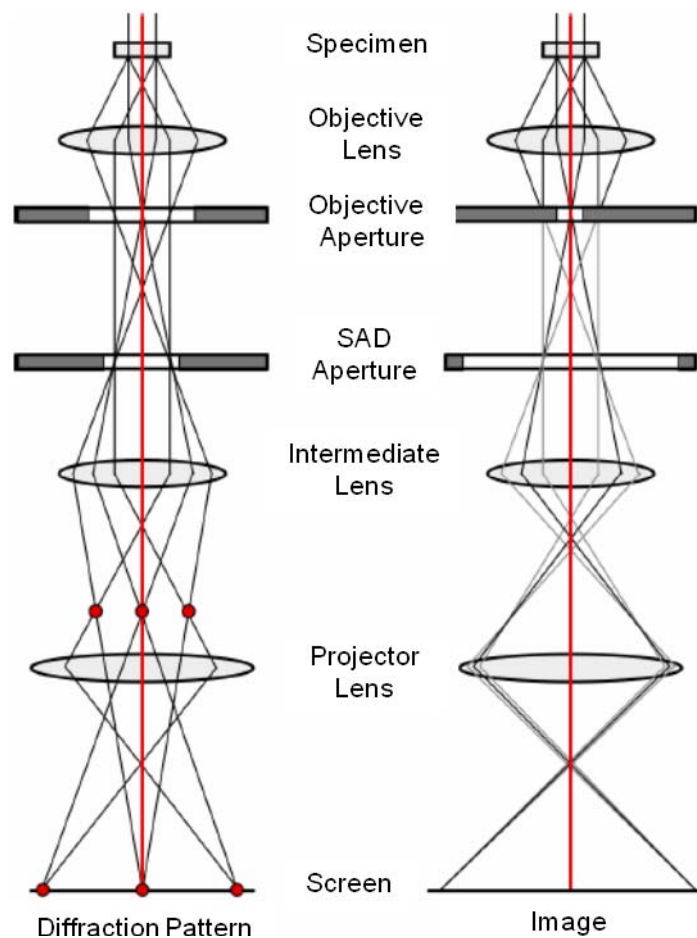


Figure 3.2.4. Schematic drawing of the components of a TEM and its electron beam path a) in diffraction mode and b) in image mode.¹

Lens aberrations

The actual resolution is limited by lens aberrations. One is the spherical aberration C_s which is effecting the off-axis rays. The lens field affects the off-axis rays differently than the on-axis rays. They are more strongly focused and this bents them toward the axis at a different point on the optical axis than the on-axis beams. Thus, rays with different distances from the optical axis possess different focal points. The rays do not converge in a point but in a disc of least confusion. The higher the incident angle is the higher the difference in focal length gets. This effect is imaged in Figure 3.2.5 and described by formula 3.5

$$d_s = \frac{1}{2} C_s \alpha^3 \quad (3.5),$$

where d_s is the diameter of the disc of least confusion, C_s the spherical aberration coefficient and α the semi-convergence angle.

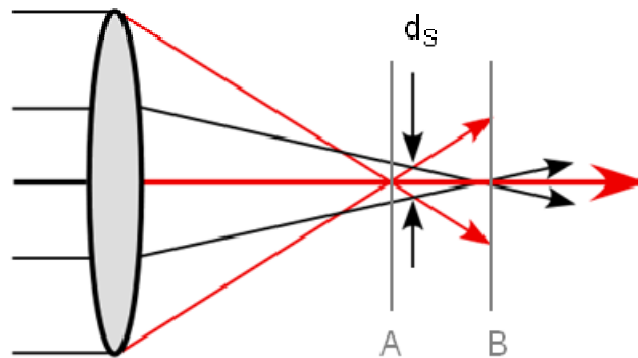


Figure 3.2.5. Schematic drawing of the spherical aberration showing the ray path and the diameter of the disc of least confusion d_s . A is the focal point of the border rays and B the focal point of the axial rays.¹

Another limiting aberration is the chromatic aberration C_c . By leaving the cathode not all electrons possess the same energy. Electrons with a lower energy are more strongly refracted on the lens than faster electrons. This results again in a disc of least confusion with a diameter of d_c as is shown in Figure 3.2.6 and given by formula 3.6:

$$d_c = C_c \frac{\Delta E}{E_0} \alpha \quad (3.6).$$

C_c is called the chromatic aberration coefficient, ΔE is the energy spread of the electron beam, E_0 the primary energy and α describes the semi-convergence angle.

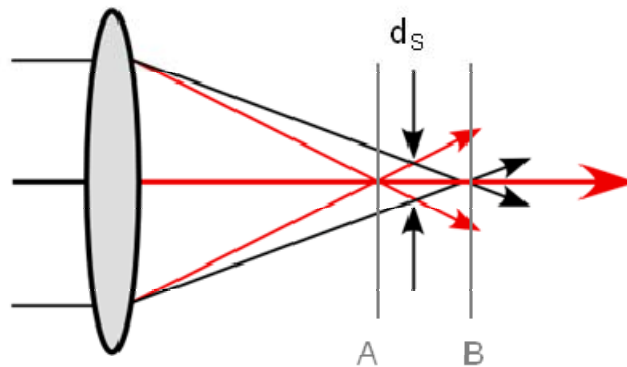


Figure 3.2.6. Schematic drawing of the chromatic aberration effect showing the ray path and the diameter of the disc of least confusion d_c . A describes the focal point of electrons exhibiting a longer wavelength and B electrons with a shorter wavelength.¹

Another factor effecting the image is the astigmatism. The magnetic field of ideal lenses is radial symmetric. This is not true for real lenses. Here, the radial symmetry is disrupted and paraxial rays are not bundled in one point but in a focal line. Horizontally incident rays possess another focal line than vertically incident rays. The astigmatism can be corrected with stigmators and its effect is displayed in Figure 3.2.7.

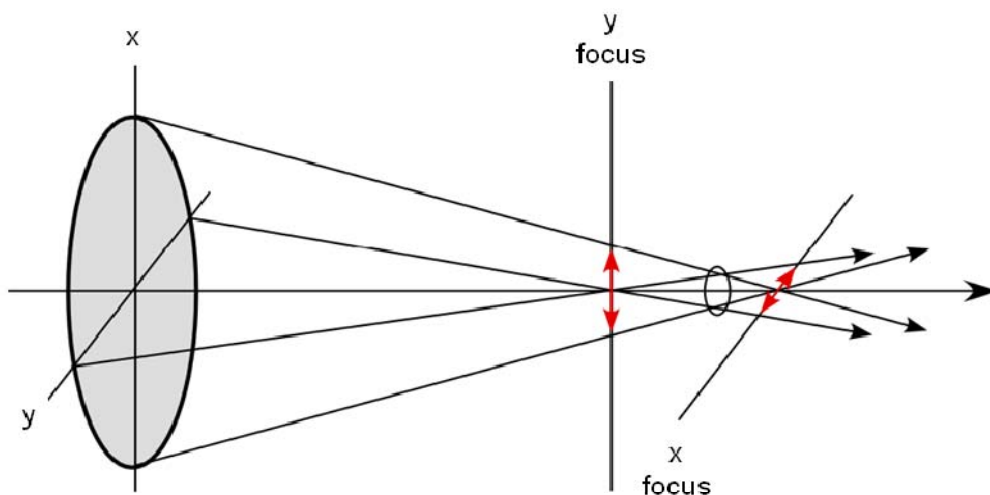


Figure 3.2.7. Schematic drawing of the ray path resulting in astigmatism arising from two principle line foci at right angles along the axis.¹

The theoretical resolution is limited by diffraction. Thereby, the rays get diffracted on the edge of the lens and interfere with non-diffracted rays. A point is then imaged as disc. The diameter of the disc d_B is given by the equation 3.7:

$$d_B = 0.61 \frac{\lambda}{\alpha} \quad (3.7)$$

and depends on the de-Broglie wavelength λ of the electron and the semi-convergence angle α .

In recent years, C_s - and C_c -correctors, which are magnetic multipoles like sextupole and octupole lenses, were developed and enhance the resolution down to $< 1 \text{ \AA}$.¹³⁻¹⁵

Electron diffraction

Electron diffraction occurs when electrons hit the atoms of the specimen and get scattered. Overlapping of scattered electrons leads to interference effects. Constructive interference is described by the Bragg equation (3.1) (see chapter 3.1). The electrons are scattered on the crystal potential or in amorphous materials on the Coulomb potentials of the atom nuclei. The diffraction pattern is produced in the back focal plane of the objective lens. Depending on the crystallinity the specimen can exhibit different diffraction patterns. Single crystalline material results in a point pattern (Laue diagram), polycrystalline material in a discrete ring pattern (Debye-Scherrer diagram) and amorphous specimen in diffuse rings. When the camera constant of the TEM is known, the lattice spacings d_{hkl} of a material can be calculated with equation 3.8:

$$\lambda L = R d_{hkl} \quad (3.8).$$

The constant λL is determined with the help of a standard, usually with a Si single crystal. R is the measured distance in the diffraction pattern in units of pixel. Different sizes of the area of a specimen can be chosen with various SAD apertures.

Conventional TEM

Two imaging modes are known in conventional TEM (CTEM) and the contrast is achieved by inserting an aperture in the back focal plane of the objective lens. The first is the bright-field (BF) mode where the scattered electrons are blocked. Hereby, the non-scattered electrons form the image. Areas exhibiting a higher scattering appear darker.

The second mode is called dark-field (DF) mode and the contrast is inverted as only scattered electrons are used for imaging. The non-scattered electrons are blocked by an aperture. This is achieved by either moving the objective aperture or by tilting the beam so that the diffracted beam is parallel oriented to the optical axis. At thicker regions of the specimen the electrons are more scattered than at thinner regions. They appear darker in BF images because more scattered electrons are captured. This effect is known as thickness contrast. Besides, material contrast is caused by the atomic number Z . A higher Z leads to a higher contrast. Diffraction contrast is the third contrast mechanism in imaging mode. Thereby, areas of a sample appear darker in the BF images when the Bragg equation is fulfilled than regions with random orientations.

High resolution TEM

With high resolution TEM (HRTEM) specimen can be investigated at the atomic scale. At this operation mode no objective aperture is needed so that scattered and unscattered electrons contribute to the image. These electrons interfere and with the help of the phase contrast the lattice planes in crystalline materials can be observed. In HRTEM a parallel beam is used which can be described as a plane wave. The electron interacts with the crystal potential of the specimen. In very thin samples the phase of the electron wave changes whereby the amplitude stays constant. The phase contrast must be converted in an amplitude contrast by shifting the phase of the scattered beam by $\pi/2$ compared to the primary beam leading to a total phase shift of π . This is achieved by defocusing the objective lens and by the lens aberrations. The phase shift depends in addition on the thickness of the sample. The specimen is tilted in zone axis so that the lattice planes are visible. The lattice planes which are observable in the HRTEM image are determined by the contrast transfer function (CTF) $\sin\chi(u)$ (equation 3.9), with

$$\chi(u) = \pi\Delta f\lambda u^2 + \frac{1}{2}\pi C_s\lambda^3 u^4 \quad (3.9).$$

Δf is the defocus, λ the wavelength, u the spatial frequency and C_s the spherical aberration coefficient. The contrast is reversed when the function passes zero. The Scherzer defocus is given where the first zero-crossing of the CTF is at the highest spatial frequency. Until this frequency no contrast inversion occurs. The CTF with the Scherzer defocus is displayed in Figure 3.2.8. The curve was calculated for 200 kV

accelerating voltage, a focal spread of 1.97 nm, a semi-convergence angle of 0.3 mrad a C_s of 1.2 mm and a C_c of 1.2 mm. The defocus value Δf is -53 nm.

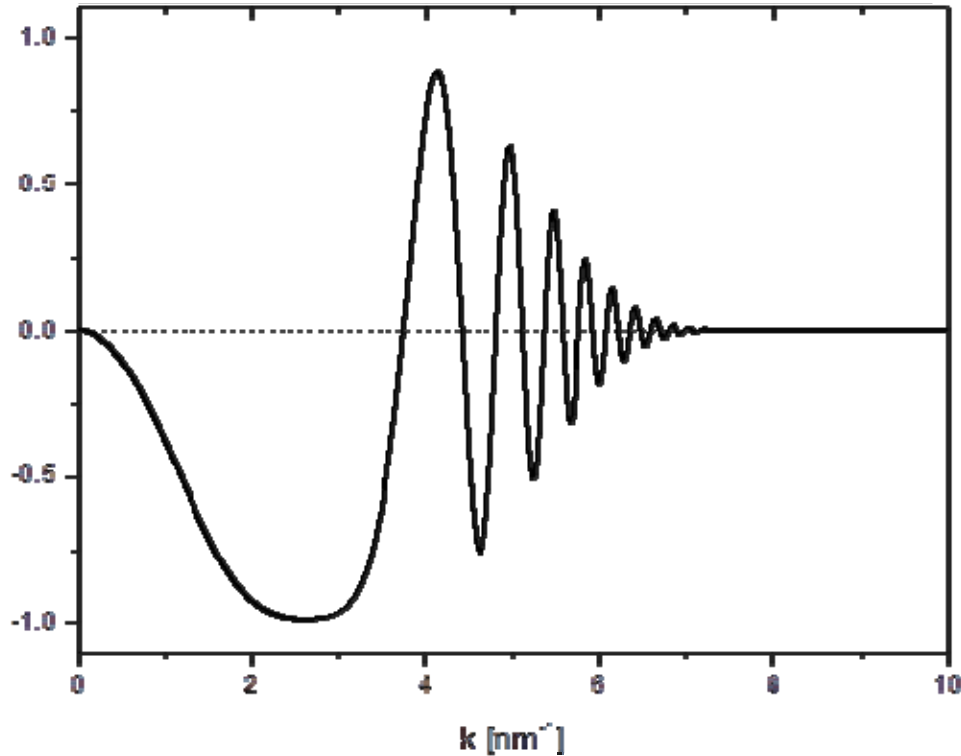


Figure 3.2.8. CTF for the Scherzer defocus with $\Delta f = -53$ nm.

A resolution of < 0.1 nm can be achieved by correcting the spherical and chromatic aberration as is done in novel aberration corrected TEMs.^{11,12}

Scanning TEM

In scanning TEM (STEM) mode a convergent electron beam is scanned across the sample and the transmitted electrons are detected. Therefore, the beam is focused with the condenser and objective lenses and deflected with magnetic dipoles without the need to change the convergence angle. The scattered electrons are detected with different detectors. These detectors are placed around the optical axis and the contributing electrons can be chosen with the right choice of the camera length. For electrons scattered in forward direction ($\theta = 10 - 25$ mrad) a BF detector is used. For small-angle scattered electrons (Bragg-scattered electrons, $\theta = 25 - 50$ mrad) an annular dark-field (ADF) image is obtained and for high-angle scattered electrons ($\theta > 75$ mrad) high-angle

ADF (HAADF) images are recorded. With the latter imaging mode chemical elements can be distinguished. The intensity of the signal is in that case proportional to the square of the atomic number Z . The beam path and the different detectors are pictured in Figure 3.2.9.

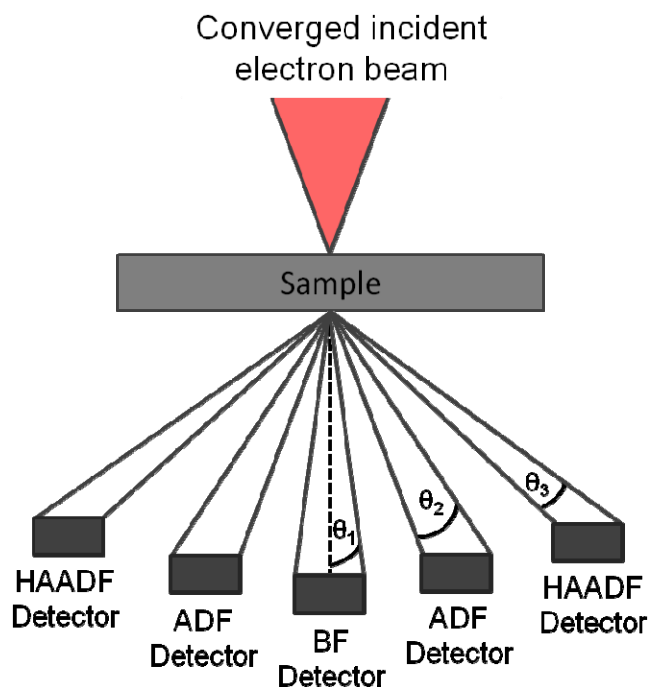


Figure 3.2.9. Schematic drawing of the different detectors used in STEM mode. Modified from Brandon and Kaplan.¹

The resolution in HAADF-STEM images is determined by the diameter of the electron beam. Sub-Å resolution can be obtained by aberration corrected STEMs.^{14,15}

3.2.4 Analytical techniques

There are several scattering processes which occur while the electrons interact with the sample. In general, the scattering signals can be subdivided in two groups. The primary or direct signals are related to elastic and inelastic scattering processes. The former is detected as Bragg scattering and used for electron diffraction analysis and imaging, whereas the second is used for EELS. Secondary effects result in SE, BSE, Cathodoluminescence, X-ray emission and Auger emission. These processes are summarized in Fig. 3.2 and can be used for several analytical techniques like SEM, EDX and Auger spectroscopy. The cross-section σ and the mean free path Λ define the probability that an electron is scattered by the material and is given by equation 3.10:

$$\Lambda = \frac{1}{N\sigma} \quad (3.10),$$

where N is the number of particles per unit volume. In general, Λ describes the distance an electron travels before getting scattered. In general, the thinner the specimen the less the electrons get scattered, meaning with a thin TEM sample the electron transmitting the material gets scattered once or not at all. With increasing thickness the electron gets scattered a few up to several times. The scattering probabilities are called single, plural and multiple scattering, respectively. The elastic scattering is mostly a coherent process whereby the energy of the incident electron is preserved and does not change, although the direction of the electron movement is usually changing. This means that the wave vector is changing its direction but not the magnitude. This process is used for diffraction experiments and imaging in the TEM and is the most likely mechanism for electron interaction with the specimen for thin samples. The elastic scattering is subdivided into Rutherford scattering, which occurs at large angles, and small-angle scattering. The former is caused by Coulomb interaction between the primary electron and the nuclei of the specimen atoms and is strongly dependent on the atomic number Z , typically Z^2 . This signal is used for HAADF imaging. The second process arises when the electron passes the atom further away from the nucleus and is caused by scattering or interactions of the electron at the electron cloud of the material. The inelastic scattering is an incoherent process, meaning that there is no phase relationship between the scattered waves and the incident wave. The energy of the incident electron is reduced. This process can occur in different manners. One is the phonon excitation where phonons are produced. These are atomic vibrations of the solid and the energy loss is less than 1 eV. Another scattering process is the PL excitation. Here, the valence electrons of a solid are excited and oscillate in a collective way which leads to an oscillations of the electron gas of the specimen. The energy loss for this process is in general in the range of 5 to 30 eV. Another inelastic scattering process of the incident electron is the single valence electron excitation, whereby as its name suggests a single electron of the solid gets excited. The transition with the lowest energy loss is corresponding to the band gap of a material. The valence loss region is up to 50 eV. The last prominent inelastic scattering process are excitations of inner shell electrons. The energy loss can be up to several hundred eV if higher bound inner-shell electrons are removed. This ionization exhibits the main analysis process type for EELS. A secondary

effect related to the excitation of the inner shell electrons is the emission of characteristic X-rays. In addition, *bremstrahlung* occurs (see Chapter 3.1). The inelastic scattering processes are used for EELS and the total cross-section is linear dependent on Z . Besides these processes electrons are absorbed by the sample and cannot be used for analytical techniques.

The nomenclature in EDX and EELS is based on standard spectroscopic notation. For the inner shell electrons the Rydberg states are used which are defined by the Bohr shells K , L , M etc. and the four quantum numbers. These are the principal quantum number n , the angular-momentum quantum number l , the magnetic quantum number m and the spin quantum number s . Electron orbitals are defined by specific combinations of these four quantum numbers. The electrons occupy subshells like s , p , d , or f depending on the total number of electrons in the atom.

Energy dispersive X-ray spectroscopy

The chemical composition of a sample in an electron microscope can be analyzed with EDX. The detector absorbs low energy X-rays (< 1 keV) and therefore elements below $Z = 5$ can usually not be quantified. Elemental characteristic X-rays are emitted when the specimen is irradiated with an electron beam (see Chapter 3.2). The principle behind this is that an electron hole is produced by knocking out an inner shell electron of an atom. A more energy-rich electron from an outer shell will filled up this hole as this state is instable. The relaxation leads to an energy difference which can be released as X-ray or to the emission of AE. Each element exhibits a characteristic X-ray wavelength so that this method enables the chemical composition analysis of a specimen. The emitted X-rays are named after the standard spectroscopic notation as K , L , M shells. The second letter (α , β , γ) denotes from which outer shell the electron came. The EDX notation is given in Figure 3.2.10.

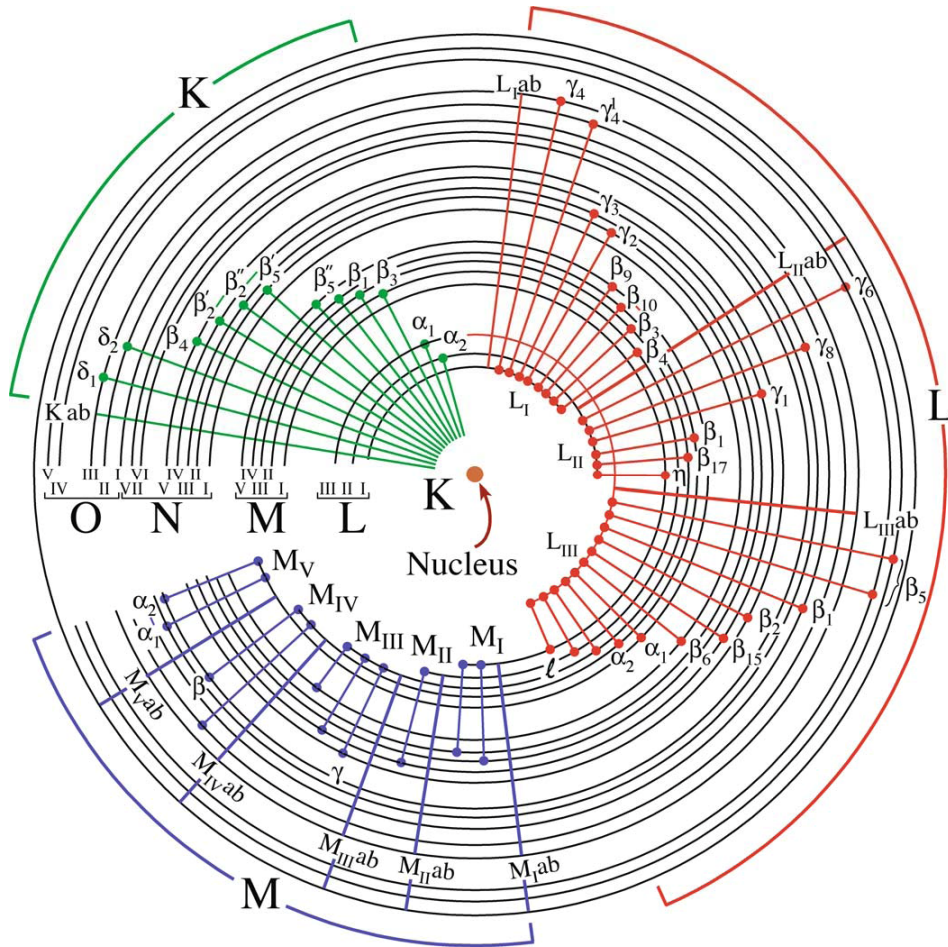


Figure 3.2.10. Schematic drawing of a relaxation process of an inner shell electron and the corresponding standard spectroscopic notation.⁴

The background of an EDX spectrum is formed by the *bremstrahlung* (see Chapter 3.1). With the Cliff-Lorimer equation (3.11) elements can be quantified:

$$\frac{C_A}{C_B} = k_{AB} \frac{I_A}{I_B} \quad (3.11),$$

where the ratio of the intensities I_A and I_B of the peaks of element A and B are proportional to the concentration ratio C_A and C_B of the element A and B in weight percent. The Cliff-Lorimer factor is given as k_{AB} and depends on the elements which are analyzed in the EM and the detector.^{1,4,16}

Electron energy loss spectroscopy

In the 1940s, J. Hillier and R. F. Baker developed the EELS technique which is nowadays widely used to analyze the chemical and electronic structure of nano- and micro-materials. The advantage of this method is the high spatial and energy resolution which

can be achieved simultaneously. Besides, light elements like Be, O, N and so forth can be easily detected and quantified which is difficult or even impossible with other techniques, e.g. EDX. The electron beam interacts with the sample and the transmitted scattered electrons and their energy losses are detected with a spectrometer.

The bonding in a solid can be described by the atomic orbitals (AO) which overlap to molecular orbitals (MO). The bonding MOs have a lower energy compared to the single AOs whereas the antibonding MOs have a higher energy. The bonds dependent on their symmetry. Rotational-symmetric bonds are the strongest and are called σ bonds. The second covalent bond type is π bond. This bond is not rotational-symmetric meaning that the MOs cannot rotate without breaking the bond. The bonding and antibonding MOs in a solid are specific allowed energy levels which form a continuous energy band of allowed energies. In bulk material the valence electrons fill these energy bands where the highest occupied level is called the Fermi level (E_F). The highest occupied band is the valence band and the lowest unoccupied band the conduction band. In semiconductors and isolators, these two bands are separated by a forbidden energy gap, the so called band gap. Here, E_F is located in between the band gap. In metals this gap does not occur, the electrons are free to move, which is why these materials are conductive. The band structure can be described with the help of density of states (DOS). The DOS is defined as the number of states per energy interval. In atoms, molecules or gas this distribution is discrete whereas in solid-state the distribution is continuous. If many states are available this is reflected in a high DOS. DFT calculations deal among others with the calculation of the local, symmetry projected DOS. EELS is able to analyze these electronic structures at the atomic scale and can be interpreted with the help of DFT calculations. A schematically drawing of the relation between the DOS and the ELNES is shown in Figure 3.2.11.

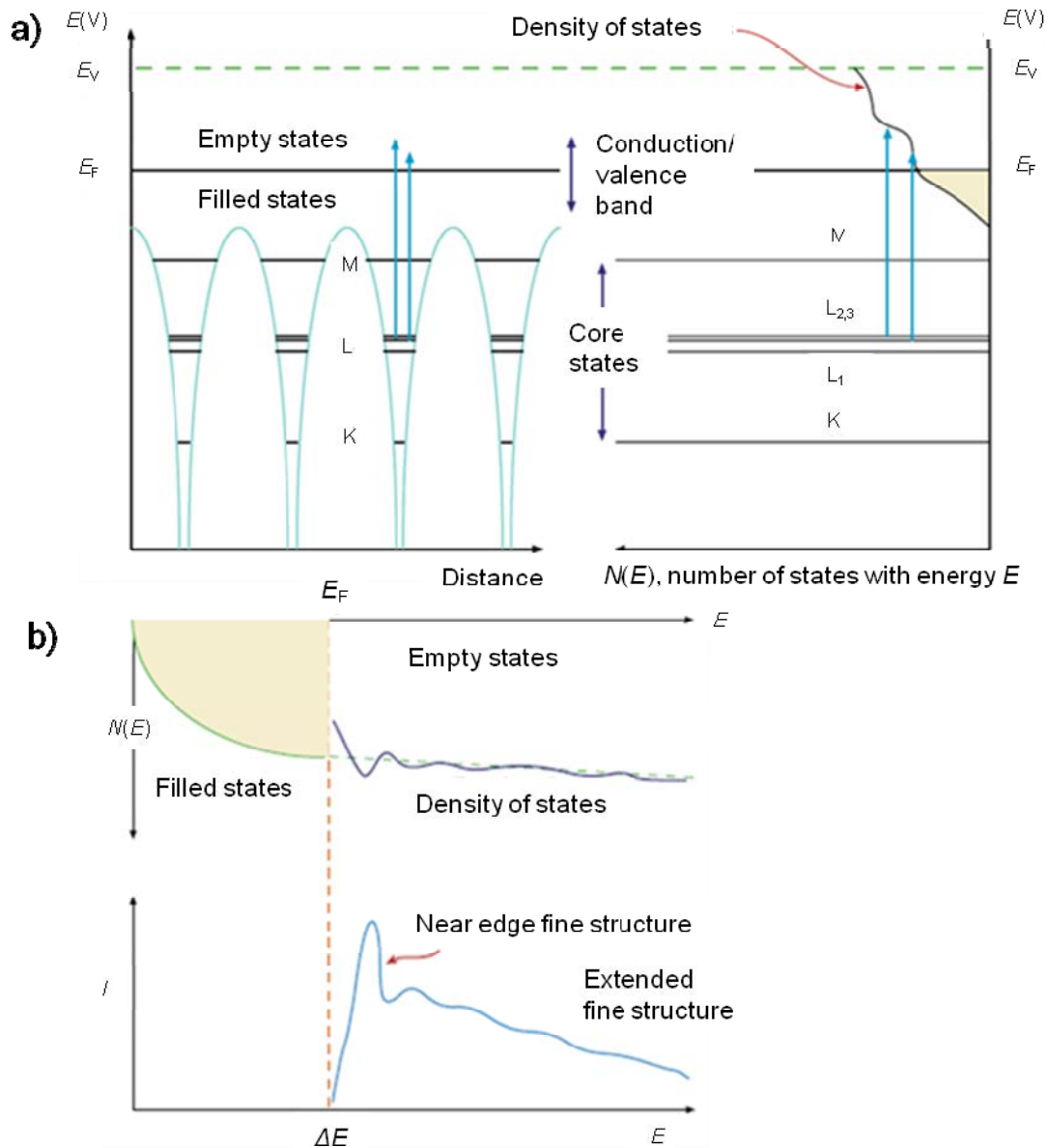


Figure 3.2.11. Relationship between the DOS and the ELNES. a) Energy diagram of a solid metal (left) and the density of filled and empty states in the conduction and valence band (right) including the Fermi level E_F . b) Correlation of the empty DOS and the ELNES intensity. The Fermi energy E_F and the edge onset are related to each other.⁴

An EEL spectrum can be classified in three regions and one is schematically pictured in Figure 3.2.12. The ZLP, which is the most intense peak of the spectrum, occurs at 0 eV and consists of all the electrons which were unscattered and did not undergo an energy loss process. Besides, there are quasi-elastically scattered electrons, which emit phonons and contribute as well to the ZLP region. The energy resolution is limited by the full width at half maximum (FWHM) of the ZLP which is dependent on the energy spread immanent to the electron source. The effect of the electron source on the FWHM is

described further below in detail. The subsequent region is called the low loss region and arises at energy losses between 0 – 50 eV. This region is characteristic for the solid state behavior of the specimen and is dominated by oscillations of the valence electrons of the solid, the PL as mentioned above. This region is affected by the density of the valence electrons of the specimen. Multiple peaks in the valence loss region arise when the sample is too thick. Interband transitions occur in insulators and semiconductors in this region. Hereby, single valence electrons are excited to low-energy unoccupied electronic states above the Fermi level. Overall, with this region the sample thickness can be estimated and, concerning insulators and semiconductors, the dielectric function and the band gap can be analyzed. The third region occurs at high energy losses above 50 eV and is called the core loss region. Here, inner-shell electrons are excited to unoccupied energy levels above the Fermi level which are specific for the atomic species and the chemical composition of the specimen. Each element has a specific energy loss and generates ionization edges with characteristic ELNES and EXELFS. Thereby, the ELNES is correlated to the oscillations from the edge onset to ~50 eV above the edge and the EXELFS beyond 50 eV (see below). The edge occurs on a background which is caused by tails of the PL peak and the background stemming from edges occurring at lower energy losses.

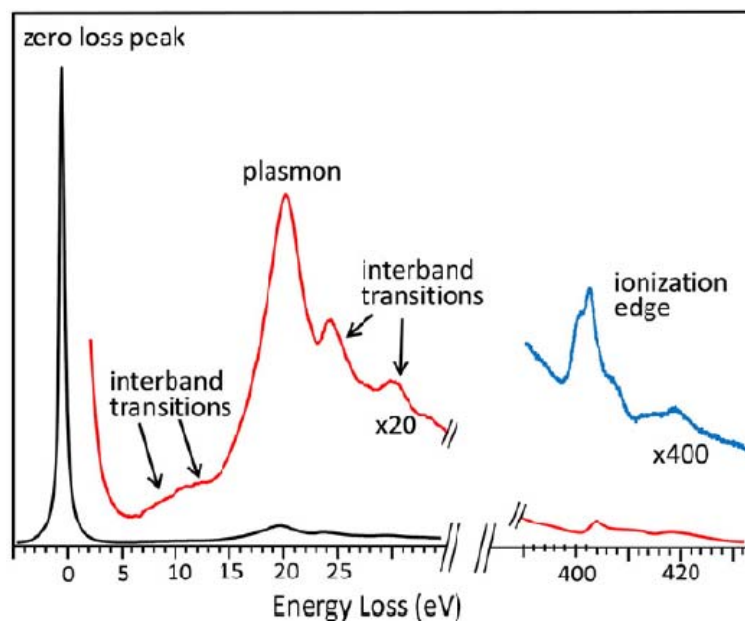


Figure 3.2.12. Schematic drawing of the basic regions of an EEL spectrum exhibiting the ZLP, the valence loss region with the PL and interband transitions as well as the core-loss region with an ionization edge.⁵

The atomic type can be determined as the energy of the threshold which is given by the binding energy of the electrons in the atom. The intensity of an ionization edge is proportional to the transition rate and is used for quantification. The transition rate $W(\Delta E)$ describes the probability per time unit and area that inner shell electrons are excited to unoccupied states above the Fermi level and is given by Fermi's golden rule (3.12):

$$W(\Delta E) \sim |M(\Delta E)|^2 N(\Delta E) \quad (3.12).$$

$M(\Delta E)$ is the transition matrix element which describes the correlation between the initial and final state and $N(\Delta E)$ the DOS in the conduction band. The edge shapes are related to the transition matrix element (Figure 3.2.11). If the transition matrix element is only changing slightly the ELNES represents the partial DOS (PDOS) of the unoccupied states of the conduction band. The ionization edges are determined, according to the standard spectroscopic notation (see Chapter 3.2.4), as K , L , and M edges depending on the orbital from where they were excited. The edge can exhibit five different shapes which are summarized in Figure 3.2.13. The saw-tooth shape (Figure 3.2.13a) exhibits a sharp onset followed by a continuous decrease of the intensity. This edge type is characteristic for K -edges which arise from the excitation of $1s$ electrons, for L_1 -edges which stem from the excitation of $2s$ electrons and for M_1 -edges coming from the excitation of $3s$ electrons. A delayed maximum (Figure 3.2.13b) is characteristic for $L_{2,3}$ -edges for elements of the third period of the main group elements. L_2 and L_3 derive from the excitation/transition of the $2p_{1/2}$ and $2p_{3/2}$ electrons, respectively. Here, the delayed maximum arises 10 to 20 eV above the edge onset. For the $L_{2,3}$ -edges of 3d and 4d transition metals two sharp peaks with a high intensity at beginning of the edge are observed and are called white lines (Figure 3.2.13c). Edges arising in the PL region (between 20 and 50 eV) exhibit a PL like profile (Figure 3.2.13d) because they overlap with the background of the valence electrons. A mixed profile (Figure 3.2.13e) is described by a sharp maximum after the edge onset followed by a rounded second maximum at around 100 eV.

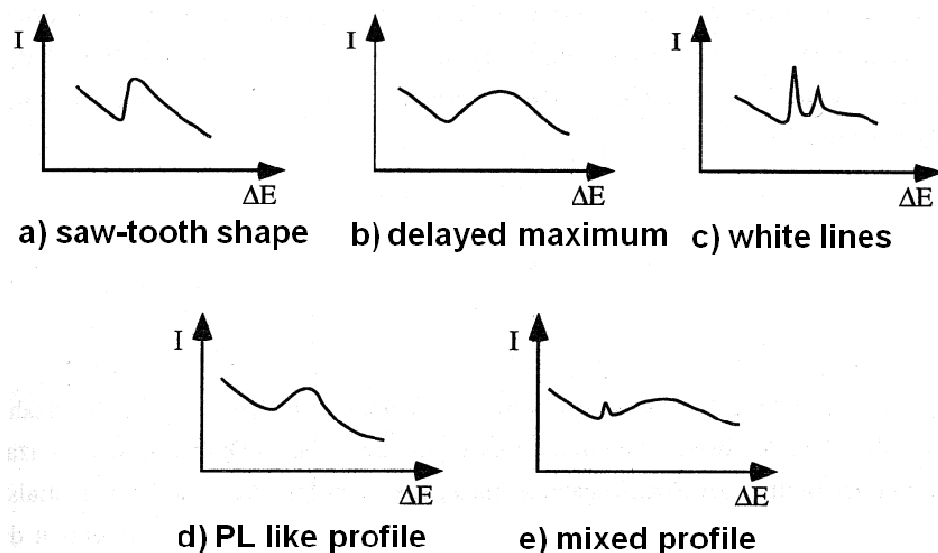


Figure 3.2.13. Schematic drawing of the five characteristic edge shapes showing a) saw-tooth shape, b) delayed maximum, c) white lines, d) PL like profile and e) mixed profile.¹⁷

The ELNES contains the information about the local structure and bonding of the atoms and appears in the first <50 eV above the edge threshold. The ELNES can be influenced by several factors. The valence or oxidation state of an atom can cause a chemical shift of the edge onset and the intensity distribution in the ELNES can vary. The chemical shift can be up to 9 eV.¹⁸ In addition, the coordination can affect the ELNES. The ELNES can be calculated with several theoretical approaches. Comparing the experimentally obtained ELNES with theoretical calculations often helps to determine the electronic structure of novel materials. The EXELFS describes the region beyond 50 eV of the edge threshold and appears therefore much weaker than the ELNES. It carries information about the bond distances and coordination numbers of the neighboring atoms. For EELS analysis the specimen should not be thicker than the mean free path. Otherwise, there would be multiple inelastic scattering which increases the PL intensity drastically and hence the background signal, leading to a decreased core loss signal. In addition, plural scattering can lead to difficulties in the ELNES interpretation since beside the single electron excitation PL excitation occurs. The background can be estimated by using a power-law function (3.13):

$$I = AE^{-r} \quad (3.13),$$

where I is the intensity, E the energy loss, A and r are fitting parameters. In general, the scattering processes can be pictured as vector diagrams. The incident wave vectors

depend on the convergence semi-angle α . The amount of collected wave vectors is determined by the collection semi-angle β . As it is important to detect as much as possible of the scattering for a good EELS signal, the parameters for EELS measurements must be considered before starting the experiment.

To collect EEL spectra several spectrometer types exist. A general setting is shown in Figure 3.2.14. Here, the spectrometer is placed below the fluorescent screen. The entrance aperture is used to select electrons with specific scattering angles. Before passing the drift tube, the electron beam is focused with several quadrupole and sextupole lenses. The following magnetic prism deflects and disperses the electron beam with a magnetic field and bends the electrons by 90° . Afterwards, several lenses magnify the spectrum before the different spreads of the energy losses are collected with a detector which is a combination of a scintillator (yttrium aluminium garnet, YAG), glass fiber system and a CCD camera or a photodiode array (PDA). The EEL spectrum can be measured in different modes, either in image mode or the diffraction mode, where a diffracted beam is used. In both modes a paraxial illumination is used. Another operation method is the STEM mode. Here, a convergent beam scans across the sample. A further technique available is the energy filtered TEM (EFTEM) imaging where the sample is illuminated by parallel illumination. An element map is obtained by using electrons with a specific energy loss. This specific energy loss is chosen with an energy selecting slit. Usually three images are taken (“three window method”). Two pre-edge images to determine the background and one after the edge (“post-edge” image). A schematic drawing of a Gatan parallel EELS (PEELS) system is shown in Figure 3.2.14. Dark current occurs when spectra are collected. This is due to thermal leakage currents and inherent electronic noise from the diodes which needs to be subtracted from the individual spectra. In addition, due to variations in the gain of the individual channels of the CCD or PDA, the channel-to-channel has to be taken into account.

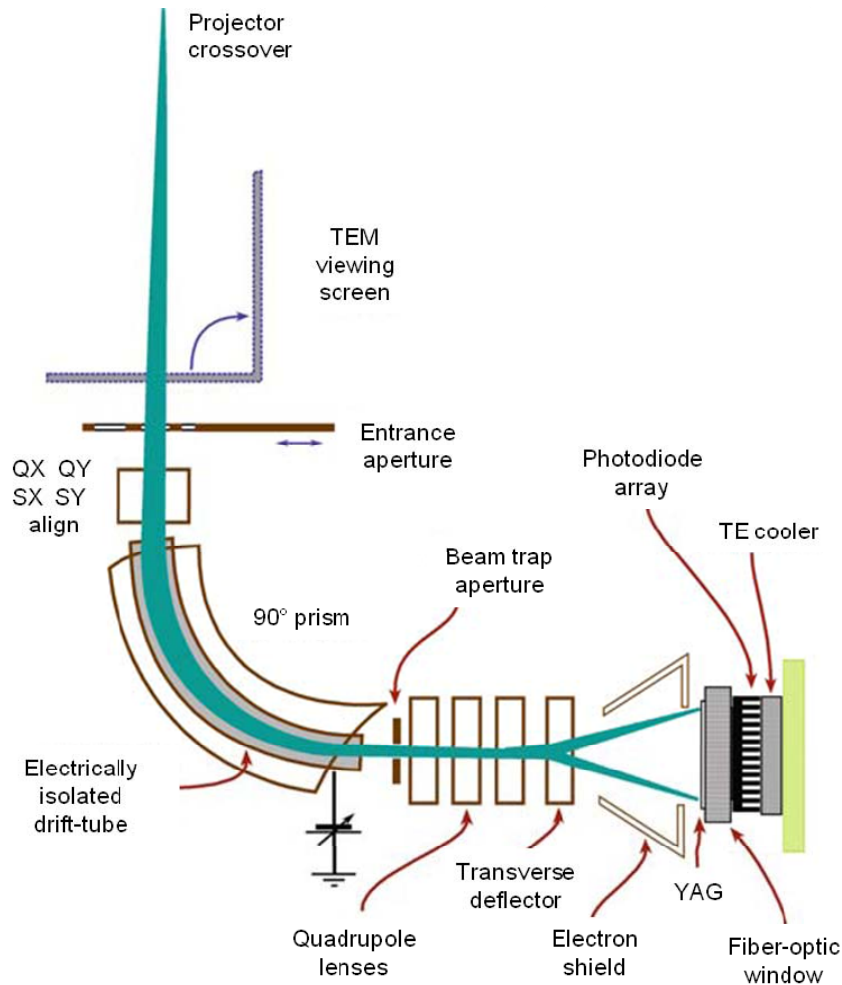


Figure 3.2.14. Schematic drawing of a Gatan PEELS system.⁴

With EELS elements can be determined qualitatively and quantitatively. Especially, for light elements this technique is ideal. For element quantification several steps must be executed. First, the background has to be subtracted for an accurate measurement of the intensities under the ionization edges. Therefore, an energy window Δ placed on the left side before the edge threshold, comprising 50 – 100 eV, is applied. The background is calculated in that region via equation 3.13. Then, a partial cross-section σ is calculated by a hydrogenic model or a Hartree-Slater model to determine and compare the different edge intensities or to analyze directly the atomic concentration of the sample. For the latter, the exact thickness of the specimen must be determined. If the sample is too thick, the spectrum has to be deconvoluted before. The chemical composition can be calculated with an accuracy of 0.1 – 5% with formula 3.14:

$$\frac{N_A}{N_B} = \frac{\sigma_B(\beta, \Delta) I_A}{\sigma_A(\beta, \Delta) I_B} \quad (3.14).$$

$\frac{N_A}{N_B}$ is the atomic ratio of the elements A and B , $\frac{I_A}{I_B}$ the intensity ratio, $\frac{\sigma_A}{\sigma_B}$ the ratio of the ionization cross section, β the collection semi-angle and Δ is the width of the energy window.

The experimental conditions have a high impact on the EELS measurements. The electron source determines the energy spread of the electron beam and therefore the energy resolution of the EEL spectrum. Thermal W sources lead to an energy spread of around 1.5 – 3 eV measured in the FWHM of the ZLP, the LaB₆ to a FWHM of 1 – 1.5 eV. Thermal assisted (Schottky emitter) or cold field emission sources have an energy spread of 0.6 – 0.8 eV and 0.3 eV, respectively. The energy resolution can be highly improved up to 0.1 eV by using a monochromator which is often a Wien filter. With perpendicular electrostatic and magnetic fields and a selecting slit, electrons with a specific energy can be guided straight line down the TEM column.

The higher the incident beam current density is chosen the more intensity is achieved leading to a better SNR. The disadvantage is that this can cause radiation damage like knock-on damage or radiolysis. The SNR can be enhanced with the right choice of the condensor aperture and the collection angle of the electrons entering the spectrometer which depends on the size of the entrance aperture and the camera length. In general, the specimen should be tilted out of a major zone axis to avoid channeling effects.

3.2.5 Electron tomography

The imaging of materials in traditional TEM is achieved as two-dimensional (2D) micrographs. To completely understand micro- and nanostructures a method to obtain 3D information is required. Electron tomography (ET) allows the analysis of 3D samples at the nanoscale in TEM.¹⁹⁻²² Here, a tilt-series of two-dimensional projections of an object is collected. Usually, the data is acquired in ADF- or HAADF-STEM mode because phase and diffraction contrast do not strongly (ADF) or not at all (HAADF) contribute to the image intensities. Furthermore, the latter mode is chemically sensitive due to its Z contrast dependency (see Chapter 3.2.3). The single-axis tilting method is one of the most commonly used techniques to record tilt-series. This is illustrated in Figure 3.2.15. Here, the sample is rotated around a fixed eucentric axis at defined tilt increments. In theory, a tilt-series implies projections between $\pm 90^\circ$ to obtain as much information of the object as possible. Most commonly, projections up to $\pm 75^\circ$ are realized at tilt

increments as low as 1° leading to a number of up to 150 projections. The remaining tilt range is known as missing wedge and leads inevitable to artefacts during reconstruction.^{23,24}

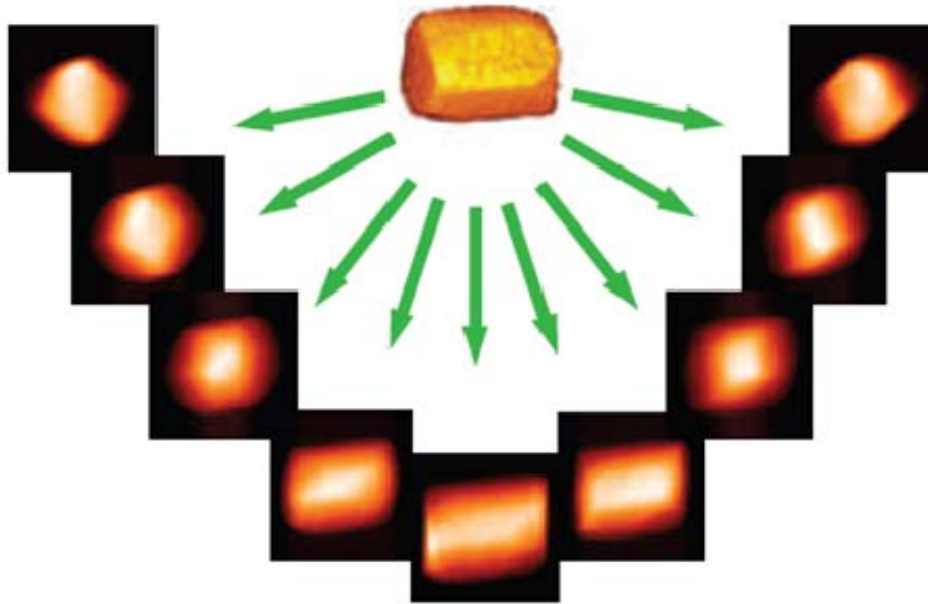


Figure 3.2.15. Schematic drawing of a single-axis tilt-series showing exemplary an ensemble of images (projections).²⁵

The most common reconstruction techniques in ET are the Filtered Back Projection (FBP)²⁶ and the Simultaneous Iterative Reconstruction Technique (SIRT)²⁷. For some specimen such a high number of projections cannot be acquired due to reasons like e.g. beam sensitivity. Then, less images have to be used and therefore a good reconstruction algorithm is needed to compensate for the low amount of information. With discrete tomography images can be reconstructed with only a small number of projections.²³ Thereby, fixed grey values are used for a set of densities of the present materials. The expected number of materials should be known so that to a specific grey value a density can be assigned. The starting volume for reconstruction is based on a previously achieved SIRT run. The following iterations only change surfaces and interfaces of the object of interest. This technique is known as Discrete Algebraic Reconstruction Technique (DART).^{23,27}

3.3 TEM sample preparation

3.3.1 Dropping method for TEM specimen preparation

The dropping method is a useful technique to prepare e.g. nanoparticles or nanostructures in a fast manner for TEM investigations. Before dissolving the material in ethanol it is often pesteled to achieve electron transparent particles. Afterwards, the solution is dropped onto a 3 mm in diameter Cu TEM grid coated with amorphous C (Figure 3.3.1). The ethanol evaporates and the material stays attached to the grid. The TEM grid can also be a finder grid where the quadrants are marked with letters to find a specific area again.

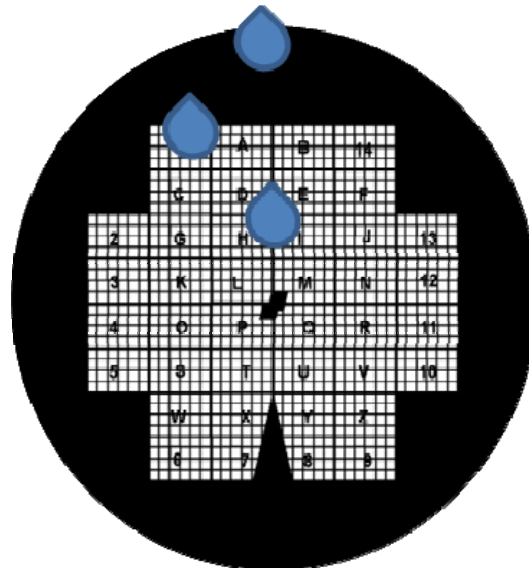


Figure 3.3.1. Schematic drawing of the dropping method showing a 3 mm TEM finder grid. Figure courtesy of R. Hoffmann.

3.3.2 FIB microscopy for TEM specimen preparation

Focused ion beam milling is a widely used method to prepare TEM specimen. Several steps for preparing a TEM lamella are needed. First, an interesting specimen area is selected with the dual-beam instrument. The milling of a sample in FIB is done by Ga^+ or He^+ ions which are accelerated up to 30 kV and scanned across the material. Before milling and cutting the area of interest, the sample must be coated with protection layers (C, Cr or Pt) to preserve the surface from damage by the high-energy ions. To bare the selected area, the sample is tilted by 45° and two trapezes on each side are milled into the material. Second, a lamella of a size of $2 \times 20 \times 5 \mu\text{m}$ is cut out but not completely and

glued onto a sharp nano-manipulator needle by depositing Pt or C with a gas-injector system. The lamella is then cut free and transferred onto a 3 mm half-ring Cu TEM grid (Figure 3.3.2) in the vacuum chamber, and glued to the grid with Pt or C. Third, the nano-manipulator needle is liberated with the ion beam. The last step is thinning the $\sim 2\ \mu\text{m}$ thick lamella down to few tens of nm with gentle ion milling to make the specimen electron transparent. Finally the lamella is cleaned and polished with a low energy ion beam.¹

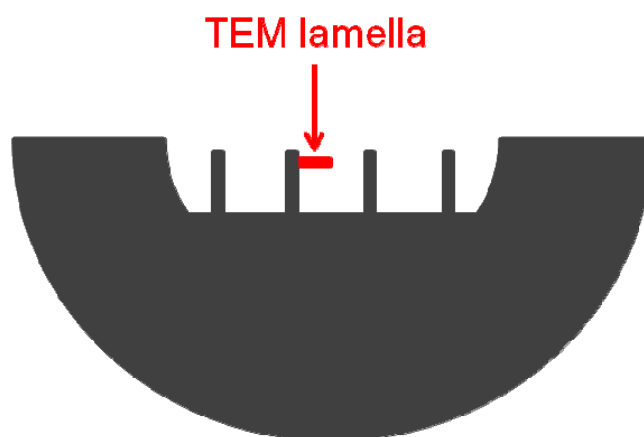


Figure 3.3.2. Schematic drawing of a 3 mm TEM half-ring grid with a FIB lamella.

3.4 Chapter references

¹ D. Brandon and W. D. Kaplan, *Microstructural Characterization of Materials*, 2 ed. (Wiley-VCH Verlag, Weinheim, 2008), p. 509.

² B. Fultz and J.M. Howe, *Transmission Electron Microscopy and Diffractometry of Materials*, 3 ed. (Springer Verlag, Berlin, 2008), p. 778.

³ W. Massa, *Kristallstrukturbestimmung*, 7 ed. (Vieweg&Teubner, Wiesbaden, 2011), p. 269.

⁴ D.B. Williams and C.B. Carter, *Transmission Electron Microscopy*, 2 ed. (Springer Science+Business Media, New York, 2009), p. 760.

⁵ V.J. Keast, *Materials Characterization* **73**, 1 (2012).

⁶ P.J. Goodhew, J. Humphreys, and R. Beanland, *Electron Microscopy and Analysis*, 1 ed. (Taylor & Francis, London, 2001), p. 251.

⁷ G. Dehm, J.M. Howe, and J. Zweck, *In-situ Electron Microscopy*, 1 ed. (Wiley-VCH Publishing, Weinheim, 2012), p. 383.

- ⁸ M. Baram and W.D. Kaplan, *Journal of Microscopy* **232**, 395 (2008).
- ⁹ D.V.S. Rao, K. Muraleedharan, and C.J. Humphreys, *Microscopy: Science, Technology, Applications and Education* **2**, 1232 (2010).
- ¹⁰ Q. Ji, K.-N. Leung, T.-J. King, X. Jiang, and B.R. Appleton, *Nuclear Instruments and Methods in Physics Research B* **241**, 335 (2005).
- ¹¹ P.C. Tiemeijer, M. Bischoff, B. Freitag, and C. Kisielowski, *Ultramicroscopy* **114**, 72 (2012).
- ¹² P.C. Tiemeijer, M. Bischoff, B. Freitag, and C. Kisielowski, *Ultramicroscopy* **118**, 35 (2012).
- ¹³ M. Haider, H. Rose, S. Uhlemann, E. Schwan, B. Kabius, and K. Urban, *Ultramicroscopy* **75**, 53 (1998).
- ¹⁴ O.L. Krivanek, N. Dellby, and a. R. Lupini, *Ultramicroscopy* **78**, 1 (1999).
- ¹⁵ M. Haider, S. Uhlemann, and J. Zach, *Ultramicroscopy* **81**, 163 (2000).
- ¹⁶ J. Goldstein, D. Newbury, D. Joy, C. Lyman, E. Echlin, E. Lifshin, L. Sawyer, and J. Michael, *Scanning Electron Microscopy and X-Ray Microanalysis*, 3 ed. (Springer, New York, 2003).
- ¹⁷ R. Brydson, *Electron Energy Loss Spectroscopy*, 1 ed. (BIOS Scientific Publishers Limited, Oxford, 2001), p. 137.
- ¹⁸ R.F. Egerton, *Electron Energy-loss Spectroscopy in the Electron Microscope*, 3 ed. (Springer Science+Business Media, New York, 2011), p. 491.
- ¹⁹ P.A. Midgley and M. Weyland, *Ultramicroscopy* **96**, 413 (2003).
- ²⁰ H. Jinnai, Y. Nishikawa, R.J. Spontak, S.D. Smith, D.A. Agard, and T. Hashimoto, *Physical Review Letters* **84**, 518 (2000).
- ²¹ J.J. Cha, M. Weyland, J.-F. Briere, I.P. Daykov, T.A. Arias, and D.A. Muller, *Nano Letters* **7**, 3770 (2007).
- ²² A.J. Koster, U. Ziese, A.J. Verkleij, A.H. Janssen, and K.P. de Jong, *The Journal of Physical Chemistry B* **104**, 9368 (2000).
- ²³ A. Zürner, M. Döblinger, V. Cauda, R. Wei, and T. Bein, *Ultramicroscopy* **115**, 41 (2012).
- ²⁴ N. Kawase, M. Kato, H. Nishioka, and H. Jinnai, *Ultramicroscopy* **107**, 8 (2007).
- ²⁵ P.A. Midgley and R.E. Dunin-Borkowski, *Nature Materials* **8**, 271 (2009).
- ²⁶ A.M. Cormack, *Physics in Medicine and Biology* **18**, 195 (1973).
- ²⁷ K.J. Batenburg, S. Bals, J. Sijbers, C. Kübel, P.A. Midgley, J.C. Hernandez, U. Kaiser, E.R. Encina, E.R. Coronado, and G. Van Tendeloo, *Ultramicroscopy* **109**, 730 (2009).

4 Experimental details

This chapter describes the synthesis of the materials as well as the used chemicals and substrates. Furthermore, the used equipments are listed.

4.1 Synthesis of silica-based nanotubes, hollow particles and flakes

4.1.1 Synthesis of the starting materials: phosphoryl triamide $\text{OP}(\text{NH}_2)_3$ and thiophosphoryl triamide $\text{SP}(\text{NH}_2)_3$

The synthesis of $\text{OP}(\text{NH}_2)_3$ and $\text{SP}(\text{NH}_2)_3$ was done according to literature.¹⁻³ POCl_3 (99%) or PSCl_3 (98%; both from Acros Organics, Geel, Belgium; 10–20 mL), which was freshly distilled before, was dropped slowly to liquid ammonia in a flame-dried three-necked 1 L flask. For the elimination of NH_4Cl from the products a Soxhlet extraction with distilled Et_2NH in dry CH_2Cl_2 for 3 days was done. The extraction product was dried in vacuum and $\text{OP}(\text{NH}_2)_3$ and $\text{SP}(\text{NH}_2)_3$ were obtained as starting materials as colorless, water sensitive powders. Their purity was confirmed by PXRD.

4.1.2 Silica-based nanotubes, hollow particles and flakes

The synthesis of SBNTs, hollow particles and flakes was done by pure inorganic solid-state chemistry following the route of Sedlmaier et al.⁴ The two triamides $\text{OP}(\text{NH}_2)_3$ (18.6 mg, 0.196 mmol) and $\text{SP}(\text{NH}_2)_3$ (70.0 mg, 0.630 mmol) were mixed and grounded in an argon-filled glove box.^{1,2} The mixture was transferred into a flame-dried silica glass ampoule (wall thickness 2 mm, inner diameter 11 mm) and SiCl_4 (33.8 μL , 0.294 mmol; Sigma-Aldrich, 99.998 %) was added drop wise. During the whole procedure dry N_2 was used as inert gas.⁵ The ampoule was sealed (to a length of approx. 11 cm) under reduced pressure after freezing the lower part of the ampoule with liquid N_2 to protect the reaction products from the arising heat. Afterwards, the ampoule was heated in a conventional tube furnace to 200 and different target temperatures from 200 – 700 °C (in steps of 100 °C) with dwell times of 12 and 48 h (heating and cooling rate: 1 Kmin^{-1}), respectively. Mostly, the condensation products (NH_3 , H_2S and HCl) are deposited as $(\text{NH}_4)_2\text{S}$ and NH_4Cl at the places in the ampoule that cool first. The reaction

products, nanotubes (NTs), hollow particles and flakes were gained as homogeneous, dry, gray solids by breaking the ampoules.

4.2 Synthesis of BeP_2N_4

Starting from the compounds P_3N_5 and Be_3N_2 , BeP_2N_4 was synthesized by F. Pucher via the multi-anvil high-pressure/high-temperature method.⁶ After compressing the binary nitrides to 5 GPa within 4.5 h they were heated to 1500 °C within 40 min and held for 30 min. Then the temperature was reduced to room temperature within 30 min with a decompression period of 10 h. The crystallinity and purity (removal of P impurities) of the black raw product was improved by annealing it for 2 h in a N_2 atmosphere at 680 °C. Details can be obtained from Pucher et al.⁶

4.3 Synthesis of thin Fe-Ti-O films

Thin films of Fe_2O_3 and $\text{Fe}_{2-x}\text{Ti}_x\text{O}_3$ were grown on (0001) $\alpha\text{-Al}_2\text{O}_3$ substrate by M. Lübke with molecular beam epitaxy (MBE).^{7,8} The annealing of the substrate was performed for 12 h at 1400 °C in air and 12 h at 300 °C in an ultra-high vacuum chamber, and final for 90 min at 600 °C in an O_2 -atmosphere ($p_{\text{O}_2} \approx 2 \cdot 10^{-8}$ mbar).^{7,8} The growth was done at 400 °C in an O_2 -atmosphere ($p_{\text{O}_2} \approx 2 \cdot 10^{-6}$ mbar, growth rate of $0.27 \text{ \AA} \cdot \text{min}^{-1}$). Before depositing a Fe-Ti-O film, a pure Fe_2O_3 film was grown on the substrate. The films were then further annealed at 400 °C in an O_2 -atmosphere ($p_{\text{O}_2} \approx 2 \cdot 10^{-5}$ mbar). Details can be obtained from Lübke et al.^{7,8}

4.4 Equipment

4.4.1 Powder X-ray diffraction

PXRD experiments were performed on a STOE Stadi P powder diffractometer (STOE, Darmstadt, Germany). A parafocusing Debye-Scherrer geometry with a Ge(111) monochromated $\text{Cu-K}\alpha_1$ -radiation (154.0596 pm) and a position sensitive detector was used. Before collecting the data the powder was filled in a capillary with an inner diameter of 0.28 mm. The analysis of the PXRD data was done with the TOPAS package.⁹

4.4.2 Electron and ion microscopes

SEM

For SEM measurements a *JEOL JSM-6500F* equipped with a field emission source and an EDX spectrometer from OXFORD INSTRUMENTS INCA ENERGY was used at 4.0 to 12.0 kV. The sample preparation was done by placing the material on a brass sample carrier and fixing it with self-adhesive carbon plates (Plano, Wetzlar, Germany). Subsequently, they were sputtered with carbon (sputter device: BAL-TEC MED 020, BAL-TEC AG, Balzers, Netherlands) before loading them into the SEM chamber. Carbon coating was done for all investigated specimen in this work, since they were not electrically conducting. The SEM measurements were performed by C. Minke and S. Schmidt.

FIB

The cross-sectional sample investigation and preparation was performed on a dual SEM/FIB from *ZEISS NVISION 40* and on a FEI Strata 400s dual-beam FIB microscope. The SEM was operated at 2.5 keV and the FIB at 30 keV and 1.5 pA. The measurements for the NTs were done by R. Hoffmann and S. Matich at the TU in Munich, the one for the $\text{Fe}_{2-x}\text{Ti}_x\text{O}_3/\text{Fe}_2\text{O}_3$ system by Dr. T. Cohen-Hyams at the Technion in Haifa.

TEM

Several TEM were used for this thesis. For clarity the instruments are listed in Table 4.1.

For the tomography, a convenient holder was used. The ET investigations were done in Munich by Dr. M. Döblinger and A. Wisnet and by P.Ercius in Berkeley.

Table 4.4.1. Used electron microscopes.

JEOL 2011	<ul style="list-style-type: none"> • Operated in Munich at 200 keV acceleration voltage • Equipped with an EDX spectrometer from EDAX
FEI Titan	<ul style="list-style-type: none"> • S/TEM operated in Munich at 80 – 300 kV acceleration voltage • Equipped with an EDX spectrometer from EDAX, a HAADF-detector from <i>FISCHIONE INSTRUMENTS</i> (Model 3000) and a Tridiem energy filter from GATAN
Cs _s -corrected FEI Titan	<ul style="list-style-type: none"> • FEG-S/TEM operated in Haifa at 80 – 300 kV acceleration voltage • Equipped with a monochromator and (image) aberration correctors.
NCEM TEAM 0.5	<ul style="list-style-type: none"> • S/TEM operated in Berkeley at 80 – 300 kV acceleration voltage • Equipped with a special high-brightness Schottky field emission electron source, a gun monochromator, two CEOS hexapole-type spherical aberration correctors, and a Gatan high-resolution GIF Tridiem energy filter • Double-aberration corrected STEM/TEM is based on FEI Titan
FEI F20 UT Tecnai	<ul style="list-style-type: none"> • S/TEM operated in Berkeley at 200 keV acceleration voltage • Equipped with a monochromator and Gatan Imaging Filter (GIF)
Zeiss LIBRA 200MC	<ul style="list-style-type: none"> • S/TEM operated in Berkeley at 200 keV acceleration voltage • Equipped with a monochromator and a dedicated in-column Omega filter

4.5 Chapter references

- ¹ R. Klement and O. Koch, *Chemische Berichte* **87**, 333 (1954).
- ² W. Schnick, *Zeitschrift Für Naturforschung B* **44b**, 942 (1989).
- ³ S. Correll, *Dreieringe in molekularionischen Imidophosphaten und kondensierten Oxonitridophosphaten mit NPO-Zeolithstruktur*, Doctoral Thesis, LMU Munich (2006).
- ⁴ S.J. Sedlmaier, T. Dennenwaldt, C. Scheu, and W. Schnick, *Journal of Materials Chemistry* **22**, 15511 (2012).
- ⁵ First, the inert gas N₂ was purified before using it for the synthesis by piping it through columns filled with blue gel (Merck KGaA, Darmstadt, Germany), KOH pellets (Merck KGaA, Purum), molecular sieve (Merck KGaA, 3 Å), Granulopent® (granulated P₄O₁₀, Roth GmbH, Karlsruhe, Germany, ≥ 99%), and a BTS catalyzer (Sigma-Aldrich, St. Louis, USA).
- ⁶ F.J. Pucher, S.R. Römer, F.W. Karau, and W. Schnick, *Chemistry - A European Journal* **16**, 7208 (2010).
- ⁷ M. Lübbe, *Präparation und magnetische Eigenschaften dünner Fe₂O₃- und FeTi_{1-x}O₃-Schichten auf Al₂O₃(0001)*, Doctoral Thesis, LMU Munich (2009).
- ⁸ M. Lübbe, A.M. Gigler, R.W. Stark, and W. Moritz, *Surface Science* **604**, 679 (2010).
- ⁹ A. A. Coelho, *TOPAS-Academic*, Version 4.1, Coelho Software, Brisbane, (2007).

5 Silica-based nanotubes

5.1 Template-free inorganic synthesis of silica-based nanotubes and their self-assembly to mesocrystals

This chapter refers to the following publication:

Stefan J. Sedlmaier, Teresa Dennenwaldt, Christina Scheu and Wolfgang Schnick, *Journal of Materials Chemistry* **2012**, 22, 15511.

5.1.1 Introduction

Silica, the most abundant solid compound on earth, occurs in a multitude of crystalline and amorphous forms and has been used for a diverse range of applications (e.g. as ceramics, quartz oscillators) for a long time.^{1,2} The discovery of one-dimensional silica nanotubes (SNTs)³ has generated considerable attention towards the search for further functionalities, e. g. in gas storage, drug-/gene-delivery, sensing, catalysis or nanofluidic systems.⁴ Triggered by this high potential, research concerning new synthesis methods for silica-based hollow NTs is a topic of great interest. While two-dimensional, layered compounds exhibit an intrinsic rolling up tendency,⁵⁻⁷ the preparation of purposeful NTs of three-dimensional, isotropic materials like silica however, usually requires structure-directing templates.^{8,9} Therefore, physical templates such as porous alumina membranes or previously fabricated nanowires (NWs) in combination with atomic layer deposition (ALD), organic surfactants in self-assembled gels or biological templates were drawn into consideration.^{3,10-15} In principle, these methods allow a precisely controlled growth of silica NTs. In some cases, however, the template-assisted synthesis exhibits laborious multiple-step reactions with partially toxic organic substances involved. Apart from that the removal process of the template could be a severe problem causing collapse of a newly prepared tubular silica nanostructure.⁴

Silica (SiO₂) is isoelectronic to PON and phosphorus oxonitride imide (PN(NH)) while a structural analogy is consequent. The related compound classes of nitridophosphates and oxonitridophosphates exhibit structural chemistry with many variants including e.g. highly condensed layer as well as open-framework structures.¹⁶⁻²² In the course of our systematic investigation of this silicate-analogous compound classes, we discovered a

novel approach for a template- and solvent-free SBNTs. In a pure inorganic reaction, actually trying to synthesize a silicon oxonitridophosphate, we simply performed a reaction of a mixture of $\text{OP}(\text{NH}_2)_3$ ²³ and $\text{SP}(\text{NH}_2)_3$ ²⁴ with SiCl_4 in a closed system of a sealed silica glass ampoule. For systematically exploring the system, we performed the synthesis at different temperatures from 300 – 700 °C (in steps of 100 °C) while maintaining all other conditions constant. Additionally, some of the syntheses were carried out with an increased amount of SiCl_4 in the ampoule. A structure-directing agent was not added at any step of the synthesis. The synthesis products were mainly recovered as homogeneous, dry, gray solids.

5.1.2 Experimental details

Synthesis

In a typical procedure, $\text{OP}(\text{NH}_2)_3$ (18.6 mg, 0.196 mmol) and $\text{SP}(\text{NH}_2)_3$ ^{23,24} (70.0 mg, 0.630 mmol) were thoroughly mixed and ground in an argon-filled glove box and transferred into a flame-dried silica glass ampoule (wall thickness 2 mm, inner diameter 11 mm). While using dry nitrogen²⁵ as inert gas, SiCl_4 (33.8 μl , 0.294 mmol; Sigma-Aldrich, 99.998 %) was added and dropped onto the mixture of the triamides. After freezing with liquid N_2 , the ampoule was sealed (to a length of approx. 11 cm) under reduced pressure and subsequently heated in a conventional tube furnace in horizontal position to 200 °C and different target temperatures ranging from 300 – 700 °C (in steps of 100 °C) with dwell times of 12 and 48 h (heating and cooling rate: 1 Kmin^{-1}), respectively. Emerging condensation products such as NH_3 , H_2S and HCl are (partially) deposited as $(\text{NH}_4)_2\text{S}$ and NH_4Cl at the places in the ampoule that cool first. After breaking the ampoules, the samples were recovered as dry, gray solids.

Electron Microscopy

First morphological investigations of the reaction products were made on a JSM-6500F SEM (JEOL Ltd., Tokyo, Japan) with a field emission source operated at 4.0 to 12.0 kV. All images shown are secondary electron images. The average chemical composition was studied with an EDX detector model 7418 (Oxford instruments, Oxfordshire, UK). Powders were placed on a brass sample carrier fixed with self-adhesive carbon plates (Plano, Wetzlar, Germany). The samples were sputtered with carbon (sputter device:

BAL-TEC MED 020, BAL-TEC AG, Balzers, Netherlands) before loading them into the SEM chamber, since the reaction products were not electrically conducting.

To obtain more detailed information about the NTs and flakes, a FEI Titan 80 – 300 S/TEM with a field emission gun, a Gatan Tridiem image filter and an EDAX EDX detector for analytical measurements was employed. Diffraction patterns were recorded with a Gatan UltraScan 1000 (2k × 2k) CCD camera. For sample preparation, the grayish solids were suspended in ethanol (99.9 %), ultrasonicated for 10 min and few drops of the suspension were placed on a copper grid coated with an amorphous, holey carbon layer (Lacey S166-2, PLANO). After plasmacleaning for 10-30 s, the TEM measurements were performed at 300 and 80 kV, respectively. For this, the grids were mounted on a double tilt holder with a maximum tilt angle of 30°.

5.1.3 Results and discussion

A SEM image of a representative as-synthesized sample is shown in Figure 5.1.1. Overall, the reaction products consist of three different morphologies. There are vitreous, shapeless flakes as the main product, amorphous clusters of hollow particles, and finally, although no structure-directing agent was added, amorphous SBNTs that usually form nettings. The length of our NTs goes up to several micrometers, while the hollow particles as the shortest version of the NTs are the lower endpoint with a size less than 150 nm. Our systematic series of experiments performed at different synthesis temperatures from 300 to 700 °C shows, besides the reproducibility, a temperature dependency concerning the relative amount of NTs and hollow particles and the NTs' cross-section dimensions. Although all morphologies emerge at each synthesis temperature, the NT structures are rather more frequent at higher temperatures than at lower ones and vice versa for the hollow particles.

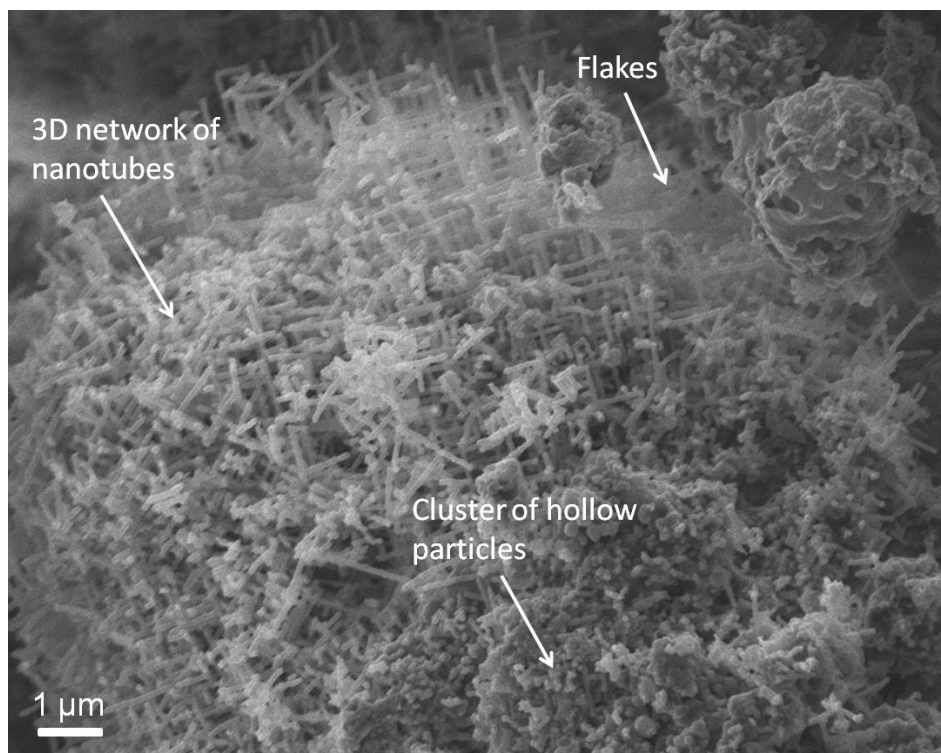


Figure 5.1.1. SEM image of the as-synthesized sample showing nanotubes tending to form 3D networks, shapeless flakes and cluster of particles.

TEM studies reveal a bamboo-like growth of the NTs (see Figure 5.1.2b) which is also observed for CN_x NTs.²⁶ From TEM images mean cross-section diameters and wall thicknesses of the NTs have been determined for each synthesis temperature. The wall thicknesses are decreasing from 24(3) nm for a synthesis temperature of 300 °C to 15(2) nm for 700 °C. The diameters are narrower when the synthesis is performed at higher temperatures. They range from 126(24) nm for a synthesis temperature of 300 °C down to 72(17) nm for 700 °C. The large deviation is due to the bamboo-like structure. Accordingly, with our new template-free approach a control concerning the diameter of SBNTs is feasible. The observed cross-section dimensions are within the typical range for reported silica nanotubes.⁴ For a deeper insight into the system and more detailed analysis of the different morphologies, we performed a series of further TEM investigations. BF images of a typical vitreous flake and an array of NTs synthesized at 700 °C are shown in Figure 5.1.2a and b. The flake appears porous with differently sized holes indicating intensive gas formation. The NTs are partially lopsided grown and orthogonally branched in all three directions in space as already illustrated in Figure 5.1.1. Furthermore, the hollow nature of the NTs is clearly observable in Figure 5.1.2b, where identification of walls by different mass-thickness contrast is possible. This is

even more evident in Figure 5.1.2c, where exemplarily a high-magnification TEM image of a single tube, synthesized at 700 °C, is presented. As obvious in Figure 5.1.2d, where different shaped hollow particles as the shortest version of NTs are shown, all NTs are originally closed. Open ends are only generated by breakings during sample preparation (Figure 5.1.2c). Electron diffraction experiments (insertion in Figure 5.1.2a and b) for all morphologies showed no Bragg intensities. Consequently, as already suggested by PXRD measurements of samples, the flakes as well as the tube structure are characterized as amorphous. This amorphous character is definitely present from the beginning (as-synthesized material) and was confirmed by independent measurements using acceleration voltages of 80 and 300 kV. No difference in shape was observed, when working at these different conditions. In addition the NTs were found to be surprisingly stable under electron bombardment.

Investigations concerning the composition were performed employing EDX. Using the TEM, we extensively analyzed the different morphologies in a sample synthesized at 700 °C (Figure 5.1.1) by recording a number of spectra at different spots. For both, the flakes and the NTs, the elements Si, P, O and N were detected (see Appendix Figure 9.1.1). Semi-quantitative analyses resulted in an atomic ratio of approximately Si : P of 4 : 1 for the NTs while inverted (1 : 4) for the flake material. While O is predominantly incorporated in the NTs (together with Si), N is mainly contained in the flakes (together with P). Another result from the EDX investigations is that the composition of the hollow particles is similar to that of the NTs. Hence, one can conclude that the NTs and the hollow particles exhibit the same material. Consequently, from our template- and solvent free inorganic synthesis approach two products, namely (Si)/P/(O)/N amorphous flakes and phosphorus- and nitrogen-doped silica or even phosphorus-doped silicon oxonitride NTs are yielded. In addition to these determined compositions, regarding the starting materials ($\text{OP}(\text{NH}_2)_3$, $\text{SP}(\text{NH}_2)_3$), one can assume that hydrogen is more or less present in all structures. This is not separately verified for each structure but experiences with other oxonitridophosphates^{19,20} and infrared spectra from the material do suggest this. Assuming that the materials are highly probably built up from 3D interconnected SiX_4 and PX_4 tetrahedra, respectively, hydrogen is either included in connecting positions X as $-\text{NH}-$ or as terminal $-\text{OH}$ or $-\text{NH}_2$ groups. As we know from silicate or nitridophosphate chemistry, these functionalities also exist after high temperature treatment. The mixing of Si/P/O/N/NH in the materials is as well fully

comprehensible regarding the structural chemistry of crystalline SiO_2 , PON and $\text{PN}(\text{NH})$. All three compounds exhibit the cristobalite structure type^{1,27,28} so that continuous solid solutions $\text{Si}_{1-x}\text{P}_x\text{O}_{2-x-y}\text{N}_x(\text{NH})_y$ ($x \leq 1$, $y \leq 2$ and $x + y \leq 2$) seem possible.

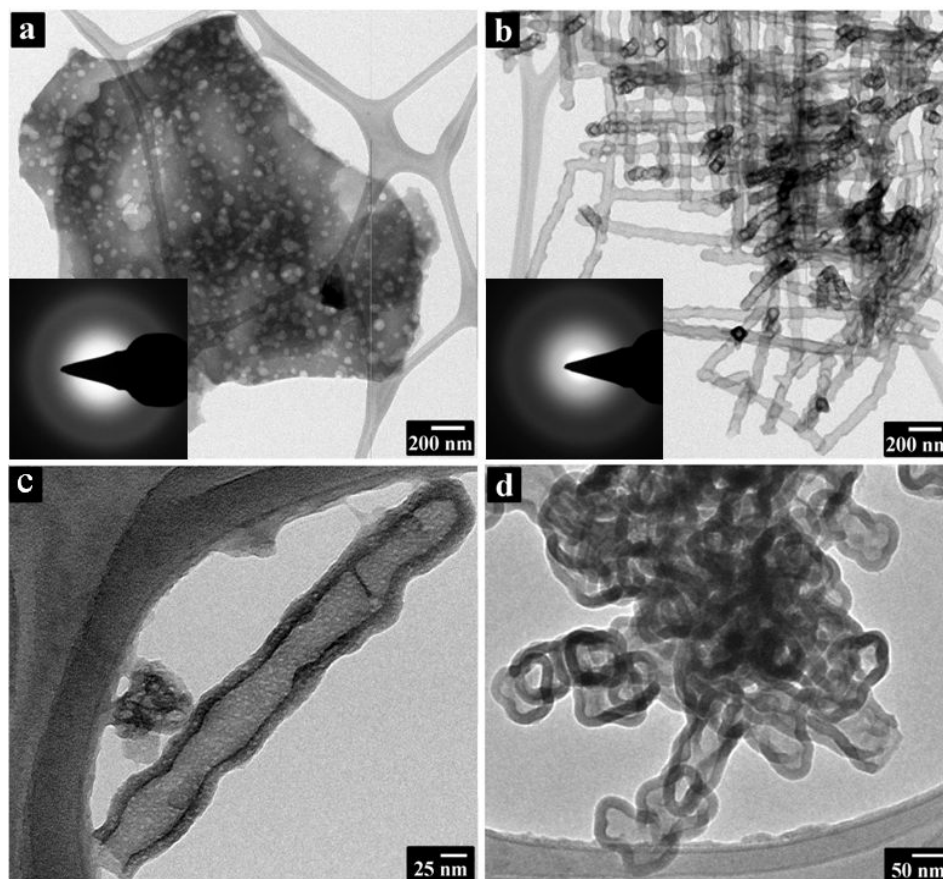


Figure 5.1.2. TEM images of as-synthesized samples of a) an amorphous flake with different sized pores, b) an array of orthogonally branched SBNTs (both with electron diffraction pattern as insertion), c) single silica-based NT synthesized at 700 °C and d) a cluster of hollow particles synthesized at 400 °C.

An important critical condition for the SBNTs is definitely the content of oxygen. As rather little O is introduced by our synthesis approach, the yield of flakes is much higher than that of the nanotubes. However, the reaction with the highest possible O content, the transformation of only $\text{OP}(\text{NH}_2)_3$ with SiCl_4 , resulted not in the formation of NTs, but in a vitreous Si/P/O/N compound. In contrast, the reaction of only $\text{SP}(\text{NH}_2)_3$ with SiCl_4 yielded no NTs as well but a nanocrystalline Si / P / N compound different from the only known phase SiPN_3 in this system.²⁷ This indicates that an interplay between the different reactants is responsible for the nanotube growth, which is currently under further investigations.

As a first hypothesis we visualize the growth of the SBNTs as follows: starting from weakly condensed inorganic polymer agglomerations Si/(P)/O/(N) nuclei are built and form small cells (hollow particles) filled with gas. The polymer agglomeration in Figure 9.1.2 (see Appendix) is a sign of such a starting point. While elevating the temperature in the following, more gas (NH₃, HCl, H₂S) is generated within the condensation process and the cells become more and more elongated and combine to more or less long and hyperbranched NTs. Thereby it seems that the growth is accompanied by a respective self-separating process towards Si/O and P/N resulting in a dropout of the flake material. This is comprehensible regarding the higher oxophilia of Si and NTs found growing nearby or on top of the flake material. The elongation and combination of the shapeable hollow particles are probably driven by the reduced pressure in the system (here, an ampoule), which also assists length growth in other assemblies.²⁹ Branching has mostly been observed orthogonally. This is probably effected by a maximal repulsion of the branches. Although of course further investigations are necessary, this model seems probable as NT structures are more frequently found at higher temperatures, while hollow particles are more frequently found at lower temperatures (see above).

As indicated, the described synthesis depends on the amount of SiCl₄. If the amount of SiCl₄ is increased to excess (67.6 μl, 0.589 mmol) keeping all other parameters like pressure, heating rate and dwell time constant, at a synthesis temperature of 700 °C impressive 3D assemblies of hyperbranched SBNTs are obtained. As presented in the SEM images in Figure 5.1.3, mesocrystals with octahedral habitus are formed. These well-regulated nanopipe systems that can be isolated from the flake materials surface, afford interesting opportunities for constructing novel 3D nanofluidic devices.

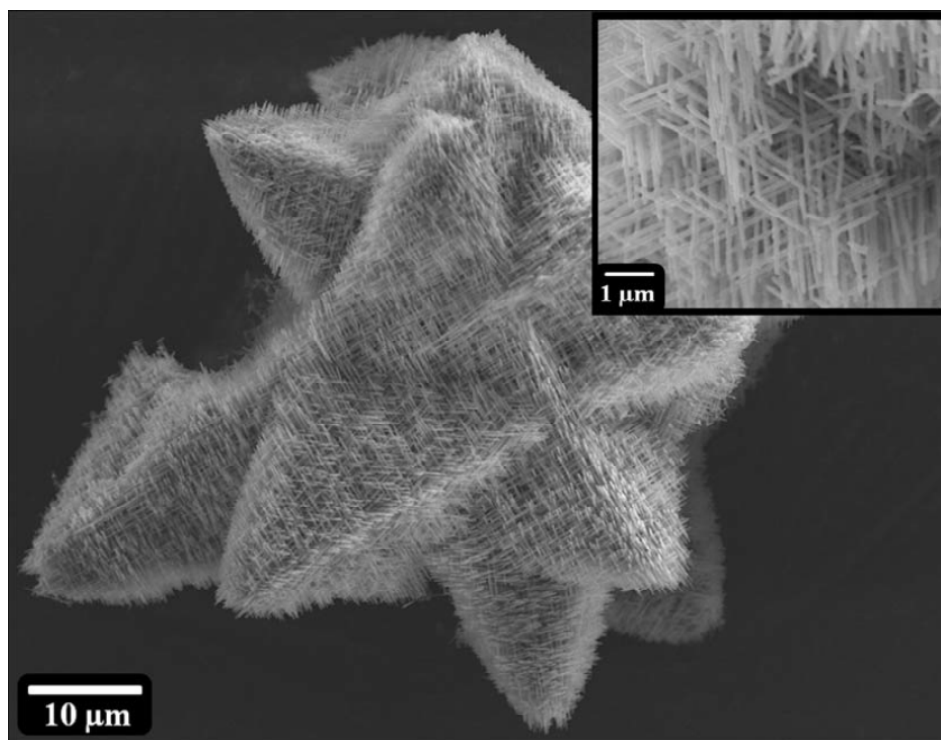


Figure 5.1.3. SEM images of an as-synthesized sample showing an isolated intergrown mesocrystal and a zoomed-in view into the mesocrystal.

While other fabrication methods for inorganic nanofluidic devices usually require multiple production steps associated with templates,^{10,28-30} our method exhibits a simple one-pot synthesis comprising only one single step. Another benefit in this context is that the SBNTs have N involved, so harder and more thermally and chemically stable pipes could be provided for e.g. bioseparation³¹ or fast mass transport³² in nanofluidic devices. Strong N-doped silica is also interesting as glasses with variable refractive indices in optical applications (e. g. fiber Bragg gratings).³³

5.1.4 Conclusion

In conclusion, a novel inorganic solvent-free synthesis approach for SBNTs is presented. This exceedingly interesting and promising system has to be further investigated concerning yield increase and growth mechanism. A detailed analysis is also desirable as this pure inorganic system creates fascinating mesostructures that are similarly found in nature.³⁴

5.1.5 Chapter references

- ¹ P.J. Heaney, *Reviews in Mineralogy and Geochemistry* **29**, 1 (1994).
- ² G.H. Beall, *Reviews in Mineralogy and Geochemistry* **29**, 469 (1994).
- ³ H. Nakamura and Y. Matsui, *Journal of the American Chemical Society* **117**, 2651 (1995).
- ⁴ X. Yang, H. Tang, K. Cao, H. Song, W. Sheng, and Q. Wu, *Journal of Materials Chemistry* **21**, 6122 (2011).
- ⁵ R. Tenne, L. Margulis, M. Genut, and G. Hodes, *Nature* **360**, 444 (1992).
- ⁶ L. Margulis, G. Salitra, R. Tenne, and M. Talianker, *Nature* **365**, 113 (1993).
- ⁷ M. Hershfinkel, L.A. Gheber, V. Volterra, J.L. Hutchison, L. Margulis, and R. Tenne, *Journal of the American Chemical Society* **116**, 1914 (1994).
- ⁸ R. Tenne, *Angewandte Chemie International Edition* **42**, 5124 (2003).
- ⁹ C.N.R. Rao and A. Govindaraj, *Advanced Materials* **21**, 4208 (2009).
- ¹⁰ M. Zhang, Y. Bando, K. Wada, and K. Kurashima, *Journal of Materials Science Letters* **18**, 1911 (1999).
- ¹¹ S.O. Obare, N.R. Jana, and C.J. Murphy, *Nano Letters* **1**, 601 (2001).
- ¹² J.-X. Wang, L.-X. Wen, Z.-H. Wang, M. Wang, L. Shao, and J.-F. Chen, *Scripta Materialia* **51**, 1035 (2004).
- ¹³ R. Fan, Y. Wu, D. Li, M. Yue, A. Majumdar, and P. Yang, *Journal of the American Chemical Society* **125**, 5254 (2003).
- ¹⁴ W.L. Liu, K. Alim, A.A. Balandin, D.M. Mathews, and J.A. Dodds, *Applied Physics Letters* **86**, 253108 (2005).
- ¹⁵ M. Numata, K. Sugiyasu, T. Hasegawa, and S. Shinkai, *Angewandte Chemie International Edition* **43**, 3279 (2004).
- ¹⁶ W. Schnick, *Angewandte Chemie International Edition* **32**, 806 (1993).
- ¹⁷ S. Correll, O. Oeckler, N. Stock, and W. Schnick, *Angewandte Chemie International Edition* **42**, 3549 (2003).
- ¹⁸ S. Correll, N. Stock, O. Oeckler, J. Senker, T. Nilges, and W. Schnick, *Zeitschrift für anorganische und allgemeine Chemie* **630**, 2205 (2004).
- ¹⁹ N. Stock, E. Irran, and W. Schnick, *Chemistry - A European Journal* **4**, 1822 (1998).
- ²⁰ S.J. Sedlmaier, E. Mugnaioli, O. Oeckler, U. Kolb, and W. Schnick, *Chemistry - A European Journal* **17**, 11258 (2011).
- ²¹ S.J. Sedlmaier, M. Döblinger, O. Oeckler, J. Weber, J. Schmedt auf der Günne, and W. Schnick, *Journal of the American Chemical Society* **133**, 12069 (2011).
- ²² F. Karau and W. Schnick, *Angewandte Chemie International Edition* **45**, 4505 (2006).
- ²³ R. Klement and O. Koch, *Chemische Berichte* **87**, 333 (1954).
- ²⁴ W. Schnick, *Zeitschrift für Naturforschung B* **44**, 942 (1989).
- ²⁵ First, the inert gas N₂ was purified before using it for the synthesis by piping it through columns filled with blue gel (Merck KGaA, Darmstadt, Germany), KOH pellets (Merck KGaA, Purum), molecular sieve (Merck KGaA, 3 Å), Granulopent® (granulated

P₄O₁₀, Roth GmbH, Karlsruhe, Germany, ≥ 99%), and a BTS catalyzer (Sigma-Aldrich, St. Louis, USA).

²⁶ A.A. Koos, M. Dowling, K. Jurkschat, A. Crossley, and N. Grobert, *Carbon* **47**, 30 (2009).

²⁷ H.-P. Baldus, W. Schnick, J. Lücke, U. Wannagat, and G. Bogedain, *Chemistry of Materials* **5**, 845 (1993).

²⁸ C.R. Martin, *Science* **266**, 1961 (1994).

²⁹ J. Zhu, H. Peng, S.T. Connor, and Y. Cui, *Small* **5**, 437 (2009).

³⁰ J. Goldberger, R. Fan, and P. Yang, *Accounts of Chemical Research* **39**, 239 (2006).

³¹ D.T. Mitchell, S.B. Lee, L. Trofin, N. Li, T.K. Nevanen, H. Söderlund, and C.R. Martin, *Journal of the American Chemical Society* **124**, 11864 (2002).

³² J.K. Holt, H.G. Park, Y. Wang, M. Stadermann, A.B. Artyukhin, C.P. Grigoropoulos, A. Noy, and O. Bakajin, *Science* **312**, 1034 (2006).

³³ R.R. Khrapko, K.M. Golant, E.M. Dianov, and A.L. Tomashuk, *Advances in Science and Technology* **17**, 541 (1999).

³⁴ J. Aizenberg, J.C. Weaver, M.S. Thanawala, V.C. Sundar, D.E. Morse, and P. Fratzl, *Science* **309**, 275 (2005).

5.2 Chemical stability and bonding behavior of silica-based nanotubes and their 3D assembly

This chapter refers to the following publication:

Teresa Dennenwaldt, Stefan J. Sedlmaier, Wolfgang Schnick and Christina Scheu.
Submitted.

5.2.1 Introduction

Silicon and oxygen are the most abundant chemical elements in the earth's crust and mantle building three quarters of its mass.¹ Hence, SiO₂ is one of the most commonly found materials in nature and arises in a variety of amorphous and crystalline forms. The SiO₂ is made up of condensed corner-sharing SiO₄ tetrahedra, where O is bridging or terminally bound.¹ It has outstanding properties like a high resistivity, an excellent dielectric strength, and a large band gap making it an interesting material as insulator in microelectronic devices.²⁻⁴ A related silicon nitride made up of condensed SiN₄ tetrahedra is Si₃N₄ which is obtained by substituting O with N. This material is kinetically more stable because of its denser network compared to SiO₂.³ Si₃N₄ is a ceramic material with high thermal, mechanical and chemical stability and finds applications in e.g. valves or semiconductor devices.¹ Another relevant material concerning its electrical and physical properties is silicon oxynitride (SiO_xN_y) which is as SiO₂ and Si₃N₄ attractive for dielectric applications.⁴

The application field can even be enlarged when considering these material classes in nanostructured morphology. Nanomaterials are of great interest because they possess an increased strength or chemical reactivity compared to their bulk counterparts. The functionalities of nanostructures depend strongly on their size and shape (e.g., sphere, tubes, wires).^{5,6} In particular, one-dimensional nanomaterials exhibit promising properties for diverse applications. Crystalline SiO_xN_y NWs have lately been studied by Xi et al.⁷ These nanostructures exhibit a highly diffuse reflectivity over the whole visible-light range making them attractive for e.g. white reflector applications. Crystalline Si₃N₄ NWs have even more outstanding properties compared to their bulk counterparts like high strength combined with good flexibility and are extremely

chemically and thermally stable.^{8,9} Recently synthesized Si_3N_4 nano-networks are promising structures for electronic and optoelectronic devices.^{10,11}

In addition, the discovery of one-dimensional amorphous SNTs in 1995 has triggered attention because of their great advantage compared to other NTs such as carbon NTs (CNTs) regarding their surface functionalization via silane chemistry, biocompatibility and facile colloidal suspension formation.¹²⁻¹⁴ However, SNTs are only stable up to pH = 8.¹⁵ At higher pH values the walls of the SNTs decompose quickly. Yang et al. and García-Calzón et al. summarized the most frequently applied synthesis methods for SNTs.^{13,14} All approaches have the use of structure-directing templates in common.^{13,14,16-18}

Recently, we have reported about a novel template-free synthesis method to obtain amorphous SBNTs at 700 °C via a solid-state chemistry method using $\text{OP}(\text{NH}_2)_3$,¹⁹ $\text{SP}(\text{NH}_2)_3$ ²⁰ and SiCl_4 .²¹ The reaction products contain Si, P, O and N and are amorphous in X-ray and electron diffraction. The SBNTs tend to arrange to 3D hyperbranched mesocrystals. These structures could be interesting for several applications e.g. optoelectronics or nanofluidic systems. In the present study, we are interested in the bonding behavior of these SBNTs. Therefore, we investigated them at the nanoscale using EELS in a TEM. Furthermore, the SBNTs are studied concerning their acid/base stability. This is an important parameter for possible medical/biological applications and for the use as nanofilters.

5.2.2 Experimental details

Scanning electron microscopy

SEM SE images were recorded on a JSM-6500F SEM (JEOL Ltd., Tokyo, Japan) with a field emission source operated at 4.0 to 12.0 kV. The machine is equipped with an EDX detector model 7418 (Oxford instruments, Oxfordshire, UK). SEM samples were prepared by placing the powder on a brass sample carrier fixed with self-adhesive carbon plates (Plano, Wetzlar, Germany). As the sample was not electrically conducting the powder was sputtered with C (sputter device: BAL-TEC MED 020, BAL-TEC AG, Balzers, Netherlands) before inserting the specimen in the SEM.

Transmission electron microscopy

The TEM samples were prepared by suspending the powder in ethanol and dropping the solution on a lacey C Cu grid (Lacey S166-2, PLANO). The amorphous reference materials SiO₂ (Merck) and Si₃N₄ (UBE Industries Ltd, Tokyo) were used as purchased without further purification. TEM investigations were done on a Titan 80-300 keV S/TEM equipped with an EDX detector and an energy filter for EELS measurements. The FWHM of the ZLP was around 1 eV. ELNES analysis was done in diffraction or STEM mode with dispersions of 0.2 and 0.3 eV/channel. A 2 mm entrance aperture for the spectrometer and a camera length of 115 mm or 128 mm respectively resulting in a collection angle of 13.5 mrad. A channel-to-channel gain variation and dark current corrections were done for all EEL spectra. For background subtraction a power-law fitting procedure was used.²³ VEELS measurements were performed on a 200 kV Zeiss LIBRA (STEM/TEM). The measurements were done in diffraction mode and the FWHM of the ZLP was around 0.2 eV. For the analysis we used a dispersion of 0.05 eV/channel and a 2.5 mm entrance aperture for the spectrometer. For investigating the chemical treated SBNTs a JEOL JEM-2010 operated at 200 kV was used.

Focused ion beam sample preparation

A TEM cross-section of a 3D assembly of the SBNTs was prepared by FIB sectioning on a Zeiss NVision40 FIB microscope. For the acquisition of secondary electron images were a low acceleration voltage of 2.5 kV was used. Before cutting the lamella, a C protection layer was deposited on the SBNT assembly with successive ion beam induced deposition with a beam current of 300 pA at 30 kV. The material was cut and thinned at 30 keV. The lamella was polished at 30 keV with a beam current of 30 pA followed by 10 pA.

5.2.3 Results and discussion

Bonding behavior of the SBNTs

Figure 5.2.1a shows a TEM image of several SBNTs synthesized at 700 °C. The inserted diffraction pattern confirms the amorphous state of these SBNTs which are several μm in length and exhibit a bamboo-like structure. Their diameter is $\sim 72 \pm 17$ nm and their wall thickness $\sim 20 \pm 5$ nm. The chemical composition has a high impact on the stability of the SBNTs. Therefore, it was determined with EDX in the TEM (Figure 5.2.1b). The

SBNTs contain mainly Si, O, N and P and a low amount of Cl coming from the starting material SiCl_4 . The Cu signal visible in the EDX spectrum stems from the Cu support grid. Particularly, the atomic ratio Si : P was analyzed with this method leading to a value of roughly 4 : 1. The quantification of light elements like N and O cannot be quantified with EDX is difficult due to a low fluorescence yield, absorption in the EDX detector and within the sample. Therefore, we further investigated the SBNTs with EELS. With EELS performed in TEM a high spatial resolution is achieved. This is important since we want to analyze possible concentration gradients along the SBNTs walls, junction points, etc. The Si- and P- $L_{2,3}$ - as well as the N- and O-K-edges of the SBNTs are shown in Figure 5.2.1c. The onset of the Si- $L_{2,3}$ -edge occurs at around 105 eV and the P- $L_{2,3}$ -edge at around 132 eV. The P- $L_{2,3}$ -edge overlaps with the Si- $L_{2,3}$ -edge which is why an exact onset of this edge is hard to determine. The onset of the N-K-edge arises at 405 eV and O-K-edge onset at around 539 eV. As the Si- and P- $L_{2,3}$ -edges overlap in the spectrum, a direct quantification of these elements is rather difficult. To overcome this problem, a combination of EDX and EELS was used resulting in an averaged atomic ratio Si : O : N : P = 25 : 45 : 23 : 7 at.% with a deviation of 3 - 5 at.%.

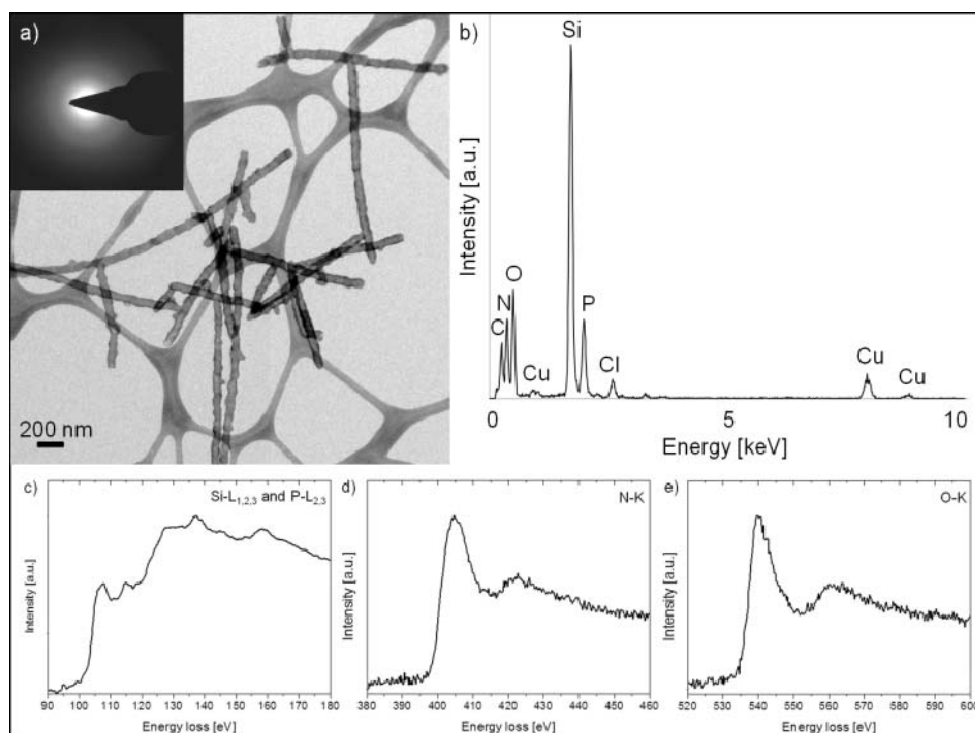


Figure 5.2.1. a) TEM image with the corresponding diffraction pattern (inserted image) of the SBNTs, b) EDX spectrum of the SBNTs, and EEL spectra of an individual SBNT (0.3 eV/channel dispersion) showing c) the Si- $L_{1,2,3}$ and P- $L_{2,3}$ -edges, d) the N-K-edge and e) the O-K-edge.

Furthermore, we investigated the bonding behavior and coordination of the Si in the SBNTs with EELS. The ELNES acts as fingerprint for coordination and bonding behavior in materials.^{22,23} The Si-L_{2,3}-edge is presented in Figure 5.2.2 and will be discussed in detail as this edge acts as fingerprint for our material. For comparison, we chose two amorphous reference bulk materials, Si₃N₄ and SiO₂. The three Si-L-edges of Si₃N₄, SiO₂ and the SBNTs are opposed in Figure 5.2.2a. Both amorphous reference compounds exhibit a tetrahedral coordination for Si and the spectra are in good agreement to those published in literature.²⁴⁻²⁶ The characteristic features of the ELNES of the SBNTs are labeled A – D. Feature A marks the first maximum of the Si-L_{2,3}-edge at 108.5 ± 0.3 eV. A similar peak can be found in the two reference spectra at 108 ± 0.5 eV for the SiO₂ compound and at 105.4 ± 0.5 eV for the Si₃N₄ material, respectively. The first maxima positions and the relative peak distances of all three compounds are summarized in Table 5.2.1. For the SBNTs the relative peak distances are 7.5 eV for feature A to B, 23.7 eV for A to C and 50.4 eV for A to D. Feature D originates from the Si-L₁-edge.²³ The P-L_{2,3}-edge of the SBNTs occurs approximately between 130 and 180 eV and overlaps with the intensity of the higher energy loss part of the Si-L-edge of the SBNTs. The SiO₂ peak distances are similar (maximum 3% deviation which corresponds to the accuracy of the measurements) to those of the SBNTs. A small shoulder is visible at the main peak A in the SiO₂ reference spectrum, which is hidden in the broader peak of the SBNT spectrum. Feature A to B has a distance of 7.3 eV, A to C 23.8 eV and feature A to D 50.7 eV for SiO₂. Feature B does not occur in the Si₃N₄ compound. This material exhibits relative peak distances of 23.5 eV for feature A to C and 51.3 eV for A to D. Thus, the ELNES of the SBNTs resembles more the ELNES of the SiO₂ reference indicating that Si-O bonds dominate. However, Si-N bonds occur in the SBNTs which explain the larger width of the first maximum/peak at the edge onset compared to the SiO₂ reference. Furthermore, Si-P bonds might occur and can also broaden this main peak. In summary, the Si-L_{2,3}-ELNES of the SBNTs is related to a tetrahedral coordination of Si with O and N as next nearest neighbors.

The spectra of the N-K- and O-K-edge are shown in Figure 5.2.2b and c, respectively. The comparison of the edges to the reference materials showed no significant difference indicating a similar environment for the N and O atoms in the SBNTs as in Si₃N₄ and SiO₂. In principle, the N-K-edge exhibits different features in the ELNES when vacancies or other defects are present in the structure.²⁷ Regarding O-K-edges, the ELNES is not only

influenced by the next neighbor atoms but also from the next coordination shell, in the case of the SBNTs O and N atoms.²⁸ Our results indicate that for the amorphous SBNTs changes in the N-K- and O-K-ELNES due to defects and second neighbor environments are only weakly changing the ELNES. It is worth to mention that our experimental data of the reference materials are similar to previous published spectra.^{27,29,30}

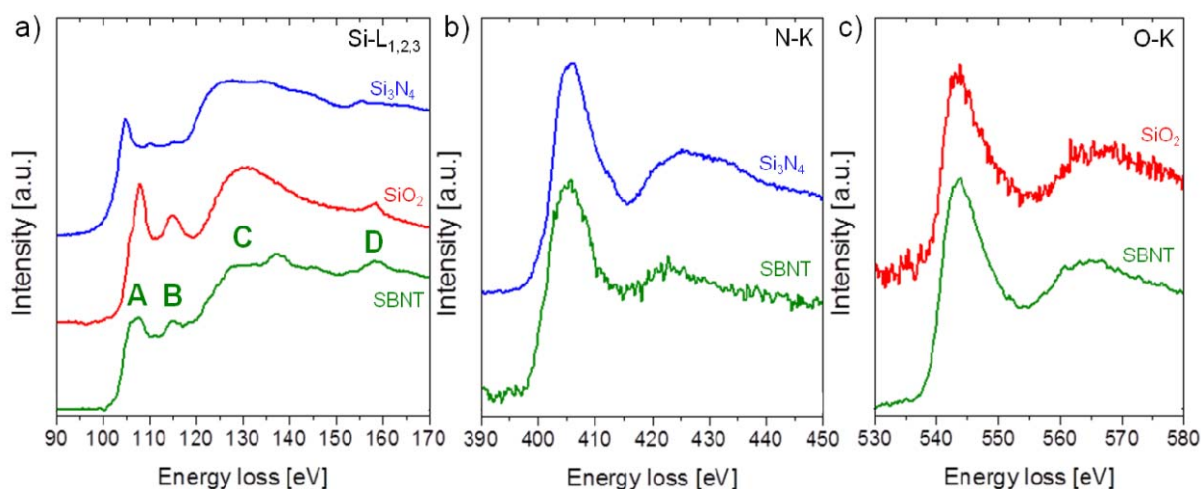


Figure 5.2.2. Comparison of the ELNES of the amorphous bulk compounds Si_3N_4 (blue), SiO_2 (red) and of an individual SBNT (green). a) Si-L_{1,2,3}- edges, b) N-K-edges and c) O-K-edges.

Table 5.2.1. Position of the first maxima and their relative peak distances for the minor features of the Si-L-edge of the SBNTs and the two references SiO_2 and Si_3N_4 . The scatter of the peak position for the features of the SBNTs is evaluated by averaging over several independent measurements.

Si-L-edge Positions [eV]	Relative peak positions			
	First Maximum	A - B	A - C	A - D
SBNTs	108.5 ± 0.3	7.5	23.7	50.4
SiO_2	108 ± 0.5	7.3	23.8	50.7
Si_3N_4	105.4 ± 0.5	---	23.5	51.3
Δ to SiO_2	0.5	0.2	0.1	0.3
Δ to Si_3N_4	3.1	---	0.2	0.9

For further analysis of the chemical distribution of the elements in the SBNTs, we prepared a cross-section lamella of a mesocrystal with FIB. Figure 5.2.3a shows 3D assemblies of SBNTs and Figure 5.2.3b a corresponding SE zoom-in image.

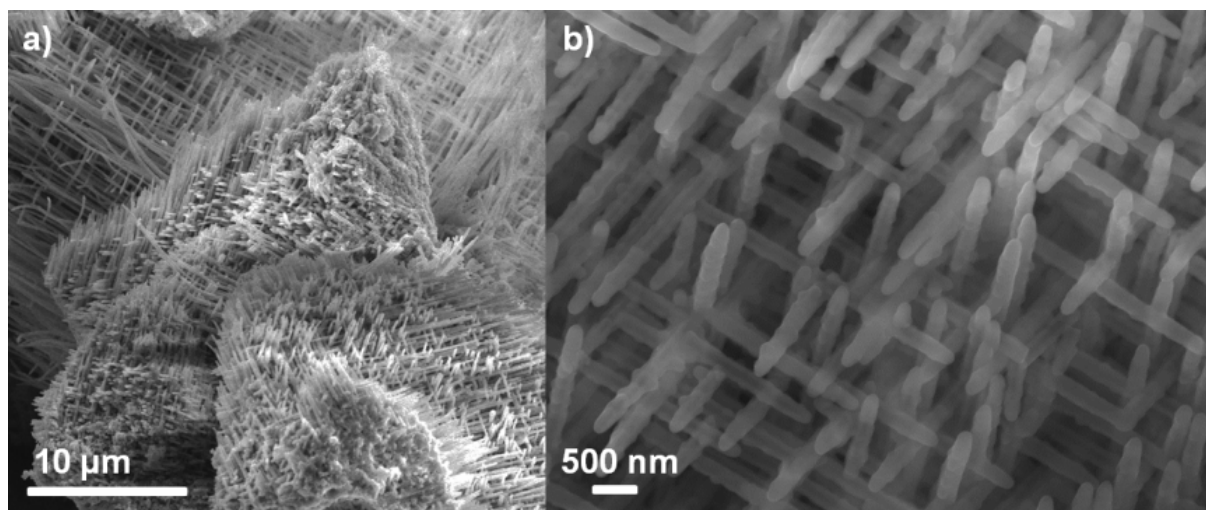


Figure 5.2.3. SEM image of SBNTs assemblies synthesized at 700 °C. a) Overview and b) a zoom-in SE image of hyperbranched SBNTs.

We were interested how the elements Si, O, N and P are distributed especially in the walls and junction points of the SBNTs. For a high spatial resolution, the lamella was analyzed in STEM mode with EDX and EELS using an electron beam size of less than 1 nm. Figure 5.2.4a shows a HAADF-STEM image of a SBNT and the EDX maps of the Si- K_{α} (Figure 5.2.4b), O- K_{α} (Figure 5.2.4c), N- K_{α} (Figure 5.2.4d), P- K_{α} (Figure 5.2.4e) and Ga- L_{α} peaks (Figure 5.2.4f). The Ga stems from the FIB specimen preparation. As the SBNTs are amorphous Ga can easily be incorporated in the SBNTs walls. Nevertheless, the elemental maps evince that the elements are homogeneously distributed in the SBNT.

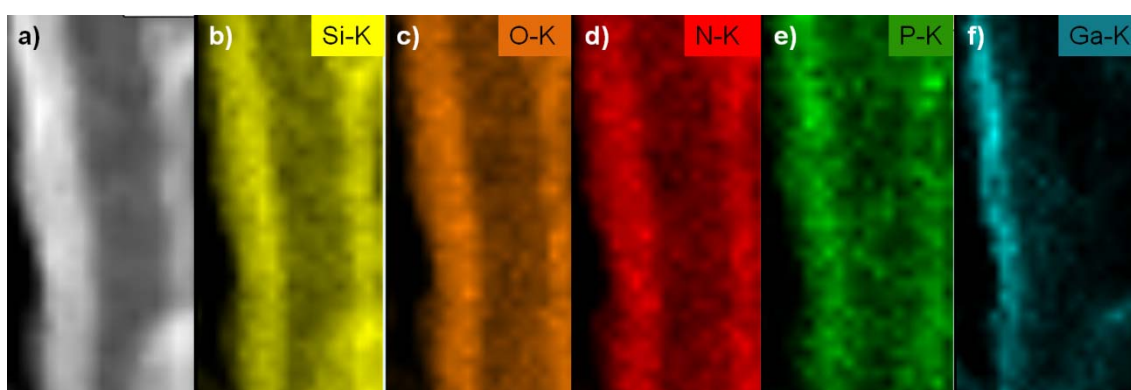


Figure 5.2.4. EDX mapping on a SBNT synthesized at 700 °C. a) STEM image of the SBNT and the maps of b) Si- K_{α} , c) O- K_{α} , d) N- K_{α} , e) P- K_{α} and Ga- L_{α} peaks. Ga is from the FIB specimen preparation.

Further, we studied the SBNTs tips, walls, interiors and junction points with EELS in depth to see if there are local changes in the chemical composition. In Figure 5.2.5a a

HAADF-STEM image of a SBNT is given. The corresponding EEL spectra of the Si-L_{2,3}-edge of this area are shown in Figure 5.2.5b. As mentioned above, the Si-L_{2,3}-edge acts as fingerprint for the SBNTs. The spectra evince that Si is homogeneously distributed in the SBNT and that no structural change is occurring neither in the walls nor at the junction points. Figure 5.2.5c shows an open end of a SBNT. EELS measurements were performed across this opening. Again, no change in the Si-L_{2,3}-edge can be observed (Figure 5.2.5d) indicating homogeneity in the SBNT wall.

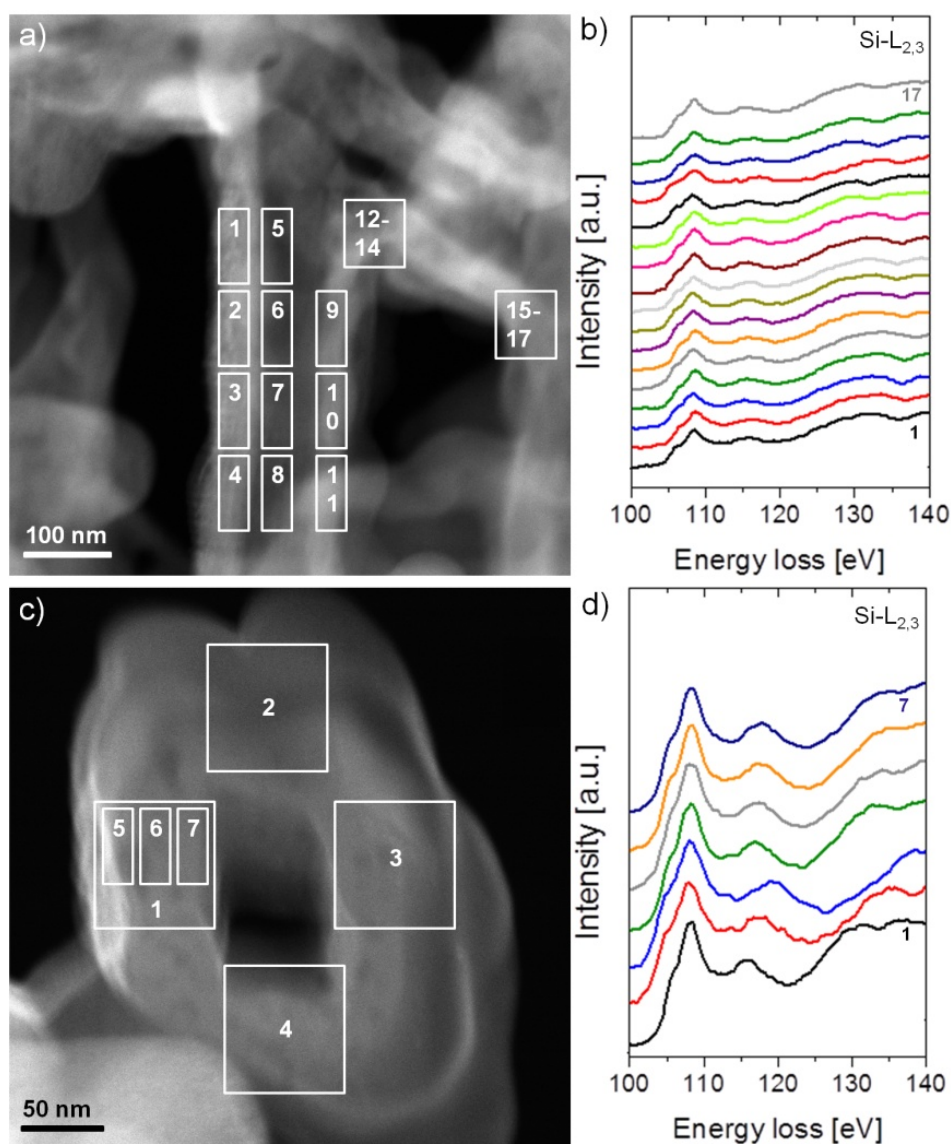


Figure 5.2.5. a) and c) STEM images of SBNTs showing where the EEL spectra had been acquired. b) and d) the corresponding EELS data evincing that the coordination is not changing along the SBNT wall and at the junction points (the lowest spectrum in b) corresponds to 1 and the highest to 17), as well as within different positions of the SBNT wall (the lowest spectrum in d) corresponds to 1 and the highest to 7) .

The energy resolution of EELS is limited by the initial energy spread of the electron source as well as by the instability of the high voltage and can be enhanced by using a monochromator resulting in values of around 0.1 eV.³¹⁻³⁴ In particular, the low loss region can be investigated in depth using a monochromator allowing the analysis of e. g. the dielectric function or band gaps of materials on a local scale.³⁴⁻⁴¹ Several silicon oxides and nitrides have been studied successfully with EELS and DFT concerning their electronic and structural properties.^{29,42-45} We analyzed experimentally the band gap of the SBNTs using VEELS and compare it to known values of bulk amorphous SiO₂ and bulk amorphous silicon nitride values from literature.^{30,42} Data for individual SBNTs and for SBNTs networks were analyzed. All spectra showed similar results for the investigation of the low loss region. Figure 5.2.6 displays exemplarily a VEELS measurement averaged over several SBNTs. To determine the band gap, we used the linear fit approach which has been successfully applied for SiO₂ and silicon nitrides.⁴² Here, straight lines from the background level and the linear fit to the onset of the low-loss signal cross in one point. This intersection is the band gap energy. The band gap energy of amorphous SiO₂ arises at 8.9 eV, its plasmon maximum at 21.5 eV and the band gap of amorphous Si₃N₄ exhibits 4.5 eV and a plasmon maximum at 23 eV.^{30,42,46} Depending on the amount of nitrogen in SiN_x materials the band gap and plasmon energies are shifted to higher energies when the content of N is increased.⁴² For a N/Si ratio of 1.46 the band gap energy exhibits 2.9 eV and the plasmon energy 19.4 eV, whereas for a ratio of 0.92 the band gap arises at 5.1 eV and the plasmon at 22.9 eV. With the linear fit method, we obtained a band gap value of the SBNTs of 5.7 eV ± 0.2 eV and the plasmon maximum was found at 23 ± 0.2 eV (Figure 5.2.6).

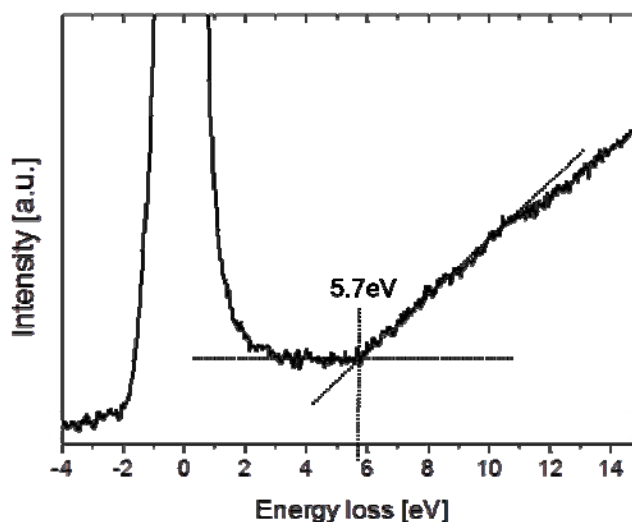


Figure 5.2.6. Low-loss region of the EELS spectrum of SBNTs where a band gap of 5.7 ± 0.2 eV was determined by a linear fit method.

The value of our band gap energy lies in between the reported SiO_2 and Si_3N_4 reference data.^{30,42} The plasmon maximum appears at the same energy loss than the Si_3N_4 . This implies that the SBNTs exhibit a similar electronic structure as SiO_2 and Si_3N_4 . The incorporation of N is known to influence the physical and electrical properties of SiO_2 e.g. the dielectric strength is increased.³

Chemical stability study

Hu et al.¹⁵ investigated the stability of SNTs in alkaline solutions because drugs can be incorporated in SNTs and released by changing the pH value of the solution.^{13,15,47} They found that SNTs decompose at pH = 8 at a temperature of 37 °C.¹⁵ Different to the SNTs, the SBNTs have P and N incorporated and a different behavior is expected. A stability at high pH values is also promising for nanofiltration as a high chemical robustness is advantageous for a wide range of applications in this field.⁴⁸ Hence, we analyzed the acid/base stability of our SBNTs. We have chosen exemplarily SBNTs synthesized at 400 °C. At this synthesis temperature large 3D assemblies are still formed, however, a lower synthesis temperature is beneficial to reduce synthesis cost. Before studying the chemical stability of the SBNTs, we analyzed the chemical composition of this sample synthesized at 400 °C with EDX and EELS. We found that the composition is similar to the sample synthesized at 700 °C. For the experiment solutions with pH values of 1 to 14 were prepared with 2M aqueous solution of hydrochloric acid (HCl) and 2M aqueous solution of sodium hydroxide (NaOH), respectively. The pH value was determined with a

pH meter (Mettler Toledo Seven Easy S20). Subsequently, a small amount (covering the tip of a spatula) of the sample which has been synthesized at 400 °C was treated with the respective solution. The study was performed at room temperature and at 37 °C for the solutions at pH = 8 to be able to directly compare the results to the findings of Hu et al.¹⁵ For TEM investigations the solution was dropped on a lacey C coated Cu grid and subsequently the specimen was dried at RT in air. Before dropping, the solution was diluted with distilled water to prevent damage of the TEM grid. The TEM image in Figure 5.2.7a shows SBNTs which were treated with a solution of pH = 1 for 2 h. The walls of the SBNTs show no changes evincing that they are not sensitive to an acidic environment. We performed measurements with solutions of different alkaline pH values at different temperatures. Even after 7 h at 37 °C no damage of the SBNTs could be observed (Figure 5.2.7b). The walls of the SBNTs are more stable at alkaline pH conditions at elevated temperature compared to the ones reported in literature.¹⁵ pH values of 9, 10, 12 and 14 were tested at room temperature to see whether the SBNTs decompose at some point. After a treatment of 3 h with pH = 9 and 10 at room temperature, respectively, the walls of the SBNTs did not show any change or damage. Figure 5.2.7c presents SBNTs after the treatment with pH = 10 revealing no obvious damage. A first change in the walls of the SBNTs could be observed after a treatment of 2 h with pH = 12. After 2 h at pH = 14 at room temperature the walls of the SBNTs exhibited clearly damage as is shown in Figure 5.2.7d. The walls appear considerably more porous (Figure 5.2.7d).

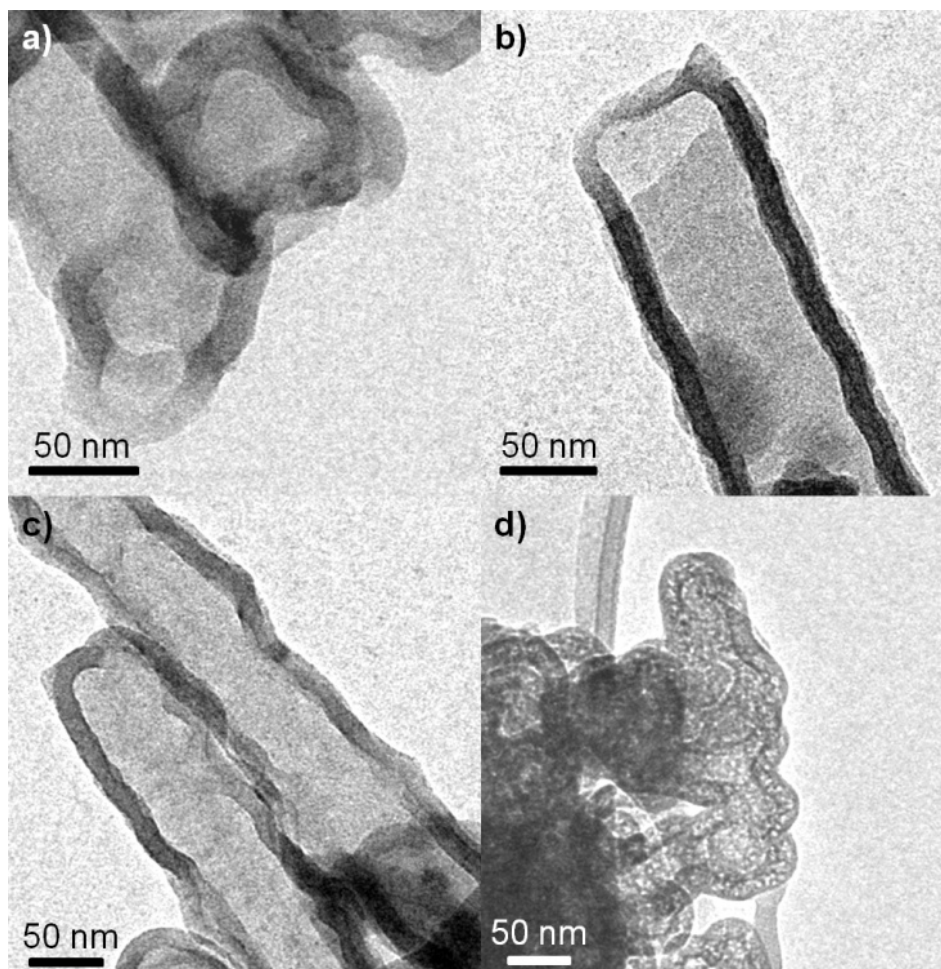


Figure 5.2.7. pH study of SBNTs synthesized at 400 °C. TEM images at a) pH = 1, b) pH = 8 at 37 °C, c) pH = 10 at room temperature and d) after 2 h treated with pH = 14 showing some damage, the walls of the structure are more porous.

The SBNTs are more stable at higher pH values as SNTs, which is most likely due to the incorporation of P and N in the walls. The increased chemical stability is interesting for potential applications in e.g. nanofluidic systems. In addition, the SBNTs are expected to be mechanically and thermally more stable because of the N incorporation.

5.2.4 Summary and conclusion

In conclusion, we investigated template-free synthesized amorphous SBNTs and their 3D assembly concerning their chemical stability and bonding behavior. We studied the structural behavior and chemical homogeneity at the nanoscale with EDX and EELS. The chemical composition of the walls and the interior of the SBNTs do not vary. EELS analysis of the Si-L_{2,3}-edge revealed that the bonding of Si in the SBNTs is a mixture of SiO₂ and Si₃N₄ exhibiting a tetrahedral coordination with mostly O and N as bonding

atoms. The band gap energy was determined at 5.7 ± 0.2 eV and the plasmon maximum at 23 ± 0.2 eV indicating that the electronic structure of the SBNTs is indeed dominated by a mixture between SiO_2 and Si_3N_4 .

The chemical stability of the SBNTs was analyzed by treating the SBNTs with solutions of pH values of 1 to 14. They were considerably more stable at high pH values compared to SNTs reported in literature.¹⁵ This is attributed to the incorporated P and N. The SBNTs could be therefore promising candidates for nanofiltration or nanofluidic systems where a high chemical stability of the assemblies is of great interest.

5.2.5 Chapter references

- ¹ M. Zeuner, S. Pagano, and W. Schnick, *Angewandte Chemie International Edition* **50**, 7754 (2011).
- ² P.J. Heaney, *Reviews in Mineralogy and Geochemistry* **29**, 1 (1994).
- ³ B. Balland and A. Glachant, *Instabilities in Silicon Devices* **3**, 3 (1999).
- ⁴ M.L. Green, E.P. Gusev, R. Degraeve, and E.L. Garfunkel, *Journal of Applied Physics* **90**, 2057 (2001).
- ⁵ C. Bréchnignac, P. Houdy, and M. Lahmani, *Nanomaterials and Nanochemistry* (Springer Publishing, Berlin, Heidelberg, New York, 2007), p. 748.
- ⁶ G. Schmid, *Nanoparticles: From Theory to Application*, 1 ed. (Wiley-VCH Publishing, Weinheim, 2004), p. 444.
- ⁷ S. Xi, T. Shi, L. Xu, Z. Tang, D. Liu, X. Li, and S. Liu, *Journal of Nanomaterials* **2012**, 1 (2012).
- ⁸ Y.J. Zhang, N.L. Wang, R.R. He, Q. Zhang, J. Zhu, and Y.J. Yan, *Journal of Material Research* **15**, 1048 (2000).
- ⁹ Y. Zhang, N. Wang, R. He, J. Liu, X. Zhang, and J. Zhu, *Journal of Crystal Growth* **233**, 803 (2001).
- ¹⁰ N. Zhu, Z. Peng, X. Fu, C. Wang, Z. Fu, L. Qi, and H. Miao, *Solid State Sciences* **12**, 1076 (2010).
- ¹¹ Z. Peng, N. Zhu, X. Fu, C. Wang, Z. Fu, L. Qi, and H. Miao, *Journal of the American Ceramic Society* **93**, 2264 (2010).
- ¹² H. Nakamura and Y. Matsui, *Journal of the American Chemical Society* **117**, 2651 (1995).
- ¹³ X. Yang, H. Tang, K. Cao, H. Song, W. Sheng, and Q. Wu, *Journal of Materials Chemistry* **21**, 6122 (2011).
- ¹⁴ J.A. García-Calzón and M.E. Díaz-García, *Trends in Analytical Chemistry* **35**, 27 (2012).
- ¹⁵ K.-W. Hu, K.-C. Hsu, and C.-S. Yeh, *Biomaterials* **31**, 6843 (2010).
- ¹⁶ R. Tenne, *Angewandte Chemie International Edition* **42**, 5124 (2003).
- ¹⁷ C.N.R. Rao and A. Govindaraj, *Advanced Materials* **21**, 4208 (2009).
- ¹⁸ S.J. Son, X. Bai, A. Nan, H. Ghandehari, and S.B. Lee, *Journal of Controlled Release* **114**, 143 (2006).
- ¹⁹ R. Klement and O. Koch, *Chemische Berichte* **87**, 333 (1954).
- ²⁰ W. Schnick, *Zeitschrift Für Naturforschung B* **44**, 942 (1989).
- ²¹ S.J. Sedlmaier, T. Dennenwaldt, C. Scheu, and W. Schnick, *Journal of Materials Chemistry* **22**, 15511 (2012).
- ²² R.F. Egerton, *Electron Energy-loss Spectroscopy in the Electron Microscope*, 3 ed. (Springer Science+Business Media, New York, 2011), p. 491.
- ²³ R. Brydson, *Electron Energy Loss Spectroscopy*, 1 ed. (BIOS Scientific Publishers Limited, Oxford, 2001), p. 137.
- ²⁴ L.A.J. Garvie and P.R. Buseck, *American Mineralogist* **84**, 946 (1999).

- ²⁵ N. Lieske and R. Hezel, *Thin Solid Films* **61**, 217 (1979).
- ²⁶ K. Kimoto, K. Kobayashi, T. Aoyama, and Y. Mitsui, *Micron* **30**, 121 (1999).
- ²⁷ P. Lazar, J. Redinger, J. Strobl, R. Podloucky, B. Rashkova, G. Dehm, G. Kothleitner, S. Sturm, K. Kutschej, C. Mitterer, and C. Scheu, *Analytical and Bioanalytical Chemistry* **390**, 1447 (2008).
- ²⁸ C. Scheu, G. Dehm, M. Rühle, and R. Brydson, *Philosophical Magazine A* **78**, 439 (1998).
- ²⁹ A. Ziegler, J.C. Idrobo, M.K. Cinibulk, C. Kisielowski, N.D. Browning, and R.O. Ritchie, *Science* **306**, 1768 (2004).
- ³⁰ G.L. Tan, M.F. Lemon, D.J. Jones, and R.H. French, *Physical Review B* **72**, 205117 (2005).
- ³¹ M. Terauchi, R. Kuzuo, F. Satoh, M. Tanaka, K. Tsuno, and J. Ohyama, *Microscopical and Microanalytical Microstructures* **2**, 351 (1991).
- ³² F. Kahl and H. Rose, in *12th European Congress on Electron Microscopy* (2000), pp. 1459–1460.
- ³³ S. Uhlemann and M. Haider, *Microscopy and Microanalysis* **8**, 584 (2002).
- ³⁴ O.L. Krivanek, J.P. Ursin, N.J. Bacon, G.J. Corbin, N. Dellby, P. Hrncirik, M.F. Murfitt, C.S. Own, and Z.S. Szilagy, *Philosophical Transactions of the Royal Society A* **367**, 3683 (2009).
- ³⁵ S. Lazar, G.A. Botton, M.-Y. Wu, F.D. Tichelaar, and H.W. Zandbergen, *Ultramicroscopy* **96**, 535 (2003).
- ³⁶ J.C. Idrobo and N.D. Browning, *Microscopy and Microanalysis* **10**, 840 (2004).
- ³⁷ R. Erni and N.D. Browning, *Ultramicroscopy* **104**, 176 (2005).
- ³⁸ K. Kimoto, G. Kothleitner, W. Grogger, Y. Matsui, and F. Hofer, *Micron* **36**, 185 (2005).
- ³⁹ L. Gu, V. Srot, W. Sigle, C.T. Koch, P.A. van Aken, F. Scholz, S.B. Thapa, C. Kirchner, M. Jetter, and M. Rühle, *Physical Review B* **75**, 195214 (2007).
- ⁴⁰ T. Kuykendall, P. Ulrich, S. Aloni, and P. Yang, *Nature Materials* **6**, 951 (2007).
- ⁴¹ B. Schaffer, W. Grogger, G. Kothleitner, and F. Hofer, *Ultramicroscopy* **110**, 1087 (2010).
- ⁴² J. Park, S. Heo, J.-G. Chung, H. Kim, H. Lee, K. Kim, and G.-S. Park, *Ultramicroscopy* **109**, 1183 (2009).
- ⁴³ N. Ikarashi, K. Manabe, K. Takahashi, and M. Saitoh, *ECS Transactions* **3**, 143 (2006).
- ⁴⁴ Y.P. Li, Ching, and W. Y, *Physical Review B* **31**, 2172 (1985).
- ⁴⁵ S.-D. Mo, L. Ouyang, W.-Y. Ching, I. Tanaka, Y. Koyama, and R. Riedel, *Physical Review Letters* **83**, 5046 (1999).
- ⁴⁶ V.A. Gritsenko, Y.N. Morokov, and Y.N. Novikov, *Applied Surface Science* **113**, 417 (1997).
- ⁴⁷ C.T. Sousa, C. Nunes, M.P. Proença, D.C. Leitão, J.L.F.C. Lima, S. Reis, J.P. Araújo, and M. Lúcio, *Colloids and Surfaces. B, Biointerfaces* **94**, 288 (2012).
- ⁴⁸ S.A. El-Safty, A. Shahat, M. Mekawy, H. Nguyen, W. Warkocki, and M. Ohnuma, *Nanotechnology* **21**, 375603 (2010).

5.3 Further investigation of the silica-based nanotubes, their 3D assembly and flakes

5.3.1 Reaction products

In additional studies we were interested in increasing the yield of the SBNTs. Therefore, we used our template-free synthesis method¹ and varied the initial weight of O and Si. Furthermore, we confirmed the reproducibility of the SBNTs synthesis using an extended temperature range of 200 – 750 °C. Figure 5.3.1a shows exemplarily a SEM image of the three reaction products synthesized at 700 °C revealing the high reproducibility of the synthesis. Figure 5.3.1b – d presents TEM images of the sample exhibiting hollow particles, SBNTs and a flake in accordance to our earlier studies.¹ Independently from the synthesis temperature the SBNTs are several μm in length. They exhibit a bamboo-like structure with closed and some opened ends. The 3D hyperbranched mesocrystals are built at every temperature but the higher the temperature the nicer the 3D assemblies.

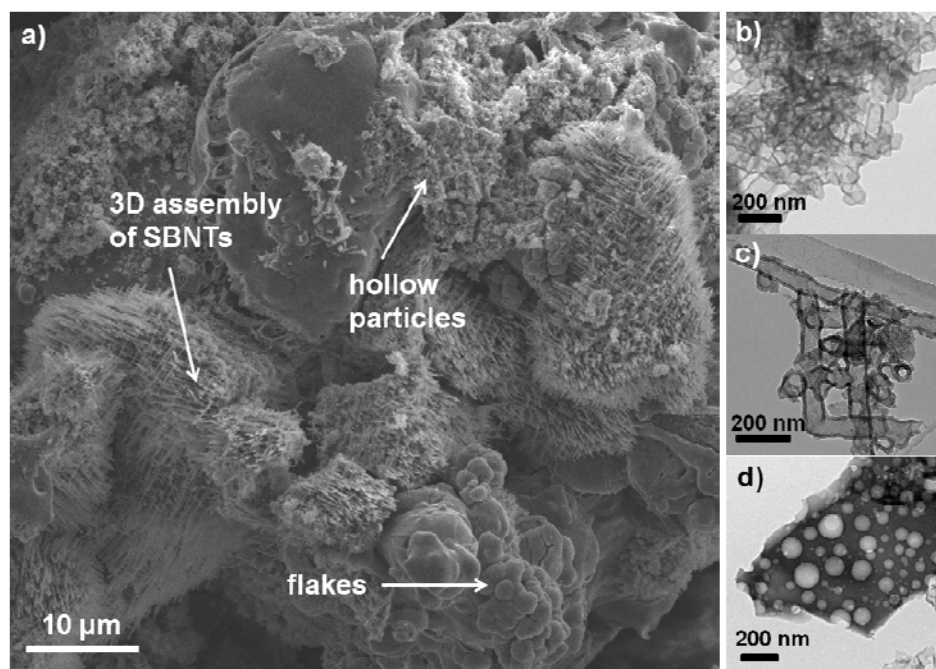


Figure 5.3.1. Sample synthesized at 700 °C a) SEM image showing an overview of the specimen with the three reaction products (SBNTs, flakes, hollow particles) and the SBNTs 3D assemblies and TEM images of b) the hollow particles, c) SBNTs and d) a flake.

The chemical composition of all reaction batches was determined with EDX and EELS. All three reaction products contain always Si, P, O and N and are amorphous in X-ray and electron diffraction. The analysis confirmed that the SNBTs and the hollow particles consist mostly of Si, O and N whereas the flakes are dominated by P and N independent of the synthesis temperature.¹

5.3.2 Synthesis with an increased amount of O

In general, the chemical composition of our nanostructures is widely independent on the synthesis temperature (see Chapter 5.3.1). To enhance the yield of SBNTs we increased the amount of Si and O during the synthesis by increasing the initial weight of SiCl_4 (50.7 μl , 0.441 mmol) and the O source $\text{OP}(\text{NH}_2)_3$. Therefore, we inverted the ratio of the initial weight of $\text{OP}(\text{NH}_2)_3$ (18.6 mg, 0.196 mmol) to $\text{SP}(\text{NH}_2)_3$ (70 mg, 0.631 mmol) which was before 1 : 3 and is now 3 : 1 ($\text{OP}(\text{NH}_2)_3$ (18.6 mg, 0.196 mmol), $\text{SP}(\text{NH}_2)_3$ (7.25 mg, 0.065 mmol)). All other reaction parameters were kept constant. We chose reaction temperatures of 500, 600 and 700 °C as the augmented temperatures are more promising for SBNTs arrays with higher order. Fig. 5.3.2 shows exemplarily a SEM (Figure 5.3.2a) and a TEM image (Figure 5.3.2b) of the reaction products observed for a synthesis temperature of 500 °C.

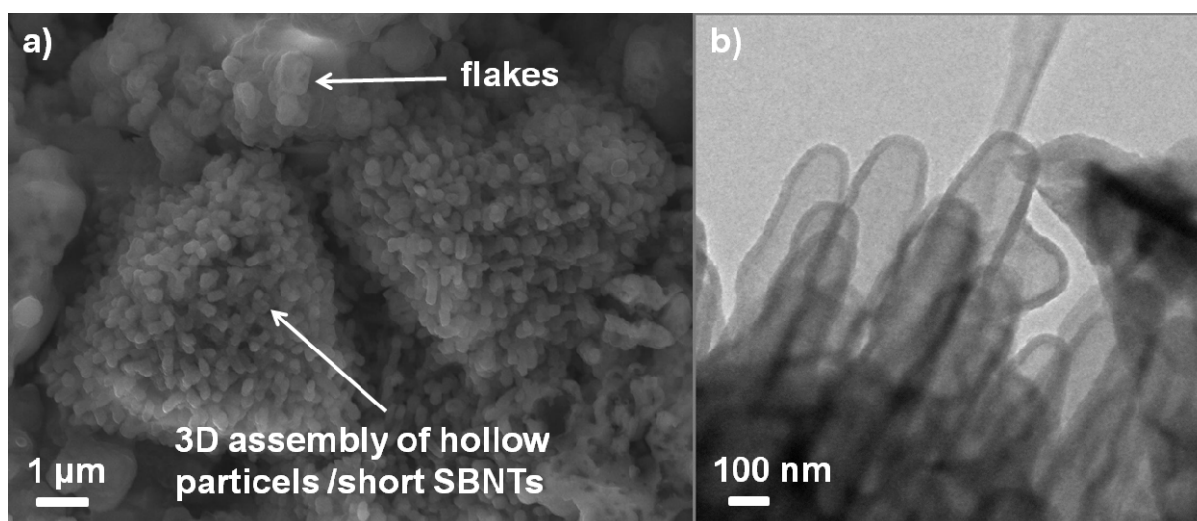


Figure 5.3.2. Sample synthesized with an increased O concentration at 500 °C a) SEM image showing flakes and 3D assemblies of hollow particles or short SBNTs, respectively and b) TEM image of short SBNTs.

Beside flakes, hollow particle like structures, which can be considered as short SBNTs, with tetrahedral arrangement arise. The TEM image shows that these tetrahedra could also be an assembly of very short NTs (Figure 5.3.2b). No mesocrystal network, as observed for synthesis with a lower O amount, was found. Similar reaction products occur at a synthesis temperature of 600 and 700 °C but exhibit another overall structure. The tetrahedra are replaced by more spheres like structures build out of hollow particles or short NTs, respectively. The chemical composition of the SBNTs synthesized with a lower O concentration (Figure 5.3.3a) and with a high O concentration (Figure 5.3.3b) differs in their O content as the EDX measurements of samples synthesized at 700 °C reveal. The Cl peak results from the starting material SiCl_4 and Cu from the Cu TEM grid.

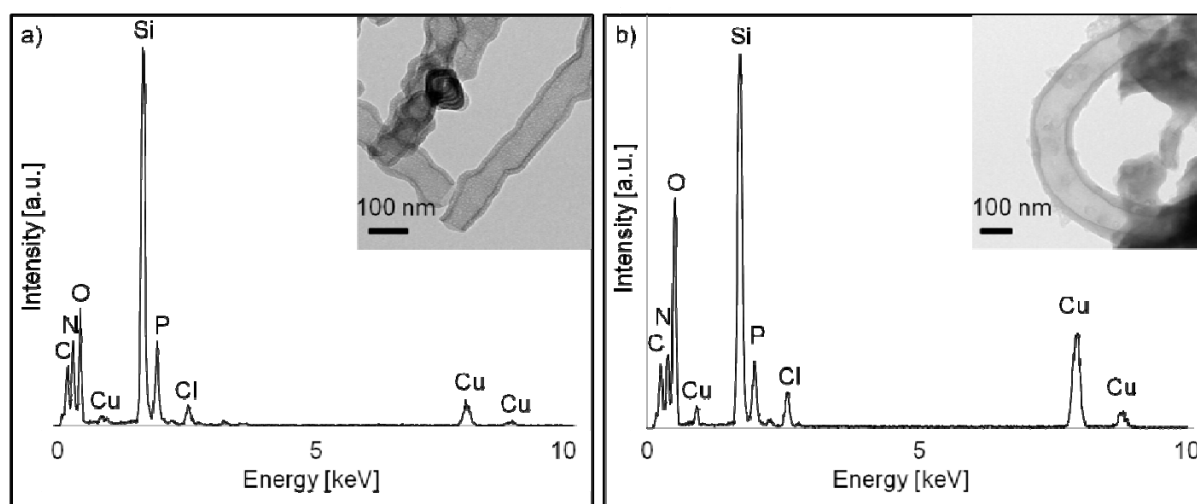


Figure 5.3.3. EDX measurements of SBNTs and corresponding TEM images. a) Synthesized at 700 °C with a lower O and Si concentration and b) synthesized at 700 °C with a higher O and higher Si concentration.

Overall, the higher O content does not change the shape of the reaction products (flakes, hollow particles, NTs) but their arrangement. The SBNTs do not form 3D assemblies anymore. Besides, the O amount increases in SBNTs when augmenting the O content in the synthesis, while the N and particular the P concentration decreases.

5.3.3 Influence of the Si content on the SBNTs diameter

First experiments concerning the influence of the SiCl_4 concentration were made at $700\text{ }^\circ\text{C}$.¹ Here, the amount of the Si source was increased while all other parameters (concentration of other starting materials, heating rate, temperature, pressure and dwell time) were kept constant. The investigated SiCl_4 concentrations are called higher and lower SiCl_4 concentrations in the following. The SBNTs form very uniform hyperbranched 3D mesocrystals as can be seen in the SEM image of a sample prepared at $700\text{ }^\circ\text{C}$ with a high Si concentration (Figure 5.3.4a). The other reaction products like flakes and hollow particles are also present. The TEM image in Figure 5.3.4b shows SBNTs. We varied the synthesis temperature in the range of 200 and $700\text{ }^\circ\text{C}$ in $100\text{ }^\circ\text{C}$ steps. Again, all three reaction products appear at every temperature also by using a higher SiCl_4 amount.

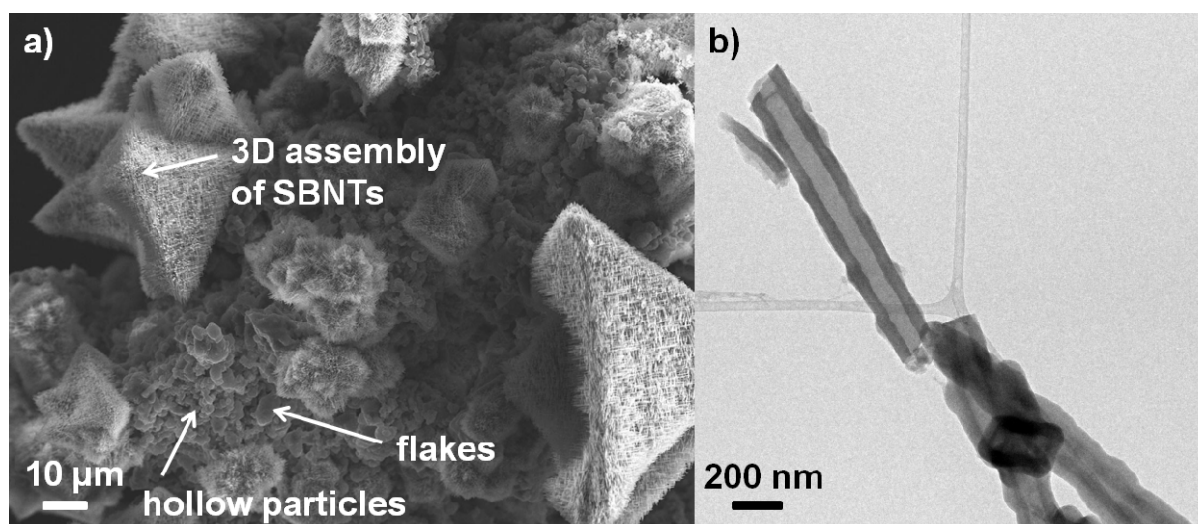


Figure 5.3.4. Sample synthesized at $700\text{ }^\circ\text{C}$ with a high Si content a) SEM image showing an overview of the specimen, the three reaction products (SBNTs, flakes, hollow particles) and the SBNTs 3D assemblies and b) TEM image of a SBNTs.

The EDX and EELS analysis reveal that the SBNTs and the hollow particles are once again Si, O and N dominated, whereas the flakes have a higher amount of P and N. The chemical composition of the reaction products is very similar (Si : O : N : P = 28 : 40 : 25 : 3 at.%), independently from the SiCl_4 concentration and temperature. The tip and walls of the SBNTs do also not exhibit another chemical composition. The elements Si, O, N and P are homogeneously distributed in the SBNTs. The ELNES of the Si- $L_{2,3}$ -edge indicates again a tetrahedral coordination for the Si which is predominantly coordinated

with O and N as for the samples with a lower Si content. The ELNES of the P-L_{2,3}-, N- and O-K-edges do not vary from those with a lower Si concentration.

As shown in our former study, we are able to tune the diameter and the length of the SBNTs by varying the temperature. The diameter was determined by averaging over several SBNTs of different areas. As the SBNTs exhibit a bamboo-like structure we used an average of the smaller and larger diameter. SBNTs from literature exhibit a straight structure most likely since they are synthesized with template-directing agents. Therefore, their diameter is constant and dependent on the template.^{2,3} The diameter and the wall thickness of our SBNTs synthesized with a lower SiCl₄ amount decrease at higher temperatures as is shown in the diagram of Figure 5.3.5a.¹ At first the diameter stays approximately constant and then decreases drastically down to about 70 – 80 nm. At lower synthesis temperature the SBNTs are wider in diameter (~120 – 130 nm). The dependency of the diameter on the temperature is different for the SBNTs synthesized with a higher Si amount. Here, the diameter is increasing with increasing temperature as can be seen in Figure 5.3.5b.

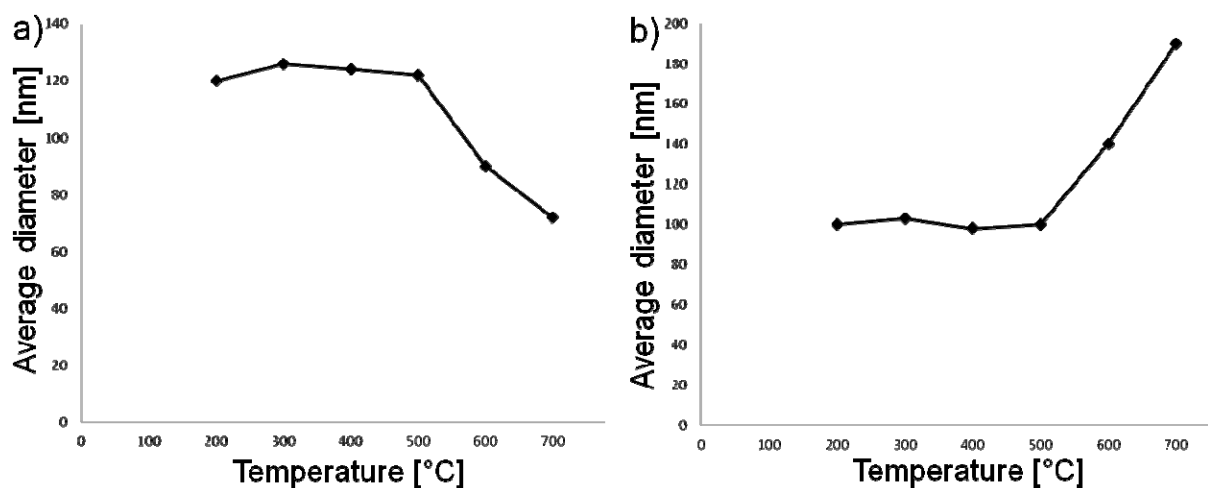


Figure 5.3.5. Diagram and table showing the dependency of the SBNTs diameter depending on the synthesis temperature. a) with a lower SiCl₄ amount and b) with a higher SiCl₄ concentration.

The higher the temperature is, the wider the SBNTs are. At 200 °C they exhibit a diameter of about 90 – 100 nm until the synthesis temperature of 500 °C. At 600 and 700 °C the diameter increases strongly up to ~180 – 190 nm. At both SiCl₄ concentrations the SBNTs exhibit a shorter length at lower synthesis temperatures. The

reason for the relationship between diameter size of the SBNTs, growth temperature and Si concentrations is still unknown and has to be investigated by further studies.

5.3.4 Focused ion beam lamella of a 3D assembly of SBNTs

To characterize the SBNTs mesocrystals we prepared FIB lamellae synthesized with a low amount of O and Si at temperatures of 300 °C and 700 °C (see Chapter 5.2). We were interested how these assemblies are built up, if they are hollow or filled and how the elements Si, O, N and P are distributed in these SBNTs. Figure 5.3.6a shows a SE zoom-in image of a 3D assembly of the SBNTs synthesized at 700 °C. A FIB cut through a mesocrystal is presented in Figure 5.3.6b. A higher magnification of the inside of the tetrahedral structures (Figure 5.3.6c) shows that the SBNTs are occurring homogeneously.

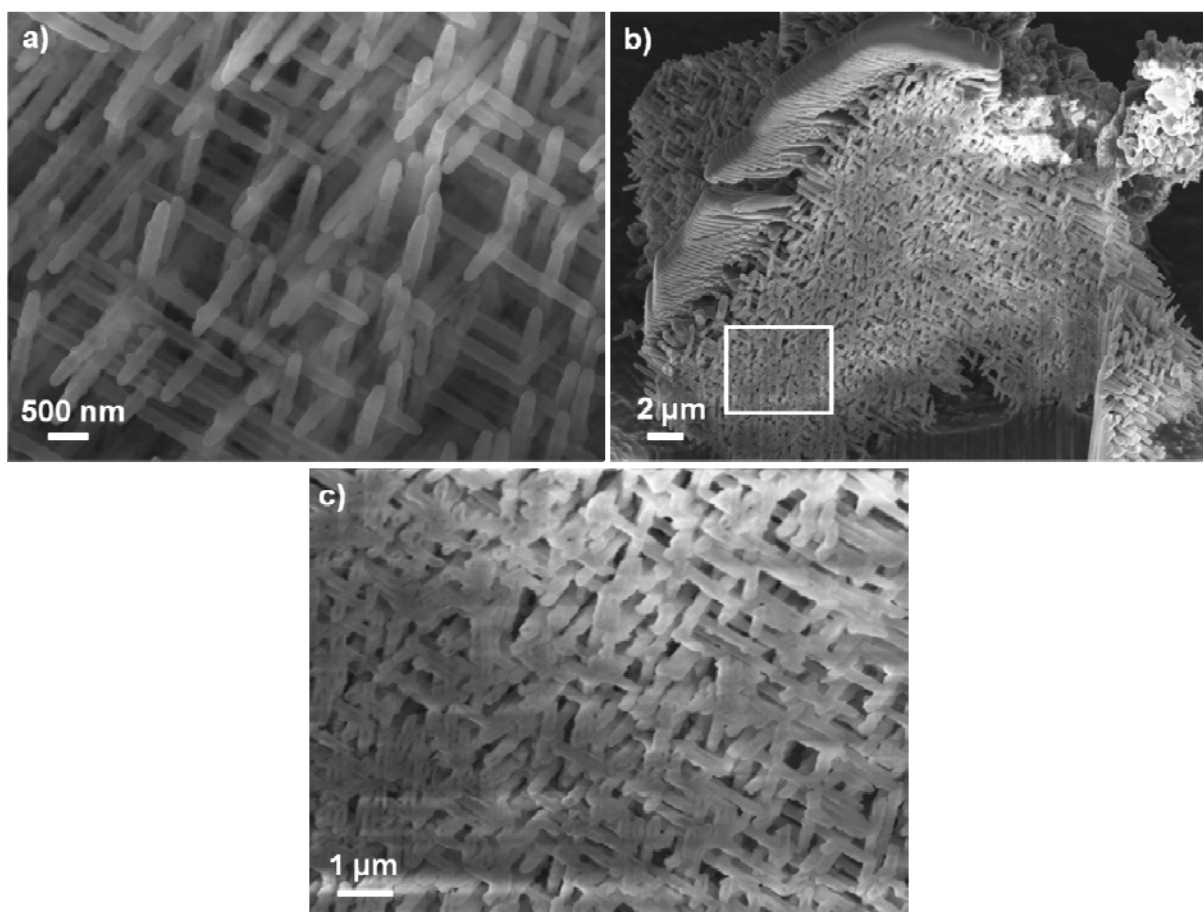


Figure 5.3.6. Samples synthesized at 700 °C a) zoom-in SE image of hyperbranched SBNTs, b) FIB cut through a SBNTs mesocrystal and c) higher magnification of the interior of this 3D assembly.

The mesocrystals consist exclusively of SBNTs. Fig. 5.3.7 shows TEM images of the lamellae prepared at 300 °C (Figure 5.3.7a) and 700 °C (Figure 5.3.7b). The well-ordered network can be observed for both samples.

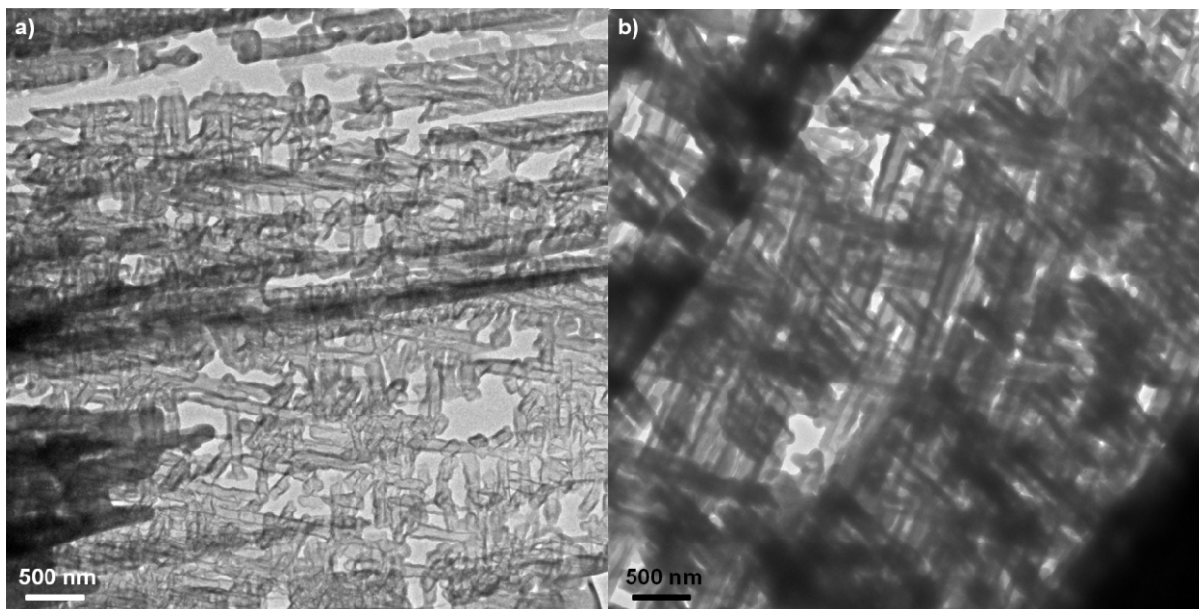


Figure 5.3.7. TEM images of a FIB lamella showing SBNTs synthesized with a low amount of Si at a) 300 °C and b) 700 °C.

Further EELS measurements on the lamella of the 300 °C sample should confirm earlier measurements on single SBNTs that the elements are homogeneously distributed. For a high spatial resolution, the sample was analyzed in scanning TEM mode with EELS using an electron beam size of less than 1 nm. Figure 5.3.8a shows a STEM image of a SBNT synthesized at 300 °C. We studied the SBNT walls in depth to see if there are local changes in the chemical composition. The corresponding EEL spectra of the Si-L_{2,3}-edge of this area are shown in Figure 5.3.8b. As discussed in Chapter 5.2, the Si-L_{2,3}-edge acts as fingerprint. The spectra evince that, as for the sample synthesized at 700 °C, Si is homogeneously distributed in the SBNT and that no structural change is occurring in the SBNT walls.

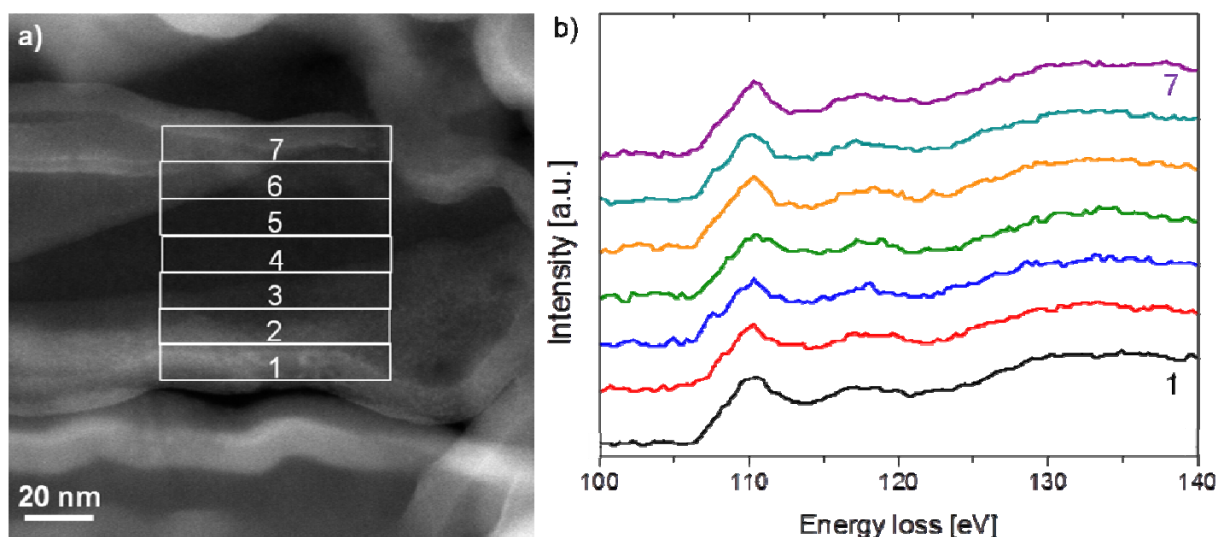


Figure 5.3.8. STEM image of a SBNT wall synthesized with a low amount of Si at 300 °C and b) the corresponding EELS measurements confirming that no structural and chemical change occur in the walls.

The analysis of the elemental distribution of the SBNTs synthesized at 300 °C and of the SBNTs synthesized at 700 °C (Chapter 5.2) indicates that the SBNTs do not grow from a specific point. Otherwise, a chemical gradient at least for one element is expected.

5.3.5 Tomography of a SBNTs 3D assembly

We were interested in the constitution of the SBNTs network. Therefore, we performed ET on a small SBNTs assembly. TEM measurements were performed on the Munich FEI Titan 80 - 300 kV S/TEM. A tilt-series was recorded in STEM-HAADF mode at 80 kV to avoid beam damage of the sample. The tilting range amounted $\pm 70^\circ$ with steps of 10° . STEM images of tilting angles of -70° (Figure 5.3.9a), -20° (Figure 5.3.9b), 10° (Figure 5.3.9c) and 50° (Figure 5.3.9d) are shown in Figure 5.3.9. The network consists of five SBNTs which are connected to each other.

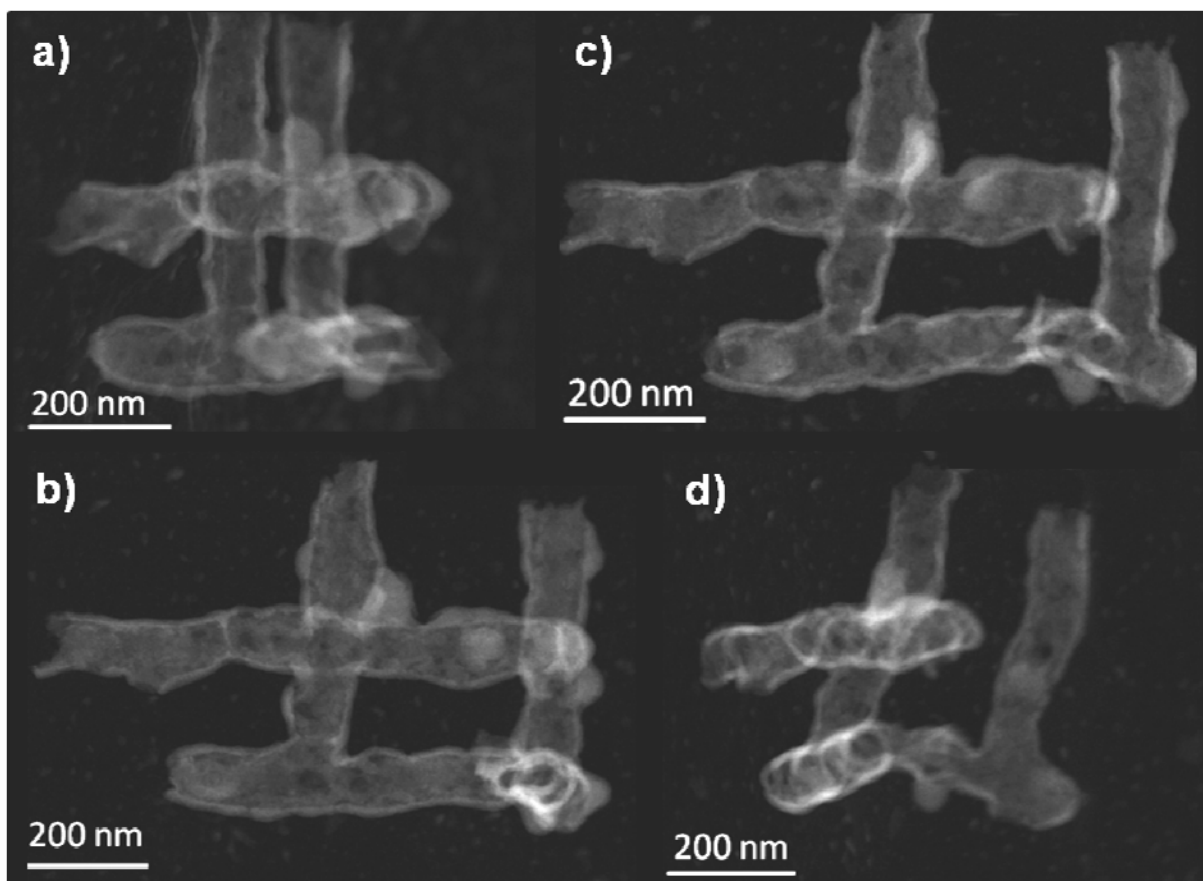


Figure 5.3.9. STEM images of the SBNTs assembly for ET showing the network recorded at tilting angles of a) -70° , b) -20° , c) 10° and d) 50° .

For reconstruction we used a discrete tomography based on a masked SIRT algorithm.⁴ A calculated projection of the SBNT fragment is given in Figure 5.3.10a. For this, thirteen STEM images were used. Some artifacts occur because not many images were available for reconstruction due to beam damage limitation. A cut through of the same fragment is shown in Figure 5.3.10b. This image proves that the SBNTs are hollow. It can clearly be seen that the junction points of the SBNTs are open and that they are connected to each other. This is of high interest for possible applications where filling of the SBNTs is required.

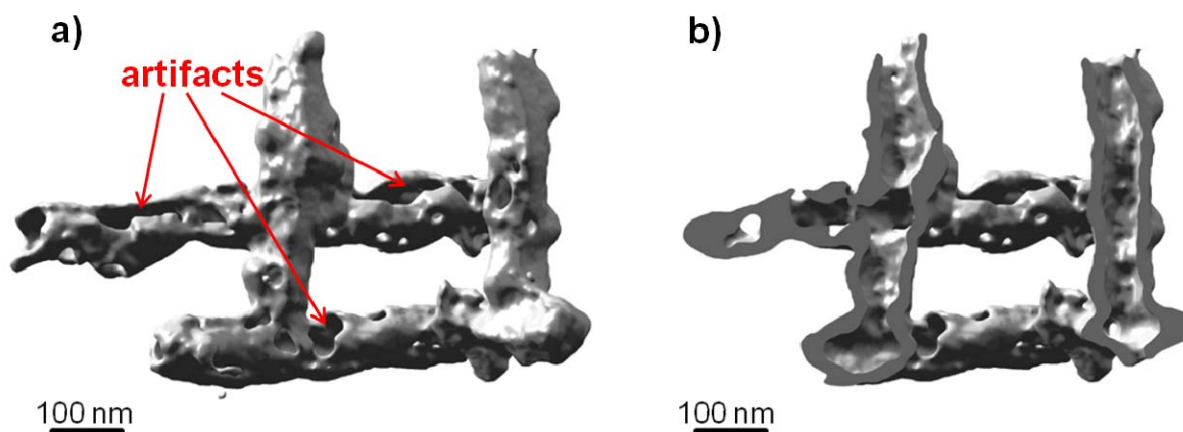


Figure 5.3.10. ET of the SBNTs assembly. a) Calculated projection of the reconstructed NT fragment and b) a cut through of the same fragment evincing that the SBNTs are hollow and that the junction points are open.

Further ET experiments were done on a several μm large SBNTs network (Figure 5.3.11) on a 200 kV FEI monochromated F20 UT Tecnai (STEM/TEM) located at the National Center for Electron Microscopy (NCEM) in Berkeley. The sample did not show conspicuous changes after radiation. As the reaction products (flakes, hollow particles and SBNTs) cannot be separated in a higher amount from each other, common analytical method for porosity determination like sorption fail. Therefore, we plan to get information about the porosity and density of the material via these ET data. The reconstruction and the porosity determination of the material are still under investigation.

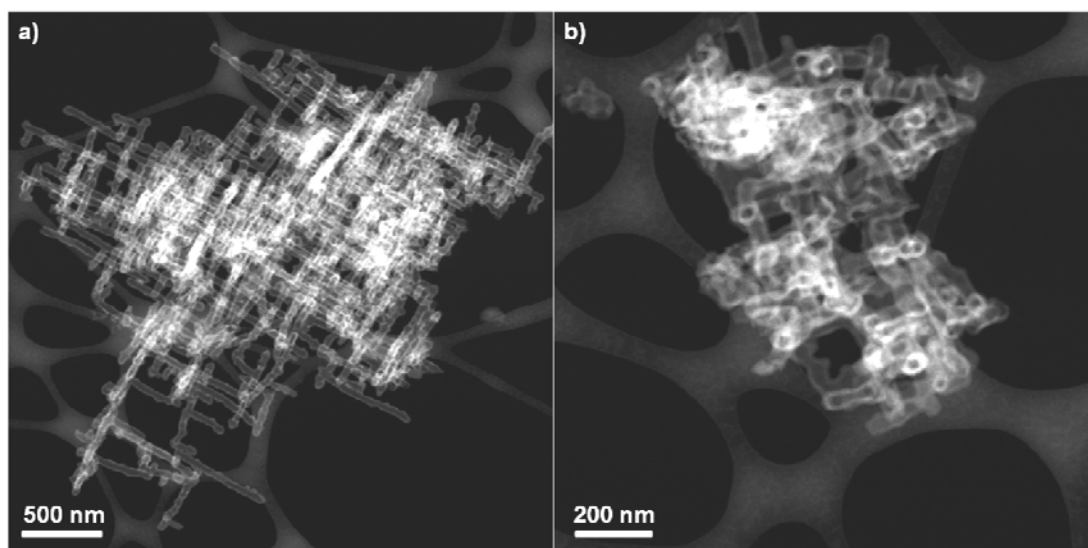


Figure 5.3.11. STEM images of SBNTs networks. a) Several μm broad SBNTs assembly and b) smaller SBNTs network.

5.3.6 Bonding behavior of the flakes

Synthesizing SBNTs, a second reaction product occurs (see Chapter 5.1). These flakes have a different chemical composition than the SBNTs, they mostly consist of P and N with smaller amounts of Si and O. To get a more detailed understanding about the coordination and valence state of these elements, the amorphous flakes were investigated by EELS and the data compared to known similar crystalline compounds, P_3N_5 and PON. TEM micrographs of these materials are given in Figure 5.3.12.

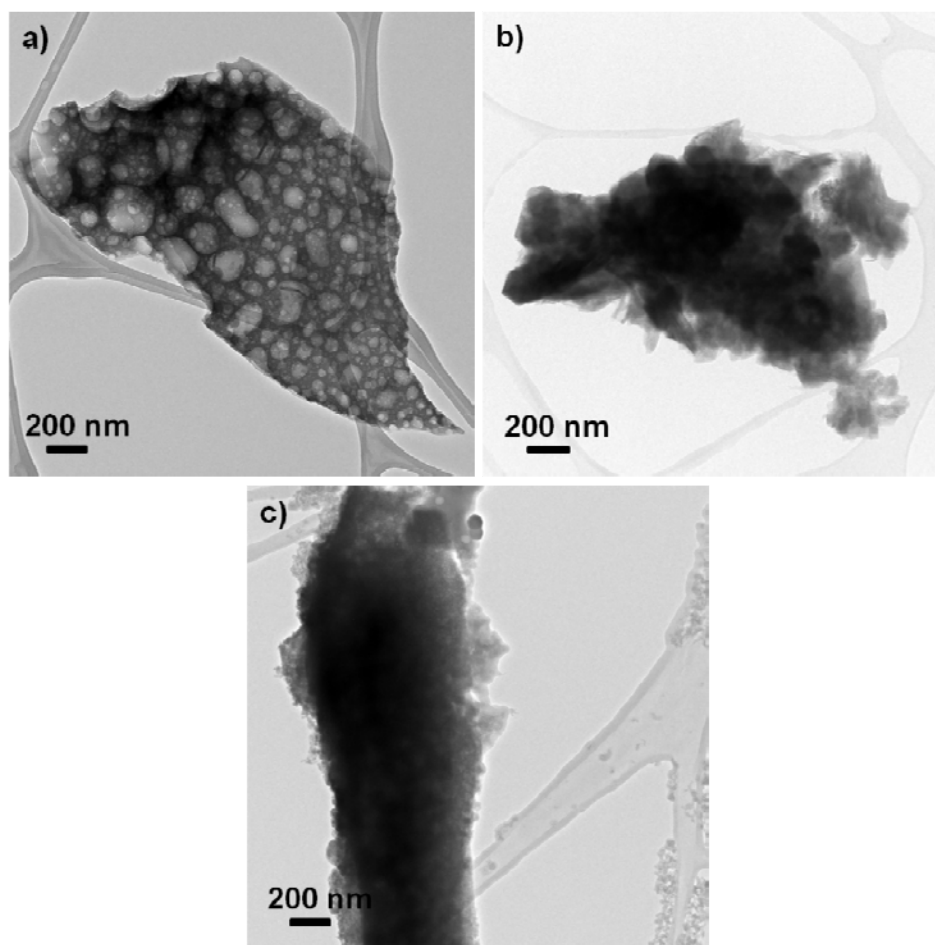


Figure 5.3.12. TEM images of a) a flake, b) a P_3N_5 particle and c) a PON particle.

The EEL spectra were acquired with a dispersion of 0.3 eV/channel and a FWHM of the ZLP of around 1.2 eV leading to a good SNR in diffraction mode on a FEI Titan (Munich) at 300 kV. The camera length was 115 mm and the entrance aperture 2 mm leading to convergence angle of 13.5 mrad.

In Figure 5.3.13 the P-L_{1,2,3}- (a), N-K- (b) and O-K-edges (c) of the three materials are shown. P is tetrahedrally coordinated with N in P₃N₅ and O and N in PON. As P acts as fingerprint for the flakes the P-L_{2,3}-edge was investigated in more detail. Feature A, B, C and D occur in all three spectra. The general shape of the ELNES of the flake is very similar to the spectrum of P₃N₅ but diverse to that of PON. Feature A and B are equally high for PON which is not the case for the spectrum of the flake where A has clearly a higher intensity than B. C is has slightly different intensities due to different thicknesses of the samples and feature D is the P-L₁-edge which is similar for all three materials. In Table 5.3.1 the first maxima and the relative peak distances are given. The first maximum of the flake (A) occurs at 139.5 ± 0.3 . Feature A for P₃N₅ arises at 139.6 ± 0.3 eV and for PON at 139.5 ± 0.3 eV. This leads to a shift of maximum 0.1 eV which is within the error of accuracy. For the flake, feature A to B have a distance of 9 eV, A to C 24.3 eV and A to D 57.3 eV. Overall, the shape of the P-L-ELNES of the flake is very similar to the spectrum of P₃N₅ and does more deviate to the ELNES of PON (Figure 5.3.13a). On the other hand, the relative peak distances are more in accordance to PON. This leads to the conclusion that the flakes exhibit a similar coordination and chemical surrounding as P₃N₅ which is not surprising as the flakes consist mostly of P and N. But the flakes also show some similarity to the PON reference indicating that also P-O-N bounds occur. The ELNES of the N-K edge in Figure 5.3.13b approve this finding, the shape of the ELNES for the flakes and for the P₃N₅ reference material is quite similar whereas the ELNES of PON looks notably different. The first maximum exhibits a much sharper shape than that of the flakes and P₃N₅. The O-K-ELNES in Figure 5.3.13c of the flake and PON shows no clear difference. This indicates that O has a similar chemical surrounding and bonding behavior in the flakes and PON.

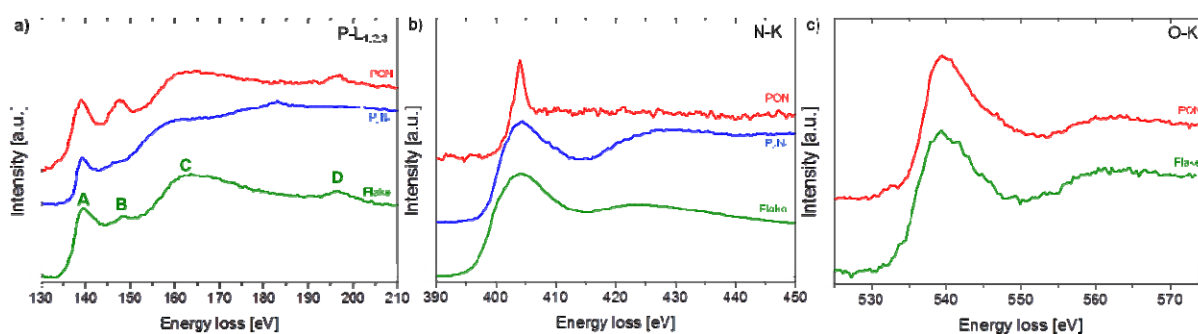


Figure 5.3.13. EEL spectra of a flake (green), P₃N₅ (blue) and PON (red) showing the a) P-L_{1,2,3}-, b) N-K- and O-K-edges.

Table 5.3.1. Position of the first maxima and their relative peak distances for the minor features of the P-L-edge of the flakes and the two references P₃N₅ and PON. The scatter of the peak position for the features of the flakes is evaluated by averaging over several independent measurements.

P-L-edge	Positions [eV]	Relative peak positions		
	First Maximum	A - B	A - C	A - D
Flakes	139.5 ± 0.3	9	24.3	57.3
P ₃ N ₅	139.6 ± 0.3	6.8	20.5	43.9
PON	139.5 ± 0.3	8.7	26.2	58.5
Δ to P ₃ N ₅	0.1	2.2	3.8	13.4
Δ to PON	0	0.3	1.9	1.2

5.3.7 Chapter references

¹ S.J. Sedlmaier, T. Dennenwaldt, C. Scheu, and W. Schnick, *Journal of Materials Chemistry* **22**, 15511 (2012).

² X. Yang, H. Tang, K. Cao, H. Song, W. Sheng, and Q. Wu, *Journal of Materials Chemistry* **21**, 6122 (2011).

³ J.A. García-Calzón and M.E. Díaz-García, *Trends in Analytical Chemistry* **35**, 27 (2012).

⁴ A. Zürner, M. Döblinger, V. Cauda, R. Wei, and T. Bein, *Ultramicroscopy* **115**, 41 (2012).

6 BeP₂N₄ compound

6.1 High resolution spectroscopy of bonding in a BeP₂N₄ compound

This chapter refers to the following publication:

Teresa Dennenwaldt, Jim Ciston, Ulrich Dahmen, Wai-Yim Ching, Florian J. Pucher, Wolfgang Schnick and Christina Scheu. *Submitted*.

6.1.1 Introduction

Nitride materials are known for their high strength and stability at elevated temperatures and mechanical stress because of their rather covalent chemical bonds to nitrogen.¹ In addition, they offer many possible applications in optoelectronics due to their wide-band gap semiconductor character. For example BeCN₂² and Be₃N₂³ possess direct band gaps between 4 – 6 eV. Nitrogen forms short bonds in these compounds leading to comparable properties with other wide-band gap semiconductors such as diamond.⁴ Be₃N₂ exhibits mechanical behavior similar to SiC and Si₃N₄.³ Another structurally related nonmetal nitride is P₃N₅ which has been fully characterized.^{5,6} DFT calculations on this material predict outstanding mechanical properties comparable to BN and Si₃N₄.⁷ α -P₃N₅ can be described as a covalent network of PN₄ tetrahedra sharing edges and corners.⁶ Starting from the compounds P₃N₅ and Be₃N₂ a new hard material BeP₂N₄ has been synthesized recently via the multi-anvil high-pressure/high-temperature method.⁸ This true double nitride which crystallizes in the phenakite-type structure is isoelectronic and isostructural to Be₂SiO₄ and β -Si₃N₄. Like α -P₃N₅ and α -Be₃N₂, BeP₂N₄ is made of TN₄ tetrahedra (T = Be, P). Under high-pressure, β -Si₃N₄ transforms into the spinel-type γ -Si₃N₄, which is known as a very hard material.⁹ By analogy, BeP₂N₄ is expected to transform under high-pressure into the spinel structure as well, leading to another super hard material where the coordination number of P would increase from 4 to 6.^{8,10} A six-fold coordination of P in polymeric nitrides has only been predicted for hypothetical δ -P₃N₅ but could not be observed in any known material so far.⁷ The synthesis of spinel-type BeP₂N₄ is challenging and currently under experimental investigations.

The phenakite-type structure of BeP₂N₄ is primitive rhombohedral with lattice parameters of $a = 12.6897$ and $c = 8.3469$ Å (space group $R\bar{3}$, no. 148, $Z = 18$).⁸ Both Be and P are tetrahedrally coordinated by four N atoms resulting in corner sharing dreier, vierer and sechser rings of BeN₄ and PN₄ tetrahedra. The terms dreier, vierer, and sechser ring were introduced by Liebau.¹¹ A sechser ring consists of six tetrahedra (P and Be as central atoms) and analogously this is valid for dreier (three tetrahedra) and vierer rings (four tetrahedra). The N atoms are arranged in a trigonal planar coordination by one Be and two P atoms.⁸ There are two crystallographically unique P and four unique N atoms which differ in their bond lengths and angles to the respective neighboring atoms. N1 and N2 are coordinated to P1 and P2 as well as to Be. N3 does not coordinate to P1 but twice to P2 and vice versa for N4. Figure 6.1.1a shows the crystal structure with [001] viewing direction. Diverse physical features such as the electronic, spectroscopic and mechanical properties of BeP₂N₄ were recently investigated using DFT calculations.¹⁰ In general, DFT methods have been successfully used for electronic structure and property calculations of various compounds.^{12,13} The results of Ching et al.¹⁰ indicate that the phenakite- as well as the spinel-type phases are wide-band gap semiconductors leading to promising applications, e.g. in optoelectronics. The orthogonalized linear combination of atomic orbitals (OLCAO), which is based on the local density approximation (LDA) of DFT, has been used as the main method for predicting the electronic structures and properties of the phenakite- and the spinel-type polymorph of BeP₂N₄.^{14,15}

EELS is a widely used method in TEM to analyze the chemical and electronic structure of materials, locally and in detail.^{16,17} One limiting factor for the energy resolution of this technique is the initial energy spread of the electron source. The energy resolution can be enhanced by using a monochromator resulting in values of around 0.1 eV.^{18,19} With this energy resolution it is possible to determine details in the electron ELNES related to the electronic structure and bonding effects, as well as to investigate the low loss region in depth to determine e. g. the dielectric function or band gaps of materials on a local scale.²⁰⁻²⁴ The electronic and structural properties of several nitrides have been studied successfully with EELS^{1,25} and it has been shown that the ELNES is strongly dependent on the bond lengths and angles. In this paper we present EELS data acquired with a monochromator from phenakite-type crystals of BeP₂N₄. The experimental ELNES of the Be-K-, P-L_{2,3}- and the N-K-edges are interpreted with the help of the calculated data

published recently.¹⁰ For the calculation of the ELNES the supercell-OLCAO^{26,27} method was applied. In this technique the core-hole effect and the dipole matrix elements calculated from *ab initio* wave functions are included. To adjust the calculated spectra to experimental conditions the calculated ELNES were broadened by a Gaussian with a FWHM of 1.0 eV. As will be shown in the results section, this value describes nicely the damping occurring in the experiments due to broadening caused by life time of excited state and core hole. As the material contains small amounts of impurities and cannot be synthesized in large quantities, EELS in a TEM is required for analyzing the local electronic structure of these phenakite-type crystals.

6.1.2 Experimental details

Monochromated EELS data were taken on the NCEM TEAM 0.5 microscope at 80 kV in Berkeley. This double-aberration corrected STEM/TEM is based on a FEI Titan 80 – 300 kV. It is equipped with a special high-brightness Schottky field emission electron source, a gun monochromator, two CEOS hexapole-type spherical aberration correctors,²⁸ and a Gatan high-resolution GIF Tridiem energy filter. The FWHM of the ZLP was around 0.12 eV during our measurements done in diffraction mode. The ELNES data were taken with a dispersion of 0.05 eV/channel leading to a high energy resolution and a good signal to noise ratio. We used a 1 mm entrance aperture for the spectrometer and a camera length of 43 mm resulting in a collection angle of 12.3 mrad. The investigated sample was thin enough (smaller than 0.3 times the inelastic mean free path), so no deconvolution of our data was necessary. All EEL spectra were corrected for channel-to-channel gain variation and dark current. The background was subtracted using a power-law fitting procedure.¹⁶ Light elements like Be can be knocked out or displaced quickly by the electron beam. To make sure that these effects did not strongly influence the Be-K ELNES, this data was taken with shorter acquisition times than the other edges, which is why the experimental spectra of the Be-edge appear noisier.

The BeP₂N₄ material was synthesized from Be₃N₂ and P₃N₅ in a Walker-type multi-anvil apparatus at a pressure of 5 GPa and 1500 °C, as described in the literature.⁸ The crude product was heated to 680 °C to remove traces of black phosphorus and to improve the crystallinity of the sample. For TEM investigations the material was pestled, suspended in ethanol and dropped on a copper grid coated with a lacey carbon film.

6.1.3 Results and discussion

Electron diffraction experiments confirmed that the compound is crystalline exhibiting the phenakite-type structure. A high-resolution TEM image and its corresponding diffraction pattern taken in [210] direction are given in Figure 6.1.1b. The crystal structure viewed along the [210] orientation is shown in Figure 6.1.1c.

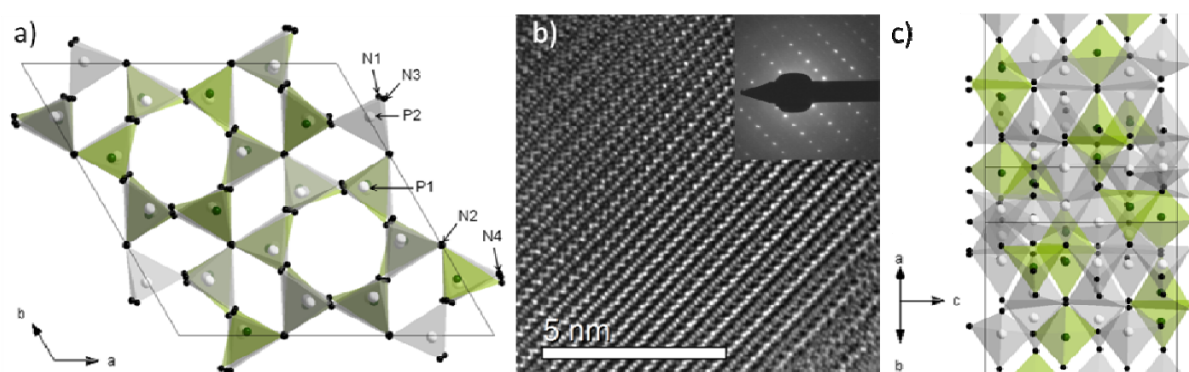


Figure 6.1.1. Crystal structure of the phenakite-type phase with BeN₄ tetrahedra highlighted in green, and PN₄ tetrahedra in gray. (a) structure viewed along [001]; the different P and N sites are indicated; (b) HRTEM image of the phenakite-type polymorph of BeP₂N₄ seen along the [210] direction and the corresponding diffraction pattern; (c) atomic arrangement of the phenakite-type phase viewed along [210].

The experimental as well as the calculated EEL spectra for the phenakite phase are given in Figure 6.1.2, where the theoretical spectra are shown in black and the monochromated data in blue. In order to prevent orientation and channeling effects the sample has been tilted out of zone axis for EELS data collection. Figure 6.1.2a shows the Be-K-edge with the characteristic features labeled A – D. In the experimental data of the Be-K-edge the first maximum, labeled A, shows the highest intensity and occurs at 116.9 ± 0.1 eV. The scatter in the peak position is estimated by averaging over several independent measurements. In the calculated spectrum this peak appears at 118 eV.¹⁰ For better comparison of all following features (B – D) we shifted the calculated data by 1.1 eV to lower energy losses (to align the first maximum of the experimental and simulated data) since we are most interested in relative peak distances. A difference in the edge onsets of the calculated and experimental values of approximately 1% is commonly reported in the literature.^{27,29} Possible explanations are errors in the calibration of the spectrometer as well as difficulties in calculating excited states.

Overall, the general shapes of the experimental and calculated Be-K ELNES are in excellent agreement. The relative peak distances in the experimental data are 2.5 eV for feature A to B, 5.4 eV for feature A to C and 11.5 eV for A to D. As shown in Table 6.1.1, these observed peak distances are in good agreement with the calculated ELNES data. Feature C is different in the experimental and calculated data which predicts two features. A possible explanation is that the synthesized phenakite crystals are not fully relaxed and the equilibrium atomic positions not yet achieved.

Figure 6.1.2b shows the P-L_{2,3}-edge, which exhibits more fine structure than the Be-K-edge. The first maximum (A) occurring at 136.1 ± 0.7 eV in the experimental data is also the highest intensity peak in the spectrum. The calculated first maximum is located at 138.2 eV¹⁰ so the calculated data was shifted by 2.1 eV to lower energy losses. Similar to the discussion of Be-K ELNES, the relative peak separations of the minor features (B – E) of the P-L_{2,3}-edge again show excellent agreement with the calculated data. Features A, B and C are present in the calculated data set as well as in the experimental measurement. The weak shoulder on the high energy side of peak A is not visible in the calculated data. This small shoulder is the signature of L₂, L₃ splitting (~ 1 eV) which is resolved by the monochromated data. The calculated L-edge is only for L₃, and omits any contributions from L₂ because the spin-orbit coupling in the core level was not taken into account. This spin-orbit splitting is important for L-edges, but not relevant to the K-edges since the 1s-level has no spin-splitting. The results for the P-L_{2,3}-edge are 6.4 eV for the relative peak distances between features A and B, 11.6 eV for A and C, 20.6 eV for A and D and 26.7 eV for the features A and E. There is a major peak at around 156 eV in the calculated ELNES which appears slightly weaker in the experimental data (D). The smoother peak in the measurement occurring above 164 eV labeled E is again caused by the P-L₂-edge. The results for the experimental and the calculated peak positions are listed in Table 6.1.1. The difference in the relative peak position is smaller than 1.1 eV. Once more, the experimental ELNES is in good agreement with the DFT calculation.

The N-K-edge is given in Figure 6.1.2c revealing that the first maximum in the experimental data appears at 404.6 ± 0.1 eV. This peak is split, and the features are denoted A and B. Minor features are labeled as C, D and E. The calculated data is an averaged spectrum over the four N sites.¹⁰ Here, the first maximum is observed at 407 eV. For a better comparison of the relative peak positions the calculated spectrum

was shifted by 2.4 eV to lower energy losses. The relative peak distances between features A to E are given in Table 6.1.1. The experimentally measured peak separations are 2.6 eV for features A and B, 8.1 eV for A and C, 17 eV for A and D and 29.3 eV for A and E. The calculated ELNES shows three broader peaks (A, C and D) with relative peak distances of 7.3 eV for features A and C and 18.5 eV for A and D. The difference between experimental and calculated peak positions of the N-K-edge is between 0.8 and 1.5 eV; the experimental and calculated ELNES are in reasonable accordance.

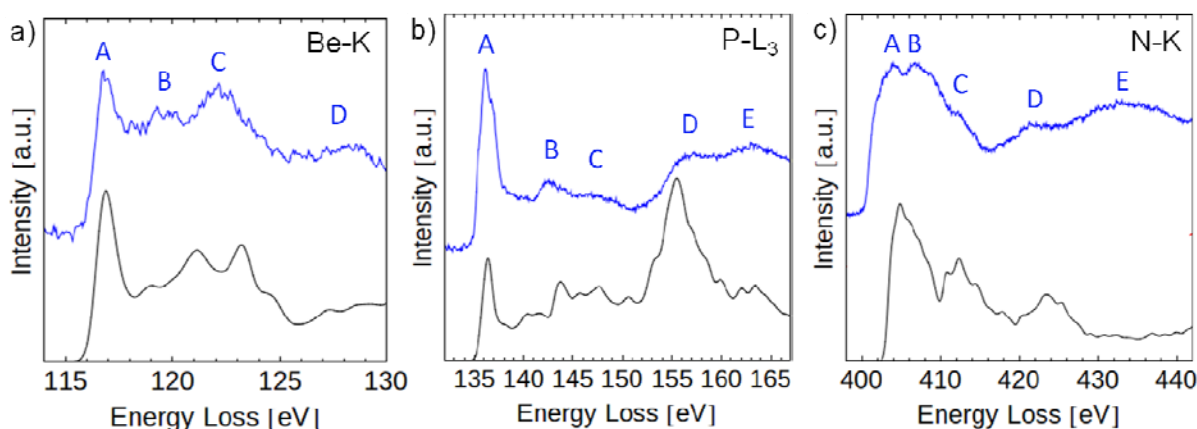


Figure 6.1.2. Calculated¹⁴ (black) and experimental EEL spectra (blue) of the phenakite-type BeP₂N₄ showing the Be-K (a), P-L_{2,3} (b), and N-K edges (c).

Table 6.1.1. Position of the first maxima of the experimental and calculated spectra for the Be-K-, P-L_{2,3}-, and N-K-edges and their relative peak distances for the minor features. The scatter of the peak position is evaluated by averaging over several independent measurements.

Edges	Positions [eV]	Relative peak positions			
	First Maximum	A - B	A - C	A - D	A - E
Exp. Be-K	116.9 ± 0.1	2.5	5.4	11.5	
Calc. Be-K	118	2	4.1 / 7.1	12	
Δ Be-K	1.1	0.5	1.3 / 1.7	0.5	
Exp. P-L _{2,3}	136.1 ± 0.7	6.4	11.6	20.6	26.7
Calc. P-L ₃	138.2	7.8	11.8	19.7	27.8
Δ P-L₃	2.1	1.4	0.2	0.9	1.1
Exp. N-K	404.6 ± 0.1	2.6	8.1	17	29.3
Calc. N-K	407		7.3	18.5	
Δ N-K	2.4		0.8	1.5	

The observed double peak labeled A and B in the experimental data is unambiguous, but is not present in the calculated curve where the spectra for the four different N sites (N1, N2, N3 and N4 in Figure 6.1.1a) were equally weighted and summed. All four N atoms have different bond lengths, bond angles and bond orders leading to different features and peak positions in the N site specific ELNES.¹⁰ The main difference between these four N sites is that N1 and N2 coordinate to each atom type (Be, P1 and P2) while N3 only coordinates to Be and twice to P2 and N4 coordinates to Be and twice to P1. For the different sites in the relaxed crystal structure, the N-P bonds are in all cases shorter than the N-Be bonds because the N valence electrons are pulled closer to the more electronegative P atoms (compared to Be). The total bond order rises in the sequence N1 (1.025) < N3 (1.031) < N4 (1.036) < N2 (1.039). N1 shows the smallest bond order leading to a higher energy loss for the main peak (occurring at position of feature B) whereas N2 has the highest bond order so a lower energy loss for its main peak is observed (occurring at position A). This is in accordance with Brydson et al.³⁰ where a longer bond length results in a lower energy of scattering shape resonance and vice versa.

Several reasons might be responsible for the difference of the calculated and experimental N-K-edge. First, using the full core-hole approximation in the DFT calculations (the excited electron was placed at the bottom of the conduction band) might not be necessary for the N-K edge in our compound. It is known from literature that, depending on how the core hole was taken into account, the intensities and peak positions can alter.³¹ Consequently, another core-hole approximation might describe the splitting of the main peak of the N-K edge more accurately. Second, orientation/channeling effects can change the ELNES significantly. We tried to minimize this effect by using out of a low-indexed zone axis orientations. Third, the N-K-edge is strongly influenced by point defects such as vacancies. Preliminary inspections of high-resolution TEM images did not give any evidence for a high density of such defects. In any case, the high energy resolution in the experimental measurement reveals two separate peaks A and B, which can be used to provide guidelines to theoretical schemes for ELNES. A splitting of the N-K-edge has been previously observed in the literature for transition metal nitrides and was related to hybridized nitrogen 2p states and transition metal 3d states with symmetries of t_{2g} and e_g .^{20,32,33}

Overall, the good agreement between experimental and calculated data reveal that 1 eV broadening in the calculated EEL spectra is sufficient to describe the experimental broadening occurring due to lifetime effects of the core hole and the excited state for our material system. Similar observations in particular for K-edges (above 400 eV) have been reported by Kothleitner et al.³⁴, Scheu et al.³⁵ and Muller et al.³⁶ Nevertheless, the use of a monochromator is still beneficial since the individual features in the ELNES are less smeared out due to the reduced tails of the zero loss peak compared to non-monochromated data.

6.1.4 Conclusion

High-energy-resolution EELS data have been successfully acquired from a new phenakite-type BeP₂N₄ wide-band gap semiconductor without altering the structure. This is important for further development of compounds with ultralight elements since the possibility of their detection is limited. In this study we could not only measure the presence of Be but could also determine its coordination and bonding behavior in the compound. This was demonstrated by an excellent agreement with calculated ELNES data for the Be-K, P-L₃-, and (partly) N-K-edges concerning shape, relative peak positions and edge onsets. To describe the experimental P-L_{2,3}-edge in more detail, future DFT calculations should include the contributions of the spin-orbit terms. Nevertheless, the experimental measurements confirm that P and Be are tetrahedrally coordinated. N is threefold coordinated and is located on four different sites in the phenakite-type structure. Overall, this type of measurement will allow an easy identification of new structure types such as hypothetical ultrahard spinel-type BeP₂N₄ material in the future.

6.1.5 Chapter references

- ¹ W. de la Cruz, G. Soto, and F. Yubero, *Optical Materials* **25**, 39 (2004).
- ² W.R.L. Lambrecht and B. Segall, *Physical Review B* **45**, 1485 (1992).
- ³ M.G.M. Armenta and A. Reyes-Serrato, *Computational Materials Science* **21**, 95 (2001).
- ⁴ A. Mokhtari and H. Akbarzadeh, *Physica B* **337**, 122 (2003).
- ⁵ W. Schnick, J. Lücke, and F. Krumeich, *Chemistry of Materials* **8**, 281 (1996).
- ⁶ S. Horstmann, E. Irran, and W. Schnick, *Angewandte Chemie International Edition* **36**, 1873 (1997).
- ⁷ P. Kroll and W. Schnick, *Chemistry - A European Journal* **8**, 3530 (2002).
- ⁸ F.J. Pucher, S.R. Römer, F.W. Karau, and W. Schnick, *Chemistry - A European Journal* **16**, 7208 (2010).
- ⁹ A. Zerr, G. Miehe, G. Serghiou, M. Schwarz, E. Kroke, R. Riedel, H. Fueß, P. Kroll, and R. Boehler, *Nature* **400**, 340 (1999).
- ¹⁰ W.-Y. Ching, S. Aryal, P. Rulis, and W. Schnick, *Physical Review B* **83**, 155109 (2011).
- ¹¹ F. Liebau, *Structural Chemistry of Silicates* (Springer, Berlin, 1985), p. 347.
- ¹² K. Lie, R. Hoier, and R. Brydson, *Physical Review B* **61**, 1786 (2000).
- ¹³ M. Nelhiebel, P.-H. Louf, P. Schattschneider, P. Blaha, K. Schwarz, and B. Jouffrey, *Physical Review B* **59**, 807 (1999).
- ¹⁴ W.-Y. Ching, *Journal of the American Ceramic Society* **73**, 3135 (1990).
- ¹⁵ W.-Y. Ching and P. Rulis, *Electronic Structure Methods for Complex Materials: The Orthogonalized Linear Combination of Atomic Orbitals* (Oxford University Press, Oxford, 2012), p. 350.
- ¹⁶ R.F. Egerton, *Electron Energy-loss Spectroscopy in the Electron Microscope*, 3 ed. (Springer Science+Business Media, New York, 2011), p. 491.
- ¹⁷ R. Brydson, *Electron Energy Loss Spectroscopy*, 1 ed. (BIOS Scientific Publishers Limited, Oxford, 2001), p. 137.
- ¹⁸ F. Kahl and H. Rose, in *12th European Congress on Electron Microscopy* (2000), pp. 1459–1460.
- ¹⁹ S. Uhlemann and M. Haider, *Microscopy and Microanalysis* **8**, 584 (2002).
- ²⁰ S. Lazar, G.A. Botton, M.-Y. Wu, F.D. Tichelaar, and H.W. Zandbergen, *Ultramicroscopy* **96**, 535 (2003).
- ²¹ R. Erni and N.D. Browning, *Ultramicroscopy* **104**, 176 (2005).
- ²² T. Kuykendall, P. Ulrich, S. Aloni, and P. Yang, *Nature Materials* **6**, 951 (2007).
- ²³ L. Gu, V. Srot, W. Sigle, C.T. Koch, P.A. van Aken, F. Scholz, S.B. Thapa, C. Kirchner, M. Jetter, and M. Rühle, *Physical Review B* **75**, 195214 (2007).
- ²⁴ B. Schaffer, W. Grogger, G. Kothleitner, and F. Hofer, *Ultramicroscopy* **110**, 1087 (2010).
- ²⁵ A. Ziegler, J.C. Idrobo, M.K. Cinibulk, C. Kisielowski, N.D. Browning, and R.O. Ritchie, *Science* **306**, 1768 (2004).
- ²⁶ S.-D. Mo and W.-Y. Ching, *Physical Review B* **62**, 7901 (2000).

- ²⁷ W.-Y. Ching and P. Rulis, *Journal of Physics: Condensed Matter* **21**, 104202 (2009).
- ²⁸ M. Haider, H. Müller, S. Uhlemann, J. Zach, U. Loebau, and R. Hoeschen, *Ultramicroscopy* **108**, 167 (2008).
- ²⁹ I. Tanaka and T. Mizoguchi, *Journal of Physics: Condensed Matter* **21**, 104201 (2009).
- ³⁰ R. Brydson, J. Bruley, H. Müllejans, C. Scheu, and M. Rühle, *Ultramicroscopy* **59**, 81 (1995).
- ³¹ P. Lazar, J. Redinger, J. Strobl, R. Podloucky, B. Rashkova, G. Dehm, G. Kothleitner, S. Sturm, K. Kutschej, C. Mitterer, and C. Scheu, *Analytical and Bioanalytical Chemistry* **390**, 1447 (2008).
- ³² M. Tsujimoto, H. Kurata, T. Nemoto, S. Isoda, S. Terada, and K. Kaji, *Journal of Electron Spectroscopy and Related Phenomena* **143**, 159 (2005).
- ³³ A.T. Paxton, M. van Schilfgaarde, M. MacKenzie, and A.J. Craven, *Journal of Physics: Condensed Matter* **12**, 729 (2000).
- ³⁴ G. Kothleitner, W. Grogger, and F. Hofer, *Microscopy and Microanalysis* **9**, 846 (2003).
- ³⁵ C. Scheu, G. Dehm, M. Rühle, and R. Brydson, *Philosophical Magazine A* **78**, 439 (1998).
- ³⁶ D. Muller, D. Singh, and J. Silcox, *Physical Review B* **57**, 8181 (1998).

6.2 Band gap determination of BeP₂N₄

6.2.1 Band gap determination in literature

VEELS performed at high energy resolution is a more and more used method for determining band gaps on a local scale and the dielectric function of a material.¹⁻⁵ One of the most limiting factors for analyzing the low loss region is the energy spread of the electron source and instabilities of the high voltage. For thermally assisted Schottky field emission sources a FWHM of around 0.8 eV is reached whereas for cold field emission electron sources a FWHM of 0.3 eV is achieved.⁶ Because of the extended tail of the ZLP the fine structure of the VEELS cannot be detected for energy losses up to 5 eV for the first named electron source and up to 3 eV for the latter electron source, respectively. Therefore, band gap determination below these values is difficult without the use of a monochromator.⁶ Figure 6.2.1 opposes VEEL spectra acquired with and without a monochromator. For monochromated spectra a FWHM of around 0.1 eV is achieved.

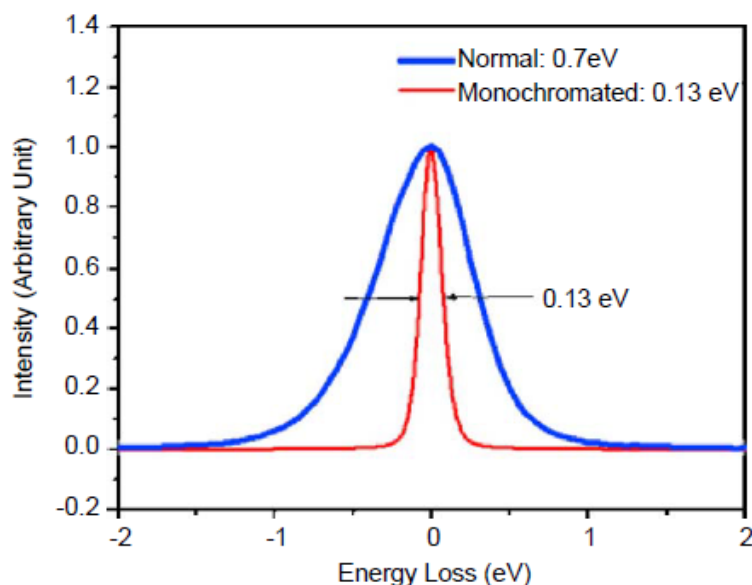


Figure 6.2.1. ZLP acquired without (blue) and with (red) a monochromator. For both measurements a Schottky field emission source was used. The FWHM exhibits 0.7 eV for the conventionally acquired spectrum and 0.13 eV for the monochromated data. Taken from Park et al.⁷

However, Cerenkov loss and surface effects can occur and complicate the determination and interpretation of the band gap energy.^{6,7} Cerenkov radiation is emitted as photons which are depending on the velocity of the electrons and the relative permittivity of the

medium.⁸ Simplified, this effect occurs when the electron velocity is faster than the speed of light.⁷ Furthermore, different materials request different methods of band gap determination.^{6,7} Thereby, especially for avoiding Cerenkov effects, materials with direct and indirect band gaps have to be treated in different ways.⁶ Park et al.⁷ and Gu et al.⁶ presented and opposed several methods for determining band gaps of different materials with direct and indirect band gaps. Table 6.2.1 shows an overview over determined band gap onsets of hexagonal GaN (*h*-GaN) using different spectrum processing methods.⁶ Optical absorption data revealed a direct band gap energy of 3.43 eV for *h*-GaN.⁹ Gu et al.⁶ showed that depending on the spectrum processing method band gap energies of 3.3 eV to 3.5 eV are obtained leading to an error of about ± 0.1 eV.⁶ Five methods are demonstrated. The first are the Fourier-log deconvolution with fitting a power-law function to the onset,¹⁰ a Fourier-ratio deconvolution¹¹ and a power-law fit to the ZLP with a fit of Lorentzian peaks to the first derivative^{12,13}. Another method is to visually determine the changing slope at the onset¹⁴ and the last one is to mirror the left tail of the ZLP to the right tail and subtract it from each other¹⁵.

Table 6.2.1. Band gap energies of *h*-GaN using different spectrum processing techniques of the ZLP. Adapted from Gu et al.⁶

Methods	Onset values [eV]	References
Fourier-log deconvolution Fit of power-law function to the onset	3.3	10
Fourier-ratio deconvolution	3.3	11
Power-law fit to ZLP Fit of Lorentzian peaks to first derivative	3.4	12,12
Visual determination of the changing slope at the onset	3.4	14
Mirroring left tail of ZLP to the tight tail Subtraction of the mirrored tail defining the inflection point as the onset	3.5	15

The thickness of the sample is crucial for minimizing Cerenkov effects.^{6,16} For direct band gap semiconductors like *h*-GaN thicknesses up to $0.5 t/\lambda$ lead to the band gap value obtained also by the optical measurements.^{6,16} In general, the thicker the sample the more the estimated band gap value is shifted to lower energy losses. These effects are summarized in Figure 6.2.2. The band gap value of indirect band gap semiconductors can be determined by blocking the Cerenkov losses in dark-field mode while the momentum transfer is kept preserved.⁶

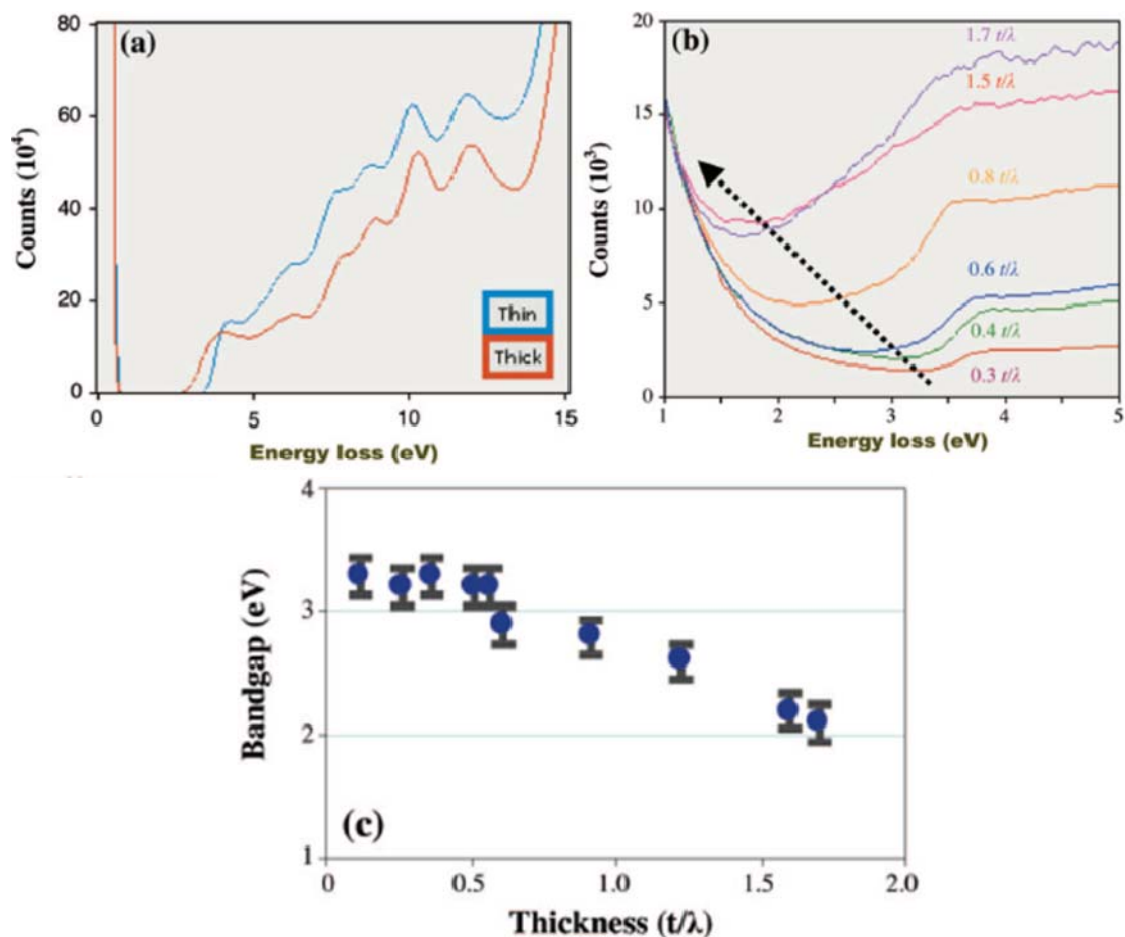


Figure 6.2.2. Correlation between sample thickness and Cerenkov effects. a) VEEL spectra of a thin (blue) and a thick (red) specimen area of *h*-GaN, b) sample thicknesses of 0.3 to 1.7 t/λ showing a falsified band gap energy shift to lower energy losses with increasing thickness and c) determination of the true band gap energy is possible up to 0.5 t/λ . Taken from Gu et al.⁶

Another way to exclude Cerenkov losses is to choose the right parameters, i.e. camera length and collection angle, before acquiring the spectrum. To avoid strong contributions from Cerenkov radiation a large camera length is required.⁶ Furthermore, the Cerenkov radiation contribution becomes smaller for larger collection angles (Figure 6.2.3). This is related to the fact that they are strongly scattered in an forward direction with scattering angles < 0.01 mrad.¹⁷

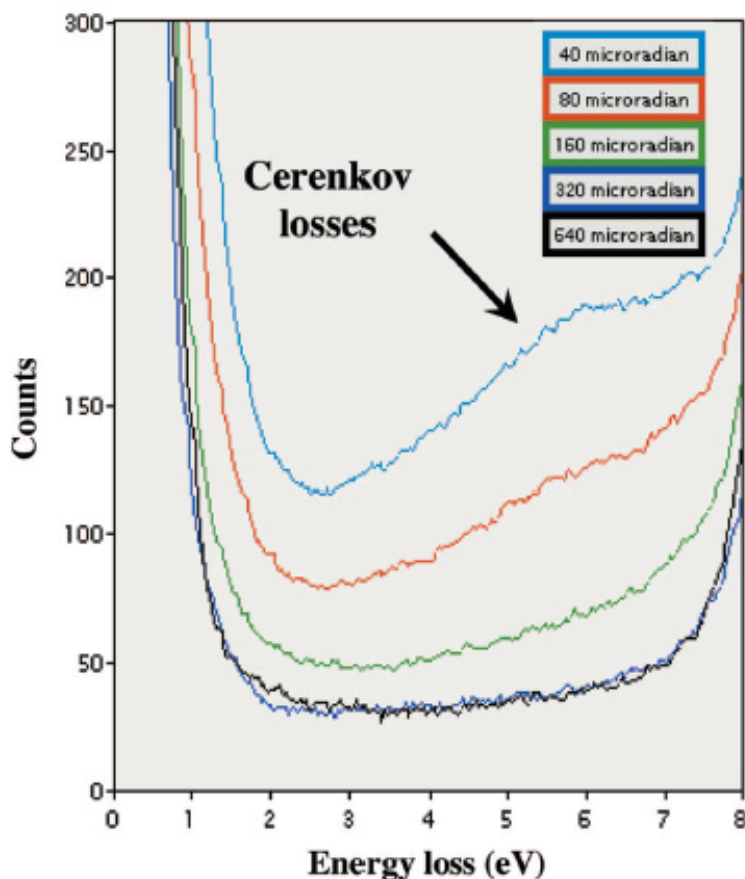


Figure 6.2.3. VEEL spectra of diamond acquired with collection angles of 40 to 640 μ rad indicating the decrease of the Cerenkov radiation contribution with higher collection angles. Taken from Gu et al.⁶

Silicon oxide and nitrides were analyzed by Park et al. and a correlation between sample thickness and Cerenkov radiation was found as well.⁷ However, for SiO₂ the linear fit method leads to a band gap energy of 8.9 eV independently of the sample thickness or Cerenkov losses. Thereby, the intersection between straight lines from the background level and the linear fit to the onset of the low-loss signal corresponds to the band gap energy.⁷ This method was applied on SiO₂ and is visualized in Figure 6.2.4.

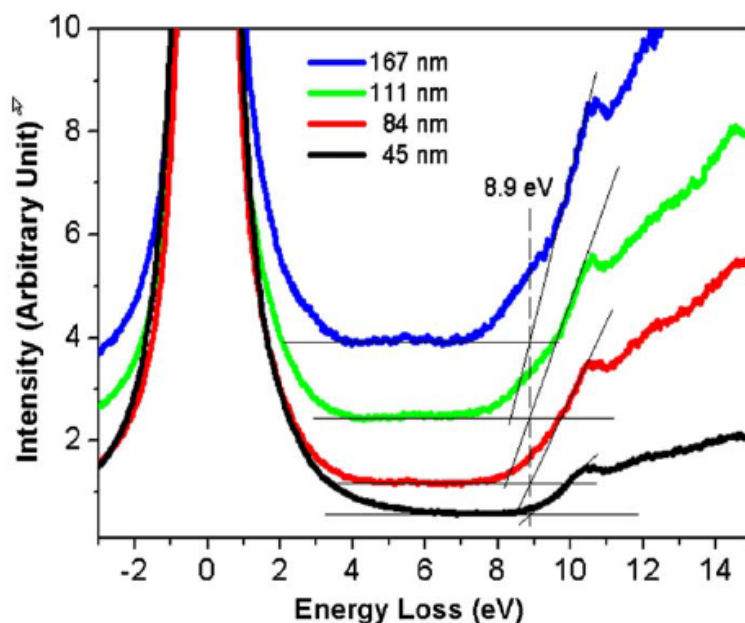


Figure 6.2.4. Band gap determination of SiO₂ leading to 8.9 eV independently of thickness and Cerenkov effects using the linear fit method on monochromated data. Taken from Park et al.⁷

6.2.2 Band gap determination of the phenakite-type BeP₂N₄

In our study we applied VEELS to determine the direct band gap of the phenakite-type structure of BeP₂N₄. Therefore, EEL spectra were collected on a 200 kV FEI monochromated F20 UT Tecnai (STEM/TEM). The measurements were done in diffraction mode and the FWHM of the ZLP was around 0.4 eV. For the analysis we used a dispersion of 0.05 eV/channel, a 2.5 mm entrance aperture for the spectrometer and a camera length of 115 mm leading to a collection angle of 13.5 mrad. DFT calculations predicted a direct band gap at 3.31 eV for the crystal structure obtained by XRD studies and 3.97 eV for the theoretically refined phenakite structure of the BeP₂N₄ compound.¹⁸ The band gap values are predicted to be slightly too low due to the used method. Our preliminary experimental band gap value was detected at 4.3 ± 0.3 eV using the linear fit method (Figure 6.2.5).⁷ The error is determined by the scatter of evaluating around 10 different sample positions. This method was found to give the best results for our material compared to the predicted values and is in reasonable agreement with the DFT calculations. However, Cerenkov radiation can falsify the results by causing artifacts.¹⁹⁻²² This limitation was considered for our interpretation. The chosen sample thickness and the large collection angle lead to minimized contributions. Besides, Park et al.⁷ showed by applying the linear fit method on SiO₂ thin films that these effects can be minimized.

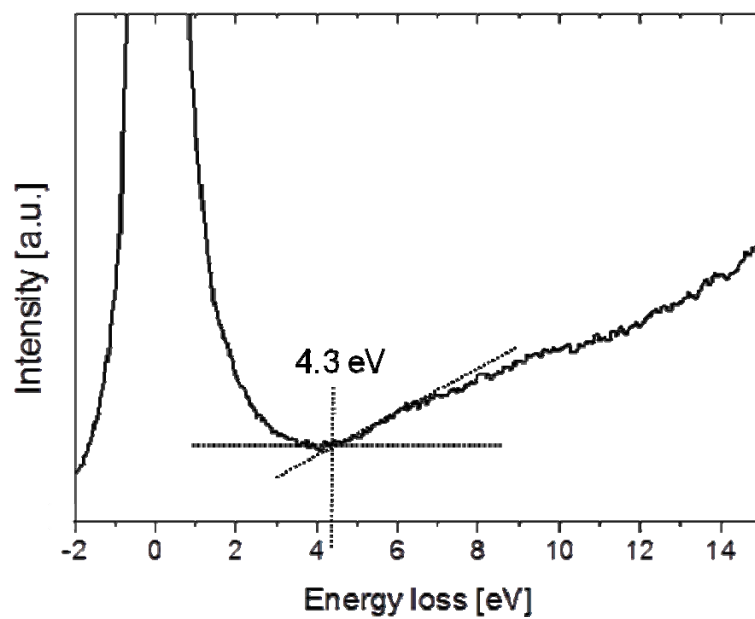


Figure 6.2.5. Band gap determination leading to a value of 4.3 eV for the phenakite-type BeP₂N₄ using the linear fit method.

6.2.3 Chapter references

- ¹ T. Kuykendall, P. Ulrich, S. Aloni, and P. Yang, *Nature Materials* **6**, 951 (2007).
- ² S.-D. Mo and W.-Y. Ching, *Physical Review B* **62**, 7901 (2000).
- ³ W.-Y. Ching and P. Rulis, *Journal of Physics: Condensed Matter* **21**, 104202 (2009).
- ⁴ M. Haider, H. Müller, S. Uhlemann, J. Zach, U. Loebau, and R. Hoeschen, *Ultramicroscopy* **108**, 167 (2008).
- ⁵ I. Tanaka and T. Mizoguchi, *Journal of Physics: Condensed Matter* **21**, 104201 (2009).
- ⁶ L. Gu, V. Srot, W. Sigle, C.T. Koch, P.A. van Aken, F. Scholz, S.B. Thapa, C. Kirchner, M. Jetter, and M. Rühle, *Physical Review B* **75**, 195214 (2007).
- ⁷ J. Park, S. Heo, J.-G. Chung, H. Kim, H. Lee, K. Kim, and G.-S. Park, *Ultramicroscopy* **109**, 1183 (2009).
- ⁸ R.F. Egerton, *Electron Energy-loss Spectroscopy in the Electron Microscope*, 3 ed. (Springer Science+Business Media, New York, 2011), p. 491.
- ⁹ W. Shan, J.W. Ager, K.M. Yu, W. Walukiewicz, E.E. Haller, M.C. Martin, W.R. McKinney, and W. Yang, *Journal of Applied Physics* **85**, 8505 (1999).
- ¹⁰ R. Erni and N.D. Browning, *Ultramicroscopy* **104**, 176 (2005).
- ¹¹ B. Rafferty, S.J. Pennycook, and L.M. Brown, *Journal of Electron Microscopy* **49**, 517 (2000).
- ¹² R. Erni and N.D. Browning, *Ultramicroscopy* **107**, 267 (2007).
- ¹³ P. Specht, J.C. Ho, X. Xu, R. Armitage, E.R. Weber, R. Erni, and C. Kisielowski, *Solid State Communications* **135**, 340 (2005).
- ¹⁴ K. Kimoto, G. Kothleitner, W. Grogger, Y. Matsui, and F. Hofer, *Micron* **36**, 185 (2005).
- ¹⁵ S. Lazar, G.A. Botton, M.-Y. Wu, F.D. Tichelaar, and H.W. Zandbergen, *Ultramicroscopy* **96**, 535 (2003).
- ¹⁶ S. Lazar, G. a Botton, and H.W. Zandbergen, *Ultramicroscopy* **106**, 1091 (2006).
- ¹⁷ C. von Festenberg, *Zeitschrift für Physik* **214**, 464 (1968).
- ¹⁸ W.-Y. Ching, S. Aryal, P. Rulis, and W. Schnick, *Physical Review B* **83**, 155109 (2011).
- ¹⁹ C. Mitterbauer, G. Kothleitner, W. Grogger, H.W. Zandbergen, B. Freitag, P.C. Tiemeijer, and F. Hofer, *Ultramicroscopy* **96**, 469 (2003).
- ²⁰ D. Holec, P.M. Costa, P. Cherns, and C.J. Humphreys, *Micron* **39**, (2008).
- ²¹ T. Mizoguchi, I. Tanaka, S. Yoshioka, M. Kunisu, T. Yamamoto, and W.-Y. Ching, *Physical Review B* **70**, 045103 (2004).
- ²² I. Tanaka, T. Mizoguchi, T. Sekine, H. He, K. Kimoto, T. Kobayashi, S.-D. Mo, and W.-Y. Ching, *Applied Physics Letters* **78**, 2134 (2001).

7 Fe_{2-x}Ti_xO₃/Fe₂O₃ thin films grown on Al₂O₃

7.1 Insights into the structural, electronic and magnetic properties of Fe_{2-x}Ti_xO₃/Fe₂O₃ thin films with x = 0.44 grown on Al₂O₃ (0001)

This chapter refers to the following publication:

Teresa Dennenwaldt, Maïke Lübbe, Michael Winklhofer, Alexander Müller, Markus Döblinger, Hasan Sadat Nabi, Maria Gandman, Tzipi Cohen-Hyams, Wayne D. Kaplan, Wolfgang Moritz, Rossitza Pentcheva and Christina Scheu. *Submitted*.

7.1.1 Introduction

The solid-solid solution of hematite-ilmenite (1-x)Fe₂O₃ xFeTiO₃ has long been known for its interesting magnetic^{1,2} and semiconducting properties with wide band gaps (2 - 3 eV) and a change from n to p type conduction at x > 0.73.³ Owing to its multifunctional character, the system has attracted a lot of interest for possible spintronic device applications in recent years, for example, as magnetically tunable varistors.⁴ Ti-doped hematite (x ~ 0.05), in particular, is intensively studied as anode material for photoelectrochemical hydrogen production ('water splitting').⁵⁻⁸

The end member hematite (α -Fe₂O₃, a = b = 5.04 Å, c = 13.75 Å) crystallizes in the corundum structure with a space group of $R\bar{3}c$.⁹ In this structure, the O²⁻ anions build a hexagonal closed packed lattice where two thirds of the octahedral sites are occupied by Fe³⁺ cations. Since not all octahedral sites are filled, the hexagonal closed packed lattice is slightly distorted. Antiferromagnetic exchange is across adjacent cation planes, and a tiny net magnetic moment is due to spin canting. The structure of the other end member, ilmenite (FeTiO₃, a = b = 5.18 Å, c = 14.27 Å), can be derived from the hematite structure, where every other (0001) layer of Fe³⁺ is replaced by a layer of nonmagnetic Ti⁴⁺ cations, whereby the symmetry is reduced to $R\bar{3}$.¹⁰ For charge compensation, the remaining Fe has to change accordingly the oxidation state to Fe²⁺. Antiferromagnetic exchange in ilmenite is across next-nearest cation planes (Fe²⁺ to Fe²⁺), which explains the low Neel temperature of (T_N = 58 K) compared to hematite (T_N = 680 K). The various

magnetic properties of the solid-solid solution $(1-x)\text{Fe}_2\text{O}_3 \cdot x\text{FeTiO}_3$ depend on the degree of ordering of the cations. Ti-doped hematite ($x \sim 0.1$) was suggested as ferrimagnetic semiconductor with magnetic transition temperature up to 1000 K, provided that Ti atoms order on alternate cation layers.¹¹ However, energy differences between ordered and randomly arranged Ti impurities are small¹²⁻¹⁴, so that the expected magnetic moment of $0.5 \mu_B/\text{Ti}$ for $x = 0.15$ is not straightforward to realize experimentally. Ordering is preferred in solid-solid solutions for $0.5 > x > 0.73$ and leads to ferrimagnetism with Néel temperature (T_N) above 300 K.² Therefore, a number of recent efforts have gone into growing thin films in the compositional range $0.5 > x > 0.8$, mostly on $\alpha\text{-Al}_2\text{O}_3$ substrates¹⁵⁻²⁵ and lately also on $\text{SrTiO}_3(001)$ substrates.^{26,27}

Hematite and ilmenite, when forming heterointerfaces with each other, give rise to a strongly ferrimagnetic contact layer²⁸, which plays a crucial role in explaining the high and stable natural remanence in massive rocks where nanoscale exsolution lamella of ilmenite occur in a hematite host (or vice versa).^{29,30} Rocks with abundant hematite-ilmenite exsolution lamella are known to have a saturation magnetization more than twenty times that of pure hematite (2 kAm^{-1}) and may produce a giant exchange bias of 1 T.^{31,32} The interface between $\alpha\text{-Fe}_2\text{O}_3(0001)$ and $\text{FeTiO}_3(0001)$ has a polar discontinuity (disruption of charge neutrality), which is compensated by a disproportionated $\text{Fe}^{2+}/\text{Fe}^{3+}$ contact layer.³³ The mixed valence layer of $\text{Fe}^{2+}/\text{Fe}^{3+}$ is strongly antiferromagnetically coupled to the next Fe^{3+} cation layer of hematite, yielding a net ferrimagnetic moment.^{28,33} Below T_N of ilmenite, this interface layer moment is exchange coupled to ilmenite, which explains the occurrence of exchange bias.³⁴⁻³⁶

So far, it is not studied what happens when ilmenite is replaced by Ti-doped hematite $\text{Fe}_{2-x}\text{Ti}_x\text{O}_3$ ($x < 0.5$) where $\text{Fe}^{2+}/\text{Fe}^{3+} < 1$. In that case, the $\text{Fe}^{2+}/\text{Fe}^{3+}$ gradient would be shallower across the chemical boundary. To explore such a chemically less abrupt interface, we have used MBE to grow thin films (~ 25 nm thickness) of $\alpha\text{-Fe}_2\text{O}_3$ on sapphire substrates ($\alpha\text{-Al}_2\text{O}_3$) with a (0001) orientation, which after annealing were capped with a ~ 25 nm thick $\text{Fe}_{2-x}\text{Ti}_x\text{O}_3$ layer ($x \sim 0.44$). The growth conditions of hematite and magnetite (Fe_3O_4) layers had been previously investigated by in-situ surface XRD and by Raman spectroscopy.³⁷ The bilayer thin films were characterized in the present work in-situ by surface XRD. Raman spectroscopy was used to analyze the formation of $\text{Fe}_{2-x}\text{Ti}_x\text{O}_3$ layers which could not be distinguished from hematite by XRD

due to limited resolution and strain in the layers. Detailed chemical and structural analysis on the atomic scale was performed by TEM. To determine the magnetic properties of the Fe-Ti-O systems and the interfaces between hematite and Fe_{2-x}Ti_xO₃ layers we used SQUID measurements.³⁸ These measurements revealed an increased magnetic moment of the layers containing Ti compared to pure hematite films.

7.1.2 Experimental details

Thin film growth

Thin films of hematite and Fe_{2-x}Ti_xO₃ were grown on (0001) single crystal sapphire substrates (α -Al₂O₃, $a = b = 4.76 \text{ \AA}$, $c = 12.99 \text{ \AA}$) by MBE using a rotating substrate holder. The substrate was annealed for 12 h at 1400 °C in air. After this treatment atomic force microscopy (AFM) images showed very large atomically smooth terraces. The substrate samples were further annealed for 12 h at 300 °C in ultra-high vacuum (UHV), and finally annealed for 90 min at 600 °C in an O₂-atmosphere ($p_{O_2} \approx 2 \cdot 10^{-8} \text{ mbar}$).^{37,38} Ar⁺ ion bombardment was not applied as radiation damages and Ar cannot be completely removed by annealing. Low energy electron diffraction (LEED) pictures displayed the (1x1) structure and some background. The TEM images showed later that obviously not all impurities, probably water or OH groups, were removed by annealing up to 600 °C. A perfect heteroepitaxial growth of Fe₂O₃ films on Al₂O₃ substrates does not occur due to the large lattice mismatch. The Fe₂O₃ films are distorted by misfit dislocations at the interface and the films are usually polycrystalline. Better hematite layers can be grown with a Cr₂O₃ buffer layer¹³, this has not been applied here because for the investigation of the hematite-ilmenite interface the existence of a second interface and possible interdiffusion might have caused additional uncertainties in the magnetic measurements: bulk Cr₂O₃ is an antiferromagnet but weak ferromagnetism has been reported for small particles, increasing with decreasing particle size.³⁹

The growth experiments were performed in an UHV X-ray diffractometer with a rotating anode as X-ray source allowing in-situ monitoring of the formation of oxide layers. The preparation of thin films of Fe₂O₃ and Fe_{2-x}Ti_xO₃ followed the procedure described previously³⁷ by MBE evaporating iron in O₂-atmosphere, $p_{O_2} = 2 \cdot 10^{-6} \text{ mbar}$. The Fe_{2-x}Ti_xO₃ layers were prepared by simultaneous deposition of Fe and Ti in an O₂-atmosphere similar to the preparation of hematite layers. The growth rate was

controlled by a flux monitor and a quartz microbalance and varied between 0.3 and 0.5 nm/min. The substrate was rotated around its surface normal to ensure a uniform coverage. The substrate temperature during evaporation was varied between 300 °C and 600 °C for different samples in order to study the influence of temperature on the growth process. The Fe-oxide phases formed at various growth conditions have been investigated in-situ by XRD and later ex-situ by Raman spectroscopy. The alternate deposition of Fe and Ti layers with subsequent oxidation did not lead to ilmenite layers but to the formation of hematite-ilmenite solid solutions. This is related to enhanced interdiffusion at elevated temperatures and is probably also associated with a growth process via island formation.³⁷ Different samples with FeTiO₃ layers, and composite layers consisting of hematite and Fe_{2-x}Ti_xO₃ layers were prepared in order to study the influence of the interface between hematite and Ti-doped hematite or Ti-lean ilmenite, respectively, on the magnetic properties. In all samples with Fe_{2-x}Ti_xO₃ layers a pure Fe₂O₃ film was deposited first. The sample was annealed afterwards at 400 K in oxygen at $p_{O_2} = 5 \cdot 10^{-5}$ mbar for 30 min to minimize the magnetite content. Then the growth continued with a Fe and Ti deposition in $p_{O_2} = 2 \cdot 10^{-6}$ mbar. The samples with a 25 nm Fe₂O₃ layer and a thin Ti_{1-x}O₂ layer were prepared by depositing hematite first, then 0.4 nm of Ti alone and finally a cap of Fe₂O₃.

XRD

Surface XRD measurements were performed in-situ on a six circle X-ray diffractometer.⁴⁰ An 18 kW rotating anode and Cu K α -radiation were used while the base pressure of the chamber was better than 10⁻¹⁰ mbar.

Raman spectroscopy

Raman spectra were acquired in air with a confocal Raman microscope (alpha300 R, WITec GmbH, Ulm, Germany) with a lateral resolution of about 400 nm and an axial focus of about 1 μ m. A long-pass edge filter was used to reject the shorter wave lengths as well as the elastically scattered photons (Rayleigh scattering and reflection). Spectra were acquired by a lens-based spectrometer with a CCD-camera (1024 x 128 pixel cooled to -65 °C) with a resolution of 3.7 cm⁻¹ per pixel of the detector using a 600 mm⁻¹ grating. For image acquisition 10 μ m x 10 μ m maps were obtained by scanning the sample while recording Raman spectra at each pixel of the image.

Magnetic measurements

Magnetization measurements were performed with a SQUID magnetometer (MPMS XL7) from Quantum Design with fields between $\mu_0H = -7$ T and $\mu_0H = +7$ T. The sample temperature was varied between 4 K and 300 K. For the measurements with the SQUID magnetometer the sample was cut in 5x5 mm pieces with a diamond wire saw and carefully cleaned, the sample surface was orientated parallel to the external field. The diamagnetic signal from the Al₂O₃ substrate has been subtracted in all diagrams.

TEM sample preparation

The TEM sample preparation was done by focused ion beam using a FEI Strata 400s dual-beam FIB microscope according to the in-situ lift-out method followed by low energy ion polishing.⁴¹ C, and Pt (were deposited in this order on the thin films) were used as protection layers and Ga⁺ ions for milling, thinning and polishing. The parameters for cutting and cleaning at 30 kV were 0.28 nA to 28 pA. The final low kV polishing was done at 5 kV and 16 pA and at 2 kV and 10 pA, respectively. The angle of incidence was $\sim 1^\circ$ at 30 kV and $5-7^\circ$ at lower kV's. Very gentle conditions (i.e. low ion energies) were chosen to avoid Ga⁺ implantation or material damage. For the hematite and ilmenite reference samples the respective powder or crystals were ground and solved in ethanol. Afterwards the powder was dropped on a copper grid coated with a holey carbon film.

TEM

For TEM measurements a FEI Titan 80-300 S/TEM TEM with a field emission gun, a Gatan Tridiem image filter and an EDAX EDX detector for analytical measurements was employed. Diffraction patterns were recorded with a Gatan UltraScan 1000 (2k × 2k) CCD camera. For STEM imaging a HAADF detector from Fischione Instruments (Model 3000) was used. After plasma cleaning for 1 min, the TEM measurements were performed at 300 kV. The sample was mounted on a double tilt holder with a maximum tilt angle of 30°. EELS measurements were performed in STEM mode using an electron probe $< 3 \text{ \AA}$ with a convergent angle of 13.3 mrad. Dispersions of 0.1 and 0.3 eV/channel were chosen, leading to a FWHM of around 1 eV. A 2 mm entrance aperture, a collection angle of 13.5 mrad and camera lengths of 102 and 128 mm were used. HRTEM studies

were additionally performed using a monochromated and (image) aberration corrected FEG-S/TEM FEI Titan 80–300 kV.

EELS data analysis

The channel-to-channel gain variation and dark current correction were done for all EEL spectra.⁴² The background was approximated by a power-law fit and subtracted from the original data. For quantification the scattering cross-section was calculated using the Hartree-Slater-model^{42–44} as implemented in Gatan Digital Micrograph. The width of the integration windows was chosen to be 25 eV for the Ti-L_{2,3}-edge and 40 eV for the O-K- and Fe-L_{2,3}-edges. Several measurements were done on different grains, grain boundaries and interfaces. For the quantification of the chemical composition of each area 10 to 20 spectra were used. Since an absolute energy scale of the edge onsets is difficult to determine, we instead compared the relative peak distances between the different edges. Numerical and analytical analysis of the EEL spectra was done with Wolfram Research Mathematica 9.0.1. To gain information about the valence of Fe, the spectra were treated as follows for quantification. Symmetric integration intervals with widths of 4 eV were defined around the L₃ and L₂ maxima. 4 eV was chosen since within this interval the slopes of the peaks are dominant compared to the SNR. Within these intervals, all intensities were added. For each sample, several L₃/L₂-ratios were calculated in this way, allowing the determination of both mean values and standard deviations. The ratios of the L₃ and L₂ areas give an indication of the oxidation state.⁴⁵

7.1.3 Results and discussion

Thin film growth

First the growth conditions were investigated. Depending on substrate temperature and oxygen pressure hematite and magnetite phases have been observed.^{37,38} The results showed that in the temperature range between 400 °C and 500 °C predominantly hematite is formed; the Raman spectrum showed a mixture of magnetite and hematite. At both, lower and higher substrate temperatures (300 °C and 600 °C) only magnetite was observed. After post-annealing in an O₂-atmosphere of 5·10⁻⁵ mbar only hematite was detectable in the Raman spectrum. Nevertheless, XRD and TEM showed that

magnetite could not be completely removed by post-annealing in an O₂-atmosphere. The films investigated in the present study were grown at 400 °C.

Various samples were prepared and investigated by magnetization and X-ray measurements. The results from three samples are shown here which are named as follows

- sample 1: 25 nm Fe₂O₃
- sample 2: 25 nm Fe₂O₃ + 0.4 nm Ti_{1-x}O₂ + 3 nm Fe₂O₃
- sample 3: 25 nm Fe₂O₃ + 25 nm Fe_{2-x}Ti_xO₃ + 3 nm Fe₂O₃.

All samples were prepared at the same growth conditions and were annealed in an O₂-atmosphere after preparation. XRD data for Fe_{2-x}Ti_xO₃ layers were similar to those with Fe₂O₃. An increase of the lattice constant could not be resolved by the X-ray measurements. The reflections are slightly broadened due to strain in the films and the diffraction angles slightly deviate from the bulk positions. Reflections occurring only in the space group $R\bar{3}$ could not be detected within the detection limit and we therefore assume a solid solution with space group $R\bar{3}c$ has been grown.

Figure 7.1.1a shows the XRD patterns from the film with 25 nm Fe₂O₃ + 25 nm Fe_{2-x}Ti_xO₃ + 3 nm Fe₂O₃ (sample 3) along the (0, 0.94, L)-rod and along the (0.9451, 0, L)-rod of Al₂O₃. On the former the (311) reflection of an epitaxially grown grain of Fe₃O₄(111) appears. The relation between the reciprocal lattices of Al₂O₃, Fe₂O₃ and Fe₃O₄ is shown in Figure 7.1.1b. Weak peaks belonging to grains with different orientation were also observed. Hematite grew on α -Al₂O₃(0001) with two different orientations: $[1000]_{Fe_2O_3} \parallel [1000]_{Al_2O_3}$ and another one rotated by 60° with $[0100]_{Fe_2O_3} \parallel [1000]_{Al_2O_3}$. The rotation by 60° corresponds to a stacking fault of the cations across the interface. While the X-ray observations indicated nearly heteroepitaxial growth, the TEM images revealed that the films were much less perfect and grains with various orientations formed. These obviously contribute to the background in the X-ray measurements and are less visible than the heteroepitaxially grown parts. Due to the limited resolution of our XRD measurements a peak shift due to an increase of the lattice constant after adding the Ti could not be detected.

Most XRD peaks observed in the L-scans not belonging to corundum or hematite could be assigned to Fe₃O₄(111) heteroepitaxially grown on α -Al₂O₃(0001). However, we discovered peaks that did not match the crystallographic directions expected for heteroepitaxial growth but agree with magnetite by their diffraction angles. Furthermore, we found the lattice constants of Fe₂O₃ and Fe₃O₄ to be strained by 1 to 2 %. We also cannot exclude that small amounts of maghemite (γ -Fe₂O₃) were formed during growth.

In order to investigate the effect of additional annealing in oxygen, the samples that were grown at a substrate temperature of 400 °C were annealed at 400 °C in an O₂-atmosphere ($p_{O_2} \approx 10^{-5}$ ·mbar) for 60 minutes. There were no significant changes in the XRD data after post-annealing except for a slight increase in the intensity along the (0,0.94,L)-rods between the Bragg points while the background intensity remained constant. This implies that magnetite is still present and that the degree of order of the surface had increased.

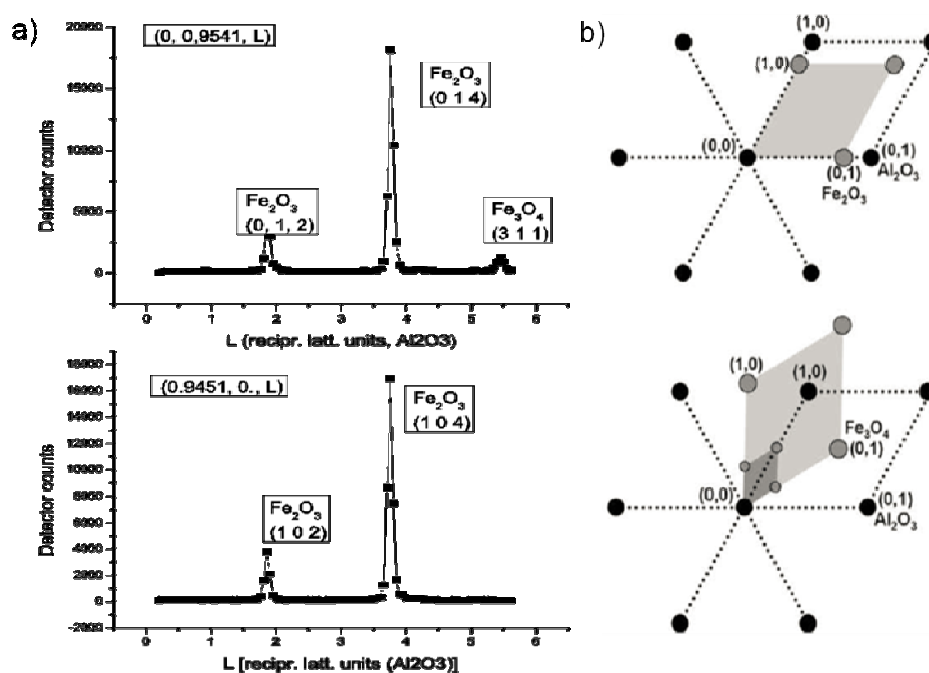


Figure 7.1.1. a) L-scans of sample 3 along the hematite (01L) and (10L) rod. The L-scale is related to the Al₂O₃ c-lattice constant. The {012} and {014} reflections occur on (01L) and (10L), respectively. This indicates the presence of two domains, one with a stacking fault in the interface. The peak at (0, 0.9451, 5.4) corresponds to a grain of Fe₃O₄ grown heteroepitaxially with Fe₃O₄(111) \parallel Al₂O₃(0001). Further reflections from Fe₂O₃ and Fe₃O₄ in non-epitaxial directions were also observed. b) Reciprocal relation between the reciprocal lattices of Al₂O₃, hematite and magnetite.

TEM measurements indeed revealed the presence of magnetite (Figure 7.1.2a, sample 1). In Figure 7.1.2 TEM images of sample 1 and 2 are shown. The textured growth is confirmed by TEM. Figure 7.1.2b shows a HAADF-STEM image of a heteroepitaxial hematite grain (sample 2) and the HRTEM image in Figure 7.1.2c a region of the hematite film with a non-epitaxial grown grain (sample 1). The X-ray and TEM results are consistent, although without TEM the X-ray measurements could lead to the conclusion that heteroepitaxial growth occurred. These findings are supported by earlier investigation on the growth of Fe-oxide layers on Al₂O₃(0001).^{46,47}

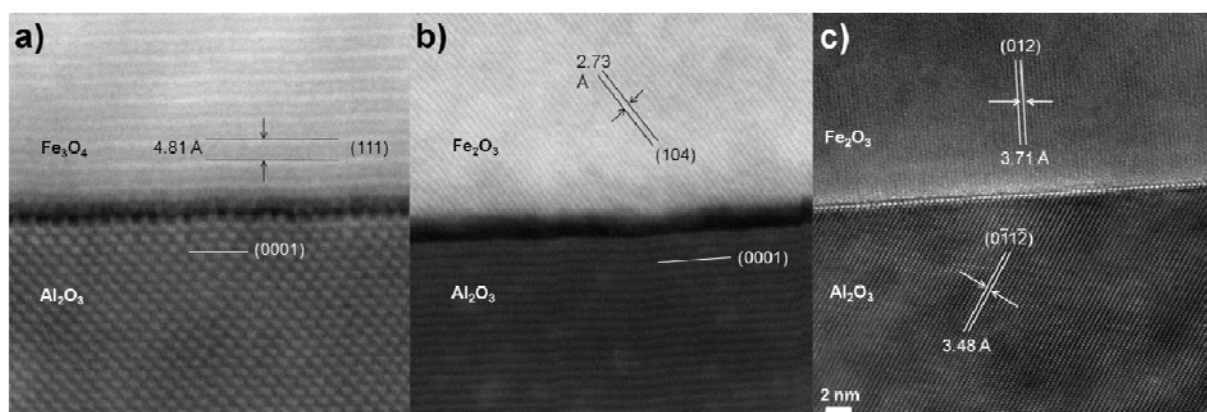


Figure 7.1.2. Interface between the substrate and the hematite thin film (sample 1 and 2). a) The STEM image reveals the presence of (111) magnetite planes parallel to the (0001) of Al₂O₃ when observed in $[2\bar{1}\bar{1}0]$ viewing direction (sample 1), b) STEM image of an epitaxial hematite grain with the (104) plane rotated about 30° (sample 2) in $[10\bar{1}0]$ viewing direction and c) HRTEM image of a non-epitaxial grown region of the hematite film (sample 1) in $[2\bar{1}\bar{1}0]$ viewing direction.

Raman spectroscopy

Raman spectra of the Fe_{2-x}Ti_xO₃ layers and a comparison with reference spectra from synthetic FeTiO₃ with the ideal composition, and a natural ilmenite samples with excess iron are presented in Figure 7.1.3. Panel a) of Figure 7.1.3 shows Raman spectra of layers with different Ti content, panel b) a Raman spectrum of a hematite layer with the characteristic peak at 1300 cm⁻¹ together with reference spectra from synthetic and natural ilmenite samples. Panel c) shows the sample with excess Ti in comparison with synthetic FeTiO₃.

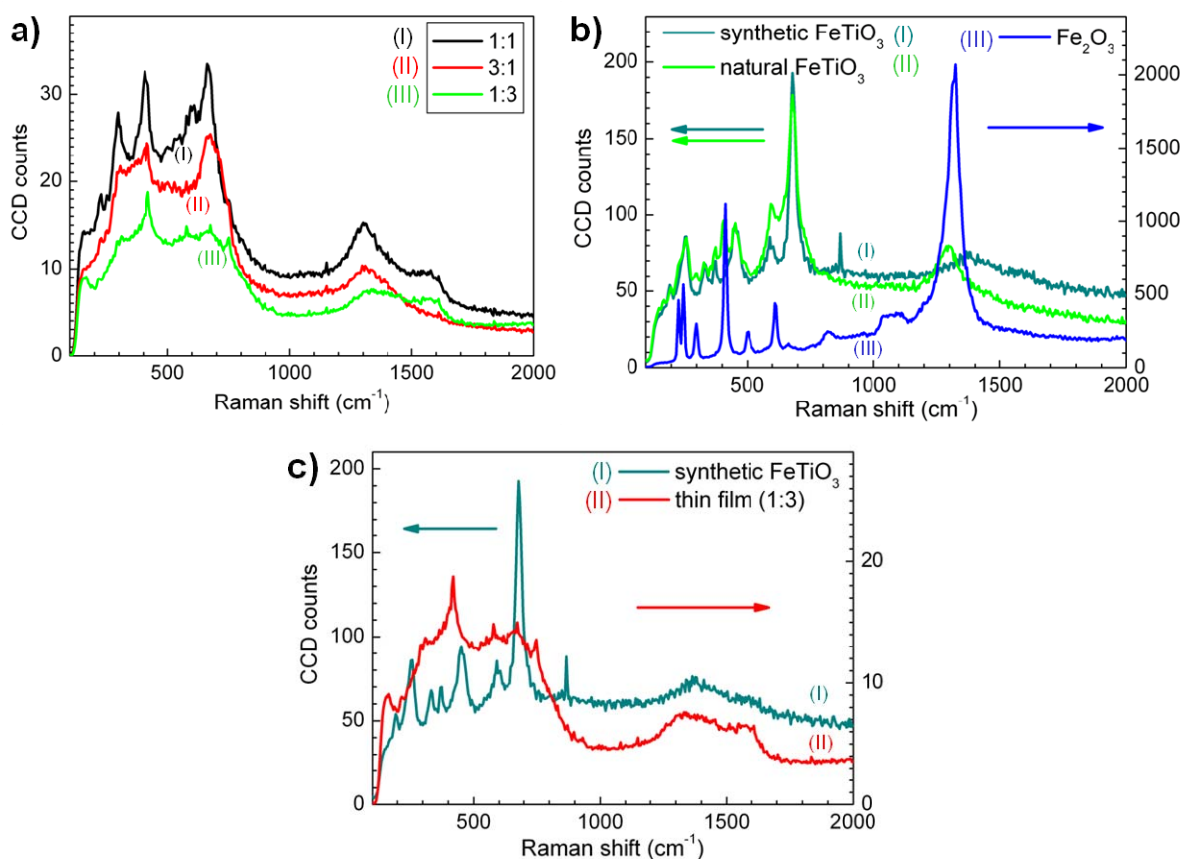


Figure 7.1.3. Raman spectroscopy. a) Raman spectra of films grown by simultaneous deposition of Fe and Ti with different relations of Fe:Ti as derived from the calibration by the quartz microbalance. **b)** Comparison of a synthetic FeTiO₃ sample, a natural ilmenite sample with excess Fe and a hematite sample. **c)** Comparison of a synthetic FeTiO₃ sample with the layer grown with a nominal relation 1:3 of Fe:Ti.

Sample 3 discussed here was grown with the nominal relation 1:1 (black curve in Figure 7.1.3a) resembling the closest similarity with the ilmenite spectrum and the characteristic peak at 700 cm⁻¹ characteristic for ilmenite. The EELS measurements in the TEM investigations showed that Fe_{2-x}Ti_xO₃ layers were in fact grown with $x \approx 0.44$. The Raman spectra of this sample evinced features of both, hematite and ilmenite and show clearly that the local symmetry differs from that of pure hematite. A comparison with reference spectra of a hematite-ilmenite solid solution is not available. Therefore the possibility remains that the sample is disordered. However, we conclude from the ilmenite like features in the Raman spectra that the layer is partially ordered and not a completely disordered solid solution of hematite-ilmenite.

Nanoscale chemical and structural analysis

TEM images of the grown films reveal the presence of two layers (Figure 7.1.4a). In addition, a C protection layer is visible which was deposited in the FIB microscope to prevent damage during the specimen preparation procedure. The TEM images show a thickness of 25 – 30 nm for each layer indicating that the calibration of the evaporation sources by the quartz microbalance was not sufficiently precise. The rough surfaces of the hematite/Fe_{2-x}Ti_xO₃ interface and Fe_{2-x}Ti_xO₃ surface can be attributed to island growth. The formation of islands of hematite on alumina during the growth process has been reported before.³⁷ The contrast in the TEM image results from diffraction and thickness contrast. The grain size in both layers is in the range of 10 – 30 nm. The diffraction patterns (inserted in Figure 7.1.4a), which were acquired over the lower and upper layer of the thin film, illustrate that the film is polycrystalline. For the acquisition of the pattern, a SAD aperture was placed in the upper part of the film (Fe_{2-x}Ti_xO₃ and C) and in the lower part of the film (hematite and Al₂O₃). Accordingly, spots from these phases are present in the respective diffraction patterns. The diffraction patterns show that the film was not single crystalline. With diffraction experiments and fast Fourier transform (FFT) analysis differentiation between the hematite and an ilmenite structure was not possible considering an error of 3% for diffraction pattern analysis. However, in the Fe_{2-x}Ti_xO₃ layer reflections belonging only to the hematite crystal structure could be observed. This confirms the assumption of the XRD measurements that this layer has a space group of $R\bar{3}c$. EDX measurements were acquired from the hematite and the Fe_{2-x}Ti_xO₃ layer (Figure 7.1.4b and c). Both spectra reveal that the film consists of Fe and O for the lower layer and of Fe, Ti and O for the upper layer. C results from the protection layer on top of the sample and Si is attributed to impurities in the Al₂O₃ substrate and to the EDX detector.

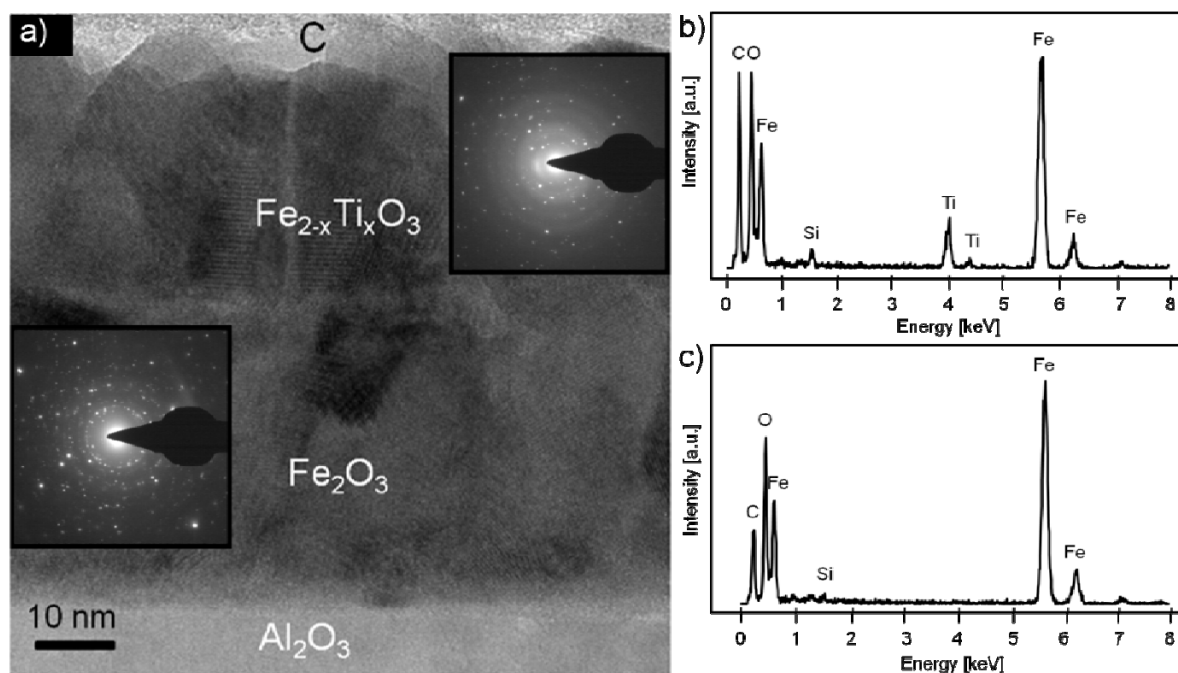


Figure 7.1.4. a) TEM image of the thin film on Al₂O₃ (sample 3). The diffraction patterns (inserted images) show that the film is polycrystalline. The EDX spectra were taken in the Fe_{2-x}Ti_xO₃ layer (b) exhibiting the elements Fe, Ti, and O and over the hematite layer (c) showing the elements Fe and O. C is from the protection layers and Si most likely from impurities of the substrate and the EDX detector.

There are some conceivable reasons why the thin film was not epitaxial. On one hand the interface between Al₂O₃ and hematite was not atomically smooth and on the other hand there might have been impurities like Si or water on top of the Al₂O₃ during growth. In the HRTEM image (Figure 7.1.5a) the interface between the Al₂O₃ substrate viewed along the (0001) basal plane and the hematite layer are shown. The HAADF-STEM image (Figure 7.1.5b) confirms that the Al₂O₃/hematite-interface is not atomically abrupt and EDX measurement (Figure 7.1.5c) reveals the presence of Si and C. O is not visible in these images only Al and Fe appear as atomic columns. The interface exhibits a dark contrast in the HAADF-STEM image indicating light elements like H and O. The second reason is the relatively large lattice mismatch of 6% between Al₂O₃ and hematite. DFT calculations have shown that the strong compressive strain makes the growth of Fe_{2-x}Ti_xO₃ on Al₂O₃(00001) energetically unfavorable.³³ To overcome this high energy cost, the first layers of thin films tend to buckle or roughen in the beginning of the growth. All this affects epitaxial growth and leads to random orientations of the crystalline grains.⁴⁸

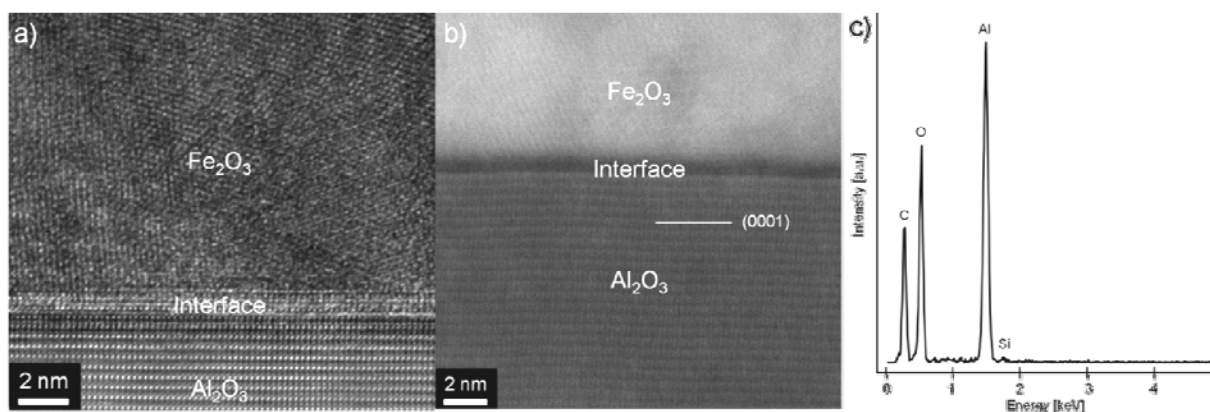


Figure 7.1.5. a) HRTEM image of the interface between substrate and the hematite layer viewed along $[10\bar{1}0]$, b) HAADF-STEM image of the same interface and c) the resulting EDX spectrum. The EDX spectrum confirms the presence of Si coming from impurities of the substrate and the EDX detector. C is due to the protection layers.

Further investigations concerning the chemical composition of the sample were done by EELS measurements in STEM-mode. EELS as a method for analyzing different oxidation states of elements is well established, e.g. in iron oxide systems. The ELNES of the two layers ($\text{Fe}_{2-x}\text{Ti}_x\text{O}_3$ and hematite) and the interface between them were analyzed and compared to an ilmenite and a hematite reference. Figure 7.1.6 shows a HRTEM image (a) of the area of interest and the corresponding EEL spectra (b - d). The hematite and $\text{Fe}_{2-x}\text{Ti}_x\text{O}_3$ layer were quantified via EELS. The average chemical composition of the hematite layer is Fe:O = 44:56 (at.%) with an error of $\pm 3 - 5$ at-% which is in good agreement with the chemical composition of hematite. The average chemical composition of the $\text{Fe}_{2-x}\text{Ti}_x\text{O}_3$ layer is Fe:Ti:O = 36:10:54 (at.%) with an error of $\pm 3 - 5$ at.%. This nonstoichiometric ratio corresponds to a $\text{Fe}_{2-x}\text{Ti}_x\text{O}_3$ layer with $x = 0.44$. The alternate deposition of Fe and Ti layers with subsequent oxidation did not lead to ilmenite layers, but rather led to the formation of hematite layers probably because the growth does not proceed layer by layer but by island formation. The interface area of the two layers was quantified as well, leading to a ratio of Fe:Ti:O = 43:2:55 (at.%) with an error of $\pm 3 - 5$ at.% for Fe and O and ± 1 at.% for Ti. The Ti concentration decreased drastically compared to the $\text{Fe}_{2-x}\text{Ti}_x\text{O}_3$ layer.

For a deeper insight into the electronic structure of the different areas the ELNES were analyzed (Table 7.1.1). The Ti-L_{2,3}-edge of both the ilmenite reference (green) and the $\text{Fe}_{2-x}\text{Ti}_x\text{O}_3$ layer (red) was detected around 460 eV (Figure 7.1.6b). The characteristic features, the white lines of the Ti-L_{2,3}-edge, are labeled A and B. The general shapes of

the ELNES and the relative peak distances A to B of the two samples are in good agreement. In general, feature A exhibits a lower intensity than feature B. For the Fe_{2-x}Ti_xO₃ layer and the ilmenite reference A and B are separated by 5.1 eV (Table 7.1.1). The two spectra differ slightly concerning the weakly resolved peak splitting (in our case only visible as a shoulder) for features A and B. For the ilmenite reference the splitting is more pronounced than in the Fe_{2-x}Ti_xO₃ spectra. This can be ascribed to a lower amount of Ti in the analyzed Fe_{2-x}Ti_xO₃ layer and differences in the O octahedra surrounding the Ti ions.

Figure 7.1.6c shows the O-K-edges of the two reference samples and the two layers at around 540 eV. The spectrum of the hematite reference is colored in black, the hematite spectrum in blue, the Fe_{2-x}Ti_xO₃ layer in green and the ilmenite reference in red. Features A, B and C can be found in all four spectra. The relative peak distances for A to B and B to C are between 10.2 and 10.8 eV and 24 to 24.9 eV, respectively (Table 7.1.1). The ELNES of the ilmenite reference exhibits the most distinctive difference. The splitting of 1.8 eV of feature A cannot be found in the other three spectra. This indicates that the Fe_{2-x}Ti_xO₃ layer has a slightly different electronic environment than the ilmenite reference. It rather resembles the spectra of hematite. This is once more most likely due to the lower amount of Ti in the Fe_{2-x}Ti_xO₃ layer.

The Fe-L_{2,3}-edge (green for the ilmenite reference, red for the Fe_{2-x}Ti_xO₃ layer, blue for the hematite layer and black for the hematite reference) at around 708 eV is shown in Figure 7.1.6d. The white lines labeled A and B were detected in all four spectra. The relative peak distance of A to B is between 12.9 and 13.5 eV (Table 7.1.1) and the general shape of the ELNES of all four spectra show no obvious deviation. The intensities of the white lines showed no clear disparity.

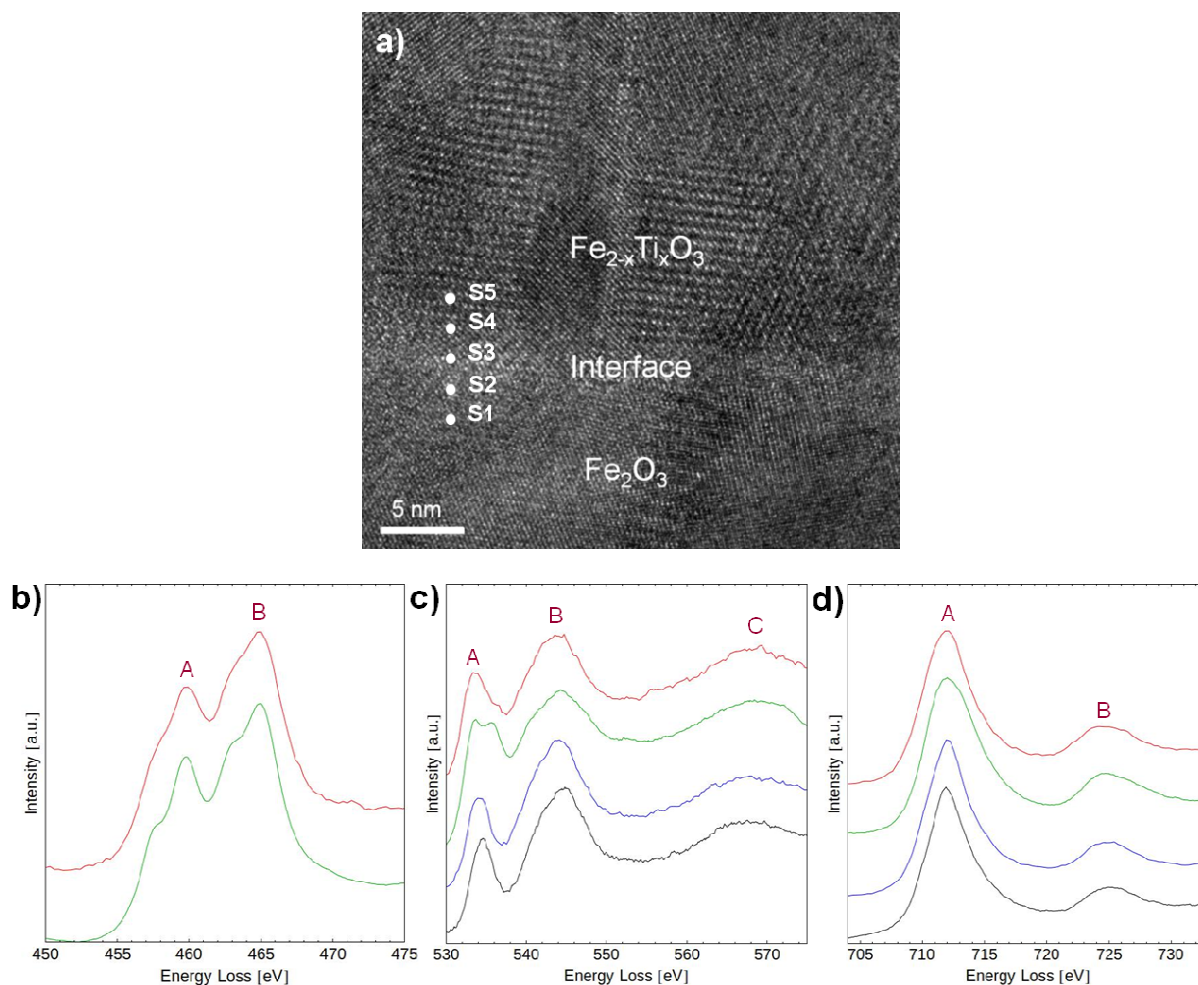


Figure 7.1.6. a) HRTEM image of the interface between the hematite and the $\text{Fe}_{2-x}\text{Ti}_x\text{O}_3$ layer exhibiting a grain boundary and EEL spectra (from top to down) of the $\text{Fe}_{2-x}\text{Ti}_x\text{O}_3$ layer (red), the ilmenite reference (green), the hematite layer (blue) and the hematite reference (black) showing the Ti-L_{2,3}- (b), O-K- (c), and Fe-L_{2,3}-edges (d). S1 to S5 in the HRTEM image denote the EELS spot measurements.

Furthermore, the L₃ to L₂ ratio of the Fe-L_{2,3}-edge was analyzed where no considerable difference, neither for the ilmenite reference (2.5 ± 0.1) and $\text{Fe}_{2-x}\text{Ti}_x\text{O}_3$ layer (2.4 ± 0.2) nor for the hematite reference (2.2 ± 0.2) and hematite layer (2.5 ± 0.2) could be found (Table 7.1.1). These results can be explained by the small Ti-content within the $\text{Fe}_{2-x}\text{Ti}_x\text{O}_3$ layer. The signal of the Fe-L_{2,3}-edge in the $\text{Fe}_{2-x}\text{Ti}_x\text{O}_3$ layer is dominated by the contribution of Fe³⁺ and less from Fe²⁺. The energy difference between the onset of the O-K-edge and the onset of the Fe-L₃-edge deviates by 1.8 ± 0.3 eV for ilmenite (177.4 ± 0.3 eV) and the hematite reference (179.2 ± 0.3 eV). The energy difference is 179.4 ± 0.3 eV for the $\text{Fe}_{2-x}\text{Ti}_x\text{O}_3$ layer and 179.5 ± 0.3 eV for the layer indicating that both layers exhibit the hematite structure (Table 7.1.1). The FWHM of the Fe-L₃-edge for

the four spectra is 5.7 eV for the ilmenite reference, 4.2 eV for the hematite reference, 4.8 eV for the Fe_{2-x}Ti_xO₃ layer and 4.2 eV for the hematite layer (Tab. 7.1.1). The values of the FWHM of the two analyzed layers are closer to that of the hematite reference value which has a difference of 1.5 eV to the ilmenite reference value, denoting the hematite structure for the two layers.

Table 7.1.1. Distances of the ELNES features A, B and C of the Ti-L_{2,3}-, O-K- and Fe-L_{2,3}-edges, distances of the onset of the O-K-edge to the onset of the Fe-L₃-edge, Fe-L₃ to Fe-L₂ ratio and FWHM values of the ilmenite reference, Fe_{2-x}Ti_xO₃ layer, hematite layer and hematite reference.

Properties Samples	A → B Ti; O; Fe [eV]	A → C O-K [eV]	O-K → Fe-L ₃ [eV]	Fe-L ₃ / Fe-L ₂	FWHM [eV]
FeTiO ₃ ref.	5.1 ; 10.2 ; 12.9	24.9	177.4 ± 0.3	2.5 ± 0.1	5.7
Fe _{2-x} Ti _x O ₃ layer	5.1 ; 10.8 ; 12.9	24.9	179.4 ± 0.3	2.4 ± 0.2	4.8
Fe ₂ O ₃ layer	--- ; 10.2 ; 13.2	24	179.5 ± 0.3	2.5 ± 0.2	4.2
Fe ₂ O ₃ ref.	--- ; 10.5 ; 13.5	24.3	179.2 ± 0.3	2.2 ± 0.2	4.2

Spot measurements (< 3 Å in diameter) were acquired across the interface, from the Fe_{2-x}Ti_xO₃ layer to the hematite layer. Since the Fe-L₃-edge has a significantly higher intensity, resulting in a better SNR compared to that of the L₂-edge, only the L₃-edge was analyzed in this way. To visualize the rather small Fe²⁺-L₃-edge contribution, the energy scales of all spectra were shifted such that the descending slopes of the L₃-edge were on top of each other. To allow for this in spite of an energy dispersion of 0.3 eV, the spectra were interpolated using splines of order 1. Figure 7.1.7a shows the overlay of 5 spectra (S1 (green) is from the hematite layer, S2 (brown) closer to the hematite/Fe_{2-x}Ti_xO₃ interface, S3 (black) is from the interface, S4 (blue) slightly away from the interface from the Fe_{2-x}Ti_xO₃ layer and S5 (red) from the Fe_{2-x}Ti_xO₃ layer). A small broadening of the L₃-edge can be observed for the black spectra (S3) indicating an enrichment of Fe²⁺ at the hematite/Fe_{2-x}Ti_xO₃ interface. A spectrum gathered in pure hematite and therefore only showing a L₃-edge stemming from Fe³⁺ was then subtracted from the spectra. The remaining contributions to the L₃-edge are plotted in Figure 7.1.7b. The contribution of Fe²⁺ increases at the hematite/Fe_{2-x}Ti_xO₃ interface (black curve) clarifying the assumption of an enrichment at the interface. The appearance of a weak shoulder indicating the presence of Fe²⁺ has been also observed in minerals such as magnetite.^{49,50}

It is worth mentioning that the ilmenite and hematite references reveal the same features as the spectra reported in literature.^{51,52} However, the white line ratio values diverge due to different analysis methods such as a Gaussian fit procedure.

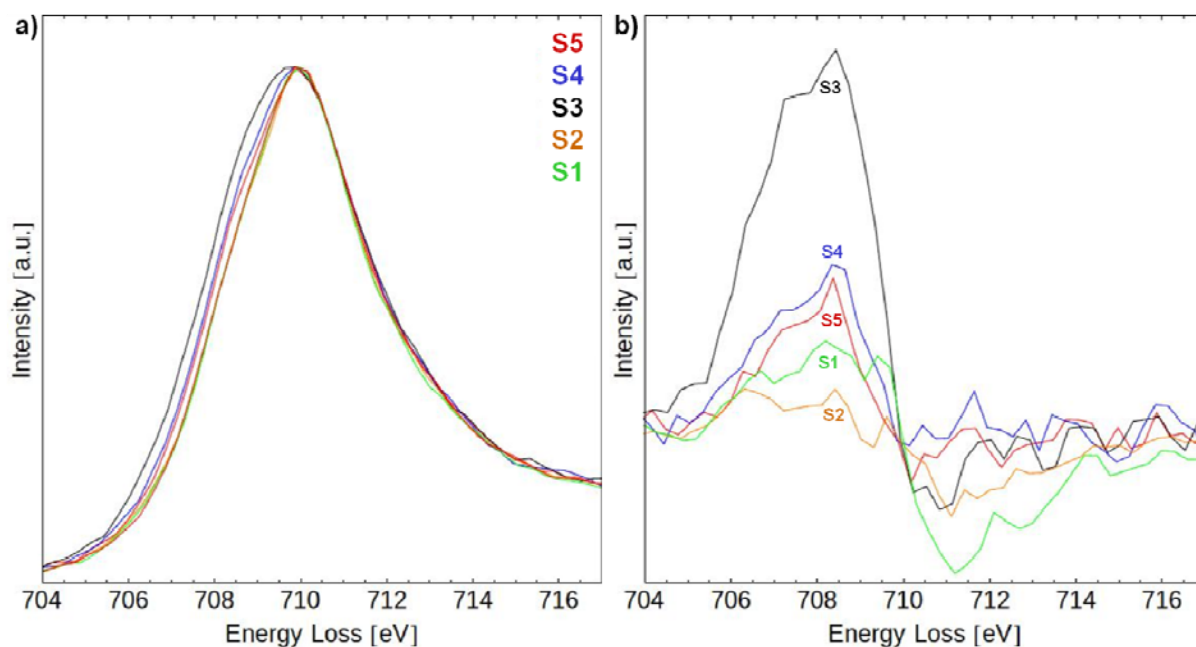


Figure 7.1.7. Fe-L₃-edges of the region around and on the hematite/Fe_{2-x}Ti_xO₃ interface. a) Overlay of 5 spectra (S1 (green) is from the hematite layer, S2 (brown) closer to the hematite /Fe_{2-x}Ti_xO₃ interface, S3 (black) from on the interface, S4 (blue) slightly away from the interface from the Fe_{2-x}Ti_xO₃ layer and S5 (red) from the Fe_{2-x}Ti_xO₃ layer). b) The 5 spectra after the removal of the L₃-edge stemming from Fe³⁺ showing the Fe²⁺ contribution of each region.

Compared to the literature, the EELS data is in good accordance concerning the relative peak positions, the absolute energy loss values, the general shapes and intensities for the Ti-L_{2,3}-, O-K- and Fe-L_{2,3}-edges (Table 7.1.1). The Ti-L_{2,3}- and the Fe-L_{2,3}-edges of ilmenite and hematite have been studied by Otten et al.⁵¹, where depending on the valence state of Ti, a small chemical shift was detected. This is also the case for hematite (Fe³⁺) and ilmenite (Fe²⁺). An overlap of the edges is observed for mixed oxidation states as is the case in our study. A chemical shift of the Fe-L_{2,3}-edge for different Fe valence states is also described by van Aken et al.^{50,52} They use iron oxide references to determine unknown Fe oxidation states. By analyzing the L₃/L₂ ratio of the Fe-L_{2,3}-edge the Fe³⁺ can be quantified with an accuracy of about ±0.02 to ±0.03. In our study the amount of Ti was small so that an obvious differentiation of the L₃/L₂ ratios of the

Fe-L_{2,3}-edges could not be seen, but a chemical shift of the Fe-L₃-edges at the hematite/Fe_{2-x}Ti_xO₃ interface was detected.

Magnetic properties of the thin films

To explore the influence of a thin Ti layer in hematite on the magnetic properties, SQUID measurements were performed on sample 1 (25 nm Fe₂O₃) and sample 2 (25 nm Fe₂O₃, then 0.4 nm Ti_{1-x}O₂ and a cap of 3nm Fe₂O₃). Both samples were annealed in O₂-atmosphere with $p_{O_2} = 5 \cdot 10^{-5}$ mbar after deposition of the Fe₂O₃ layer to reduce the magnetite content. As shown above the magnetite content could not be completely removed by annealing in O₂-atmosphere, and a quantitative interpretation of the magnetization measurements is therefore problematic. Nevertheless, the two samples prepared in the same way exhibit a significant increase of the magnetization in the sample 2, the amount of Ti in this sample corresponds to 2 atomic layers of Ti. Figure 7.1.8 and Figure 7.1.9 show the magnetization measurements of the two samples. The comparison of the remanent and saturation moments of the samples with and without Ti content revealed an increase of the magnetic moments. A similar increase has been observed in all other samples which had been investigated. Assuming that the magnetite content was similar in the different samples which were prepared under identical conditions, indicates that the presence of Ti induces the enrichment of Fe²⁺ at the bilayer interface consistent with theoretical calculations.¹⁴ The results of the ELNES investigations shown above were made on sample 3 and demonstrate the enrichment of Fe²⁺ at the interface. The small signal of Ti and Fe²⁺ in sample 2 which contained only 2 atomic layers of Ti could not be quantitatively evaluated but we assume that an enrichment of Fe²⁺ occurs in the same way and causes the increased magnetic moment.

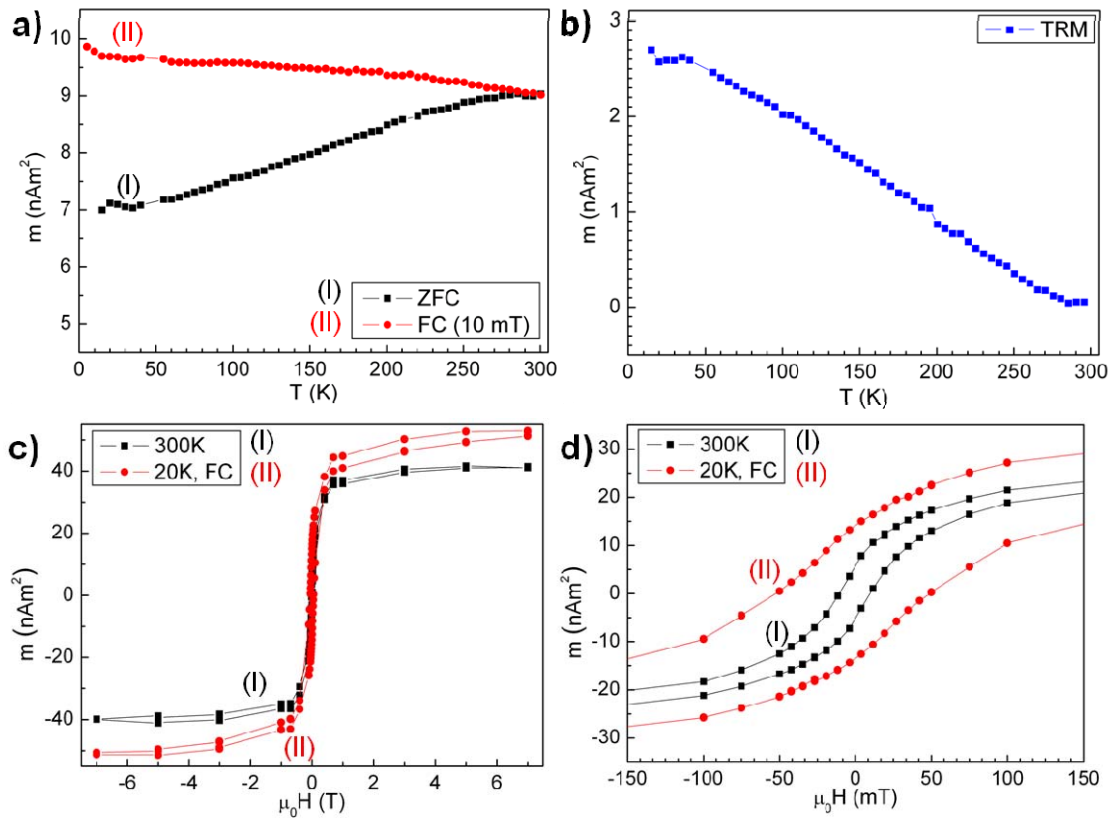


Figure 7.1.8. 25 nm Fe₂O₃ annealed in O₂ (sample 1). a) Temperature dependence of the magnetic moment after cooling in zero field and in external field of 10 mT. b) Remanent magnetic moment as a function of temperature. c) Magnetic moment as function of the external field at 300 K and 20 K. d) Enlarged section of c. All data were corrected for the diamagnetic contribution of the Al₂O₃ substrate.

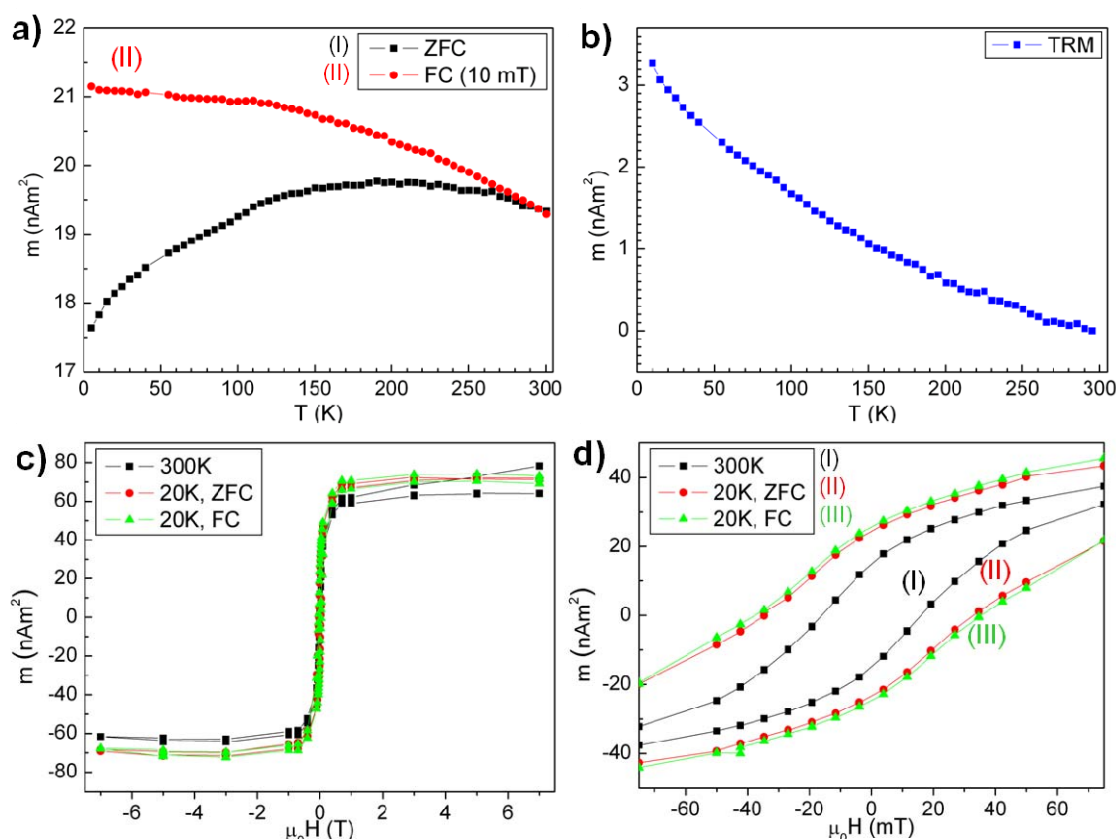


Figure 7.1.9. 25 nm Fe₂O₃ + 0.4 nm Ti_{1-x}O₂ + 3 nm Fe₂O₃ annealed in O₂ (sample 2). a) Temperature dependence of the magnetic moment after cooling in zero field and in external field of 10 mT. b) Remanent magnetic moment as a function of temperature. c) Magnetic moment as function of the external field at 300 K and 20 K. d) Enlarged section of c. All data were corrected for the diamagnetic contribution of the Al₂O₃ substrate. The points at 50 K are missing due to a signal arising from oxygen freezing out at this temperature as the vacuum was not completely free of oxygen.

The temperature dependency of the magnetic moments differs for the samples with and without Ti but shows no indication for a phase transition like the Morin transition in hematite around 263 K or the Verwey transition at about 120 K in magnetite. Most obvious is the increase of the saturation magnetization from about 50 nAm² of the hematite sample to about 65 nAm² of sample 2 with the Ti layer. Though sample 2 is only about 3 nm thicker than sample 1 the increase is significant.

The third sample consisted of 25 nm Fe₂O₃, 25 nm Fe_{2-x}Ti_xO₂ and a cap of 3 nm Fe₂O₃. The sample was also annealed in an O₂-atmosphere. The TEM images and the EELS data of this sample are shown in Figure 7.1.6 and Figure 7.1.7. The magnetization measurements are shown in Figure 7.1.10.

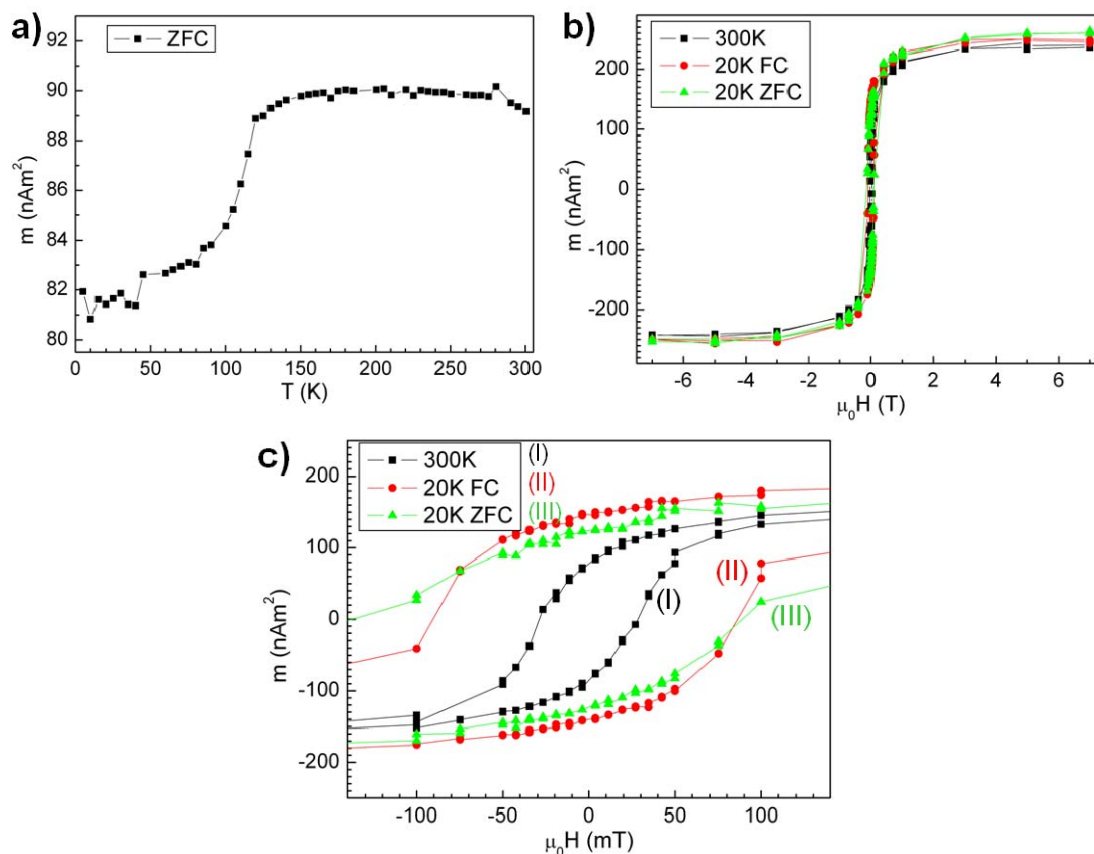


Figure 7.1.10. 25 nm Fe₂O₃ + 25 nm Fe_{2-x}Ti_xO₃ + 3nm Fe₂O₃ (sample 3). a) Temperature dependence of the magnetic moment after cooling in zero field. b) Magnetic moment a function of the external field. c) Enlarged section of b. All data were corrected for the diamagnetic contribution of the Al₂O₃ substrate.

The temperature dependence of the magnetic moment of this sample shows an increase from 82 nAm² to 90 nAm² between 100 and 130 K, which is very probably caused by magnetite as it coincides with the Verwey transition at about 120 K. The saturation magnetization and the remanent magnetization are much larger compared to the sample with a small Ti layer (Figure 7.1.9). This may be caused to some extent by magnetite, also the thickness of sample 3 is doubled compared to sample 2 but there remains still an increase of the saturation magnetization due to the Ti content. The Ti lean solid solution Fe_{2-x}Ti_xO₃ with $x < 0.5$ should be antiferromagnetic and should not contribute to the increased magnetization.^{2,3} The discrepancy can be explained if a partially ordered film is assumed. The magnetic behavior depends on the degree of order. Ferrimagnetism has been found in thin films with space group $R\bar{3}$ which occurs at ilmenite concentrations $x \geq 0.5$.²⁵⁻²⁷ A disordered thin film with space group $R\bar{3}c$ and $x = 0.8$ was proven to be antiferromagnetic while the ordered films were ferrimagnetic.²⁴ Also for

low ilmenite concentrations ferromagnetic behavior has been predicted.¹¹ The assumption of a partially ordered film is also supported by the Raman spectra which exhibited characteristic lines of both, hematite and ilmenite. Also the EELS measurements support this interpretation. The partially ordered film exhibits disordered domains and domains where Ti occupies preferentially alternate layers. The magnetic moment therefore can result from the interfaces with an increased Fe²⁺ concentration. The results of the EELS analysis and of the magnetization measurements presented here support the hypothesis of lamellar magnetism explaining the large remanent magnetism in rocks exhibiting hematite-ilmenite exsolution lamellae.²⁸

7.1.4 Summary and conclusion

Three thin films deposited on α -Al₂O₃, 25 nm Fe₂O₃ (sample 1), 25 nm Fe₂O₃ + 0.4 nm Ti_{1-x}O₂ + 3 nm Fe₂O₃ (sample 2) and 25 nm Fe₂O₃ + 25 nm Fe_{2-x}Ti_xO₃ + 3 nm Fe₂O₃ (sample 3), were studied with regards to their growth conditions, magnetic properties, chemical composition and structural behavior. Raman spectra revealed that in the temperature range between 400 °C and 500 °C predominantly hematite is formed, but XRD and TEM investigations showed the presence of magnetite. XRD measurements revealed that hematite formed with two different orientations on α -Al₂O₃ (0001), $[1000]_{\text{Fe}_2\text{O}_3} \parallel [1000]_{\text{Al}_2\text{O}_3}$ and another one rotated by 60° with $[1000]_{\text{Fe}_2\text{O}_3} \parallel [0100]_{\text{Al}_2\text{O}_3}$. TEM analysis clarified that the thin films possess grains with various orientations. Raman spectra showed that the exact stoichiometry of ilmenite was not reached for the Fe_{2-x}Ti_xO₃ layer. In fact, EELS investigations showed for the thin film with 25 nm Fe₂O₃ + 25 nm Fe_{2-x}Ti_xO₃ + 3 nm Fe₂O₃ (sample 3) an ilmenite concentration of $x \approx 0.44$. The Raman spectra indicate a partially ordered solid solution as characteristic lines from ilmenite and hematite occur. The interface between hematite and the Fe_{2-x}Ti_xO₃ layer was analyzed by EELS concerning the oxidation state of Fe. We found that the interface between this layer and the hematite layer shows an enrichment of Fe²⁺, which can explain the increased magnetization of the thin film system with Fe_{2-x}Ti_xO₃. Although a quantitative interpretation of the magnetization measurements is problematic due to the presence of magnetite content, a significant increase of the magnetization is obtained in the sample with Ti doping.

7.1.5 Chapter references

- ¹ T. Nagata and S. Akimoto, *Pure and Applied Geophysics* **34**, 36 (1956).
- ² Y. Ishikawa and S. Akimoto, *Journal of the Physical Society of Japan* **12**, 1083 (1957).
- ³ Y. Ishikawa, *Journal of the Physical Society of Japan* **13**, 37 (1958).
- ⁴ R.K. Pandey, P. Padmini, R. Schad, J. Dou, H. Stern, R. Wilkins, R. Dwivedi, W.J. Geerts, and C. O'Brien, *Journal of Electroceramics* **22**, 334 (2009).
- ⁵ C. Jorand Sartoretti, B.D. Alexander, R. Solarska, I.A. Rutkowska, J. Augustynski, and R. Cerny, *The Journal of Physical Chemistry B* **109**, 13685 (2005).
- ⁶ J.A. Glasscock, P.R.F. Barnes, I.C. Plumb, and N. Savvides, *Journal of Physical Chemistry C* **111**, 16477 (2007).
- ⁷ T.-Y. Yang, H.-Y. Kang, U. Sim, Y.-J. Lee, J.-H. Lee, B. Koo, K.T. Nam, and Y.-C. Joo, *Physical Chemistry Chemical Physics : PCCP* **15**, 2117 (2013).
- ⁸ D. Cao, W. Luo, M. Li, J. Feng, Z. Li, and Z. Zou, *Crystal Engineering Communications* **15**, 2386 (2013).
- ⁹ E.N. Maslen, V.A. Streltsov, N.R. Streltsova, and N. Ishizawa, *Acta Crystallographica* **B50**, 435 (1994).
- ¹⁰ R.J. Harrison, S.A.T. Redfern, and R.I. Smith, *American Mineralogist* **85**, 194 (2000).
- ¹¹ W.H. Butler, A. Bandyopadhyay, and R. Srinivasan, *Journal of Applied Physics* **93**, 7882 (2003).
- ¹² J. Velev, a. Bandyopadhyay, W. Butler, and S. Sarker, *Physical Review B* **71**, 205208 (2005).
- ¹³ T. Droubay, K.M. Rosso, S.M. Heald, D.E. McCready, C.M. Wang, and S.A. Chambers, *Physical Review B* **75**, 104412 (2007).
- ¹⁴ R. Pentcheva and H. Nabi, *Physical Review B* **77**, 172405 (2008).
- ¹⁵ F. Zhou, S. Kotru, and R.K. Pandey, *Thin Solid Films* **408**, 33 (2002).
- ¹⁶ T. Fujii, M. Kayano, Y. Takada, M. Nakanishi, and J. Takada, *Solid State Ionics* **172**, 289 (2004).
- ¹⁷ H. Hojo, K. Fujita, K. Tanaka, and K. Hirao, *Applied Physics Letters* **89**, 142503 (2006).
- ¹⁸ J. Dou, L. Navarrete, P. Kale, P. Padmini, R.K. Pandey, H. Guo, a. Gupta, and R. Schad, *Journal of Applied Physics* **101**, 053908 (2007).
- ¹⁹ E. Popova, B. Warot-Fonrose, H. Ndilimabaka, M. Bibes, N. Keller, B. Berini, K. Bouzehouane, and Y. Dumont, *Journal of Applied Physics* **103**, 093909 (2008).

- ²⁰ K. Rode, R.D. Gunning, R.G.S. Sofin, M. Venkatesan, J.G. Lunney, J.M.D. Coey, and I. V Shvets, *Journal of Magnetism and Magnetic Materials* **320**, 3238 (2008).
- ²¹ Y. Takada, M. Nakanishi, T. Fujii, J. Takada, and Y. Muraola, *Journal of Applied Physics* **104**, 033713 (2008).
- ²² Y. Takada, M. Nakanishi, T. Fujii, and J. Takada, *Applied Physics Letters* **92**, 252102 (2008).
- ²³ H. Hojo, K. Fujita, T. Mizoguchi, K. Hirao, I. Tanaka, K. Tanaka, and Y. Ikuhara, *Physical Review B* **80**, 075414 (2009).
- ²⁴ T. Matoba, K. Fujita, S. Murai, and K. Tanaka, *Journal of Physics: Conference Series* **200**, 062011 (2010).
- ²⁵ T. Fujii, T. Sugano, M. Nakanishi, and J. Takada, *Journal of Physics: Conference Series* **200**, 072029 (2010).
- ²⁶ A. Hamie, Y. Dumont, E. Popova, J. Scola, A. Fouchet, B. Berini, and N. Keller, *Journal of Applied Physics* **108**, 093710 (2010).
- ²⁷ A. Hamie, E. Popova, Y. Dumont, E. Chikoidze, B. Warot-Fonrose, B. Berini, and N. Keller, *Applied Physics Letters* **98**, 232501 (2011).
- ²⁸ P. Robinson, R.J. Harrison, S.A. McEnroe, and R.B. Hargraves, *Nature* **418**, 517 (2002).
- ²⁹ C.M. Carmichael, *Proceedings of the Royal Society A* **263**, 508 (1961).
- ³⁰ T. Kasama, U. Golla-Schindler, and A. Putnis, *American Mineralogist* **88**, 1190 (2003).
- ³¹ S.A. McEnroe, B. Carter-Stiglitz, R.J. Harrison, P. Robinson, K. Fabian, and C. McCammon, *Nature Nanotechnology* **2**, 631 (2007).
- ³² K. Fabian, S.A. McEnroe, P. Robinson, and V.P. Shcherbakov, *Earth and Planetary Science Letters* **268**, 339 (2008).
- ³³ H. Sadat Nabi and R. Pentcheva, *Journal of Applied Physics* **106**, 073912 (2009).
- ³⁴ R.J. Harrison, S.A. McEnroe, P. Robinson, B. Carter-Stiglitz, E.J. Palin, and T. Kasama, *Physical Review B* **76**, 174436 (2007).
- ³⁵ V.P. Shcherbakov, K. Fabian, and S.A. McEnroe, *Physical Review B* **80**, 174419 (2009).
- ³⁶ H. Sadat Nabi, R.J. Harrison, and R. Pentcheva, *Physical Review B* **81**, 214432 (2010).
- ³⁷ M. Lübbe, A.M. Gigler, R.W. Stark, and W. Moritz, *Surface Science* **604**, 679 (2010).
- ³⁸ M. Lübbe, *Präparation und magnetische Eigenschaften dünner Fe₂O₃- und FeTi_{1-x}O₃-Schichten auf Al₂O₃(0001)*, Doctoral Thesis, LMU Munich (2009).
- ³⁹ U. Balachandran, R.W. Siegel, Y.X. Liao, and T.R. Askew, *NanoStructured Materials* **5**, 505 (1995).

- ⁴⁰ M. Albrecht, H. Antesberger, W. Moritz, H. Plöckl, M. Sieber, and D. Wolf, *Review of Scientific Instruments* **70**, 3239 (1999).
- ⁴¹ P. Thangadurai, Y. Lumelsky, M.S. Silverstein, and W.D. Kaplan, *Materials Characterization* **59**, 1623 (2008).
- ⁴² R.F. Egerton, *Electron Energy-loss Spectroscopy in the Electron Microscope*, 3 ed. (Springer Science+Business Media, New York, 2011), p. 491.
- ⁴³ R. Brydson, *Electron Energy Loss Spectroscopy*, 1 ed. (BIOS Scientific Publishers Limited, Oxford, 2001), p. 137.
- ⁴⁴ D.B. Williams and C.B. Carter, *Transmission Electron Microscopy*, 2 ed. (Springer Science+Business Media, New York, 2009), p. 760.
- ⁴⁵ H.K. Schmid and W. Mader, *Micron* **37**, 426 (2006).
- ⁴⁶ M. Aronniemi, J. Lahtinen, and P. Hautojärvi, *Surface and Interface Analysis* **36**, 1004 (2004).
- ⁴⁷ Y. Gao, Y.J. Kim, S.A. Chambers, and G. Bai, *Journal of Vacuum Science & Technology A* **15**, 332 (1997).
- ⁴⁸ S.H. Oh, C. Scheu, T. Wagner, and M. Rühle, *Applied Physics Letters* **91**, 141912 (2007).
- ⁴⁹ C. Colliex, T. Manoubi, and C. Ortiz, *Physical Review B* **44**, 11402 (1991).
- ⁵⁰ P.A. van Aken and B. Liebscher, *Physics and Chemistry of Minerals* **29**, 188 (2002).
- ⁵¹ M.T. Otten, B. Miner, J.H. Rask, and P.R. Buseck, *Ultramicroscopy* **18**, 285 (1985).
- ⁵² P.A. van Aken, B. Liebscher, and V.J. Styrsa, *Physics and Chemistry of Minerals* **25**, 323 (1998).

7.2 Fe₂O₃ thin film grown on Al₂O₃ (0001) containing nominal one unit cell of Fe_{2-x}Ti_xO₃

7.2.1 EELS analysis

As devices are getting smaller and smaller, we investigated a thin film with only nominal one unit cell of Ti in the Fe_{2-x}Ti_xO₃/Fe₂O₃ system. This film has been studied concerning its structure and chemical composition. The FIB sample was highly contaminated with C and Pt which is why the Ti could not be found in an earlier work.¹ Here, we further thinned the specimen by ion-milling for additional measurements. Figure 7.2.1a shows an overview of the thinned sample. In the TEM image the Al₂O₃ substrate, the thin film consisting of a Fe₂O₃ layer and nominal one unit cell of Ti as well as the C protection layers of the FIB sample preparation are shown. Furthermore, Pt was applied as protection layer (not visible). The black dots appearing all over are Pt contamination. Figure 7.2.1b is a HRTEM image showing the substrate viewed along [10 $\bar{1}$ 0]. The thin film is not epitaxially grown on the Al₂O₃ and exhibits individual grains and grain boundaries. Furthermore, the rough surface indicates island growth.

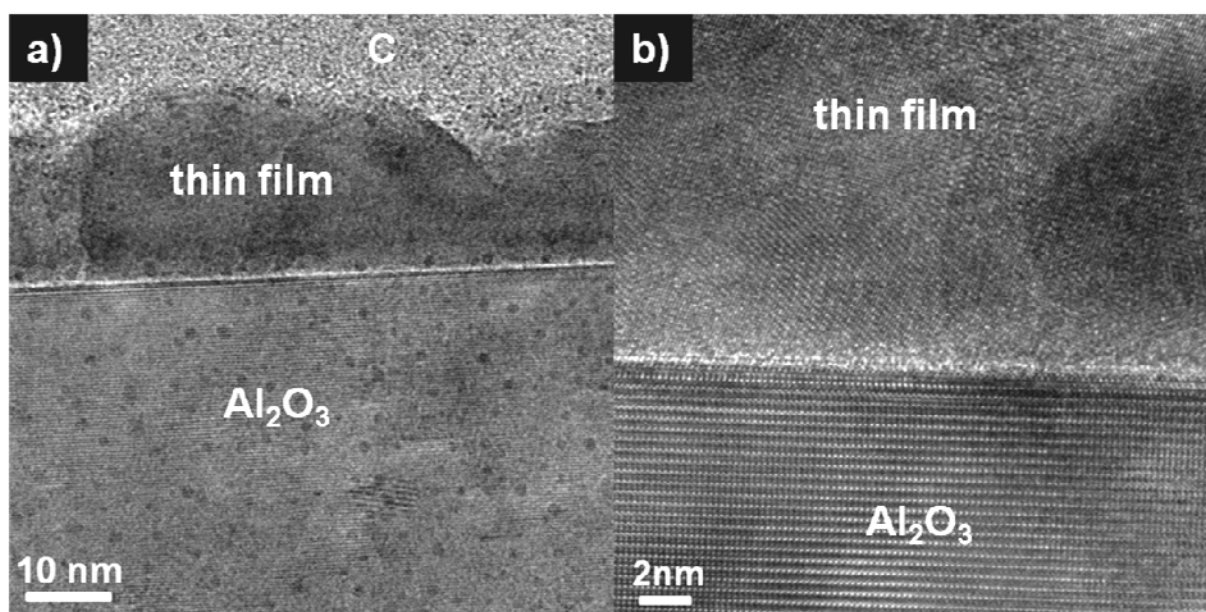


Figure 7.2.1. Thin film of a Fe₂O₃ layer and nominal one unit cell of Fe_{2-x}Ti_xO₃. a) TEM overview showing the substrate the thin film and the C protection layer and b) HRTEM image of the substrate viewed along [10 $\bar{1}$ 0] and the non-epitaxial grown thin film.

The Ti could not be detected with EDX measurements in our previous work.¹ Therefore, we performed EELS in STEM mode with a beam diameter of ~ 3 Å. Spot measurements across the thin film reveal the presence of Ti close to the film's surface. In Figure 7.2.2a a HRTEM image showing exemplarily the area of the EELS analysis and EEL spectra of the Fe_{2-x}Ti_xO₃ layer are given showing the Ti- and Fe-L_{2,3}-edges (Figure 7.2.2b and c) as well as the O-K-edge (Figure 7.2.2d). The quantification of the EEL spectra lead to a chemical composition of Fe : Ti : O = 36 : 1 : 63 at.% with a relative error of $\pm 20\%$ in the Fe_{2-x}Ti_xO₃ layer. The Fe₂O₃ layer exhibits a chemical composition of Fe : O = 37 : 63 at.% with an error of $\pm 3 - 5$ at.%.

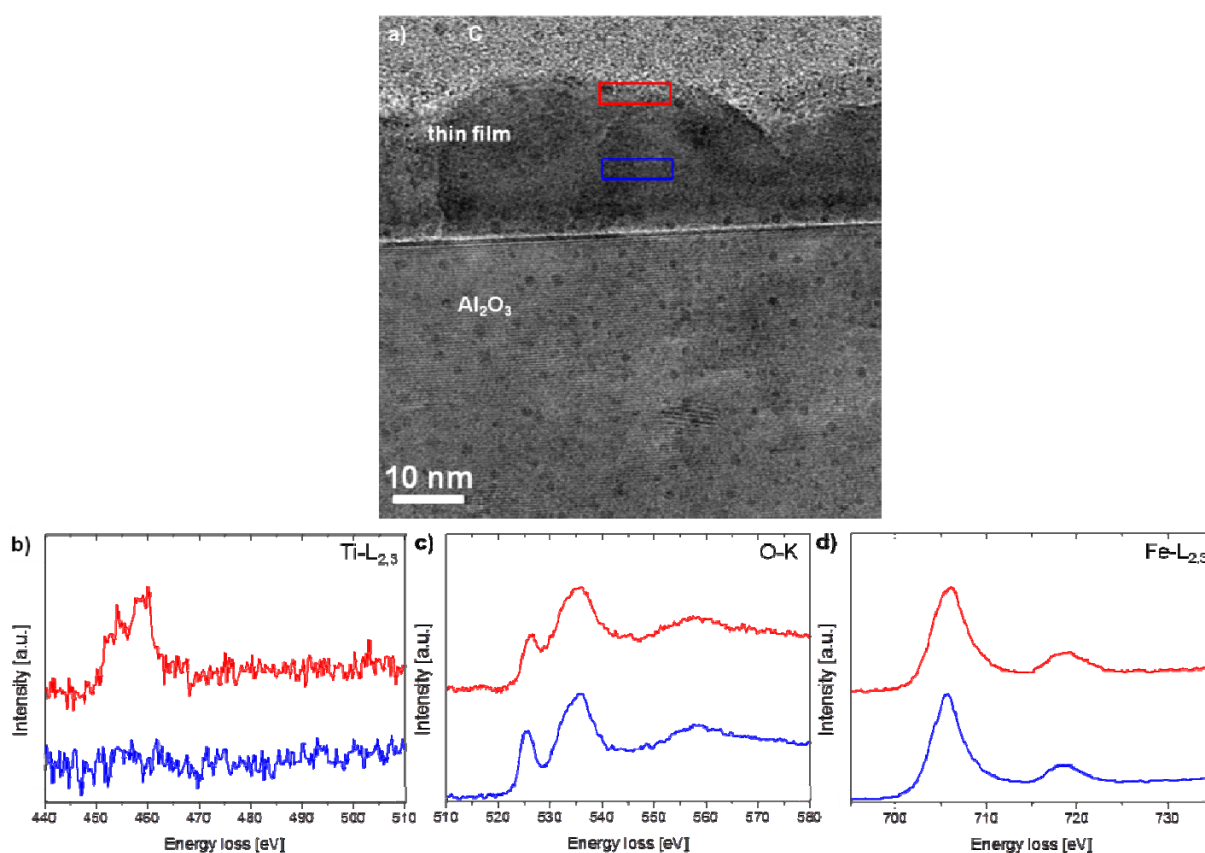


Figure 7.2.2. EEL spectra of the Fe_{2-x}Ti_xO₃ layer showing the Ti- and Fe L_{2,3}-edges and the O-K-edge. The HRTEM shows exemplarily the area where the data was collected.

With additional thinning the specimen we were able to detect Ti on the upper site of the thin film. This is of interest for further investigation as this thin film is expected to have other magnetic properties than the thin film system with nominal five unit cells of Fe_{2-x}Ti_xO₃.^{2,3}

7.2.2 Chapter references

- ¹ T. Dennenwaldt, *Transmissionselektronenmikroskopische Untersuchungen von Si-P-O-N-Verbindungen und Eisenoxid-Dünnschichten*, Diploma Thesis, LMU Munich (2009).
- ² M. Lübbe, *Präparation und magnetische Eigenschaften dünner Fe₂O₃- und FeTi_{1-x}O₃-Schichten auf Al₂O₃(0001)*, Doctoral Thesis, LMU Munich (2009).
- ³ M. Lübbe, A.M. Gigler, R.W. Stark, and W. Moritz, *Surface Science* **604**, 679 (2010).

8 Summary and conclusion

8.1 Silica-based nanotubes

Recently discovered amorphous SBNTs were synthesized via a purely inorganic reaction with the starting materials $OP(NH_2)_3$, $SP(NH_2)_3$ and $SiCl_4$. Reaction temperatures from 200 to 700 °C and evacuated, sealed silica glass ampoules were used. Beside the SBNTs two other reaction products with different morphologies occurred, flakes and hollow particles. Without adding any structure directing template 3D hyperbranched assemblies were formed consisting of the SBNTs. The reaction products were analyzed with EM concerning their chemical and structural composition. All synthesis products were amorphous in XRD and electron diffraction. EDX and EELS analysis in the TEM revealed that the hollow particles exhibit a similar chemical composition than the SBNTs, consisting mostly of Si, O and N with a small amount of P. In contrast, the flakes were P and N dominated. The SBNTs exhibited a bamboo-like structure and were several μm in length. Depending on the synthesis temperature and the amount of $SiCl_4$, the diameter of the SBNTs varied between 70 – 190 nm. The increase of the O content during the synthesis did not lead to an increase of the SBNTs yield.

The chemical composition and the element distribution in the SBNTs were analyzed in depth at the nanoscale with EDX and EELS. The elements were homogeneously distributed in the SBNTs walls, their interior and at their junction points. Furthermore, the bonding behavior of the elements Si, O, N and P of the SBNTs and flakes were examined. EELS analysis of the Si-L_{2,3}-edge of the SBNTs synthesized at 300 and 700 °C revealed that the bonding of Si in the SBNTs is a mixture of SiO_2 and Si_3N_4 exhibiting a tetrahedral coordination with mostly O and N as bonding atoms. Nevertheless, P atoms might occur in the nearest coordination sphere of Si as the Si-L_{2,3}-edge main peak showed a broadening, which could not be attributed to a mixture of the amorphous reference SiO_2 and Si_3N_4 . The N-K- and O-K-edges of all three compounds showed no obvious difference. The P-L_{2,3}-, N-K- and O-K-edges of the flakes synthesized at 700 °C were compared to the crystalline reference material PON and P_3N_5 . A higher agreement for the general shapes of the P-L_{2,3}- and N-K-ELNES could be found for P_3N_5 than for PON. Overall, P of the flakes is tetrahedrally coordinated with mostly N atoms and smaller amounts of O atoms. Its bonding behavior is rather similar to that in P_3N_5 . Again,

P atoms most likely occur in the nearest coordination sphere. Furthermore, the band gap of 5.7 eV of the SBNTs was determined with VEELS lying between the band gap values of Si_3N_4 and SiO_2 .

The treatment of the SBNTs synthesized at 400 °C with aqueous solutions of different pH values (1 to 14) showed that the SBNTs exhibited a higher resistance to basic solutions than SNTs. This leads to the assumption that the incorporation of P and N increases their chemical stability.

FIB investigation of the SBNTs 3D mesocrystals synthesized at 300 and 700 °C showed that the assembly is homogeneously built of SBNTs. The constitution of the SBNTs network was analyzed with ET revealing that the SBNTs are hollow. Their junction points are open and they are connected to each other.

The SBNTs and their 3D assemblies could act as 3D template for other materials when filling them and they are promising candidates for nanofiltration or nanofluidic device applications.

8.2 BeP_2N_4 compound

The recently discovered compound BeP_2N_4 crystallizing in the phenakite-type structure has potential application as high strength optoelectronic material. Its electronic structure was analyzed with high-energy-resolution EELS without altering the structure. In general, the detection of light elements like Be is challenging due to their low atomic number and easy removal under electron bombardment. The bonding behavior and coordination of the individual atomic species including Be could be investigated. The experimental ELNES of the Be-K-, P-L_{2,3}-, and (partly) N-K-edges showed excellent agreement with the DFT calculations concerning shape, relative peak positions and edge onsets. Be and P are tetrahedrally coordinated whereas N is threefold coordinated exhibiting four different sites in the phenakite-type structure.

A direct band gap of 4.3 ± 0.3 eV of the phenakite-type structure of BeP_2N_4 was determined with VEELS using the linear fit method. This is in reasonable accordance with the predicted value of 3.97 for the theoretically refined structure by DFT calculations. In principle, the predicted band gap values are supposed to be slightly underestimated.

The combination of high-energy-resolution EELS with DFT calculations enables a facile investigation of new structure types such as hypothetical ultrahard spinel-type BeP_2N_4 compound in the future. Furthermore, materials with ultralight elements can be analyzed which is important for their further development.

8.3 $\text{Fe}_{2-x}\text{Ti}_x\text{O}_3/\text{Fe}_2\text{O}_3$ thin films grown on Al_2O_3

The interface between hematite ($\alpha\text{-Fe}^{\text{III}}_2\text{O}_3$) and ilmenite ($\text{Fe}^{\text{II}}\text{TiO}_3$), a weak ferrimagnet and an antiferromagnet, respectively, has been shown to be strongly ferrimagnetic. This is due to the formation of a mixed valence layer of $\text{Fe}^{2+}/\text{Fe}^{3+}$ (1:1 ratio) caused by compensation of charge mismatch at the chemically abrupt boundary. It is not known, however, if a similarly distinct interface layer emerges when the $\text{Fe}^{2+}/\text{Fe}^{3+}$ gradient is less steep across the chemical boundary, i.e., when ilmenite is replaced by Ti-doped hematite $\text{Fe}_{2-x}\text{Ti}_x\text{O}_3$ ($x < 0.5$, weak ferrimagnetic), in which the $\text{Fe}^{2+}/\text{Fe}^{3+}$ ratio is already less than unity in the bulk. Using MBE, we have grown thin films (~ 25 nm thickness) of $\alpha\text{-Fe}_2\text{O}_3$ on $\alpha\text{-Al}_2\text{O}_3$ (0001) substrates, which were capped with a ~ 25 nm thick $\text{Fe}_{2-x}\text{Ti}_x\text{O}_3$ layer ($x = 0.44$). The films were structurally characterized in-situ with surface XRD, which showed the partial epitaxial relationship between film and substrate in terms of the [0001] axis and revealed two predominant types of crystallographic domains, an epitaxial one with $[1000]_{\text{Fe}_2\text{O}_3} \parallel [1000]_{\text{Al}_2\text{O}_3}$, and another one rotated by 60° with $[0100]_{\text{Fe}_2\text{O}_3} \parallel [1000]_{\text{Al}_2\text{O}_3}$. Magnetization measurements were performed with a SQUID magnetometer. Comparison of samples of hematite layers with and without a thin Ti layer exhibit a significant increase of the remanent and saturation magnetization of the sample with Ti. EELS profiles across the $\text{Fe}_{2-x}\text{Ti}_x\text{O}_3/\text{Fe}_2\text{O}_3$ interface show that $\text{Fe}^{2+}/\text{Fe}^{3+}$ ratios peak right at the interface rather than assuming an intermediate value according to the expected gradient in Fe^{2+} across the boundary. This strongly suggests the formation of a chemically distinct interface layer, which might also be magnetically distinct as indicated by the observed magnetic enhancement in the $\text{Fe}_{2-x}\text{Ti}_x\text{O}_3/\text{Fe}_2\text{O}_3/\text{Al}_2\text{O}_3$ system compared to the uncapped $\text{Fe}_2\text{O}_3/\text{Al}_2\text{O}_3$ system.

In this thesis, it could be demonstrated that TEM and its analytical techniques in particular EELS are appropriate to study diverse micro- and nanomaterials concerning their chemical and structural behavior. Furthermore, the focus was put on the analysis of light elements in different materials as well as the investigation of the physical properties of novel compounds with EELS and VEELS, respectively. This led to interesting results which are of high interest for future material development and characterization.

9 Appendix

Figure 8.3.1a shows the EDX spectrum of SBNTs. The elements Si, O, P and N were detected. Cu results from the Cu grid and Cl from the starting material. The EDX measurement of a flake (Figure 8.3.1b) reveals the presence of the elements Si, O, P and N. The Cu stems again from the grid and S from the starting material. The amount of Si is much higher than the amount of P in the NTs and vice versa for the flakes.

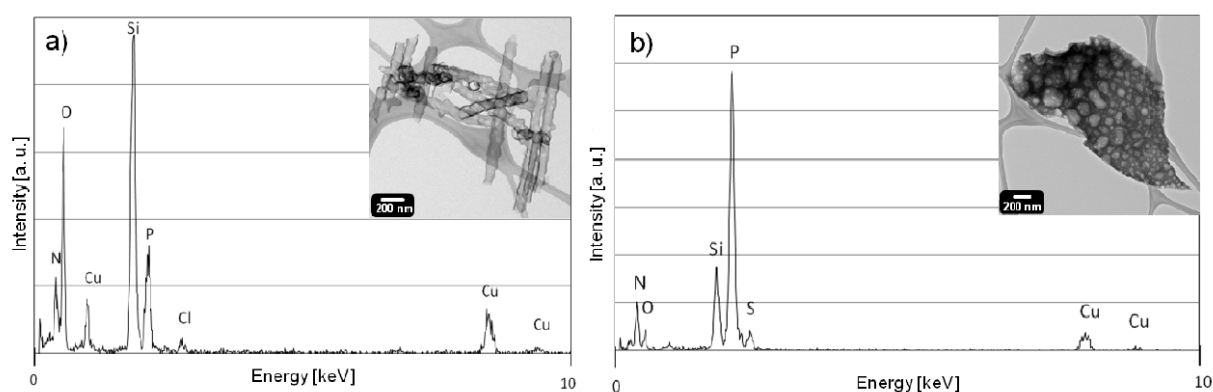


Figure 8.3.1. EDX measurements of a) SiO₂-based NTs and b) a flake.

Figure 8.3.2 shows a polymeric Si/P/O/N/H agglomeration which could be the starting point of the growth of the SBNTs.

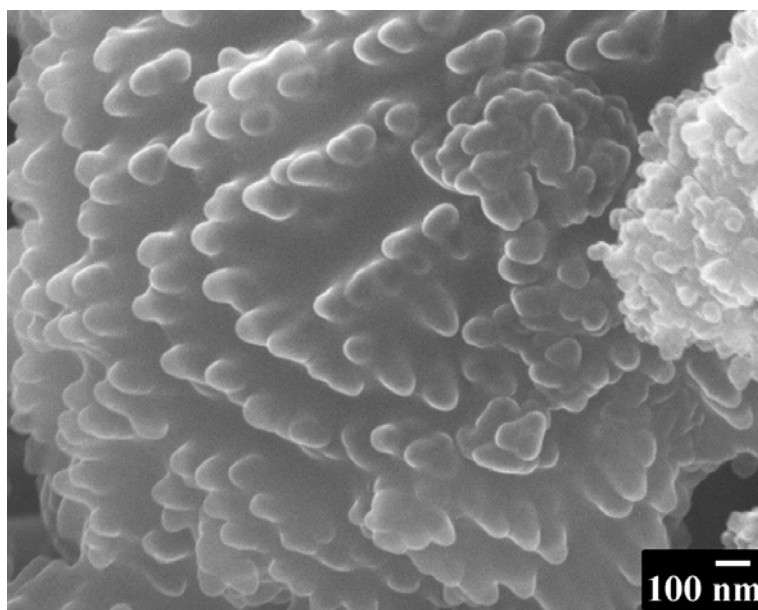


Figure 8.3.2. SEM image of a polymeric agglomeration indicating the starting point for NT growth.

10 Curriculum vitae

Personal information

Name: Teresa Katharina Dennenwaldt

Email: teresa.dennenwaldt@cup.uni-muenchen.de

Nationality: German

Academic Studies

- 2010 until now PhD studies at the physical chemistry section, Ludwig-Maximilians-University Munich in the group of Prof. Scheu
- December 2009 Certificate: diploma in chemistry
- 2004 – 2009 Study of chemistry, Ludwig-Maximilians-University Munich
- 2002 – 2004 Study of physics, Ludwig-Maximilians-University Munich

Education

- July 2002 Certificate: University-Entrance diploma
- 2000 - 2002 Oskar-von-Miller- Gymnasium (grammar school) Munich, Germany
- 1993 – 2000 Käthe-Kollwitz-Gymnasium (grammar school) Munich, Germany
- 1989 – 1993 Ecole primaire Vence/St. Paul de Vence (primary school), France

Membership

- Graduate Program of the Nanosystems Initiative Munich (NIM)
- Center of NanoScience (CeNS)
- Deutsche Gesellschaft für Elektronenmikroskopie (DGE)
- Materials Research Society (MRS)

Grants

- 2013 Travel funding for the EDGE 2013 in Sainte-Maxime from CeNS and the EDGE Committee
- 2012 Travel funding for the EMC 2012 Manchester of the DGE and NIM fellowship for a 3 months research visit at the National Center for Electron Microscopy (NCEM) at the Lawrence Berkeley National Laboratory (LBNL) Berkeley, USA
- 2011 Travel funding for the MC 2011 Kiel of the DGE

Skills

Since 2010 Chemical synthesis

Autonomous working at Transmission Electron Microscopes (TEM), conventional TEM, electron diffraction, high resolution TEM, HAADF imaging, Energy Electron Loss Spectroscopy (EELS), Energy-dispersive X-ray Spectroscopy (EDX), TEM sample preparation

Autonomous working at Scanning Electron Microscopes (SEM)

Since 2010 Training and supervising of bachelor students, supervising of practical courses in inorganic and physical chemistry

Languages

German native speaker

English good, spoken and written

French fluent

EDV Microsoft office, Wolfram Mathematica (basic knowledge)

11 List of publications and presentations

11.1 Scientific Publications

Journals

1. T. Dennenwaldt, S. J. Sedlmaier, A. Binek, W. Schnick, C. Scheu, *Bonding behavior and chemical stability of silica-based nanotubes and their 3D assembly*, submitted.
2. T. Dennenwaldt, M. Lübke, M. Winklhofer, A. Müller, M. Döblinger, H. Sadat Nabi, M. Gandman, T. Cohen-Hyams, W. D. Kaplan, W. Moritz, R. Pentcheva and C. Scheu, *Insights into the structural, electronic and magnetic properties of $Fe_{2-x}Ti_xO_3/Fe_2O_3$ thin films with $x = 0.44$ grown on $Al_2O_3(0001)$* , submitted.
3. T. Dennenwaldt, J. Ciston, U. Dahmen, W.-Y. Ching, F. J. Pucher, W. Schnick, C. Scheu, *High resolution spectroscopy of bonding in a novel BeP_2N_4 compound*, submitted.
4. S. J. Sedlmaier, T. Dennenwaldt, C. Scheu, W. Schnick, *Template-free inorganic synthesis of silica-based nanotubes and their self-assembly to mesocrystals*, *J. Mater. Chem.* **22**, 15511 (2012).
5. L. Melzig, T. Dennenwaldt, A. Gavryushin, P. Knochel, *Direct aminoalkylation of arenes, heteroarenes, and alkenes via Ni-catalyzed Negishi cross-coupling reactions*, *J. Org. Chem.* **76**, 8891 (2011).
6. J. Schuster, A. Keilbach, R. Köhn, M. Döblinger, T. Dörfler, T. Dennenwaldt, T. Bein, *Cubic and hexagonal mesoporous carbon in the pores of anodic alumina membranes*, *Chem. Eur. J.* **17**, 9463 (2011).

Conference proceedings

1. T. Dennenwaldt, S. J. Sedlmaier, A. Wisnet, M. Döblinger, W. Schnick, C. Scheu, *Discrete tomography of SiO_2 -based nanotubes and their 3D network*, EMC 2012 Manchester, UK.
2. T. Dennenwaldt, S. J. Sedlmaier, W. Schnick, C. Scheu, *TEM analysis of different nanomorphologies of Si-P-O-N compounds*, MC 2011 Kiel, Germany.

11.2 Conference contributions

Oral presentation

1. *Silica and silica-based nanotubes: synthesis and applications*, Mechanics meets energy 2013, MPIE Düsseldorf, Germany.
2. *TEM investigations of SiO₂-based nanotubes and BeP₂N₄*, NCEM Berkeley 2012, USA.
3. *TEM investigations on thin Ti-Fe-O films on Al₂O₃ (II)*, E-MRS 2011 Nice, France.
4. *TEM investigations on thin Fe_xO_y films on Al₂O₃*, MACAN summer meeting 2010 Bohinj, Slovenia.

Poster presentation

1. *Tomography of a 3D assembly of silica-based nanotubes (II)*, NIM graduate program 2013, summer retreat, Lenggries, Germany.
2. *Investigation of the electronic structure of a novel BeP₂N₄ compound*, EDGE 2013, Sainte-Maxime, France.
3. *Tomography of a 3D assembly of silica-based nanotubes (I)*, MACAN Capstone meeting 2013, Haifa, Israel.
4. *Electronic structure study of the phenakite-type phase of BeP₂N₄*, NIM winter school 2013 Kirchberg, Austria.
5. *Discrete tomography of SiO₂-based nanotubes and their 3D network*, EMC 2012 Manchester, UK.
6. *TEM analysis of different nanomorphologies of Si-P-O-N compounds (II)*, MC 2011 Kiel, Germany.
7. *TEM analysis of different nanomorphologies of Si-P-O-N compounds (I)*, NIM graduate program 2011, summer retreat, Aschau im Chiemgau, Germany.
8. *Nanoscale characterization of Ti-Fe-O thin films on α -Al₂O₃ substrates*, NIM winter school 2011 St. Christoph am Arlberg, Austria.
9. *TEM investigations on thin Ti-Fe-O films on Al₂O₃ (I)*, NIM and CENS summer school 2010, Venice, Italy.

12 Danksagung

„Leider lässt sich eine wahrhafte Dankbarkeit mit Worten nicht ausdrücken.“

(Johann Wolfgang von Goethe 1749 - 1832)

Dennoch möchte ich meinen herzlichen Dank an all' die Menschen, die mich bis jetzt auf meinem wissenschaftlichen Weg begleitet und unterstützt haben, aussprechen.

Im Besonderen danke ich:

Frau Prof. Dr. Christina Scheu, die es mir ermöglicht hat einen tiefen Einblick in das interessante Arbeitsgebiet der Elektronenmikroskopie zu gewinnen und mich unermüdlich motivierte, meinem Thema näher zu kommen,

Herrn Prof. Dr. Wolfgang Schnick für die engagierte Zweitbetreuung meiner Dissertation,

Herrn Dr. Stefan Sedlmaier für die Überlassung des Themas der Silicium-basierten Nanoröhren und der geduldigen Einarbeitung,

Herrn Florian Pucher für die Bereitstellungen der BeP_2N_4 -Proben und den damit verbundenen weiterführenden Gesprächen, sowie dem restlichen Arbeitskreis Prof. Schnick für eine angenehme Laboratmosphäre,

Herrn Prof. Dr. Wolfgang Moritz, Frau Dr. Rossitza Pentcheva, Herrn Dr. Michael Winklhofer, Herrn Dr. Hasan Sadat Nabi und Frau Dr. Maike Lübke für die sympathische Zusammenarbeit und den anregenden Diskussionen über Eisenoxid-Dünnschichten,

Herrn Prof. Dr. Wayne D. Kaplan für die freundliche Betreuung während meines Aufenthaltes am Technion in Haifa, sowie Frau Dr. Tzipi Cohen-Hyams für die Probenpräparation der FIB-Lamellen der Eisenoxid-Dünnschichten,

Herrn Prof. Dr. Ulrich Dahmen, Herrn Dr. Jim Ciston, Herrn Dr. Peter Ercius und allen weiteren Mitgliedern des NCEMs für die herzliche Aufnahme und die hervorragende Betreuung in Berkeley,

Frau Dr. Maria Gandman für ihre Unterstützung bei meinen wissenschaftlichen Themen und ihre phantastische Freizeitgestaltung in Haifa und Berkeley,

Herrn Dr. Markus Döblinger für seine geduldige und zeitintensive Einweisung am TEM, sowie für die Hilfe bei der Tomographie der Silicium-basierten Nanoröhren,

Herrn Christian Minke und Herrn Steffen Schmidt für die hervorragenden Aufnahmen am REM,

Frau Sonja Matich und Frau Ramona Hoffmann für die FIB-Probenpräparation der Silicium-basierten Nanoröhren,

Frau Regina Huber für ihre Hilfe bei Verwaltungsangelegenheiten und organisatorischen Belangen,

meinen Praktikanten Herrn Christian Mende, Herrn Stefan Datz, Herrn Andreas Binek, Frau Ursula Pachmayr und Herrn Philipp Ratza für ihre tatkräftige Unterstützung in Form von Bachelorarbeiten und F-Praktika,

Herrn Stephan Hug, Herrn Christian Ziegler, Herrn Stephan Werner und Herrn Sebastian Schneider für die willkommenen Auszeiten in Form des ein oder anderen isotonischen Kaltgetränkes,

dem Arbeitskreis Prof. Scheu für das herzliche Arbeitsklima. Nicht nur eure Unterstützung bei wissenschaftlichen Themen, sondern auch die freizeithlichen Aktivitäten haben die letzten Jahre zum besten Arbeitsplatz der Welt gemacht! Meinen Bürokollegen Frau Ramona Hoffmann, Herr Alexander Müller und Herr Andreas Wisnet danke ich für die freundschaftliche und konstruktive Arbeitsatmosphäre. Danke Ramona für die netten kleinen Ratschpausen bei einer Tasse Tee. Alex, dir danke ich herzlich für die geduldige Unterstützung bei Auswertungen meiner EELS-Messungen mit Mathematica. Vielen Dank Andi für die aufwendige Rekonstruktion der Tomographie der Silicium-basierten Nanoröhren. Herr Dr. Sriram Venkatesan, Frau Dr. Angela Wochnik, Herr Christian Ziegler, Herr Christoph Heinzl, Frau Sophia Betzler, Frau Anna Frank und allen anderen Kollegen möchte ich für eine unvergessliche Zeit danken. Danke Angi für die wohltuenden verlängerten Konferenzaufenthalte, sowie dir und Chris für das gründliche Korrekturlesen meiner Dissertation. Vielen Dank an alle für eure stetige Hilfe und Motivation bei der Erstellung meiner Dissertation.

Meinen Freunden, meinen Herzensmenschen, danke ich, dass sie mich immer unterstützt und motiviert haben.

Der größte Dank gebührt meinen Eltern und meinem Onkel. Ich danke euch für eure unerschöpfliche Liebe, für euer Vertrauen und für eure Motivation. Ihr habt immer an mich geglaubt!